Interannual North Atlantic Sea Surface Height Dynamics and Associated Predictability

Robert Fraser

Exeter College

University of Oxford

A thesis submitted for the degree of

Doctor of Philosophy in Atmospheric, Oceanic and Planetary Physics

Hilary 2018

This thesis is dedicated to Erin

Abstract

A significant degree of uncertainty is associated with interannual sea surface height (SSH) forecasts. This thesis investigates the physical origins of this uncertainty, by examining the contributions of atmospherically-modulated and ocean intrinsic processes to interannual SSH dynamics and its associated interannual predictability. The analysis is based on several numerical simulations at eddy-permitting resolution, ranging in complexity from barotropic and baroclinic models, with idealised geometries and forcings, to a state-of-the-art coupled climate model. Using the output of these various simulations, I diagnosed the relevant dynamical responses of sea level variability and statistically estimated the associated predictability timescales. The three main results can be summarized as follows. (1) New insights into the mechanisms by which eddy-fluxes of momentum and buoyancy, in mid-latitude jet regions, act to modulate interannual intrinsic ocean variability. This includes the identification of interannual equatoward migrations of anomalous baroclinic eddy-driven jets arising due to a meridional asymmetry in the Eady growth rate. (2) In idealised models, the components of SSH variability associated with the intrinsic dynamical mechanisms related to eddy momentum fluxes only display predictability on sub-annual timescales. However, the aforementioned buoyancy-driven mechanism introduces multi-year predictability. (3) In the coupled climate model, the dynamical response to external forcing, modulated by modes of atmospheric variability, is shown to be predictable on interannual timescales (1-2 years) and contributes to predictable SSH signals along the US east coast and in the vicinity of the Gulf Stream. This demonstrates that the chaotic variability introduced by mesoscale eddies does not completely obscure signals of interannual SSH predictability. These results highlight the importance of ocean-atmosphere interactions in interannual SSH forecasts, and demonstrate the relevance of mesoscale eddies in modulating interannual variability in mid-latitude ocean jets.

Acknowledgements

I begin by thanking my Oxford supervisor Laure Zanna. It has been a privilege to work with such a diligent and creative scientist. Without her astute advice, persistent support and considerable patience, this thesis would not have been possible. Many thanks to my supervisor Chris Wilson, who offered insightful advice and discussion throughout my studies. He always offered his time and support, no matter how small the request and helped me immensely. Thanks, also to my Met Office supervisor Matthew Palmer, for all his detailed feedback and his help with acquiring the coupled climate model output.

I would also like to thank all the members of the Ocean Climate group for creating a stimulating and entertaining environment to be a part of. I am particularly indebted to my good friends and academic siblings, Tomos David and Tom Bolton. Tomos' boundless enthusiasm and ingenuity, offered great amusement and aided me tremendously throughout my studies. Whilst Tom's rational temperament complimented Tomos' exuberance well, and discussions with him assisted me greatly, especially through the final few months. Thanks also to David Marshall and Thierry Penduff for acting as my examiners and for their helpful comments.

A special mention also goes to the other DPhil students in my year group: Graeme MacGilchrist, Geoff Stanley, and Joe Hitchen, whom each offered great comradery and advice. I would also like to thank several others who provided constructive feedback and discussions on the work presented, in particular: Helen Johnson, Andrew Wells, Chris Roberts, Chris Hughes, Dave Munday, James Anstey, Markus Huber, Liam Brannigan, Chris O'Reilly, Fenwick Cooper, Edward Doddridge and Benjamin Bronselaer.

I am grateful to my friends and family, for their assistance and perspective. Finally, I would like to thank Erin, for her constant support, belief, and understanding.

Contents

List of Figures

List of Tables

Chapter 1

Introduction

Global mean sea level is estimated to be rising at a rate of $3.2 \pm 0.4\,\mathrm{mm\,year}^{-1}$, and this rate has increased significantly since 1900 (Fig. 1.1 and Church and White, 2011). The impact of global sea level rise on coastal regions promises to be a major challenge in the 21^{st} century (Church et al., 2010). This threat is particularly significant when one considers the large global populations that are already vulnerable to coastal flooding and those that are projected to be at risk. By 2080, up to an additional 50 million people per year will experience coastal flooding (Nicholls, 2004). The predicted economic implications of such flooding are considerable; without adaption, the annual losses due to coastal flooding in 2100 are expected to be 0.3-9.3% of the global gross domestic product (Hinkel et al., 2014). Such losses are unlikely to be tolerated, but the costs of adaption are also substantial, with estimated global annual costs of coastal protection in 2100 of 12-71 billion US dollars (Hinkel et al., 2014).

Global sea level rise over the past century is primarily due to a combination of thermal expansion and glacial melting (Fig. 1.2). However, future changes in sea level are not projected to be uniform over the globe (Fig. 1.3a), as regional sea level trends can be several orders of magnitude larger than the global mean value, and can even be of a different sign (Stammer et al., 2013). These regional differences are due to variations in ocean currents, surface winds, ocean heat uptake and salinity (Sterlini et al., 2016). At the end of the 21^{st} century, sea level rise in some coastal regions around the North Atlantic Ocean, is expected to be 30% higher than the global mean

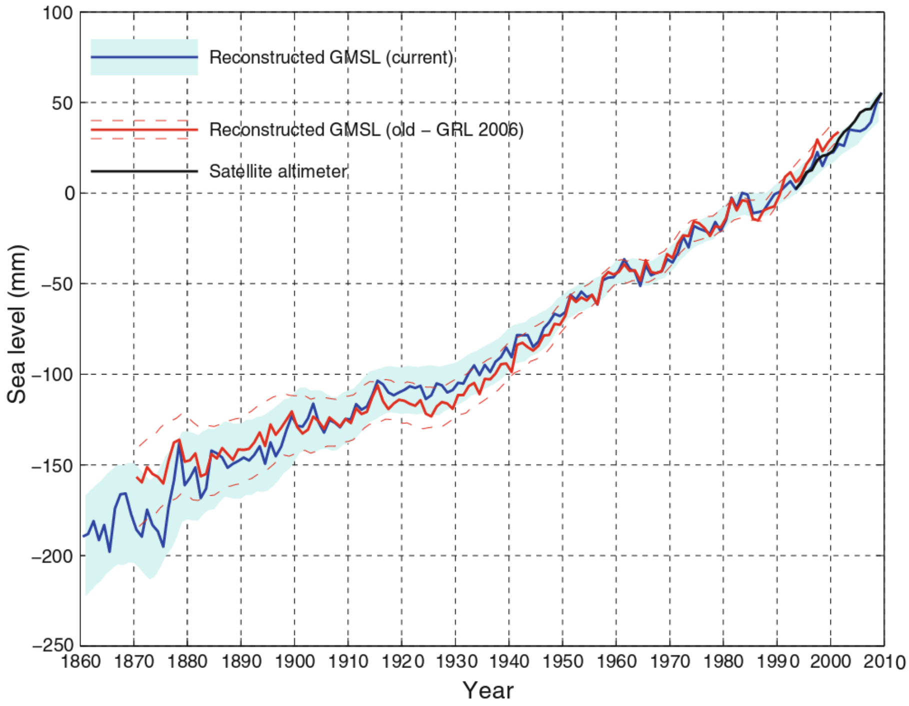

Figure 1.1: Estimates of global average sea level: firstly, generated with coastal and island tide gauge sea-level data from 1860-2009 (blue) with the one standard deviation uncertainty shaded, and secondly, the estimates from Church and White (2006), again estimated using tide gauge data (red) with the one standard deviation uncertainty in dashed. The satellite altimetry measurements since 1993 are also shown in black (Figure from Church and White, 2011).

(Slangen et al., 2014). This variation is already noticeable along the US east coast, where the current rate of sea level rise is larger than the global mean rate (Yin et al., 2009; Sallenger et al., 2012).

There is still a considerable amount of uncertainty associated with regional sea level changes on interannual (timescales $>$ 1 year and $<$ 10 years) to decadal timescales ($>$ 10 years). This is demonstrated in Figure 1.3b, which shows that current climate simulations have a large spread in their sea level projections, particularly in the North Atlantic. This uncertainty is related to a combination of both the climate system's natural variability, and its response to anthropogenic forcings. Moreover, there are additional uncertainties which are not taken into account for in current projections, as many climate models incorporate low resolution ocean models and therefore don't

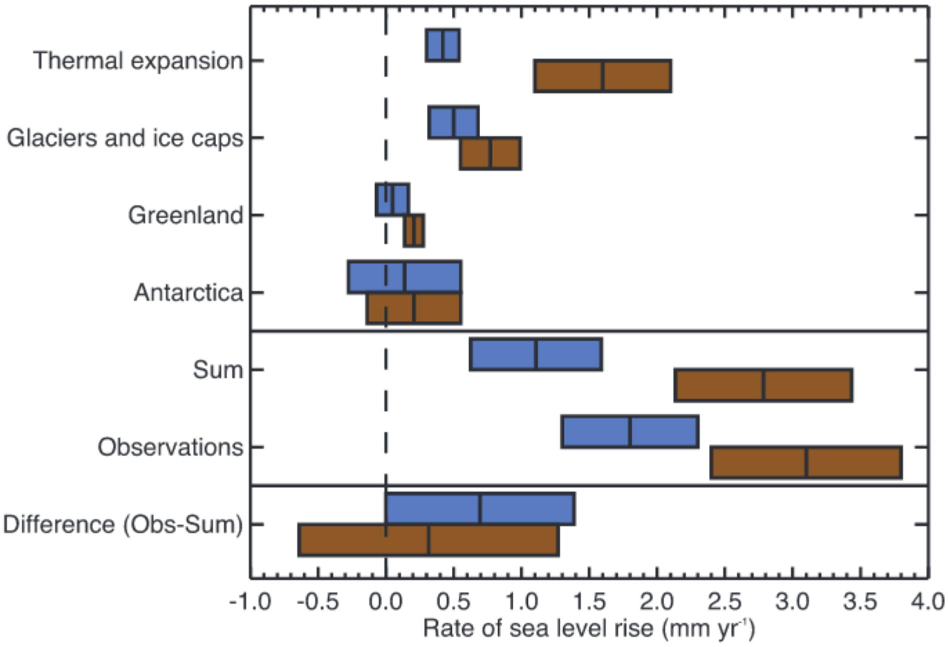

Figure 1.2: Estimates of the contributions of different terms to the rate of global mean sea level rise. The blue values are for all the contributions from 1961-2003, whereas the brown values are from 1993-2003. The bars represent the 90% error range (Figure from Bindoff et al., 2007).

include the effects related to mesoscale eddies. Over the next few decades, it is likely that the uncertainty in regional sea level change will be dominated by variations caused by natural climate variability (Hu and Deser, 2013). Therefore, further research is required to potentially constrain such uncertainty. Moreover, futher work is needed to improve our understanding of interannual sea level predictability (the extent to which future states of a system may be predicted based on knowledge of current and past states of the system (AMS, 2012)).

1.1 Sea Surface Height Variability

Sea surface height (SSH) is influenced by numerous forcings, dynamical processes and displays complex spatial and temporal variability. A simple framework based on the hydrostatic and Boussinesq approximations, can be used to identify the mechanisms responsible for variations in SSH. Following Gill and Niller (1973), sea level anomalies,

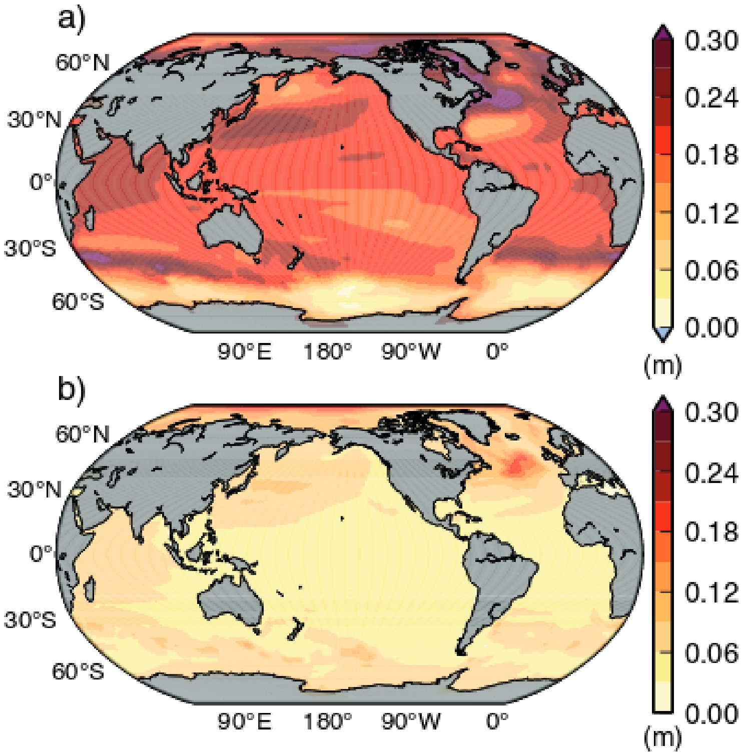

Figure 1.3: a) The ensemble mean projections of the time averaged dynamic and steric sea level changes (the figure includes the globally averaged steric sea level increase of 0.18 ± 0.05m), for 2081–2100 relative to 1986–2005, from 21 Coupled Model Intercomparison Project Phase 5 (CMIP5) models using Representative Concentration Pathways (RCP) 4.5; b) the root mean square deviation of the individual models, relative to the ensemble mean (Figure from Church et al., 2013).

η' can be expressed as the sum of three terms,

$$\eta' = \eta'_a + \eta'_b + \eta'_s = -\frac{p'_a}{g\rho_0} + \frac{p'_b}{g\rho_0} - \frac{1}{\rho_0}\int_{-H}^{0} \rho'(T,S,p)dz, \tag{1.1}$$

where z is depth, p'_b is the anomalous pressure at the bottom of the ocean ($z = -H$), p'_a is the anomalous atmospheric surface pressure (at $z = \eta$), g is the acceleration due to gravity, ρ_0 the reference density and $\rho'(T,S,p)$ is the density deviation from the reference density, which is a function of temperature T, salinity S and pressure p. The three terms on the right-hand side of equation 1.1, are the barometric term $\eta'_a = -\frac{p'_a}{g\rho_0}$, the water density related steric term, $\eta'_s = -\frac{1}{\rho_0}\int_{-H}^{0}\rho'(T,S,p)dz$ and $\eta'_b = \frac{p'_b}{g\rho_0}$, which depends on bottom pressure and gravity.

The barometric term is related to changes in the atmospheric pressure. This effect is not considered in this thesis, as this response is isostatic on interannual timescales (Meyssignac et al., 2017). The contribution from the bottom pressure arises due to water mass redistribution, in response to changes in the atmospheric forcings (Meyssignac et al., 2017). This is the dominant component of SSH variability on short timescales (periods <1 month). However on interannual timescales, it is generally smaller than the variations due to density changes (Meyssignac et al., 2017). The steric component arises due to variations in buoyancy forcing at the ocean's surface and the redistribution of salinity and heat by ocean processes (advection and mixing) in response to variations in the external wind forcings (Meyssignac et al., 2017). Density changes that result from thermal expansion are called thermosteric, and those that are due to variations in the salinity of the water are termed halosteric (Church et al., 2010). Globally, the thermosteric component is the primary driver for the observed trends in regional sea level patterns, shown in Fig. 1.3a (Lombard et al., 2005; Cazenave and Llovel, 2010). The halosteric component has a more modest impact on such trends; however, it can be significant in specific regions, including the North Atlantic (Gregory and Lowe, 2000; Bouttes et al., 2013; Church et al., 2013). The thermosteric component is the most significant contributor to interannual steric SSH variability, and over most of the ocean is dominated by changes in buoyancy fluxes and heat advection.

1.2 Interannual Variability of Sea Surface Height in the North Atlantic

In the North Atlantic, the SSH adjusts on interannual timescales in response to both the applied atmospheric forcings (wind stress and buoyancy forcings), and the variations due to intrinsic ocean processes (that are generated in the absence of variability in the atmospheric forcings). Within the North Atlantic the relative contributions of the different forcings and adjustment processes, to the interannual variability, are regionally dependent (Cabanes et al., 2006).

Many dynamical mechanisms drive the oceans adjustment to changes in the wind forcing on interannual timescales. These include wind stress curl anomalies acting locally on the ocean through Ekman transport and adjusting both the height of the thermocline and the sea level. Moreover, it is the wind forcing which drives the large-scale ocean gyres, and therefore variations in the wind stress could cause large-scale SSH adjustments (Cabanes et al., 2006). In the North Atlantic, the adjustments related to changes in the wind forcings are also seen to be correlated with the largest mode of atmospheric variability, the North Atlantic Oscillation (NAO) (Häkkinen et al., 2011). However, it is uncertain how important such correlations are as others have argued that much of the interannual SSH variability is set by the baroclinic response to stochastic wind forcing, and is less dependent on the low-frequency modes of atmospheric variability (Frankignoul et al., 1997).

In large parts of the North Atlantic, the adjustments of steric SSH to surface heat fluxes, is the largest contributor to interannual SSH variability(Cabanes et al., 2006). The forcing provided by freshwater fluxes also merits consideration due to the recent sizeable freshwater influx from Greenland. This could potentially have a substantial effect on North Atlantic steric SSH variability (Bamber et al., 2012). In the North West Atlantic interannual SSH variability is thought to be primarily buoyancy driven, and possibly related to fluctuations in the Atlantic meridional overturning circulation (AMOC) (Roberts et al., 2016).

Intrinsic nonlinear ocean variability may also play a crucial role in driving interannual variability. This effect is particularly relevant in eddy active regions, where instabilities generate mesoscale eddies on scales of 10-100km. These eddies can interact with the mean flow to drive variability on interannual timescales. Penduff et al. (2011) demonstrated in a series of Ocean General Circulation Model (OGCM) experiments, that intrinsic mechanisms contribute 60%-80% of the total interannual sea

Dynamical mechanisms and components	Driver	Time scale	References
Remotely forced baroclinic Rossby waves	Wind Stress	Months to decades	(Frankignoul et al., 1997) (Cabanes et al., 2006) (Qiu and Chen, 2006)
Boundary forced Rossby waves	Perturbations at eastern boundary	Months to decades	(Cabanes et al., 2006) (Qiu and Chen, 2005)
Kelvin Waves	Wind stress	Months to years	(Enfield and Allen, 1980) Forget and Ponte (2015)
Time dependent Sverdrup balance	Zonal integral of wind stress curl	Months to years	(Qiu, 2002) (Stammer, 2008) (Cabanes et al., 2006)
Steric (advection)	Advection of temperature/salinity anomalies	Years to decades	(Cabanes et al., 2006) (Polkova and Stammer, 2015)
Buoyancy forced circulation changes	Heat and freshwater fluxes in regions of water mass formation	Years to decades	(Häkkinen et al., 2011)
Barotropic adjustments	Wind stress and mass fluxes, steric changes over sloping topography	Days to years	(Fukumori et al., 1998)
Locally forced Ekman pumping	Local wind stress curl	Months to years	(Häkkinen, 2001) (Cabanes et al., 2006) (Köhl, 2014)
Steric (local)	Local air-sea buoyancy fluxes	Months to decades	(Gill and Niller, 1973) (Cabanes et al., 2006) (Piecuch and Pontre, 2011)
Unforced (intrinsic) eddies	Barotropic and baroclinic instability	Days to years	(Cabanes et al., 2006) (Sérazin et al., 2015)
Mixing	Temperature and salinity gradients	Years to decades	(Piecuch and Pontre, 2011)

Table 1.1: Dynamical mechanisms and components which contribute to interannual SSH variability, closely based on a table by Roberts et al. (2016).

level anomaly variance, along the path of the Gulf Stream and in the North Atlantic subpolar gyre. Several other studies have looked at such variability in idealised eddy-resolving models (Spall, 1996; Dijkstra and Ghil, 2005; Berloff et al., 2007). However, it is still uncertain which timescales of the intrinsically generated variability are predictable.

A summary of the processes and drivers, which are known to contribute to the variability of sea level on interannual timescales are detailed in Table 1.1. These include: Rossby wave propagation, barotropic and baroclinic instabilities, ocean-atmosphere interactions, topographic interactions and nonlinear eddy-mean flow interactions (Pierini et al., 2014).

There are also other processes which influence SSH variability in the North Atlantic, but which do not act on interannual timescales. For example, geodynamical effects are known to act on centennial timescales. Such effects occur when the earth below-melting land ice, undergoes a deformational response, with an uplift in the near field and subsidence in the far field, resulting in variations of the relative sea level (Church et al., 2010). As the ice melts, there are also changes in the gravitational attraction between the land ice and the sea (Cazenave and Llovel, 2010). The magnitude of these effects are specific to each ice mass, therefore the resulting impact on sea level has a distinct pattern (Mitrovica et al., 2009). Gravity and inertio-gravity waves are not considered in this thesis because the frequencies on which they act are deemed to be unimportant on interannual and decadal timescales.

1.3 Predictability of Interannual Sea Surface Height

Although the predictability of several oceanic fields in the North Atlantic has been previously examined in the literature (Wunsch, 2013), few studies have investigated the predictability of interannual SSH. Of those which have, many are global studies or are focused in the Pacific (Xue and Leetmaa, 2000; Chowdhury et al., 2007; Qiu and Chen, 2010; Wang et al., 2013). Only a few studies have addressed the predictability of the aforementioned intrinsic variability, and it is still uncertain how this variability impacts SSH predictability (Giannakis and Majda, 2012; Wang et al., 2013).

Studies by Nonaka et al. (2016) and Roberts et al. (2016) focused on interannual SSH variability in eddy-resolving and eddy-permitting ocean models. Nonaka et al. (2016) investigated the associated predictability of mid-latitude ocean currents, using an ensemble of eddy-resolving ($\sim 1/10°$) ocean general circulation model (OGCM) experiments, finding a lack of predictability in the jet regions due to the contributions from the mesoscale eddies. Roberts et al. (2016) examined interannual SSH predictability using the eddy-permitting ($\sim 1/4°$), Hadley Centre Global Environment Model version 3 (HadGEM3), and found predictive skill in tropics on timescales of years, but again with a lack of skill in jet regions.

Other studies, have used low resolution OGCMs (1°-2°) to investigate dynamic and steric SSH predictability (Schneider and Griffies, 1999; Miles et al., 2014; Polkova and Stammer, 2015). Polkova and Stammer (2015) found predictive skill in interannual steric SSH predictions in the subtropics on 2-5 years. Such skill was related to adjustments due to baroclinic Rossby waves. Skill was also found in the North Atlantic subpolar gyre on timescales of 2-5 years, which was related to changes due to movement of spiciness along isopycnals. Sea level predictability has also been diagnosed in models on longer timescales. Schneider and Griffies (1999) found SSH predictability in the North Atlantic on times of up to 17 years, using an ensemble of coupled climate model runs.

1.4 Thesis Aims

This thesis investigates the interannual variability and predictability of SSH anomalies in the North Atlantic in the presence of eddies. A hierarchy of numerical simulations and several different methods for evaluating predictability are used to examine the dynamical mechanisms which influence interannual SSH predictability.

The specific aims of this thesis are:

- **to examine the role of mesoscale eddies in driving interannual SSH variability;**
- **to quantify the predictability of SSH due to the sensitivity in ocean initial conditions and surface forcings in the presence of resolved eddies;**
- **to investigate the relative contributions of the intrinsic and externally forced SSH components, to both the total interannual SSH variability and any associated predictability.**

The thesis is organised as follows. Chapter 2 provides a discussion of the dynamical mechanisms related to interannual SSH variability, and discusses the definitions and methods relevant to evaluating any related predictability. These include methods for assessing predictability, related to both the initial and boundary conditions of the different models considered. Chapter 3 introduces the idealized ocean-only models and momentum budgets, which are used extensively in the results chapters.

Chapter 4 addresses the intrinsic variability present in both barotropic and baroclinic double gyre experiments. Interannual variability is found in the jet region in the barotropic double gyre, and in all areas in the baroclinic experiment. In the barotropic model, this variability corresponds to interannual variations in both the jet position and transport. A momentum budget decomposition indicates the potential for the eddies to control the latitudinal position of the jet. In the baroclinic model, there is an interannual meridional migration of zonal velocity anomalies; the migration is attributed to variations in the eddy heat fluxes.

Chapter 5 consists of an evaluation of predictability related to intrinsic mechanisms, in the barotropic and baroclinic models. In both models, even though interannual variability is present, the predictions only give skill on time scales of a month to one year in most of the model's domain. However, the meridional migrations of the zonal velocity anomalies in the baroclinic model display predictability on longer time scales (4-5 years). An investigation of the influences of variations in the external atmospheric forcings on forecast skill, in the baroclinic double gyre model is also presented. These experiments examine a relationship between the baroclinic pressure gradients and SSH variability time in the jet. A short study is also performed which probes the potential for a time-dependent Sverdrup balance to influence gyre scale SSH predictability.

Chapter 6 examines the role of eddies on SSH predictability in a fully coupled Atmosphere-Ocean Global Circulation Model (AOGCM). Forecasts of SSH are found to be particularly sensitive to perturbations at the detachment point of the Gulf Stream. Moreover, linear predictability occurs on timescales of 1-2 years. Large-scale predictable components, which display predictability on times in the range of 26-28 months are also presented. These SSH components are found to lag changes in the wind stress by 15 months. Finally, Chapter 7 consists of a discussion of future work and presents the conclusions of the thesis.

Chapter 2

Background and Theory

2.1 Ocean Dynamics

This section will briefly review the dynamical mechanisms which shape the mean SSH field, as well as those relevant to generating interannual SSH variability (detailed in Table 1.1). Based on the work discussed in Section 1.2, it is hypothesised that the mechanisms of SSH variability can be broadly separated by both geographical regions within the North Atlantic and driving mechanisms.

Firstly, I will discuss the processes which are responsible for large-scale mean SSH. Secondly, the adjustments related to variations in the external wind and buoyancy forcings are considered. Finally, as it is hypothesised that intrinsic ocean processes will play a substantial role in the interannual variability in the Gulf Stream, the relevant eddy-mean flow interactions will be reviewed.

2.1.1 Mean Sea Surface Height

Figure 2.1a shows the time-mean SSH in the North Atlantic from 21 years of satellite altimeter data between 1 Jan 1993 – 31 May 2014 (AVISO, 2012). The major features are wind-driven gyres, namely the Subpolar (northern and cyclonic) and the Subtropical (southern and anticyclonic) gyres. The SSH gradients are related to the underlying ocean currents; on timescales longer than several days and spatial scales larger than several kilometers, the majority of the ocean, including the ocean gyres, is to a good approximation in geostrophic balance (the Rossby number is sufficiently

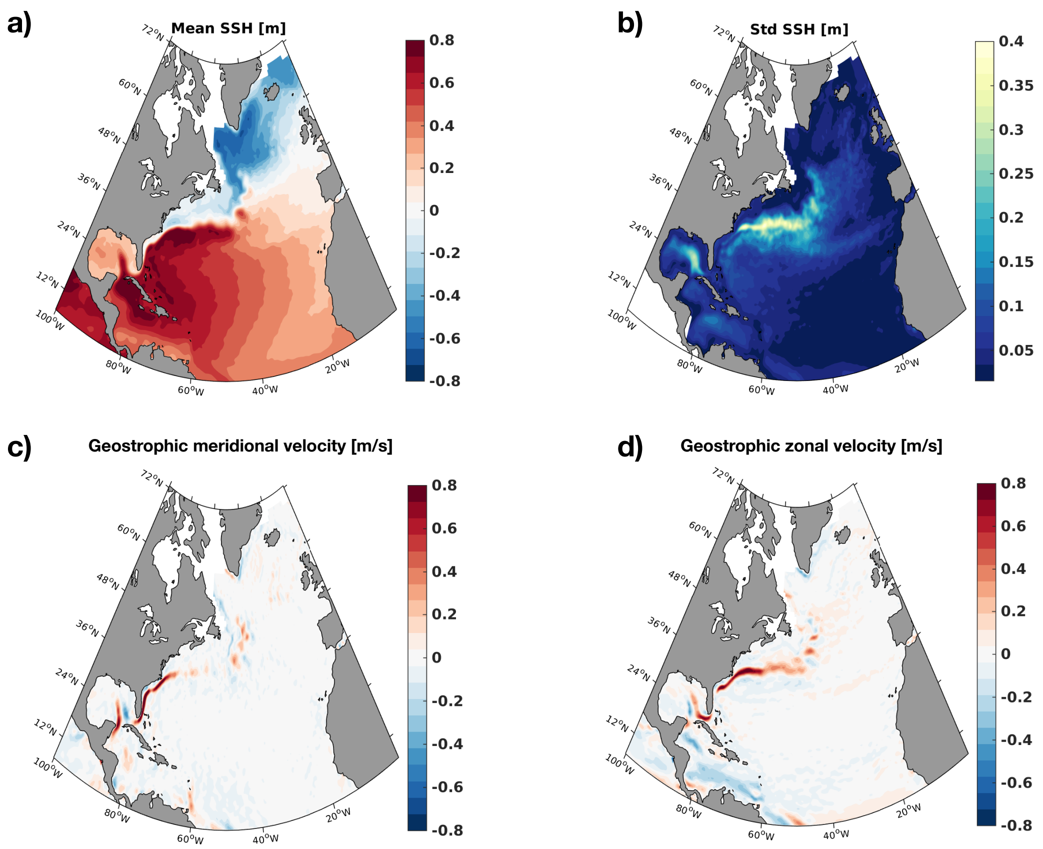

Figure 2.1: Values calculated from monthly averaged altimetry data (AVISO, 2012): a) mean SSH, b) standard deviation of SSH, c) the mean meridional geostrophic velocity, d) the mean zonal geostrophic velocity.

small). The horizontal geostrophic velocities are given as a balance of the pressure gradient and the Coriolis force such that

$$v_g = \frac{1}{f\rho_0}\frac{\partial p}{\partial x} \quad \text{and} \quad u_g = -\frac{1}{f\rho_0}\frac{\partial p}{\partial y}, \tag{2.1}$$

where x and y refer to distances directed eastward and northward in Cartesian coordinates. The Coriolis parameter, $f = 2\Omega sin(\phi)$ is approximated using the mid-latitude beta plane approximation $f(y) = f_0 + \beta y$, where $f_0 = 2\Omega sin(\phi_0)$ and $\beta = 2(\Omega/a)cos\phi_0$, where ϕ is the latitude, ϕ_0 is a chosen reference latitude, Ω is the angular velocity of the Earth, and a is the radius of the Earth. These geostrophic velocities can be related to the gradient of SSH through the hydrostatic approximation,

$$\frac{\partial p}{\partial z} = -g\rho, \tag{2.2}$$

where z is the vertical co-ordinate, resulting in,

$$v_g = \frac{g}{f}\frac{\partial \eta}{\partial x} \quad \text{and} \quad u_g = -\frac{g}{f}\frac{\partial \eta}{\partial y}, \tag{2.3}$$

where η is the SSH and g is gravity. Thus, another major feature of the mean field is that the geostrophic flow, calculated from the time mean altimeter data, is intensified along both the western boundary and Gulf Stream path (Figure 2.1, panels c and d). The region with the largest SSH variability (Figure 2.1b) is also situated in the western boundary current regions.

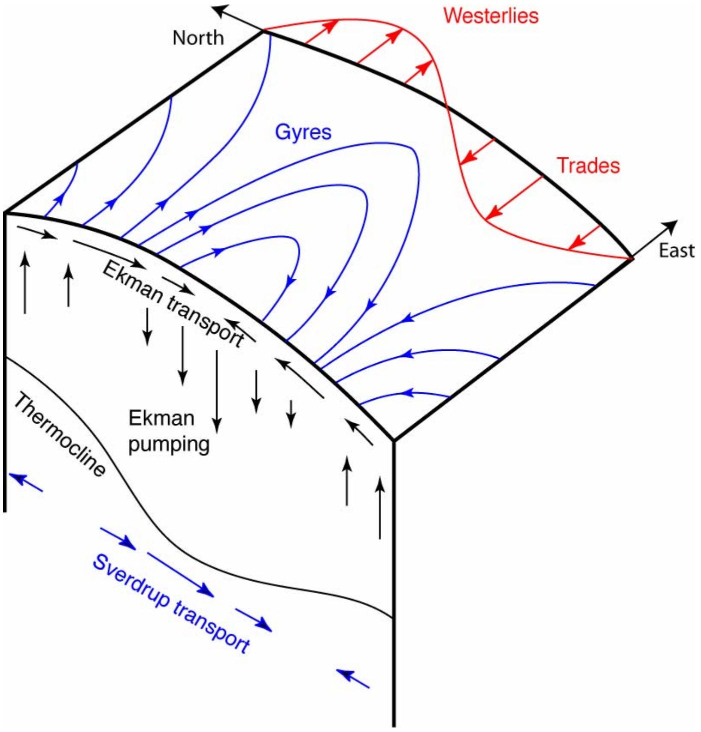

Figure 2.2: Sverdrup balance in the northern hemisphere, where westerlies and trade winds generate Ekman pumping and suction which results in Sverdrup balance (Figure from Talley et al., 2011).

The large scale gyre structures were first explained by Sverdrup (1947), through a consideration of the mid-ocean vorticity balance. The geostrophic equations (2.1), can be combined to give the vorticity equation (Talley et al., 2011):

$$f(\frac{\partial u_g}{\partial x} + \frac{\partial v_g}{\partial y}) + \beta v_g = 0, \tag{2.4}$$

then using the continuity equation,

$$\nabla \cdot \mathbf{u} = \frac{\partial u}{\partial x} + \frac{\partial v}{\partial y} + \frac{\partial w}{\partial z} = 0, \tag{2.5}$$

where w is the vertical velocity, results in,

$$\beta v_g = f\frac{\partial w}{\partial z}. \tag{2.6}$$

Finally, by vertically integrating from the bottom of the ocean (assuming w is negligible at the sea floor) to the surface (assuming the vertical velocity is due to Ekman pumping/suction), we obtain

$$\beta V_g = f w_{Ek}, \tag{2.7}$$

where V_g is the vertically integrated meridional transport and the Ekman pumping is,

$$w_{Ek} = \left[\frac{\partial}{\partial x}(\frac{\tau^y}{\rho f}) - \frac{\partial}{\partial y}(\frac{\tau^x}{\rho f})\right] = \nabla \times \frac{\boldsymbol{\tau}}{\rho f}, \tag{2.8}$$

where (τ^x, τ^y) are the components of the surface wind stress, $\boldsymbol{\tau}$. This results in the Sverdrup balance,

$$\beta V_g = f\nabla \times \frac{\boldsymbol{\tau}}{\rho f}, \tag{2.9}$$

which is shown schematically in Figure 2.2. This balance relates the meridional transport in the gyre interior to the wind stress curl. In the ocean interior, where the inertial and frictional terms can be neglected there is a balance between the advection of planetary vorticity and the input of vorticity by the curl of the wind stress.

Stommel (1948) and Munk (1950) proposed the first explanations of western intensification which included frictional effects. As the ocean flow is bounded, dissipative effects cannot be neglected, and therefore a boundary layer must be included. Only at the western boundary is the creation of a frictional curl that opposes that of the wind stress possible, therefore only a western boundary layer is physically realisable (Vallis, 2006).

2.1.2 Wind and Buoyancy Forced Sea Surface Height Variability

The external wind forcings can impact interannual SSH variability through several mechanisms, detailed in Table 1.1. Wind stress curl anomalies can interact locally with the ocean by establishing Ekman transports. Convergence and divergence of the Ekman transports adjust both the height of the thermocline and the SSH, as shown in Figure 2.2. Only a small proportion of interannual SSH variability can be related directly to Ekman pumping, as a more substantial response is seen in the oceans non-local adjustment to the wind (Cabanes et al., 2006). Variations in the time-dependent barotropic Sverdrup balance can explain 20-50% of the observed interannual variability in the North Atlantic, between latitudes of 40°-50°N (Cabanes et al., 2006). This response is related to large-scale patterns of variability in the wind stress curl, which correlate with low-frequency weather phenomena such as the NAO (Cabanes et al., 2006; Häkkinen et al., 2011). Such SSH patterns can be attributed to wind-driven variations, leading to changes in the relative strength of the subtropical and subpolar gyres. The subtropical gyre is a region where interannual SSH variability is primarily governed by changes in the wind-driven, surface momentum fluxes (Wang et al., 2015; Roberts et al., 2016).

Interannual SSH variability is also dependent on variations in heat and freshwater fluxes. In the east of the North Atlantic and in the subpolar gyre, interannual variability is dominated by the local adjustments to surface heat fluxes (Cabanes et al., 2006; Wang et al., 2015). The steric components of SSH also adjust on interannual timescales, to changes in the buoyancy forcings, both locally and through advection (Cabanes et al., 2006; Köhl, 2014; Polkova and Stammer, 2015). In the North West Atlantic, interannual SSH variability is thought to be primarily buoyancy driven and is related to fluctuations in the Atlantic meridional overturning circulation (AMOC) (Roberts et al., 2016). The link between SSH along the US east coast and the strength of the AMOC has been established both in observations and in eddy-permitting ocean models (Bingham and Hughes, 2009).

2.1.3 Wave Adjustment Mechanisms

Changes in the wind and buoyancy forcings also result in dynamical adjustments of the large-scale ocean circulation, driven by large-scale planetary waves. Rossby and Kelvin waves act, both independently and in combination, to change interannual oceanic adjustments.

Rossby waves have been shown to cause SSH variability on interannual timescales (Frankignoul et al., 1997; Cabanes et al., 2006; Qiu and Chen, 2006). The dispersion relations for barotropic Rossby waves, with uniform zonal background flow, is given by

$$\omega = Uk - \frac{\beta k}{k^2 + l^2}, \tag{2.10}$$

where ω is the angular frequency, k and l are the zonal and meridional wave numbers respectively and U is the zonal velocity of the mean flow. In the baroclinic case, the dispersion relation is

$$\omega = Uk - \frac{\beta k}{k^2 + l^2 + (1/L_n)^2}, \tag{2.11}$$

where the baroclinic Rossby deformation radius is,

$$L_n = \frac{NH_l}{n\pi f_0}, \qquad n = 0, 1, 2... \tag{2.12}$$

for the first n baroclinic modes, where N is the Brunt-Väisälä frequency and H_l is the scale height of the flow. The baroclinic Rossby deformation radius varies from about 10km at high latitudes to 200km in the tropics. As a result, the Rossby wave phase velocities vary as a function of latitude, with Rossby waves at mid-latitudes propagating on interannual to decadal timescales. However, both observational and model studies suggest that large scale Rossby waves are unable to cross the North Atlantic at mid to high latitudes. This is because there is a critical latitude (≈20°) whereby large-scale baroclinic Rossby basin modes, which emanate from the eastern boundary succumb to instabilities and fail to cross the ocean basin (Isachsen et al., 2007). Also as it theoretically takes interannaul to decadal timescales for baroclinic Rossby waves to cross the ocean basin, they may succumb to dissipation (Osychny and Cornillon, 2004).

Kelvin waves also respond to changes in the wind stress. In observations, they have been seen to be responsible for SSH variability on monthly timescales, in equatorial and coastal regions (Enfield and Allen, 1980; Forget and Ponte, 2015). They are a type of low-frequency gravity wave which is trapped to the coast or the equator. In the Northern hemisphere, they propagate anticlockwise around the basin, and under the shallow water approximation have a dispersion relation,

$$\omega = +\sqrt{gH}m, \tag{2.13}$$

where m is the along boundary wavenumber. Away from the boundary, they decay with an e-folding length scale equal to the Rossby radius of deformation. Kelvin waves can be further subdivided into surface (barotropic) and internal (baroclinic) waves. The surface waves penetrate the whole water column, whereas, the internal waves are often found in layers with large density gradients. Therefore, the wave amplitude of internal waves is small at the surface compared to that due to surface waves. Internal Kelvin waves also exhibit a slower phase speed of $\mathcal{O}(1)ms^{-1}$ compared to the $\approx 200ms^{-1}$ speed found for the surface waves (Wang, 2015).

Kelvin and long Rossby waves can also act in combination and have been linked to interannual basin-scale adjustment processes. Several studies have looked at the adjustment of the ocean in abrupt climate change scenarios, where there is an increase in SSH in the polar regions of the North Atlantic, or similarly there is a spin down of the thermohaline circulation (Hsieh and Bryan, 1996; Johnson and Marshall, 2002). This increase would be initially propagated around the basin by Kelvin waves on a timescale of months (Johnson and Marshall, 2002). Subsequently, long Rossby waves emanating from the eastern boundary can communicate the rise to the rest of the basin on timescales of months-years (Hsieh and Bryan, 1996; Johnson and Marshall, 2002). Johnson and Marshall (2002) formulated an equation which can be used to calculate the time-varying circulation in the entire basin, using only the thermocline depth on the eastern boundary.

The frequencies of SSH variability also have a strong dependence on the underlying bathymetry (Cabanes et al., 2006; Hughes and Williams, 2010). There is an observed transition in variability between regions on the coastal shelf, compared to the ocean basin. As on the shelf, there is more high-frequency variability, which is likely due to an increased response to wind forcing. In addition to this change, the coastal shelf is hypothesised to act as a low pass filter to signals propagating from the basin to the coast (Huthnance, 1989). This means that only low-frequency components of SSH variability propagating from the ocean interior can reach the coastal regions. Furthermore, the observed contrast in SSH variability between the coastal and ocean basin regions, is indicative that SSH anomalies may possess different predictable timescales in the two regions.

2.1.4 Interannual Variability of Double-Gyres

Double-gyre systems in high forcing, low dissipation regimes have been shown to display interannual variability. The variability manifests itself in changes in the meridional position and strength of the jet (McCalpin and Haidvogel, 1996; Jiang et al., 1995; Dijkstra and Ghil, 2005; Berloff et al., 2007). This behaviour has been studied extensively, using a dynamical systems framework to determine the bifurcations of states corresponding to the meridional position of mid-latitude jets (Jiang et al., 1995; Simonnet and Dijkstra, 2002; Dijkstra and Ghil, 2005). These studies propose mechanisms whereby the intrinsic interannual variability is steered by unstable low dimensional attractors. Figure 2.3 shows two stable solutions present in a double gyre quasi-geostrophic model at a certain wind forcing. The variability related to the meridional jet position is seen to fluctuate as the magnitude of the steady wind forcing applied is changed (or equivalently as the Reynolds number changes). It remains uncertain what causes the transitions in the jet strength and position. One possible mechanism was proposed by McCalpin and Haidvogel (1996), who examined a reduced gravity quasi-geostrophic double gyre model, which displayed interannual variability in the strength of the jet. They concluded that the variability was on a timescale relating to eddies impinging on the western boundary currents.

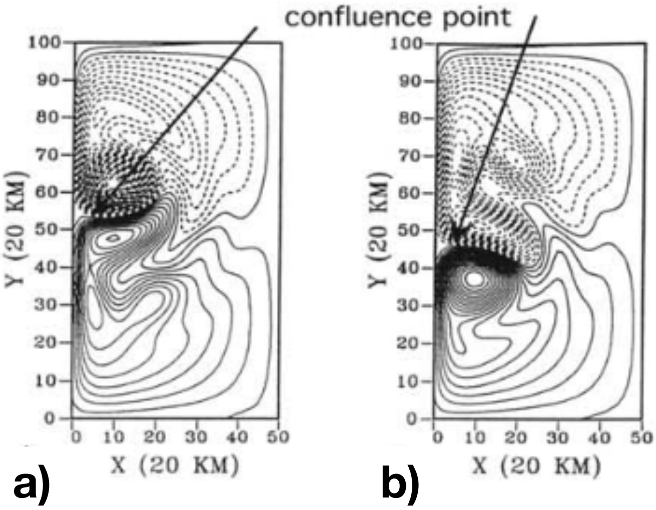

Figure 2.3: Patterns of a quasi-geostrophic model's layer's thickness, for two stable steady state solutions, occurring for the same wind forcing and illustrating different positions of the double-gyre's confluence point (Figure from Jiang et al., 1995).

Intrinsic processes in double gyre systems are also hypothesised to be partly responsible for the observed interannual variability in mode water formation (for example the variability discussed in Talley and Raymer (1982)). Using an isopycnic model, Hazeleger and Drijfhout (2000) suggested that low frequency modes of intrinsic variability evolve due to interactions with the mean flow and that these modes play a role in mode water formation. Studies in eddy-resolving OGCMs have investigated such effects and confirmed that intrinsic processes play an influential role in the variability of the mode water's volume, temperature and age in both the Pacific and North Atlantic (Douglass et al., 2012, 2013).

Several recent studies, have examined the effects eddies have on driving interannual variability in jet systems, in both idealised models (Spall, 1996; Berloff et al., 2007; Waterman, 2009), global eddy-resolving models (1/12°) (Sérazin et al., 2015) and observations(Qiu, 2000). Berloff et al. (2007) examined variability in a quasi-geostrophic, baroclinic, eddy-resolving, double gyre system model. They concluded that the intrinsic interannual variability originates from the presence of mesoscale eddies and their interactions with the mean flow, via a competition between the jet rectification processes and the inter-gyre transport of potential vorticity anomalies. It remains to be seen if such mechanisms exist in more complex models. Moreover, the specific eddy-mean flow interactions anticipated to drive meridional jet shifts are poorly understood.

2.1.5 Eddy-Mean Flow Interactions

Altimetry measurements show that the interannual SSH variability in the North Atlantic and Pacific is largely located in the vicinity of the western boundary current extension regions (Fu, 2004; Cabanes et al., 2006; Qiu and Chen, 2010; Hughes and Williams, 2010). For example, in the North Atlantic the Gulf Stream displays interannual variability in both its position and transport (Sasaki and Schneider, 2011). It is hypothesized that such variability may be driven intrinsically through eddy-mean flow interactions. Eddies (defined in this discussion as variations from a time mean) can impact the mean flow of the system through their fluxes of both momentum and vorticity. These eddy-mean flow interactions can act to accelerate the mean flow, as well as impacting the position of the jet through variable momentum convergences. Such interannual variability has been in seen in several idealised studies (Spall, 1996; Qiu, 2000; Berloff et al., 2007). Figure 2.4 demonstrates an eddy-wave-mean flow interaction which is hypothesized to be important in generating interannual variability in the jet's transport and position. It has several key stages:

- Instabilities in the jet (both baroclinic and barotropic) generate Rossby waves.
- Rossby waves propagate away from the jet.
- The direction of momentum flux is in the opposite direction, towards the jet.

- The eddy momentum flux acts to drive the jet and maybe change its latitudinal position.

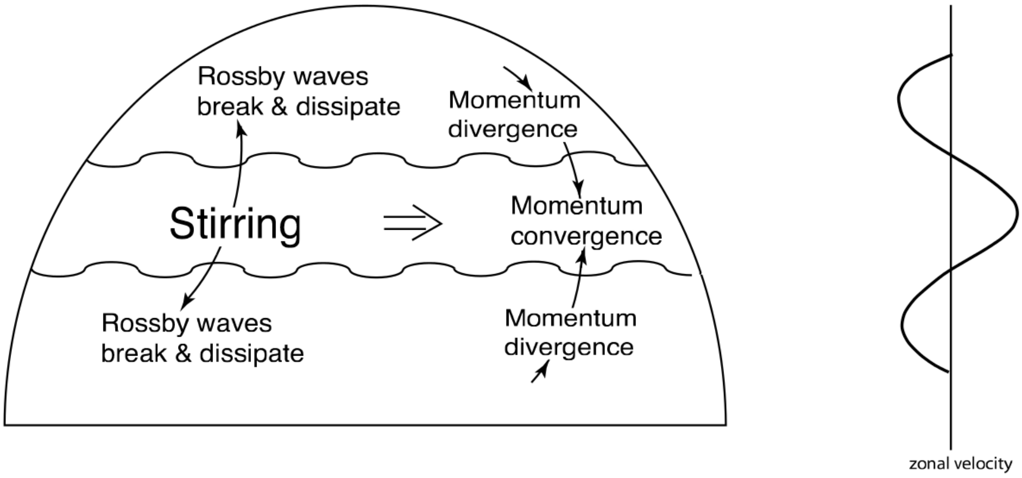

Figure 2.4: Schematic illustrating a conceptual model of eddy momentum flux driven by Rossby waves, and eddy mean flow interactions (Figure from Vallis, 2006).

The mechanism of momentum flux convergences can be elucidated through consideration of the following derivation, which follows Vallis (2006). Stirring in the mid-latitudes generates Rossby waves, which propagate away, break and dissipate. If the waves are approximated as being quasi-linear and are assumed not to interact, then just away from the source region they have the form:

$$\psi = \mathrm{Re}\left(Ce^{i(kx+ly-\omega t)}\right), \tag{2.14}$$

where ψ is a stream function ($u = -\partial\psi/\partial y$ and $v = \partial\psi/\partial x$), C is constant, $\omega = kc$ and the waves obey the barotropic Rossby wave dispersion relation (equation 2.10). Thus the meridional component of the group velocity is given by,

$$c_g^y = \frac{\partial\omega}{\partial l} = \frac{2\beta kl}{(k^2+l^2)^2}, \tag{2.15}$$

assuming no zonal shear. The direction of the group velocity is away from the source region (radiation condition), as the Rossby waves must transport energy away from the disturbance. Therefore north of the source kl is positive and southwards kl is negative. This is possible as there are two possible values of l, for each k using equation 2.10:

$$l = \pm\left(\frac{\beta}{U-c} - k^2\right)^{1/2}. \tag{2.16}$$

The velocity variations due to the Rossby waves are given by

$$u^{'} = -\mathrm{Re}\left(Cile^{i(kx+ly-\omega t)}\right), \qquad v^{'} = \mathrm{Re}\left(Cike^{i(kx+ly-\omega t)}\right), \tag{2.17}$$

and the associated momentum flux is

$$\overline{u'v'} = -\frac{1}{2}C^2kl. \tag{2.18}$$

Since the sign of kl is known, the momentum flux north of the disturbance is directed southward, while the momentum flux south of the disturbance is northward. This momentum convergence causes an eastward flow in the region of stirring and westward flow on either side, which leads to the formation of banana-shaped eddies. Therefore variations in these momentum fluxes around the jet, may cause changes in both the jet's position and transport.

Since it is hypothesised that the interannual SSH variability in the jet regions may be driven by eddies and that such effects will act locally in the jet region, we review the impact of eddies on the mean field of ocean jets. Recirculation gyres flank ocean jets, greatly increasing their transport (Hogg, 1992). The occurrence of these gyres has been related to eddies driving the mean flow (Haidvogel and Rhines, 1983; Jayne et al., 1996; Waterman, 2009). Waterman and Jayne (2011) examined the eddy-mean flow interactions, in the recirculation gyres of a barotropic model. The dynamics in the model were governed by the barotropic vorticity equation such that

$$\frac{\partial\overline{q}}{\partial t} + \nabla\cdot(\overline{\mathbf{u}}\overline{q}) + \nabla\cdot\overline{\mathbf{u}'q'} = \overline{F} + \overline{D}, \tag{2.19}$$

where q is the potential vorticity (PV), $\mathbf{u}$ is the velocity field, F is the forcing on the system, and D is the dissipation. Here any field X is decomposed into components representing the time mean ($\overline{X}$) and fluctuations from the mean flow (X') i.e. $X =$

$\overline{X} + X'$. Thus, the divergence of eddy potential vorticity flux or 'eddy potential vorticity forcing' term is given by $-\nabla \cdot \overline{\mathbf{u}'q'}$, and is shown in Figure 2.5a. The mean eddy forcing has two major effects on the jet. In the upstream region, eddies act to stabilise the jet and reduce the potential vorticity gradient between the gyres. Whereas in the downstream region, where the flow becomes barotropically unstable, the eddies act to drive transport in the recirculation gyres. The eddy forcing term displays a large amount of variability. It is therefore likely that this variability in the eddy forcing, acts to drive intrinsic interannual variability in the jet region (Berloff et al., 2007).

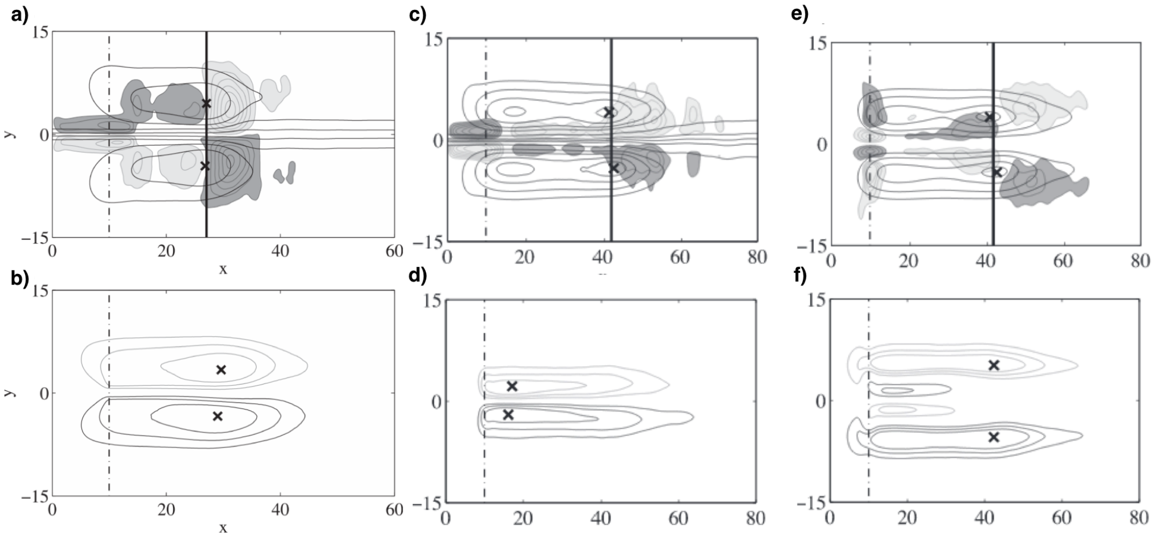

Figure 2.5: Barotropic simulation: a) Eddy potential vorticity forcing (filled contours), light (dark) gray indicates positive (negative) values. Black contours show the time-mean stream function. The × denotes the location where the jet becomes barotropically unstable. b) The time-mean circulation driven by linear dynamics forced by the above eddy forcing. Two-layer baroclinic simulation: (panels c and e) eddy potential vorticity forcings for the upper and lower layer, respectively. (panels d and f) The time mean circulation driven by linear dynamics forced by the vorticity fields in panels c and e. The time-mean circulations, driven by linear dynamics, forced by the eddy vorticity forcing fields directly above each panel. Black contours indicate positive values of the eddy-driven stream functions, and gray contours indicate negative values. The × symbol denotes the locations of the maximum time-mean eddy-driven transport (Figure from Waterman and Jayne, 2011).

Waterman and Jayne (2011) also used a quasigeostrophic model in a two-layer set-up to investigate the effects due to baroclinicity. In a similar manner to the barotropic case, Figure 2.5c demonstrates that in the downstream region the eddies act to drive the recirculation gyres, indicating this region is governed by barotropic behaviour (Waterman and Jayne, 2011). In the stable upstream region, there is a difference in the action of the eddies, relative to the barotropic case, with the eddies acting to accelerate the jet in the upper layer but to decelerate it in the lower layer (Waterman and Jayne, 2011).

In addition to these variations in momentum forcings, several model and observation-based studies have reported the presence of jets migrating in meridional directions on interannual timescales (Chan et al., 2007; Chemke and Kaspi, 2015). These studies pursue similar approaches to their assessment of the dynamical mechanism behind such variability. They deduce any asymmetries in the dominant terms in the eddy momentum budget. This analysis is carried out by approximating the system as being quasi-geostrophic. Chemke and Kaspi (2015) found the most significant terms to be related to the eddy momentum flux convergence, which was asymmetric along the jet. However, Chan et al. (2007) found this not to be the case in their ocean model, finding no asymmetries in the eddy momentum flux convergence. Instead, asymmetries were found in the eddy heat fluxes. In both models, the reason behind the asymmetries was seen to be due to asymmetries in the baroclinicity around the migrating jets. These asymmetries occurred for different reasons, which were uncovered by analysing the spatial variation in each of the terms contributing to the Eady growth rate. Chemke and Kaspi (2015) found the most significant asymmetry on either side of the jet was due to the Coriolis parameter. Conversely, Chan et al. (2007) attributed the asymmetry to a difference in the static stability, due to variations in the depth-averaged temperature.

2.2 Review of Predictability: Theory and Evaluation

Since Lorenz (1963) first realised that chaotic dynamics could limit predictability of the weather and climate, there has been much interest in quantifying the predictability of processes in both the atmosphere and the ocean. If the climate possesses any predictability on decadal scales, it will be likely due to the influence of the long timescale processes of the ocean rather than the comparatively short atmospheric processes (Wunsch and Heimbach, 2013). The North Atlantic is one region where a significant amount of variability is observed on interannual to decadal timescales (Latif et al., 2006). As a result, there has been substantial community interest in evaluating interannual to decadal predictability in the North Atlantic (Sutton and Allen, 1997; Wunsch, 2013; Meehl et al., 2014). The predictability of several variables in the North Atlantic has been assessed on these timescales, with many studies examining sea surface temperature and volume transports, and a few studies examining SSH (Griffies and Bryan, 1997; Wunsch, 2013; Meehl et al., 2014; Polkova and Stammer, 2015).

To obtain a reliable result for the predictable timescales of the system, one must check that the results are not overly sensitive to the measure used. In recent times there has been growing interest in measures based on information theory (Schneider and Griffies, 1999; Kleeman, 2002; DelSole, 2004). In addition to these measures, techniques based on non-normal mode stability theory can give an increased understanding of dynamical systems by identifying initial conditions that will give rise to the most substantial growth of initial perturbations (Farrell and Ioannou, 1996). These techniques can potentially provide insight into which mechanisms set the predictability, on interannual timescales, of SSH in both idealised and more complex model studies.

2.2.1 Definition of Predictability

Three main factors lead to uncertainty in predictions. The first of these are uncertainties in the initial state of the system. Since the Earth's climate is a chaotic system, slightly different initial conditions can lead to very divergent predictions (Lorenz, 1993). This feature was famously discovered by Lorenz (1963) and is reproduced in Figure 2.6. Here panels a and b show widely diverging evolutions of states which possess similar initial conditions. This feature is also seen in Figure 2.6c, where a small set of similar initial conditions propagates into a wide range of final states. The second reason for the uncertainty is due to model error; models are imperfect representations of the real world, and have inevitable errors when representing processes on the model's truncation scale (Palmer and Hagedorn, 2006). Finally, there is uncertainty due to changes in the prescribed external climate forcings, such as future variations in wind stress and buoyancy forcings, due to greenhouse gas emissions.

As predictions in weather and climate are intrinsically uncertain, they should be thought of as consisting of equations whose prognostic variables are probability densities $\rho(X,t)$, where X is some climate variable and t denotes time (Palmer and Hagedorn, 2006). X is deemed predictable if the forecast probability density is sufficiently different from a climatological estimate. This difference needs careful examination depending on the desired purpose of the predictions. Figure 2.7a shows an example where there is a clear difference between the climatological and forecast distributions, meaning the forecast probability distribution is predictable. In Figure 2.7b the predictions may be indistinguishable from the climatology until some threshold X_{crit}, where they are then separable. A measure of the difference between the forecast and climatological distributions is, therefore, a plausible measure of predictability (DelSole and Tippett, 2007). Thus, predictability is defined as the capability to make skillful forecasts, where skill is measured as an improvement over a chosen benchmark.

A further distinction can be made about the type of predictability that is being assessed. On interannual and longer timescales, predictability can be thought of

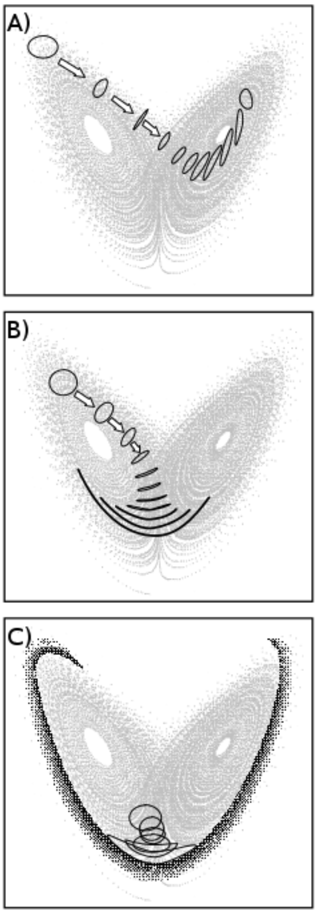

Figure 2.6: The evolution of three probabilistic predictions initialized at different points on the Lorenz (1963) attractor. a) Is a case with high predictability, with a transition to a different regime. b) As this initial state evolves this is firstly a region of high predictability followed by uncertainty in the future regime. c) The forecasts for this initial state, which as at a transtion point between regimes, rapidly becomes very uncertain (Figure from Palmer and Hagedorn, 2006).

as to depend on both the internal variability present and the external forcings applied (both anthropogenic and natural components such as volcanoes) (Collins et al., 2006). Thus, predictability studies can be divided into two main types. The *first type* of predictability study examines how uncertainties in the initial conditions affect predictions at later times (Lorenz, 1975). The *second type* of predictability study addresses the predictability of the response to a change in boundary conditions of the system (Lorenz, 1975). Both types of predictability studies are featured in this thesis, and both require the use of a model and a quantitative measure of predictability.

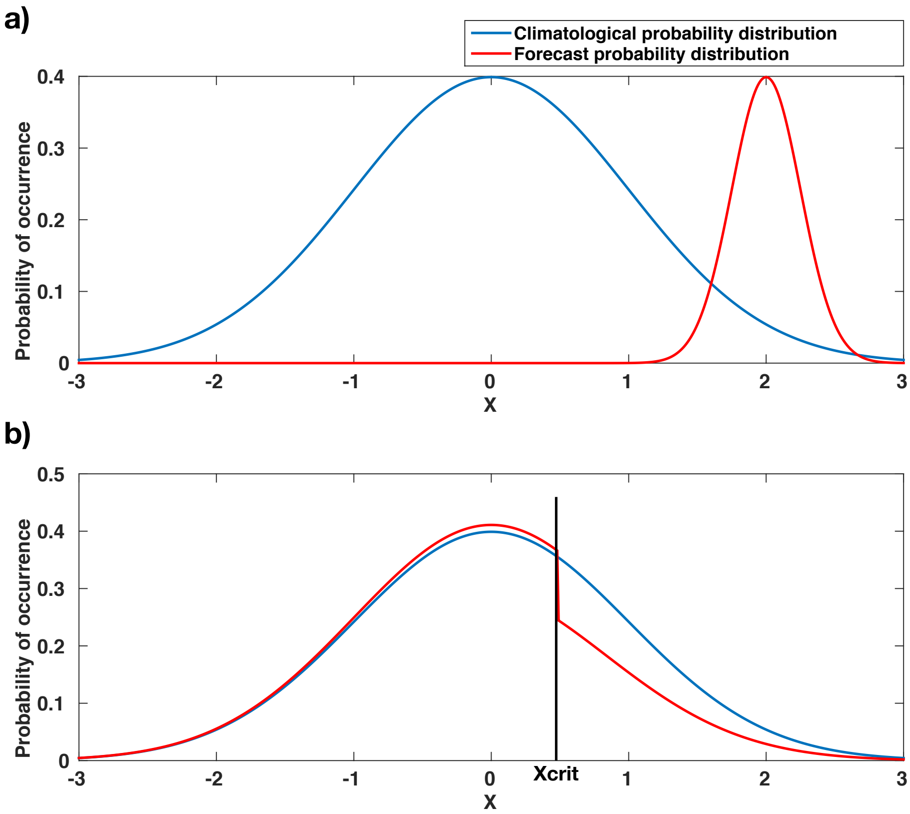

Figure 2.7: Two different scenarios of potential forecast and climatological probability distributions of a variable X. a) Demonstrates a scenario where the forecasts are predictable. b) Shows a forecast which is unpredictable unless X exceeds some critical value X_{Crit} (Palmer and Hagedorn, 2006).

Figure 2.8 illustrates the timescales on which different types of predictability study are most relevant.

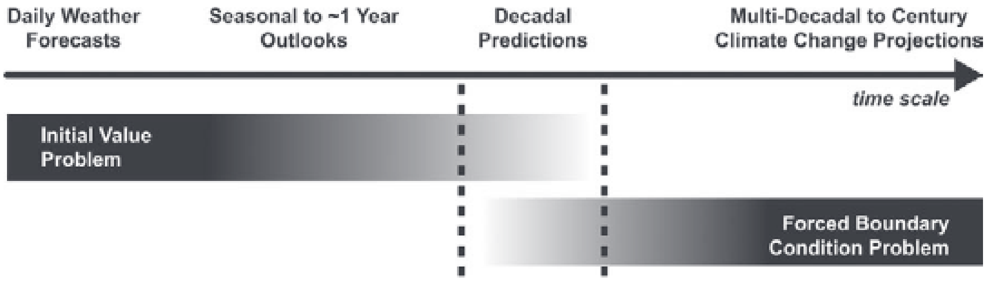

Figure 2.8: Schematic illustrating progression from initial value problems with daily weather forecasts at one end, and multidecadal to century projections as a forced boundary condition problem at the other, with seasonal and decadal prediction in between (Figure from Meehl et al., 2009).

2.2.2 Statistical Models

Traditionally, to generate the probability distributions necessary to evaluate predictability, an ensemble of model runs are carried out with the prediction model. Depending on the model used, and the size of the ensemble, this process can be very computationally expensive. However, recent studies which make use of statistical forecast models, those which simplify the dynamics of the system based on the historical record or an extended model control run, have been used to examine predictability (Penland and Sardeshmukh, 1995; Newman, 2007; Hawkins et al., 2011; Zanna, 2012). Such models have the advantage of being less computationally expensive than the full numerical models, as well as providing information about the predictability of the systems underlying dynamics. This thesis will make use of a hierarchy of numerical models, and several statistical models.

2.2.2.1 Climatology and Persistence Forecasts

In order to create a benchmark for the other statistical forecast techniques lagged correlation forecasts are made (Lorenz, 1963),

$$x(t_0+\tau) = \beta(\tau)x(t_0), \tag{2.20}$$

where β is the auto-correlation of the time series at a point in space, x is time series of the quantity being predicted and τ is the lag time of the forecast. This is a type of ‘damped persistence’ forecast which may provide forecasts better than climatology (β=0) and persistence (β=1) forecasts.

2.2.2.2 EOF Decomposition and Linear Inverse Models

Linear Inverse Modeling (Penland, 1989, LIM) has previously been used to evaluate predictability in sea surface temperature, in both models and observations (e.g., Penland, 1989; Hawkins et al., 2011; Zanna, 2012). The method models the evolution of the desired fields as a linear process forced by white noise. In doing so, the linear inverse model (LIM) gives information about the predictability of the fluctuations in the system. To enable this calculation, we construct a reduced state space based on the empirical orthogonal functions (EOFs) of SSH anomalies and their related principal components (PCs).

EOFs were first used to decompose space-time fields in the 1940s and 1950s (Obukhov, 1947; Fukuoka, 1951; Lorenz, 1956). This method can be thought of decomposing a time-varying system into a series of orthogonal spatial modes of variability. Before this method is applied the data is first arranged into a matrix where each row is a spatial map, and each column is a time series at a certain point (Bjornsson and Venegas, 1997),

$$\mathbf{F} = \begin{bmatrix} x_{11} & \dots & \dots & x_{1p} \\ \vdots & & & \vdots \\ \vdots & & & \vdots \\ x_{n1} & \dots & \dots & x_{np} \end{bmatrix}. \tag{2.21}$$

The covariance matrix of **F** is found (Bjornsson and Venegas, 1997),

$$\mathbf{R} = \mathbf{F}^T\mathbf{F}, \tag{2.22}$$

then the eigenvalue problem,

$$\mathbf{RD} = \mathbf{D\Lambda}, \tag{2.23}$$

is solved where $\mathbf{\Lambda}$ is a diagonal matrix containing the eigenvalues λ_i of **R** and the column vectors of **D**, $\mathbf{d_i}$ are the corresponding eigenvectors. These eigenvectors can be regarded as a map, and are known as the EOFs of the system. **D** has the property that $\mathbf{D}^T\mathbf{D} = \mathbf{D}\mathbf{D}^T = \mathbf{I}$, meaning the EOFs are orthogonal. Each EOF represents a map of a standing oscillation; the times series on which this map varies, i.e. the principal component time series, can be found using (Bjornsson and Venegas, 1997)

$$\mathbf{P_i} = \mathbf{Fd_i}, \tag{2.24}$$

where i is the number of the eigenvector. Therefore, the original data is expressed as (Bjornsson and Venegas, 1997)

$$\mathbf{F} = \sum_{j=1}^{p} \mathbf{P_j}(\mathrm{EOF}_j). \tag{2.25}$$

The techniques diagnose not only spatial patterns of variability, but also the time series by with which they vary and the amount of variance each mode explains.

The evolution of the PCs of SSH anomalies is approximated by a linear model (Penland and Sardeshmukh, 1995). To derive this a dynamical system is represented in the form,

$$\frac{d\chi}{dt} = \alpha\chi + \mathbf{n}(\chi) + \mathbf{f}, \tag{2.26}$$

where χ is a state vector, α a linear system matrix, $\mathbf{n}$ is the nonlinear term and $\mathbf{f}$ is the external forcing term. The components of χ represent the values of all the system variables in some vector space. As a simplification to this we examine the trial subsystem of a linear system driven by Gaussian white noise by re-expressing equation 2.26 as,

$$\frac{d\mathbf{P}}{dt} = \mathbf{A}\mathbf{P}(t) + \xi. \tag{2.27}$$

where $\mathbf{P}$ is the vector of n-PCs, ξ is a stochastic forcing term, and $\mathbf{A}$ is a linear matrix defining the temporal evolution of the n-PCs. Here $\mathbf{A}$ is a submatrix of α and ξ contains both the nonlinear and external forcing terms. Both sources of noise are therefore assumed to act similarly in this model. Even though the linear inverse model does explicitly include nonlinear effects, it still contains dynamical information about the eddy-mean flow interactions via the linearized operator $\mathbf{A}$, and through the addition of a stochastic noise term. Forecasts, $\hat{\mathbf{P}}$, are then generated using the model such that

$$\hat{\mathbf{P}}(t+\tau) = \mathbf{B}(\tau)\mathbf{P}(t), \tag{2.28}$$

where τ is the forecast lead time and $\mathbf{B}$ is the forecast propagator,

$$\mathbf{B}(\tau) = \exp(\mathbf{A}\tau) = \left[\mathbf{C}(\tau_0)\mathbf{C}(0)^{-1}\right]^{\tau/\tau_0}, \tag{2.29}$$

where the covariance matrices at lag-τ_0 and lag-0 given by

$$\begin{aligned} \mathbf{C}(\tau_0) &= \langle \mathbf{P}(t+\tau_0)\mathbf{P}^T(t)\rangle, \\ \mathbf{C}(0) &= \langle \mathbf{P}(t)\mathbf{P}^T(t)\rangle. \end{aligned} \tag{2.30}$$

Here $\langle\rangle$ indicates an average over all times. Predictability can then be evaluated by examining the difference between the probability distribution of the predictions and that of the climatology. For LIM to be applied, the system being examined has to possess several characteristics (Penland and Sardeshmukh, 1995):

- it can be described by Gaussian statistics;
- $\mathbf{A}$ is independent of the time lag, τ_0, used to calculate it;
- all real parts of the eigenvalues of $\mathbf{A}$ must be negative and therefore decay.

As the operator $\mathbf{A}$ needs to be independent of the τ_0 used to determine it. The tau test test, as described in Penland and Sardeshmukh (1995), is used to select a suitable τ_0. This test consists of examining the Euclidean norm of $\mathbf{A}$ as a function of the τ_0s used to construct it. The τ_0 selected is in the range where there are only small changes ($< 10\%$) changes in $|\mathbf{A}|$. As suggested in Penland and Sardeshmukh (1995), the behaviour of $|\mathbf{A}\lambda|$ as a function of τ_0 (where λ is a typical state vector i.e. one where the components are proportional to the square root of the SSH variance explained by the corresponding EOF), is also examined and in the cases discussed in this thesis, there is strong agreement between these two tests. Finally, to prevent overfitting of the linear models, the data used in each experiment is separated into a training and a verification data set. The linear model is constructed using the training data set. This model is then used to make predictions for the verification set, and the skill of these predictions is then used to evaluate the system's predictability.

2.2.3 Non-Normal Mode Analysis and Optimal Initial Conditions

The characteristics of the trained linear model can be used to infer information about a system's sensitivity to initial conditions. In a series of papers, Farrell and co-authors developed a methodology, generalised linear stability theory, to investigate the transient behaviour resulting from initial perturbations to its mean state (Farrell and

Ioannou, 1996). This methodology has been used to examine a range of geophysical problems including: Couette flow (Farrell, 1982), atmospheric forecast error growth (Farrell, 1990), quasi-geostrophic turbulence (Farrell and Ioannou, 1995), the El Niño Southern Oscillation (Penland and Sardeshmukh, 1995), Gulf Stream dynamics (Farrell and Moore, 1992) and the Atlantic meridional overturning circulation (Zanna and Tziperman, 2005, 2008; Hawkins and Sutton, 2009).

This analysis investigates the transient growth in linearly-stable fluid dynamical systems. It may appear counter-intuitive that there can exist disturbances which lead to growth in a stable system. However, when the operator $\mathbf{A}$ is non-normal, i.e. $\mathbf{A}\mathbf{A}^{\mathbf{T}} \neq \mathbf{A}^{\mathbf{T}}\mathbf{A}$, it is possible for the eigenmodes of the system to interact and give a large amplification of variance at a finite-time (Farrell and Ioannou, 1996). The solutions to

$$\frac{d\mathbf{P}}{dt} = \mathbf{A}\mathbf{P}(t), \tag{2.31}$$

can be written in terms of the eigenvectors, $\mathbf{e}_i$ as

$$\mathbf{x}(t) = \sum_i \mathbf{e}_i a_i \exp \lambda_i t, \tag{2.32}$$

where λ_i are the eigenvalues of $\mathbf{A}$ and a_i is a complex constant. An example of two decaying modes ($\lambda < 0$) undergoing a growth is illustrated in Figure 2.9. Panel a, shows the initial state, where the the unit sphere is dotted. Panel b shows that at time t there is an overall growth, because one normal mode decays more rapidly than the other. The SSH anomaly growth at time τ by non-normal eigenmode interference is given by

$$\mu(\tau) = \frac{\mathbf{P}(\tau)^{\mathbf{T}}\mathbf{P}(\tau)}{\mathbf{P}(0)^{\mathbf{T}}\mathbf{P}(0)}. \tag{2.33}$$

The longest timescale on which this growth occurs can be thought of as an optimistic upper bound on the predictability of linear events without forcing.

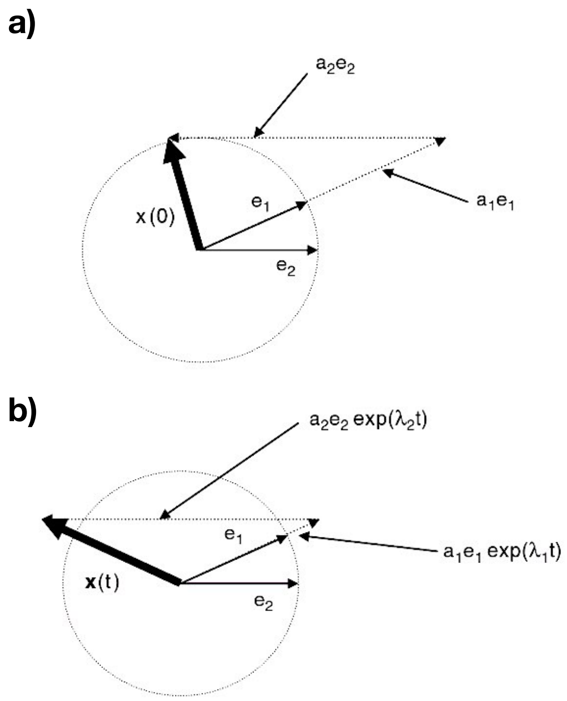

Figure 2.9: The temporal evolution of a system (equation 2.32) consisting of two modes where λ_1 is $<<$ than λ_2: a) at its initial state, and (b) at time t (Figure from Sarachik and Cane, 2010).

2.2.4 Measures of Predictability

As illustrated in Figure 2.7, a predictability measure compares the climatological probability distribution with the forecast distribution. There are several ways to do this, and some possible measures are now discussed.

2.2.4.1 Relative Root Mean Square Error

The most common measure of predictability is to assess the mean square error of a perfect model forecast (Schneider and Griffies, 1999). Meaning that model output is used as a substitute for observations with the aim of predicting the subsequent model output. This approach assumes the model has a realistic representation of the actual climate system (Hawkins et al., 2011).

The relative root mean square error, $RMSE_{Relative}$ can be used compare the predictions to the climatological forecasts (Hawkins et al., 2011):

$$RMSE_{Relative} = \frac{RMSE_{pred}}{RMSE_{clim}} \tag{2.34}$$

where $RMSE_{clim}$ is the root mean square error of the climatology over the forecast period and $RMSE_{pred}$ is the root mean square error of the predicted field. A value greater than unity indicates that the model's forecasts are inferior to those generated using the climatology, whereas, a value less than unity demonstrates forecast skill superior to climatology. The reason for choosing this metric is because it is well grounded in the literature, and therefore will enable a useful comparison with a newer less well-established metric.

2.2.4.2 Average Predictability Time

In designing a predictability measure, it is beneficial for the measure to obey two underlying principles (DelSole and Tippett, 2007). Firstly, the variable is shown to be unpredictable if its forecast distribution is the same as its climatological distribution. Secondly, the measure should be invariant to linear transformations of the variables. One proposed measure that meets these criteria is average predictability time (APT) (DelSole and Tippett, 2009a). This index of predictability was based on the Mahalanobis signal (DelSole and Tippett, 2007),

$$S(\tau) = \frac{1}{k} tr[(\mathbf{\Sigma}_{\infty} - \mathbf{\Sigma}_{\tau})\mathbf{\Sigma}_{\infty}^{-1}], \tag{2.35}$$

where k is a constant related to the number of principal components used in the analysis, tr is the trace of the matrix, $\mathbf{\Sigma}_{\tau}$ is the covariance matrix of the forecast error at lead time τ, $\mathbf{\Sigma}_{\infty}$ is covariance matrix of the forecast distribution at long lead times. Here, $S(\tau)$ has a value of 1 when the system is completely predictable, and a value of 0 when the forecast covariance matrix is the same as the climatological covariance matrix, meaning the system is unpredictable. This method has been used before to examine the predictability of several geophysical fields, including the upper ocean temperature and the AMOC (Branstator et al., 2012; Branstator and Teng, 2014).

The APT can be defined by integrating the Mahalanobis signal over all lead times (DelSole and Tippett, 2009a), leading to

$$APT = 2\sum_{\tau=1}^{\infty} S(\tau). \tag{2.36}$$

The factor of two makes APT agree with the e-folding time in the univariate case. In one dimension, APT resembles a root mean square error and is given by (DelSole and Tippett, 2009b)

$$APT = 2\sum_{\tau=1}^{\infty} \frac{\sigma_{\infty}^2 - \sigma_{\tau}^2}{\sigma_{\infty}^2} = 2\sum_{\tau=1}^{\infty}\left(1 - \frac{\sigma_{\tau}^2}{\sigma_{\infty}^2}\right). \tag{2.37}$$

Since APT is the integral of predictability over all times, it is independent of the chosen lead time. This measure can also be used to define predictable components by finding the projection vectors $\mathbf{q}$ that maximize APT. In which case, the component $\mathbf{q^T P}$, with $\mathbf{P}$ being the principal component state vector, has forecast and climatological variances given by $\sigma_\tau^2 = \mathbf{q^T \Sigma_\tau q}$ and $\sigma_\infty^2 = \mathbf{q^T \Sigma_\infty q}$ respectively.

In this thesis, the APT of the whole system and of the leading predictable components are calculated using the method contained in DelSole and Tippett (2009b). Firstly, to prevent overfitting, the data is separated into training and verification data sets. Forecasts are then generated by forming linear regression models from the training data (DelSole and Tippett, 2009b), i.e. the projections $\hat{\mathbf{P_L}}(t+\tau)$, are given by

$$\hat{\mathbf{P_L}}(t+\tau) = \mathbf{C}(\tau)\mathbf{C}(0)^{-1}\mathbf{P}(t). \tag{2.38}$$

Using such models and in the case of a zero mean stationary process, meaning $\mathbf{C}(0) = \mathbf{\Sigma_\infty}$, the forecast error covariance matrix is given by

$$\mathbf{\Sigma}_\tau = \mathbf{C}(0) - \mathbf{C}(\tau)\mathbf{C}(0)^{-1}\mathbf{C}(\tau)^T. \tag{2.39}$$

These values for $\boldsymbol{\Sigma}_\infty$ and $\boldsymbol{\Sigma}_\tau$ can be substituted into equation 2.36 to calculate the APT of the entire system. In order to maximize APT in equation (2.37), the problem reduces to solving the generalized eigenvalue problem (See DelSole and Tippett (2009b) for a full derivation),

$$\mathbf{Gq} = \lambda \mathbf{C}(0)\mathbf{q} \tag{2.40}$$

where

$$\mathbf{G} = \sum_{\tau=1}^{\infty} \mathbf{C}(\tau)\mathbf{C}(0)^{-1}\mathbf{C}(\tau)^T. \tag{2.41}$$

The projection vectors $\mathbf{q}$ are uncorrelated with each other because $\mathbf{G}$ and $\boldsymbol{\Sigma}_{\boldsymbol{\infty}}$ are symmetric. The spatial patterns, $\mathbf{p}$, associated with the projection vectors $\mathbf{q}$ are found by using

$$\mathbf{p} = \langle \mathbf{PP^Tq} \rangle = \boldsymbol{\Sigma}_\infty \mathbf{q}; \tag{2.42}$$

these spatial patterns can be projected back onto the EOFs and are referred to as the predictable components. The predictable components of the system are calculated using only the training data set. To prevent overfitting and calculate APT of each predictable component, the projection vector, $\mathbf{q}$, calculated from the training data is applied to verification data set. Thus, the squared multiple correlation between the component time series and the verification data is

$$\mathbf{R}_\tau^2 = \frac{\mathbf{q}^T\mathbf{C}(\tau)\mathbf{C}(0)^{-1}\mathbf{C}(\tau)^{\mathbf{T}}\mathbf{q}}{\mathbf{q}^T\mathbf{C}(0)\mathbf{q}}, \tag{2.43}$$

where q is calculated from the training data set and the correlations are calculated from the verification set. Therefore, $\mathbf{R}_\tau^2$ can be interpreted as the variance of the predictable component time series, which is explained by a linear regression prediction at time lag τ. The predictability time of each component, APT_p, is then calculated as,

$$APT_p = 2\sum_{\tau=1}^{\infty} \mathbf{R}_\tau^2. \tag{2.44}$$

However, two significant difficulties arise when calculating APT using equation 2.40 and a finite time series; (1) the time lag co-variances can't be estimated at large lags, as the series is finite; (2) there is the danger of over-fitting if the dimensions of state space exceed the number of samples. The first issue is addressed by calculating the APT using a truncated weighted sum, with a lag window, known as the Parzen window, (DelSole and Tippett, 2009b)

$$APT = 2\sum_{\tau=1}^{M} y_\tau S(\tau), \tag{2.45}$$

where,

$$y_\tau = \begin{cases} 1 - 6(\frac{\tau}{M})^2 + 6(\frac{\tau}{M})^3, & \text{if } 0 \ \leq \ \tau \ \leq \ M/2, \\ 2(1 - \frac{\tau}{M})^2, & \text{if } M/2 \ \leq \ \tau \ \leq \ M, \end{cases} \tag{2.46}$$

and M is the defined truncation time. To overcome the second difficulty the APT is calculated in EOF space.

To validate the predictable components and ensure the statistical significance of the calculated APT, two significance tests are employed. Firstly, as $\mathbf{R}_\tau^2$ can be interpreted as a multivariate generalization of the correlation coefficient, and therefore its statistical significance can be calculated using standard methods such as the student's t-test (Jia and DelSole, 2011). Secondly, the statistical significance of the APT is evaluated relative to the null hypothesis that the principal component time series are unpredictable, as in Jia and DelSole (2011). This is done by carrying out several Monte Carlo experiments: for N_s spatial distributions and N_t time steps, we generate $2N_sN_t$ random numbers from a Gaussian distribution with zero mean and unit variance. These distributions are substituted into equation 2.40 and the eigenvalues of the problem are calculated. This is repeated 100 times, and the 95th percentile of each eigenvalue is selected. If the APT value calculated from the training data for each component exceeds the eigenvalue's 95th percentile, the hypothesis that there is no predictability is rejected (Jia and DelSole, 2011).

Chapter 3

Model Details and Momentum Budget Decompositions

Idealised double-gyre simulations are commonly used as simplifications of the North Atlantic Ocean circulation. Several studies have used such double gyre systems, in conjunction with steady applied wind forcings, to examine intrinsic interannual variability of the ocean circulation (that which is generated in the absence of time varying atmospheric forcings) (Dijkstra and Ghil, 2005; Berloff et al., 2007). These studies have hypothesized that the observed variability may be driven by interactions between nonlinear elements of the wind-gyre circulation dynamics: the mesoscale eddies, the western boundary currents, and the recirculation gyres. However, the majority of idealised modelling studies investigating intrinsic interannual variability have used quasi-geostrophic models (Dijkstra and Ghil, 2005; Berloff et al., 2007). The studies comprising the first part of this thesis investigate the intrinsic effects present, using both a barotropic shallow water model and a primitive equation model in idealised geometry. The baroclinic model will possess several dynamical mechanisms, which are thought to act on interannual timescales including: baroclinic Rossby waves, buoyancy forced circulation changes and mixing due to temperature gradients (Roberts et al., 2016). These mechanisms are relevant to interannual predictability, which is likely due to the steric components of SSH (Polkova and Stammer, 2015).

The later parts of this thesis will examine how perturbations to the applied wind and buoyancy forcings alter the variability and predictability of the idealised models.

The final main results chapter will examine the SSH variability and predictability in a state-of-the-art Atmosphere-Ocean Global Circulation Model (AOGCM), which will be described in Chapter 6.

This chapter will introduce the idealised models used in this thesis. Moreover, it will present the Reynolds decomposed forms of the model equations, which underpin the momentum and buoyancy budget analysis used in several of the later results chapters.

3.1 Barotropic Double Gyre

3.1.1 Barotropic Model Features

The first model used to represent the North Atlantic is a barotropic, flat bottom, double gyre, which solves the shallow water equations on a beta plane. The model is a modified version of the MITgcm (Massachusetts Institute of Technology General Circulation Model) which was described by Marshall et al. (1997a). All the parameters used in this model are contained in Table 3.1. The equations are solved in Cartesian coordinates, x, y, z, in the zonal, meridional and vertical directions. The currents are given by, $\mathbf{u} = (\mathbf{u_h}, w)$ which corresponds to the velocity field (u, v, w). The operator ∇ is equal to $(\nabla_h, \frac{\partial}{\partial z}) = (\frac{\partial}{\partial x}, \frac{\partial}{\partial y}, \frac{\partial}{\partial z})$.

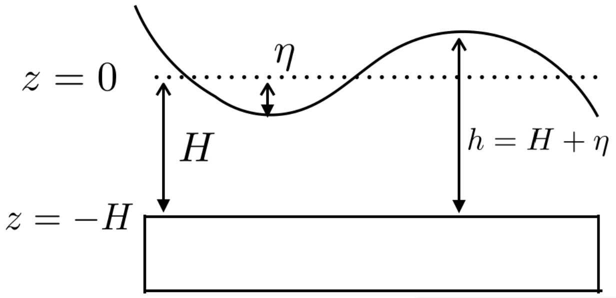

Figure 3.1: Schematic of the shallow water model.

The model solves the zonal,

$$\frac{\partial u}{\partial t} + (\mathbf{u_h} \cdot \nabla_h)u - fv = -g\frac{\partial \eta}{\partial x} + \frac{\tau_x}{\rho_0 h} - \frac{C_{drag}}{h}u\sqrt{u^2 + v^2} + A_h \nabla_h^2 u, \tag{3.1}$$

and meridional,

$$\frac{\partial v}{\partial t} + (\mathbf{u_h} \cdot \nabla_h)v + fu = -g\frac{\partial \eta}{\partial y} - \frac{C_{drag}}{h}v\sqrt{u^2+v^2} + A_h\nabla_h^2 v, \tag{3.2}$$

momentum equations. Here η is the sea surface height, H is the mean free surface height, with h equal to $H + \eta$, as illustrated in Figure 3.1. τ_x is the zonal wind stress, C_{drag} is a coefficient controlling the magnitude of the bottom drag, g is the acceleration due to gravity and A_h is the horizontal eddy viscosity coefficient. As it is a barotropic model the density of the fluid, ρ_0, is constant. The system is said to be shallow, as the depth H is much smaller than the horizontal scale of the fluid. A small aspect ratio of the system implies that vertical velocities are much smaller than horizontal velocities. The Coriolis parameter, $f = 2\Omega sin(\phi)$ is approximated through the mid-latitude beta plane equation as $f(y) = f_0 + \beta y$ (as discussed in section 2.1.1), with $f_0 \approx 2\Omega sin(\phi_0)$ and $\beta = 2(\Omega/a)cos\phi_0$, where ϕ is latitude , ϕ_0 is a chosen reference latitude and Ω is the angular velocity of the Earth, a is the radius of the Earth. Hydrostatic balance is also assumed as the vertical momentum equation such that

$$\frac{\partial p}{\partial z} = -\rho_0 g. \tag{3.3}$$

where p is pressure. The solutions also obey the mass continuity equation which can be derived by vertically integrating the incompressibility condition:

$$\nabla \cdot \mathbf{u} = \frac{\partial u}{\partial x} + \frac{\partial v}{\partial y} + \frac{\partial w}{\partial z} = 0, \tag{3.4}$$

resulting in,

$$\frac{\partial h}{\partial t} + \nabla_h \cdot (\mathbf{u_h}h) = 0. \tag{3.5}$$

Finally, the applied wind forcing for the barotropic experiment is,

$$\tau_x(y) = A\ sin(\frac{\pi y}{L_y}) \text{ and } \tau_y = 0, \tag{3.6}$$

where A is the magnitude of the wind forcing and L_y is the meridional extent of the domain.

Definition	Parameter	Value
Horizontal eddy viscosity	A_h	30 m^2/s
Reference density	ρ_0	999.8 kgm^{-3}
Wind amplitude	A	0.2 Nm^{-2}
Quadratic Bottom Drag Coefficient	C_{drag}	1×10^{-3}
Coriolis parameter at ϕ_0	f_0	1×10^{-4} s^{-1}
Rossby parameter	β	2×10^{-11} $m^{-1}s^{-1}$
Gravitational acceleration	g	9.81 ms^{-2}
Ocean depth	H	3000 m
Number of zonal grid points	N_x	512
Number of meridional grid points	N_y	512
Zonal domain extent	L_x	3840 km
Meridional domain extent	L_y	3840 km
Model time step	τ_s	300 s

Table 3.1: The parameters used in the barotropic model.

The equations are solved in a square domain of size $L_x \times L_y$ of 3840km×3840km, with $N_x \times N_y$ gridpoints. The basin is 3000m deep with a horizontal resolution of 7.5km×7.5km, so as to resolve mid-latitudes eddies. No-slip boundary conditions are imposed on the domain's lateral boundaries. The model is spun up for 50 years and run for a further 150 years. Figure 3.2a shows the steady wind stress profile applied across the basin. Figure 3.2b shows the time-mean SSH, with a double gyre structure and an eastward jet extension, as expected from Sverdrup balance. The standard deviation of the SSH is shown in Figure 3.2c, with the largest variance located in the jet region, as observed in mid-latitudes jet regions in the North Atlantic and the Pacific oceans (Fu, 2004).

3.1.2 The Reynolds Decomposed Shallow Water Equations

To explore the role of eddies in driving interannual variability, we examine their effects on the mean flow, by diagnosing the Reynolds stresses (as briefly introduced above in Section 2.1.5). Reynolds decomposition relies on the ability to describe a state variable (X) as a combination of a mean quantity ($\bar{X}$) and perturbations around the mean (X') i.e. $X = \bar{X} + X'$. The mean can be defined using an ensemble average, which

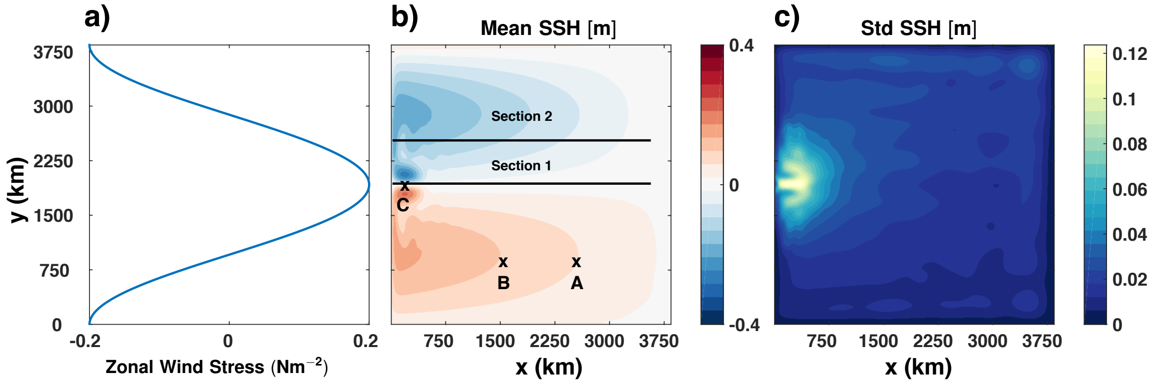

Figure 3.2: a) Steady zonal wind stress profile. b) Time mean SSH, η, and c) Standard deviation of SSH, η, calculated using 150 years of model output after spin up.

in practice can be a spatial or temporal average. In this thesis temporal averages are used, and thus the time-averaged part of the flow is constructed as

$$\overline{X} = \lim_{T\to\infty} \frac{1}{T} \int_t^{t+T} X(t)dt. \tag{3.7}$$

The limit of the integral in Equation 3.7 needs to be larger than the timescales of the resolved fluctuations. Meaning, if T is sufficiently long then the mean should filter out the eddies, and the deviation from the mean will correspond to these eddies. We will discuss how we chose T in later results chapters. A derivation of the Reynolds averaged form of the shallow water equations is presented in Appendix 3.A. The resultant zonal and meridional Reynolds averaged momentum equations are

$$\begin{aligned}\frac{\partial \bar{u}}{\partial t} = -\nabla_h \cdot (\bar{\mathbf{u}}_\mathbf{h} \bar{u}) - \overline{\frac{u}{h}\frac{Dh}{Dt}} - g\frac{\partial \bar{\eta}}{\partial x} + f\bar{v} - \nabla_h \cdot (\overline{\mathbf{u}_\mathbf{h}' u'}) - \overline{\frac{u'}{h}\frac{Dh'}{Dt}} \\ + \overline{\frac{\tau_x}{\rho h}} - \overline{\frac{C_{drag}}{h} u\sqrt{u^2+v^2}} + A_h \nabla_h^2 \bar{u},\end{aligned} \tag{3.8}$$

and

$$\begin{aligned}\frac{\partial \bar{v}}{\partial t} = -\nabla_h \cdot (\bar{\mathbf{u}}_\mathbf{h} \bar{v}) - \overline{\frac{v}{h}\frac{Dh}{Dt}} - g\frac{\partial \bar{\eta}}{\partial y} - f\bar{u} - \nabla_h \cdot (\overline{\mathbf{u}_\mathbf{h}' v'}) - \overline{\frac{v'}{h}\frac{Dh'}{Dt}} \\ - \overline{\frac{C_{drag}}{h} v\sqrt{u^2+v^2}} + A_h \nabla_h^2 \bar{v}.\end{aligned} \tag{3.9}$$

3.2 Baroclinic Double Gyre

The baroclinic model solves the implicit free surface form of the hydrostatic primitive equations (HPEs). The equations are solved on a spherical polar grid and their derivation is now presented.

3.2.1 Spherical Polar Coordinates

The model set up makes use of spherical polar coordinates, latitude ϕ, longitude λ and r the distance from the Earth's center, as shown in Figure 3.3. The zonal, u, and meridional, v, velocities are given by

$$u = rcos\ \phi \frac{D\lambda}{Dt}, \tag{3.10}$$

and

$$v = r\frac{D\phi}{Dt}. \tag{3.11}$$

The vertical velocity, w, which is directed away from the sphere's center is given by

$$w = \frac{Dr}{Dt}. \tag{3.12}$$

These definitions lead to the 3D velocity vector

$$\mathbf{u} = (rcos\phi\frac{D\lambda}{Dt}, r\frac{D\phi}{Dt}, \frac{Dr}{Dt}) = (\mathbf{u}_h, w) = (u, v, w). \tag{3.13}$$

Furthermore, the gradient operator

$$\nabla \equiv \left(\frac{1}{rcos\phi}\frac{\partial}{\partial\lambda}, \frac{1}{r}\frac{\partial}{\partial\phi}, \frac{\partial}{\partial r}\right), \tag{3.14}$$

can be used in to derive the incompressibility condition in spherical polar coordinates:

$$\nabla \cdot \mathbf{u} = \frac{1}{rcos\ \phi}\left(\frac{\partial u}{\partial\lambda} + \frac{\partial}{\partial\phi}(vcos\ \phi)\right) + \frac{1}{r^2}\frac{\partial\left(r^2 w\right)}{\partial r} = 0. \tag{3.15}$$

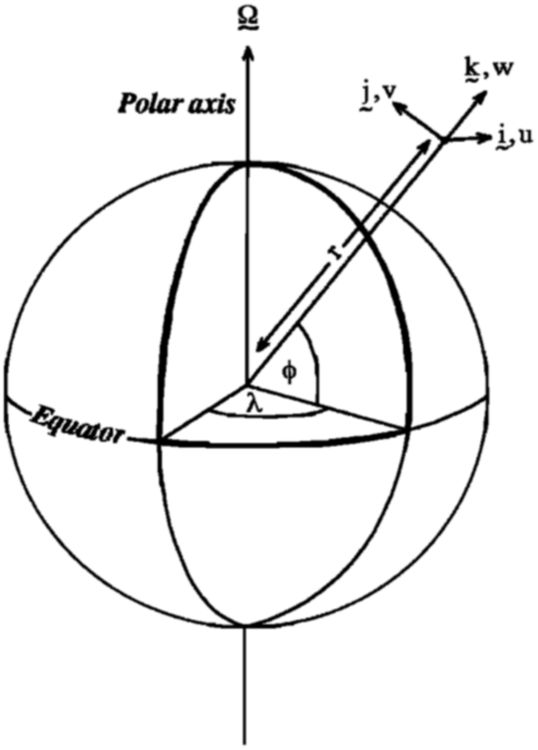

Figure 3.3: Spherical polar coordinates: longitude, λ, latitude, ϕ, and the distance from the center, r and Ω is the earth's rotation rate (Figure from Marshall et al., 1997b).

3.2.2 Hydrostatic Primitive Equations

The general form of the hydrostatic primitive equations for a Boussinesq fluid, are as detailed in Marshall et al. (1997b). Three main approximations are used in their derivation:

- the hydrostatic approximation;
- the traditional approximation; and
- the thin shell approximation.

At any time the state of the ocean is characterized by several fields: the currents $\mathbf{u}$, the potential temperature θ, salinity S, pressure p and density ρ. The HPEs govern the evolution of these fields and consist of, the zonal

$$\frac{\partial u}{\partial t} = -(\mathbf{u} \cdot \nabla)u + \frac{uv\ tan\phi}{a} + fv - \frac{1}{acos\phi}\frac{\partial p}{\partial \lambda} + F_\lambda + D_\lambda. \tag{3.16}$$

and meridional

$$\frac{\partial v}{\partial t} = -(\mathbf{u} \cdot \nabla)v - \frac{u^2 tan\phi}{a} - fu - \frac{1}{a}\frac{\partial p}{\partial \phi} + F_\phi + D_\phi \tag{3.17}$$

momentum equations, the conservation of both heat

$$\frac{\partial \theta}{\partial t} = -\nabla \cdot (\mathbf{u}\theta) + F_\theta \tag{3.18}$$

and salinity

$$\frac{\partial S}{\partial t} = -\nabla \cdot (\mathbf{u}S) + F_S, \tag{3.19}$$

and an equation of state which governs the density of the fluid

$$\rho = \rho(\theta, S, p), \tag{3.20}$$

which depends on heat, salinity and pressure. In these equations $p = \delta p/\rho_0$ where δp is the deviation of the pressure from a resting hydrostatically balanced ocean. The Coriolis parameter is not approximated i.e. $f = 2\Omega sin(\phi)$. The radius of the Earth is given by the constant a. The system is also solved for an incompressible fluid (obeying equation 3.15), assuming hydrostatic balance,

$$\frac{\partial p}{\partial z} = -g\frac{\delta \rho}{\rho_0}. \tag{3.21}$$

3.2.3 Baroclinic Model Features

The baroclinic model is based on an idealised set-up of the MITgcm (Marshall et al. 1997) and solves modified versions of the HPEs. The equations solved are based on those in Section 3.2.2 with an implicit free surface and the following representations of the forcing, dissipation and pressure terms. Potential temperature, θ, is included as an active tracer. However, the treatment of salinity is explicitly switched off in this model. The other relevant model parameters are contained within Table 3.2.

The applied zonal forcing, F_λ, is set to zero in the ocean's interior (denoted by the suffice $_i$),

$$F_{\lambda|i} = 0, \tag{3.22}$$

Definition	Parameter	Value
Smagorinsky eddy viscosity	A_{SmagC}	3.5
Vertical eddy viscosity	A_z	$1 \times 10^{-5}\ m/s^2$
Reference density	ρ_0	$999.8\ kgm^{-3}$
Wind amplitude	A	$0.2\ Nm^{-2}$
Quadratic Bottom Drag Coefficient	C_{drag}	3×10^{-3}
Gravitational acceleration	g	$9.81\ ms^{-2}$
Horizontal diffusivity of tracers	K_h	$100\ m^2/s$
Vertical diffusivity of tracers	K_z	$1 \times 10^{-5}\ m^2/s$
SST Restoring timescales	τ_T	1 month
Thermal Expansion coefficient	α_θ	$2 \times 10^{-4}{}^\circ C^{-1}$
Ocean depth	H	4000 m
Number of zonal grid points	N_x	360
Number of meridional grid points	N_y	360
Zonal domain extent	L_x	60 °
Meridional domain extent	L_y	60 °
Radius of Earth	a	6.37×10^3 km
Tracer and momentum time step	τ_s	$300\ s$
Reference temperature	θ_{ref}	layers: 1-15 [20C°] 16-35[10C°] 36-44 [5C°]
Layer Thickness	Δ_z	1-5 [10m] 6-10[15m] 11-15 [25m] 16-25[30m] 26-35[45m] 26-40[100m] 41-42[250m] 43-44[1000m]

Table 3.2: The parameters used in the baroclinic model.

but non-zero at the surface (denoted by the suffice $_s$) and given by,

$$F_{\lambda|s} = \frac{\tau_x}{\rho_0 \delta z_s}, \tag{3.23}$$

where the steady wind forcing is given by

$$\tau_x(y) = A\ sech^2(y - \frac{L_{yn}}{2}) - C, \tag{3.24}$$

δz_s is the depth of the model's surface vertical layer, L_{yn} is 40°, y is defined in the meridional distance in degrees, from 10°N and C is a constant of value $0.75Nm^{-2}$. The zonal dissipation in the ocean's interior has the form,

$$D_{\lambda|i} = A_{Smag}\nabla^4 u + A_z \frac{\partial^2 u}{\partial z^2}. \tag{3.25}$$

The viscosity coefficient, A_{Smag} is calculated online using the Smagorinsky eddy viscosity scheme (Smagorinsky, 1963) (using equation 12 in Griffies and Hallberg (2000): $A_{Smag} = (\frac{A_{SmagC}}{\pi})^2 \frac{\Delta^4}{8} |D|$, where A_{SmagC} is a user defined non-dimensional value, Δ is the grid spacing and D is a deformation rate). The non-dimensional value used to calculate this coefficient, A_{SmagC} (C in equation 12 of Griffies and Hallberg (2000)), is chosen based on the work by (Griffies and Hallberg, 2000). This viscosity scheme depends on the resolved motions of the model. A range of different viscosity schemes were trialled prior to selecting the Smagorinsky scheme. However, the Smargorinsky scheme viscosity is chosen because it prevents the model becoming over-dissipated, which would obscure the eddy effects. Moreover, it produces a numerically stable model, with a suitably turbulent jet. In the bottom layer (denoted by the suffice $_b$), there is an additional dissipation term, given by a quadratic bottom friction:

$$D_{\lambda|b} = -\frac{C_{drag}}{\delta z_b}\ u\sqrt{u^2 + v^2}, \tag{3.26}$$

where δz_b is the depth of the bottom layer. In order to simplify the analysis there is no meridional forcing in any layer,

$$F_\phi = 0. \tag{3.27}$$

In a similar manner to the zonal case, the meridional dissipation term in the ocean interior is given by,

$$D_{\phi|i} = A_{Smag}\nabla_h^4 v + A_z \frac{\partial^2 v}{\partial z^2}, \tag{3.28}$$

with an additional quadratic bottom drag present in the lower layer,

$$D_{\phi|b} = -\frac{C_{drag}}{\delta z_b}\ v\sqrt{u^2+v^2}. \tag{3.29}$$

The equation of state used in the model is linear

$$\rho = \rho_0(1-\alpha_\theta(\theta-\theta_{ref})), \tag{3.30}$$

where θ_{ref} is predefined reference temperature dependent only in depth. The pressure field, p, is separated into a barotropic part due to variations in sea-surface height, η, and a hydrostatic part due to variations in density, integrated through the water column

$$p = \frac{\delta p}{\rho_0} = g\eta + \int_{-z}^{0} -\alpha_\theta(\theta-\theta_{ref})dz. \tag{3.31}$$

The implicit free surface is calculated by,

$$\frac{\partial\eta}{\partial t} + \frac{\partial(H\hat{u})}{\partial\lambda} + \frac{(\partial H\hat{v})}{\partial\phi} = 0, \tag{3.32}$$

where H is the ocean depth and the hats indicate a vertical integration through the whole water column. Finally, the temperature forcing and dissipation is given by,

$$F_\theta = K_h\nabla_h^2\theta + K_z\frac{\partial^2\theta}{\partial z^2} + F_T, \tag{3.33}$$

where the term F_T is a surface restoring term for temperature with a timescale of one month.

As the model represents a Boussinesq fluid it neglects the contributions of variations in density to the continuity equation. This means in practice that the SSH in the model will show the steric height gradients but not the overall global steric height expansion or contraction. This simplification is suitable in this thesis, as it is the steric height gradients, not any offsets, which influence the SSH variability. The model domain extends between -10° to 50° in latitude, with 60° in longitude, and a depth of 4000 m. It has 44 layers and a horizontal resolution of 1/6°. It obeys no slip boundary conditions along the sides of the domain. At the surface it relaxes to a temperature profile that varies linearly with latitude (Fig. 3.4d). The steady zonal wind stress profile is at a maximum at $30°N$ and is flat in the equatorial region (Fig. 3.4 e). The baroclinic model was firstly spun up for 100 years at 1/3 °resolution. Then an initial condition (zonal velocity, meridional velocity, SSH and temperature) was taken and interpolated to the 1/6 °grid and the model restarted. This model was spun up for a further 100 years. After this, the model was run for a further 100 years, and it is output from this period which is analysed. No drift was detected in this period in either the domain integrated SSH and kinetic energy. Moreover, time series of temperature, SSH and velocity did not exhibit drifts in the vicinity of the jet where the majority of the interannual variability was detected. The variability, shown in Fig. 3.4 c, is largely located in the jet region.

In the particular viscosity regime of the model, it was difficult to establish a zonal jet with the required characteristics (several 100km in length and with an average zonal velocity of 1-2 m/s). In addition to this the required profile needed to have zero wind stress curl at the boundaries of the domain. Several different viscosity parameterisations (including Laplacian viscosity and biharmonic viscosity) and wind stress profiles were trialled (including the classic sinusoidal profile). After these preliminary experiments the combination of the sech^2 wind stress profile and biharmonic viscosity was selected as it generated the appropriate jet characteristics. However, one drawback was present as due to the narrow wind stress profile the gyres were smaller than desired.

3.2.4 The Reynolds Decomposed Hydrostatic Primitive Equations

The derivation of the Reynolds decomposed HPEs is included in Appendix 3.B. The approach, used to decompose the state variables into mean and eddy components, is

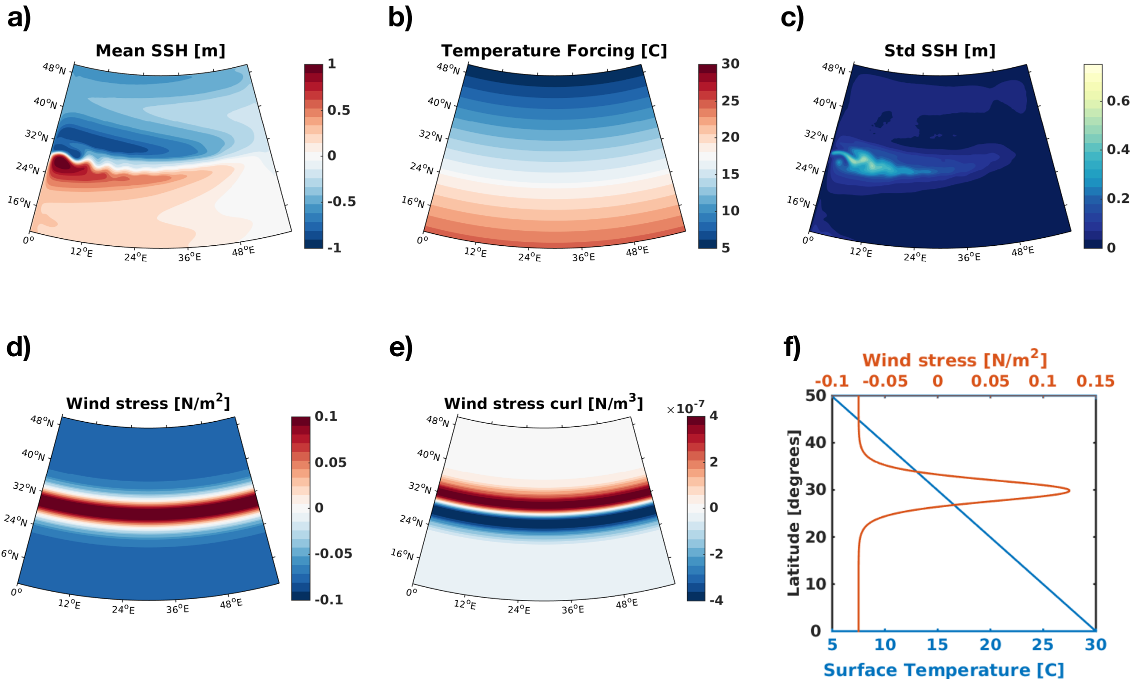

Figure 3.4: a) Time mean SSH (η) averaged over 100 years; b) surface restoring of temperature profile; c) standard deviation of SSH (η) calculated using 100 years of 10-day means; d) profile of steady, zonal wind stress and e) its curl; f) surface restoring of temperature profile and the profile of the steady, zonal wind stress. The equatorial region is not shown in these subplots.

the same as that adopted in Section 3.1.2. The resultant equations are: the Reynolds decomposed zonal

$$\underbrace{\frac{\partial \bar{u}}{\partial t}}_{U_a} = -\overbrace{\frac{1}{acos\phi}\frac{\partial \bar{u}\bar{u}}{\partial \lambda}}^{U_b} \underbrace{-\frac{1}{a}\frac{\partial \bar{v}\bar{u}}{\partial \phi}}_{U_c} -\overbrace{\frac{\partial \bar{w}\bar{u}}{\partial z}}^{U_d} \underbrace{-\frac{g}{acos\phi}\frac{\partial \bar{\eta}}{\partial \lambda}}_{U_e} \underbrace{+\frac{g}{acos\phi}\frac{\partial \int_z^0 \alpha_\theta(\bar{\theta}-\theta_{ref})dz}{\partial \lambda}}_{U_f} \underbrace{+f\bar{v}}_{U_g}$$

$$-\overbrace{\frac{1}{acos\phi}\frac{\partial \overline{u'u'}}{\partial \lambda}}^{U_h} \underbrace{-\frac{1}{a}\frac{\partial \overline{v'u'}}{\partial \phi}}_{U_i} -\overbrace{\frac{\partial \overline{w'u'}}{\partial z}}^{U_j} \underbrace{+\overline{F_\lambda}+\overline{D_\lambda}}_{U_k} \overbrace{+uvtan\phi}^{U_l}, \tag{3.34}$$

and meridional

$$\underbrace{\frac{\partial \bar{v}}{\partial t}}_{V_a} = \overbrace{-\frac{1}{acos\phi}\frac{\partial \bar{u}\bar{v}}{\partial \lambda}}^{V_b} \underbrace{-\frac{1}{a}\frac{\partial \bar{v}\bar{v}}{\partial \phi}}_{V_c} \overbrace{-\frac{\partial \bar{w}\bar{v}}{\partial z}}^{V_d} \underbrace{-\frac{g}{a}\frac{\partial \bar{\eta}}{\partial \phi}}_{V_e} \underbrace{+\frac{g}{a}\frac{\partial \int_z^0 \alpha_\theta(\bar{\theta}-\theta_{ref})dz}{\partial \phi}}_{V_f} \underbrace{-f\bar{u}}_{V_g}$$
$$\overbrace{-\frac{1}{acos\phi}\frac{\partial \overline{u'v'}}{\partial \lambda}}^{V_h} \underbrace{-\frac{1}{a}\frac{\partial \overline{v'v'}}{\partial \phi}}_{V_i} \overbrace{-\frac{\partial \overline{w'v'}}{\partial z}}^{V_j} \underbrace{+\overline{F_\phi}+\overline{D_\phi}}_{V_k} \overbrace{+\frac{u^2 tan\phi}{a}}^{V_l}, \qquad (3.35)$$

momentum equations, and the Reynolds decomposed temperature equation

$$\underbrace{\frac{\partial \overline{\theta}}{\partial t}}_{T_a} = \overbrace{-\frac{1}{acos\phi}\frac{\partial \overline{u}\overline{\theta}}{\partial \lambda}}^{T_b} \underbrace{-\frac{1}{a}\frac{\partial \overline{v}\overline{\theta}}{\partial \phi}}_{T_c} \overbrace{-\frac{\partial \overline{w}\overline{\theta}}{\partial z}}^{T_d} \underbrace{-\frac{1}{acos\phi}\frac{\partial \overline{u'\theta'}}{\partial \lambda}}_{T_e} \overbrace{-\frac{1}{a}\frac{\partial \overline{v'\theta'}}{\partial \phi}}^{T_f} \underbrace{-\frac{\partial \overline{w'\theta'}}{\partial z}}_{T_g} \overbrace{+k_h \nabla_h^2 \overline{\theta}}^{T_h} \underbrace{+k_z \frac{\partial^2 \overline{\theta}}{\partial z^2}}_{T_i}. \qquad (3.36)$$

The over and under bracketed terms include the preceding sign in their definitions.

3.A Appendix: Derivation of the Reynolds Decomposed Shallow Water Equations

The mean and eddy components of the state variables are defined as in Section 3.1.2. The zonal velocity, the meridional velocity and SSH can be deconstructed as,

$$u = \overline{u} + u' \qquad \text{and} \qquad v = \overline{v} + v', \qquad \text{and} \qquad \eta = \overline{\eta} + \eta', \qquad (3A.37)$$

where u', v' and η' denote fluctuations relative to the mean flow with $\overline{u'} = \overline{v'} = \overline{\eta'} = 0$. Equations 3A.37 are substituted into equation 3.1 resulting in the zonal momentum equation for the mean and eddy component as

$$\frac{\partial(\overline{u}+u')}{\partial t} + ((\overline{\mathbf{u_h}} + \mathbf{u_h'}) \cdot \nabla_h)(\overline{u}+u') - f(\overline{v}+v') =$$
$$-g\frac{\partial(\overline{\eta}+\eta')}{\partial x} - \frac{C_{drag}}{h}(\overline{u}+u')|\mathbf{u_h}| + A_h \nabla_h^2(\overline{u}+u') + \frac{\tau_x}{\rho h}, \quad (3A.38)$$

and similarly for the meridional momentum equation. The advection terms can be expressed as

$$
\begin{aligned}
\left(\mathbf{u_h'} \cdot \nabla_h\right) u' &= u'\frac{\partial u'}{\partial x} + v'\frac{\partial u'}{\partial y}, && \text{(3A.39)}\\
&= \frac{1}{2}\frac{\partial (u'u')}{\partial x} + \frac{\partial (v'u')}{\partial y} - u'\frac{\partial v'}{\partial y}, && \text{(3A.40)}
\end{aligned}
$$

Then using the three dimensional incompressibility condition (equation 3.4) leading to

$$
-u'\frac{\partial w'}{\partial z} - u'\frac{\partial v'}{\partial y} = u'\frac{\partial u'}{\partial x}, \tag{3A.41}
$$

we obtain

$$
\left(\mathbf{u_h'} \cdot \nabla_h\right) u' = \frac{\partial (u'u')}{\partial x} + \frac{\partial (v'u')}{\partial y} + u'\frac{\partial w'}{\partial z}. \tag{3A.42}
$$

By using similar operations for terms related to the mean flow such that

$$
\begin{aligned}
\left(\overline{\mathbf{u_h}} \cdot \nabla_h\right) \overline{u} &= \overline{u}\frac{\partial \overline{u}}{\partial x} + \overline{v}\frac{\partial \overline{u}}{\partial y}, && \text{(3A.43)}\\
&= \frac{\partial (\overline{u}\,\overline{u})}{\partial x} + \frac{\partial (\overline{v}\,\overline{u})}{\partial y} + \overline{u}\frac{\partial \overline{w}}{\partial z}. && \text{(3A.44)}
\end{aligned}
$$

Finally, we can time-average equation 3A.38 to obtain

$$
\begin{aligned}
\frac{\partial \bar{u}}{\partial t} = -\nabla_h \cdot \left(\overline{\mathbf{u_h}}\bar{u}\right) - \overline{u}\frac{\partial \overline{w}}{\partial z} - g\frac{\partial \bar{\eta}}{\partial x} + f\bar{v} - \nabla_h \cdot \left(\overline{\mathbf{u_h'}u'}\right) - \overline{u'\frac{\partial w'}{\partial z}}\\
+\frac{\overline{\tau_x}}{\rho h} - \overline{\frac{C_{drag}}{h}u\sqrt{u^2+v^2}} + A_h\nabla_h^2\bar{u},
\end{aligned} \tag{3A.45}
$$

and similarly, when repeating the operations for equation 3.2,

$$
\begin{aligned}
\frac{\partial \overline{v}}{\partial t} = -\nabla_h \cdot \left(\bar{\mathbf{u}}_\mathbf{h}\bar{v}\right) - \overline{v}\frac{\partial \overline{w}}{\partial z} - g\frac{\partial \bar{\eta}}{\partial y} - f\bar{u} - \nabla_h \cdot \left(\overline{\mathbf{u_h'}v'}\right) - \overline{v'\frac{\partial w'}{\partial z}}\\
-\overline{\frac{C_{drag}}{h}v\sqrt{u^2+v^2}} + A_h\nabla_h^2\bar{v}.
\end{aligned} \tag{3A.46}
$$

It is then possible to re-express the vertical velocities through the use of the boundary conditions and by integrating in the vertical direction and using no-normal flow at the bottom:

$$
\int_{-H}^{\eta} \frac{\partial w}{\partial z} dz = w(\eta) + w(-H) = \frac{D\eta}{Dt} \tag{3A.47}
$$

Thus, by vertically integrating equations 3A.45 and 3A.46, and noting the independence of several terms to z, we obtain

$$\begin{aligned}\frac{\partial \bar{u}}{\partial t} = -\nabla_h \cdot (\bar{\mathbf{u}}_\mathbf{h}\bar{u}) - \overline{\frac{u}{h}\frac{Dh}{Dt}} - g\frac{\partial \bar{\eta}}{\partial x} + f\bar{v} - \nabla_h \cdot (\overline{\mathbf{u}'_\mathbf{h}u'}) - \overline{\frac{u'}{h}\frac{Dh'}{Dt}} \\ + \frac{\overline{\tau_x}}{\rho h} - \overline{\frac{C_{drag}}{h}u\sqrt{u^2+v^2}} + A_h\nabla_h^2\bar{u},\end{aligned} \tag{3A.48}$$

and

$$\begin{aligned}\frac{\partial \bar{v}}{\partial t} = -\nabla_h \cdot (\bar{\mathbf{u}}_\mathbf{h}\bar{v}) - \overline{\frac{v}{h}\frac{Dh}{Dt}} - g\frac{\partial \bar{\eta}}{\partial y} - f\bar{u} - \nabla_h \cdot (\overline{\mathbf{u}'_\mathbf{h}v'}) - \overline{\frac{v'}{h}\frac{Dh'}{Dt}} \\ - \overline{\frac{C_{drag}}{h}v\sqrt{u^2+v^2}} + A_h\nabla_h^2\bar{v},\end{aligned} \tag{3A.49}$$

where the overbar in these two equations now represents both a time-mean and vertical integral.

3.B Appendix: Derivation of the Reynolds Decomposed Hydrostatic Primitive Equations

The HPE equations are decomposed using a similar methodology as that in employed for the barotropic model. An example of how the Reynolds stresses are derived is now explained using the zonal momentum equation. The nonlinear terms in the equations are related to the advection operator, in order to find the Reynolds stresses the advection term in the zonal baroclinic momentum equation is time averaged and rearranged as,

$$\overline{(\mathbf{u}\cdot\nabla)u} = \overline{(\overline{\mathbf{u}}\cdot\nabla)\overline{u}} + \overline{(\mathbf{u}'\cdot\nabla)u'}. \tag{3B.50}$$

The first term on the right-hand side (rhs) is

$$(\overline{\mathbf{u}}\cdot\nabla)\overline{u} = \frac{\overline{u}}{rcos\phi}\frac{\partial \overline{u}}{\partial \lambda} + \frac{\overline{v}}{r}\frac{\partial \overline{u}}{\partial \phi} + \overline{w}\frac{\partial \overline{u}}{\partial r}. \tag{3B.51}$$

In order to find the related Reynolds stresses this is combined with the incompressibility condition multiplied by the mean zonal velocity:

$$\overline{u}\nabla\cdot\overline{\mathbf{u}} = \frac{\overline{u}}{rcos\phi}\left(\frac{\partial \overline{u}}{\partial \lambda} + \frac{\partial}{\partial \phi}(\overline{v}cos\phi)\right) + \frac{\overline{u}}{r^2}\frac{\partial r^2\overline{w}}{\partial r} = 0. \tag{3B.52}$$

This addition leads to

$$(\bar{\mathbf{u}} \cdot \nabla)\bar{u} + \bar{u}\nabla \cdot \bar{\mathbf{u}} = \bar{w}\frac{\partial \bar{u}}{\partial r} + \frac{\bar{u}}{r^2}\frac{\partial r^2 \bar{w}}{\partial r} + \frac{\bar{u}}{rcos\phi}\frac{\partial \bar{v}cos\phi}{\partial \phi} + \frac{\bar{v}}{r}\frac{\partial \bar{u}}{\partial \phi} + \frac{1}{rcos\phi}\frac{\partial \bar{u}\bar{u}}{\partial \lambda} \tag{3B.53}$$

which on rearrangement this is

$$\frac{1}{rcos\phi}\frac{\partial \bar{u}\bar{u}}{\partial \lambda} + \frac{\partial \bar{w}\bar{u}}{\partial r} + \underline{2\frac{\bar{u}\bar{w}}{r}} + \frac{1}{r}\frac{\partial \bar{v}\bar{u}}{\partial \phi} - \underline{\frac{\bar{u}\bar{v}tan\phi}{r}} \tag{3B.54}$$

The underlined terms are removed due to both the traditional and the hydrostatic approximations, and the time average of equation 3B.54 results in the first part of the decomposed advection operator. The eddy terms on the rhs of equation 3B.50 are found in the same manner:

$$\overline{(\mathbf{u}' \cdot \nabla)u'} = \frac{1}{rcos\phi}\frac{\partial \overline{u'u'}}{\partial \lambda} + \frac{\partial \overline{w'u'}}{\partial r} + \underline{2\frac{\overline{u'w'}}{r}} + \frac{1}{r}\frac{\partial \overline{v'u'}}{\partial \phi} - \underline{\frac{\overline{u'v'}tan\phi}{r}}. \tag{3B.55}$$

These procedures are repeated for the meridional momentum and heat equations resulting in the Reynolds decomposed equations. After the thin shell approximation is applied and defining pressure as in equation 3.31, the Reynolds decomposed zonal,

$$\begin{aligned}\underbrace{\frac{\partial \bar{u}}{\partial t}}_{U_a} = & \overbrace{-\frac{1}{acos\phi}\frac{\partial \bar{u}\bar{u}}{\partial \lambda}}^{U_b} \underbrace{-\frac{1}{a}\frac{\partial \bar{v}\bar{u}}{\partial \phi}}_{U_c} \overbrace{-\frac{\partial \bar{w}\bar{u}}{\partial z}}^{U_d} \underbrace{-\frac{g}{acos\phi}\frac{\partial \bar{\eta}}{\partial \lambda}}_{U_e} \underbrace{+\frac{g}{acos\phi}\frac{\partial \int_z^0 \alpha_\theta(\bar{\theta} - \theta_{ref})dz}{\partial \lambda}}_{U_f} \underbrace{+f\bar{v}}_{U_g} \\ & \overbrace{-\frac{1}{acos\phi}\frac{\partial \overline{u'u'}}{\partial \lambda}}^{U_h} \underbrace{-\frac{1}{a}\frac{\partial \overline{v'u'}}{\partial \phi}}_{U_i} \overbrace{-\frac{\partial \overline{w'u'}}{\partial z}}^{U_j} \underbrace{+\overline{F_\lambda} + \overline{D_\lambda}}_{U_k} \overbrace{+uvtan\phi}^{U_l},\end{aligned} \tag{3B.56}$$

and meridional,

$$\begin{aligned}\underbrace{\frac{\partial \bar{v}}{\partial t}}_{V_a} = & \overbrace{-\frac{1}{acos\phi}\frac{\partial \bar{u}\bar{v}}{\partial \lambda}}^{V_b} \underbrace{-\frac{1}{a}\frac{\partial \bar{v}\bar{v}}{\partial \phi}}_{V_c} \overbrace{-\frac{\partial \bar{w}\bar{v}}{\partial z}}^{V_d} \underbrace{-\frac{g}{a}\frac{\partial \bar{\eta}}{\partial \phi}}_{V_e} \underbrace{+\frac{g}{a}\frac{\partial \int_z^0 \alpha_\theta(\bar{\theta} - \theta_{ref})dz}{\partial \phi}}_{V_f} \underbrace{-f\bar{u}}_{V_g} \\ & \overbrace{-\frac{1}{acos\phi}\frac{\partial \overline{u'v'}}{\partial \lambda}}^{V_h} \underbrace{-\frac{1}{a}\frac{\partial \overline{v'v'}}{\partial \phi}}_{V_i} \overbrace{-\frac{\partial \overline{w'v'}}{\partial z}}^{V_j} \underbrace{+\overline{F_\phi} + \overline{D_\phi}}_{V_k} \overbrace{+\frac{u^2tan\phi}{a}}^{V_l},\end{aligned} \tag{3B.57}$$

momentum equations are derived. Finally, the Reynolds decomposed temperature equation is

$$\underbrace{\frac{\partial \overline{\theta}}{\partial t}}_{T_a} = -\overbrace{\frac{1}{acos\phi}\frac{\partial \overline{u}\overline{\theta}}{\partial \lambda}}^{T_b} - \underbrace{\frac{1}{a}\frac{\partial \overline{v}\overline{\theta}}{\partial \phi}}_{T_c} - \overbrace{\frac{\partial \overline{w}\overline{\theta}}{\partial z}}^{T_d} - \underbrace{\frac{1}{acos\phi}\frac{\partial \overline{u'\theta'}}{\partial \lambda}}_{T_e} - \overbrace{\frac{1}{a}\frac{\partial \overline{v'\theta'}}{\partial \phi}}^{T_f} - \underbrace{\frac{\partial \overline{w'\theta'}}{\partial z}}_{T_g} \overbrace{+k_h \nabla_h^2 \overline{\theta}}^{T_h} \underbrace{+k_z \frac{\partial^2 \overline{\theta}}{\partial z^2}}_{T_i} . \tag{3B.58}$$

The physical processes associated with all these tendencies are presented Section 4.3.1, in Tables 4.1, 4.2 and 4.3.

Chapter 4

Intrinsic Sea Surface Height Variability: from seasonal to interannual timescales

4.1 Introduction

This study focuses on the emergence of interannual intrinsic variability in western boundary current (WBC) jet extension regions. Intrinsic here means that the variability is generated by oceanic dynamical processes, in the presence of an applied time-independent atmospheric forcing.

As the use of high-resolution ocean models in climate predictions becomes more common, it is pertinent to examine how the presence of mesoscale eddies influence the models' interannual variability. The introduction of eddies will likely have significant impacts, as studies with OGCM models have already demonstrated that an increase in model resolution (from 2° to 1/4°) yields an increase in interannual variability (Penduff et al., 2011). This increase brings model variability closer to that observed by altimeter measurements, where interannual SSH variability is primarily located in ocean jets (Fu, 2004; Qiu and Chen, 2005; Thompson and Richards, 2011). In agreement with these findings, numerous studies utilizing quasi-geostrophic and shallow water models, in configurations with idealised geometries and steady or seasonal forcings, have shown the emergence of interannual intrinsic variability (Jiang et al., 1995; Spall, 1996; Dewar, 2003; Simonnet et al., 2005; Berloff et al., 2007; Quattrocchi et al., 2012). Moreover, such variability is principally located in mid-latitude jets, influencing both their strength and position (Jiang et al., 1995; Berloff et al., 2007).

Several studies have proposed mechanisms responsible for driving the intrinsic interannual variability. These include: using dynamical systems theory to consider the early bifurcations in forced and dissipative dynamical systems (reviewed by Dijkstra and Ghil (2005)), the excitation of basin modes by the applied external forcings (Cessi and Paparella, 2001), interactions of the deep WBCs with the wind-driven gyres (Katsman et al., 2001), and the rectification of eastern jets in WBCs by mesoscale eddies (Berloff et al., 2007). However, only a few studies have addressed the processes which generate interannual intrinsic variability in ocean models which solve the primitive equations (Taguchi et al., 2010; Thompson and Richards, 2011; Sérazin et al., 2018). Moreover, although mesoscale eddies have been identified as essential contributors to interannual intrinsic variability (Kwon et al., 2010), the eddy-mean flow interactions which generate such variability, remain poorly understood phenomena. However, the effects attributed to eddies may not be the sole cause of intrinsic interannual variability, indeed Huck et al. (2015) demonstrated that in some cases modes of intrinsic variability may even be robust to the resolution of eddies.

The chapter contains an examination of the dynamical mechanism of SSH intrinsic variability in two idealised model setups described in Chapter 3. The work presented aims to:

- Identify any interannual variability present in both barotropic and baroclinic gyre models and examine the associated dynamical mechanisms.
- Identify the regions where eddy momentum tendencies are important in driving interannual intrinsic variability.
- Investigate how the addition of buoyancy affects any interannual variability present.

The interannual intrinsic variability is shown to be concurrent with several different eddy-mean flow interactions. The barotropic model displays interannual variability (timescales of 1-2 years) in both the jet's zonal velocity and its latitudinal position. These variations occurred due to two different mechanisms, involving eddy momentum flux convergences. The variability in the jet's position is attributed to fluctuations in the transports within the western boundary currents. On the other hand, the variations in the jet's transport are shown to be concurrent with eddy-mean flow interactions, acting to rectify the jet. In the baroclinic model, the effect of eddy heat fluxes on the stratification in mid-latitude led to the meridional migration of anomalous jets on interannual timescales (≈ 5 years). This migration is shown to be due to eddy-jet interactions caused by asymmetries in the eddy heat fluxes, resulting in the migration of the anomalous jets' baroclinic zones.

This Chapter is divided into three sections. The first two sections address the mechanisms by which interannual intrinsic variability is generated in both a barotropic double gyre model and a baroclinic multi-gyre model. The final section contains a discussion of the results.

4.2 Interannual Intrinsic Variability in Mid-latitude Barotropic Jets

Power spectra of SSH taken at several locations in the domain (indicated in Figure 3.2b), are shown in Figure 4.1. The power spectrum of SSH anomalies in the jet region (location C) exhibits enhanced interannual variability on timescales of 1-3 years. Such power is not present in the spectra taken in subtropical gyre's interior (locations A and B), which has white spectral characteristics on multi-year timescales. These differences are indicative that the dynamical processes present are regionally dependent. The peaks which occur in all regions at higher frequencies (periods of less than a year), are potentially related to basin-scale adjustment processes, such as barotropic Rossby waves.

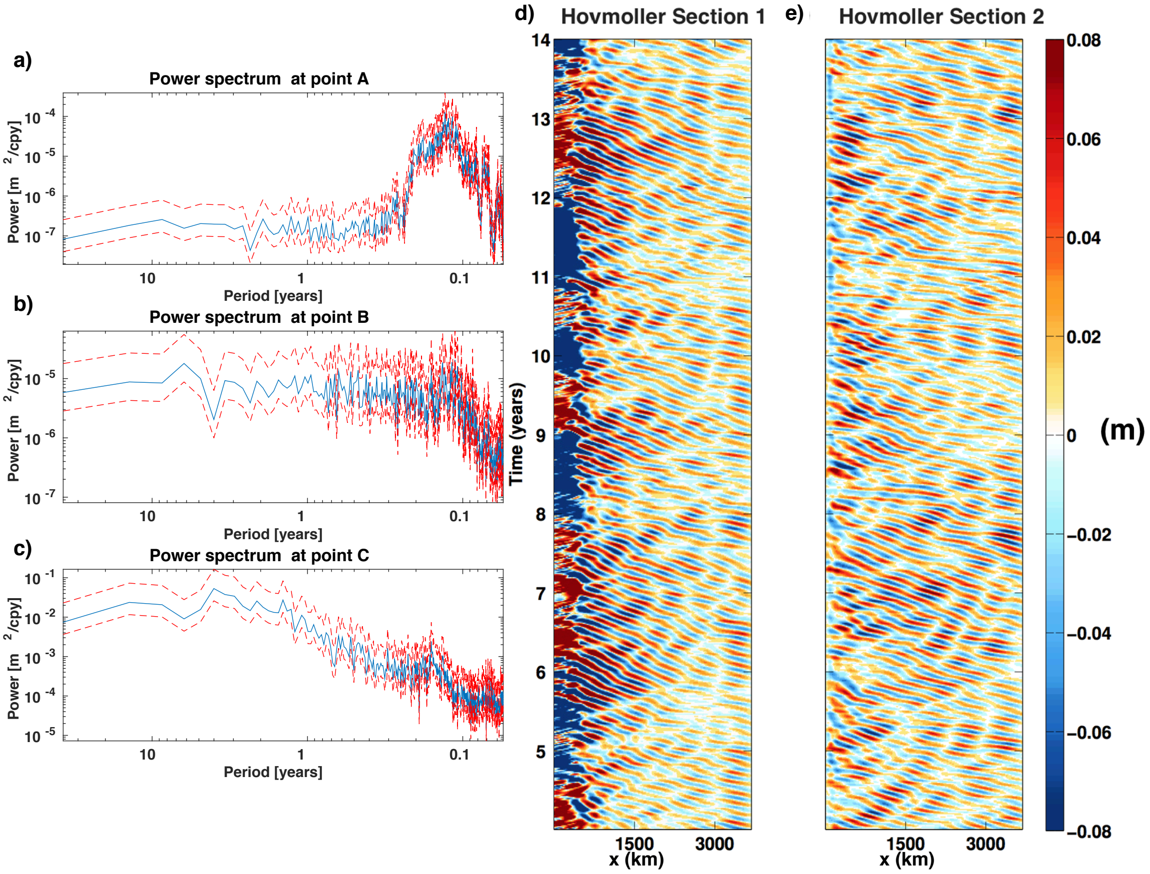

Figure 4.1: a-c) Power spectra constructed from 90 years of SSH anomaly data taken at three different locations marked in Figure 3.2b, showing spectral power (in units of m^2/cpy where, cpy, is cycles per year) as a function of time period in years. Hövmoller diagrams of SSH anomalies taken at the latitude (d) coinciding with the time-mean jet position (Section 1) and (e) in the gyre interior (Section 2) marked in Figure 3.2 b. The dashed red lines show the 95%-confidence intervals of the power spectra, calculated using an inverse chi-squared distribution.

Figure 4.1, panels d and e, shows Hövmoller diagrams at two sections as indicated in Figure 3.2b, one at the same latitude of the time mean jet (Section 1) and one at a latitude in the subpolar gyre (Section 2). The Hövmoller taken in the jet (Section 1), displays significant SSH anomalies in the vicinity of the western boundary that can persist for several years. The timescale of this variability is in agreement with the large values of spectral power found on interannual timescales (Figure 4.1c). In Figure 4.1 panels d and e, there are also features which have eastward group velocities and westward phase speeds. These are hypothesized to be short Rossby waves reflected from the western boundary (as discussed by Moore et al. (2002) and Section 7 of Rhines (1977)). The phase speeds are similar to those hypothesised from the dispersion relation (equation 2.10). In ocean observations it is difficult to detect short Rossby waves as mixing acts strongly on short and slow waves.

An empirical orthogonal function (EOF) analysis of 150 years of 5-day mean SSH model output, is used to determine the spatial patterns and timescales of the statistical modes of variability present. Figure 4.2a shows that 20 EOFs are needed to reconstruct about 65% of the variability. Although this is a relatively low figure, repeat analysis using monthly and 3-monthly means resulted in the same key results which described in this chapter. Figure 4.2b depicts the leading EOF which consists of a latitudinal tri-polar pattern in SSH anomalies. Such a tri-polar pattern relates to meridional shifts in the jet position (Berloff et al., 2007). The second EOF, shown in Figure 4.2c, displays a dipolar structure, which controls the gradient of SSH across the jet and therefore the geostrophic transport in the jet.

The interpretations of the leading EOFs and associated principal components (time series) are confirmed through comparisons with other properties of the system. Consider two series $x(i)$ and $y(i)$ where $i = 0, 1, 2..N-1$. The lagged cross correlation r at time d is defined as,

$$r(d) = \frac{\sum_i (x(i) - \overline{x})(y(i-d) - \overline{y})}{\sqrt{\sum_i (x(i) - \overline{x})^2}\sqrt{\sum_i (y(i-d) - \overline{y})^2}}, \tag{4.1}$$

where $\overline{x}$ and $\overline{y}$ are means of the corresponding series. The meridional jet position, defined as the meridional location of the maximum value of the zonally integrated zonal velocity, strongly correlates with the first principal component at zero lag times (Figure 4.2h). It also displays significant correlation at both lead and lag times of 3-6 months. Moreover, the transport in the jet, defined as the maximum value of the zonally averaged zonal velocity, correlates strongly with the second principal component at zero time lag (Figure 4.2i). This zonal velocity is seen to vary between $\approx$ 0.3-0.55 m/s, and the jet moves meridionally between $\approx$ 1850km and 2000km, a distance which spans 20 model gridboxes.

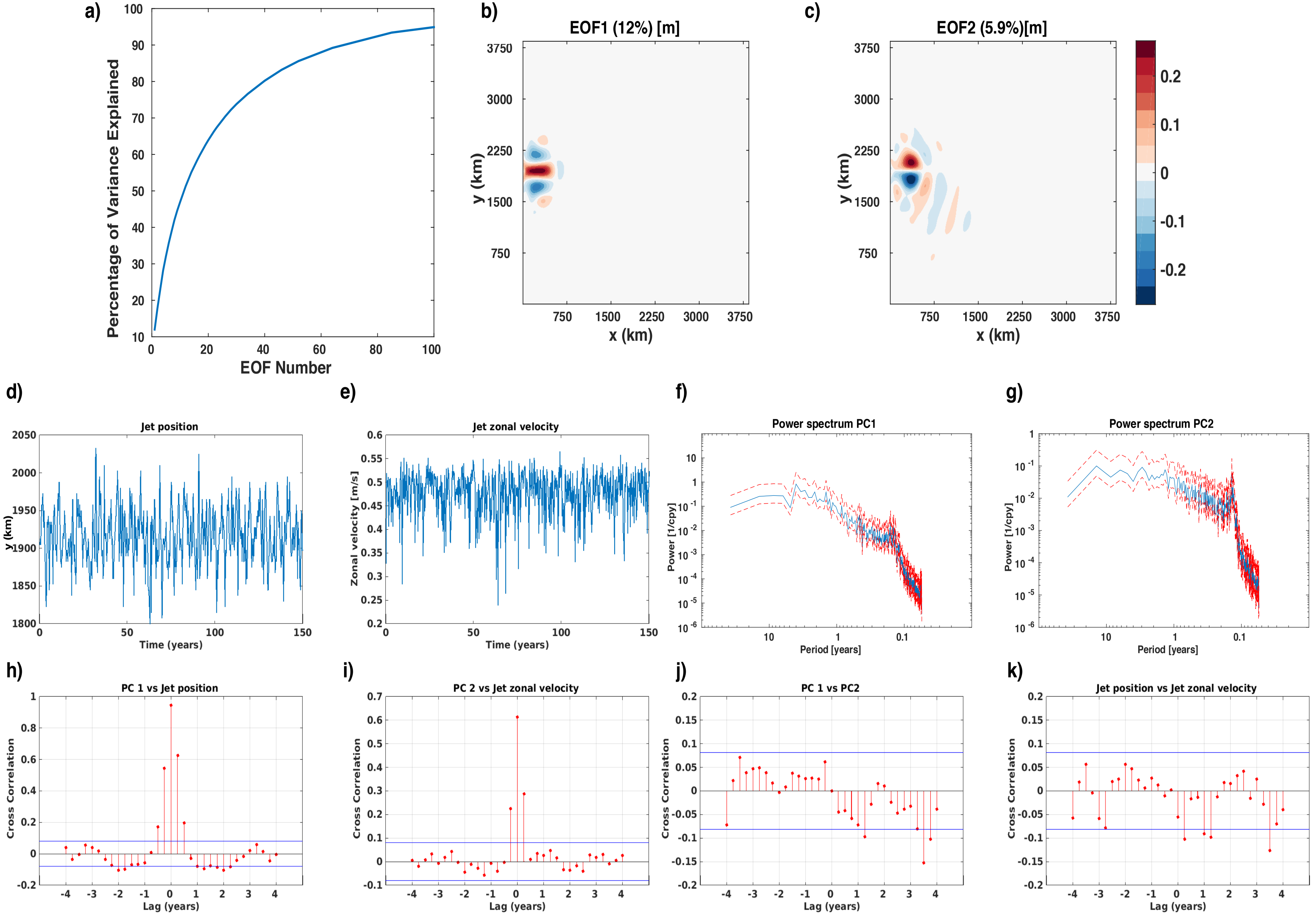

Figure 4.2: (a) The cumulative percentage of variance explained by the leading 100 EOFs. (b-c) The leading two EOFs of SSH, the quantity in brackets corresponds to the fraction of the variance each explains. Time series of the jet's: (d) meridional position and (e) zonal transport. (f-g) Power spectra of the first two principal components. The cross-correlations of: (h) the first principal component and the jet's meridional position, (i) the second principal component and the zonal velocity in the jet, (j) the first and second principal components, (k) the jet's meridional position and the zonal velocity in the jet. The blue lines are the upper and lower 95% confidence bounds for a normal distribution, N(0,1/L) with a standard deviation of $1/\sqrt(L)$, where L is the number of time means used in the analysis.

Figure 4.2j shows that the leading two principal components are not strongly correlated at any lag time. At only a few times are any of the correlations significant, and at these times they are very weakly correlated. This is indicative that the barotropic jet transport is not related to the meridional jet position, which is confirmed in panel k. The lack of any substantial and significant correlations indicate that smaller scale processes local to the jet, may be acting to influence its strength.

While the raw time series of jet's meridional position and transport (panels d and e) appear to exhibit interannual variability in both the jet's meridional position and transport, the power spectra of the two principal components associated with the EOFs are white on interannual timescales (Figure 4.2f and g). This indicates that they may, therefore, be unpredictable on interannual timescales.

4.2.1 Barotropic Rossby Wave Basin Modes

The Hövmoller plots in Figure 4.1 show the presence of westward propagating waves in basin interior, away from the western boundary. Both the Hövmoller plots and the power spectra (Figures 4.1) show that these waves act with periods of approximately 0.1-0.2 years. All the power spectra in Figure 4.1 show a peak in spectral power on a timescale of 0.1-0.2 years, and peaks on timescales of less than 0.1 years. It is hypothesised that such peaks are the result of the presence of barotropic basin modes. Such modes have been previously detected in reduced gravity models and arise due to basin-wide resonances of Rossby waves, which span the basin an integral number of times (Cessi and Paparella, 2001). Such waves have zonal wave numbers

$$k = \frac{2\pi N}{L_x}, \tag{4.2}$$

which depend on the width of the basin (where N is an integer number and L_x is the length of the basin (3840 km)).

An ultra-simplified calculation, whereby a constant mean flow and a single Rossby wave crossing time are assumed is used to estimate the time periods of the barotropic basin modes. This approach is relevant in quasi-geostrophic systems which have

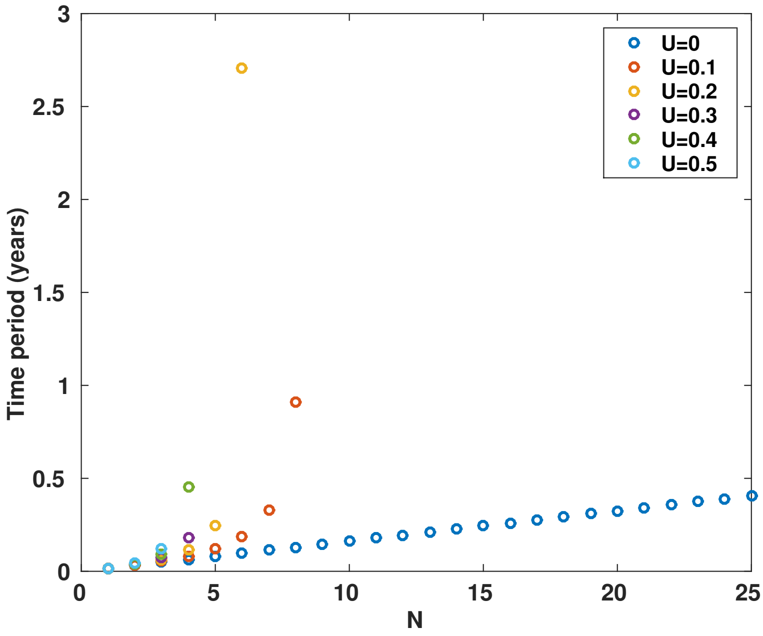

Figure 4.3: Time periods of ultra-idealised barotropic Rossby wave basin modes as a function of the integer number N, calculated using equations 2.10 and 4.2, for several different velocities of the zonal mean flow, U (m/s). Only time periods of westward propagating waves are shown.

a constant basin width, however, is not applicable to systems with more complex geometries such as those discussed by Primeau (2002). The barotropic basin mode time periods are calculated using equation 2.10 with various constant mean flow velocities, and are shown in Figure 4.3. In the gyre regions the mean zonal flow is approximately zero, and the Rossby basin modes with the longest wavelengths act on timescales of 0.1-0.2 years, in agreement with the peak shown in Figure 4.1a.

The spectra which are taken in the jet region, Figure 4.1c, contains spectral power on interannual frequencies (periods longer than 1 year), which is not present in the gyre regions. One possible cause of this behaviour is that in the jet region the Rossby waves can be Doppler shifted by the mean flow, which can result in waves having longer time periods in the vicinity of the jet (months-years). The interannual variability does not possess any sharp peaked features and therefore cannot be attributed to a specific combination of the basin modes and zonal mean flow velocities. Therefore, further investigation is required to establish the origin of the interannual variability in the jet.

4.2.2 Influence of Transport on the Jet's Position and Strength

Although the interannual variability in jet position is not seen to correlate with variations in transport in the jet, it might be related to non-local changes in the transport at different times. To investigate these changes, the SSH, and the zonal (u) and meridional (v) velocities are used to create composites of times when the meridional jet position, defined by the meridional location of the zonally integrated zonal velocity, is northward or southward of certain thresholds. If the jet latitude is north of 1980km (southward 1860 km), it is referred to as being in the northward (southward) state. The mean jet meridional position is at 1920 km. The most notable differences between northward and southward jet states are apparent when diagnosing the meridional velocities, as shown in Figure 4.4. A comparison between the meridional averages of v at the two different jet positions (Figure 4.4 i), shows a reversal in sign, in not only the western boundary currents but also between the regions south of the recirculation gyres. The composites in panels b and e exhibit differences in zonal transport north and south of the recirculation gyres. Such a difference could correspond an eddy being shed and advected around the recirculation gyres. This difference is also noticeable in both the meridional and zonal averages of SSH (Figure 4.4 g and j). The zonal velocity averages do not undergo any major variations in magnitude as the jet shifts position. Therefore it is the relative differences in the subpolar and subtropical boundary currents and recirculation gyres which govern the variability in the jet's meridional position. In this model set up, it is hypothesised that the variations in the strength of the western boundary currents, are a result of changes in the relative gyre strengths due to the eddy components, and eddy-boundary current interactions, as in McCalpin and Haidvogel (1996).

Figure 4.5 analyses the variations in the strength of the jet. The jet's state is

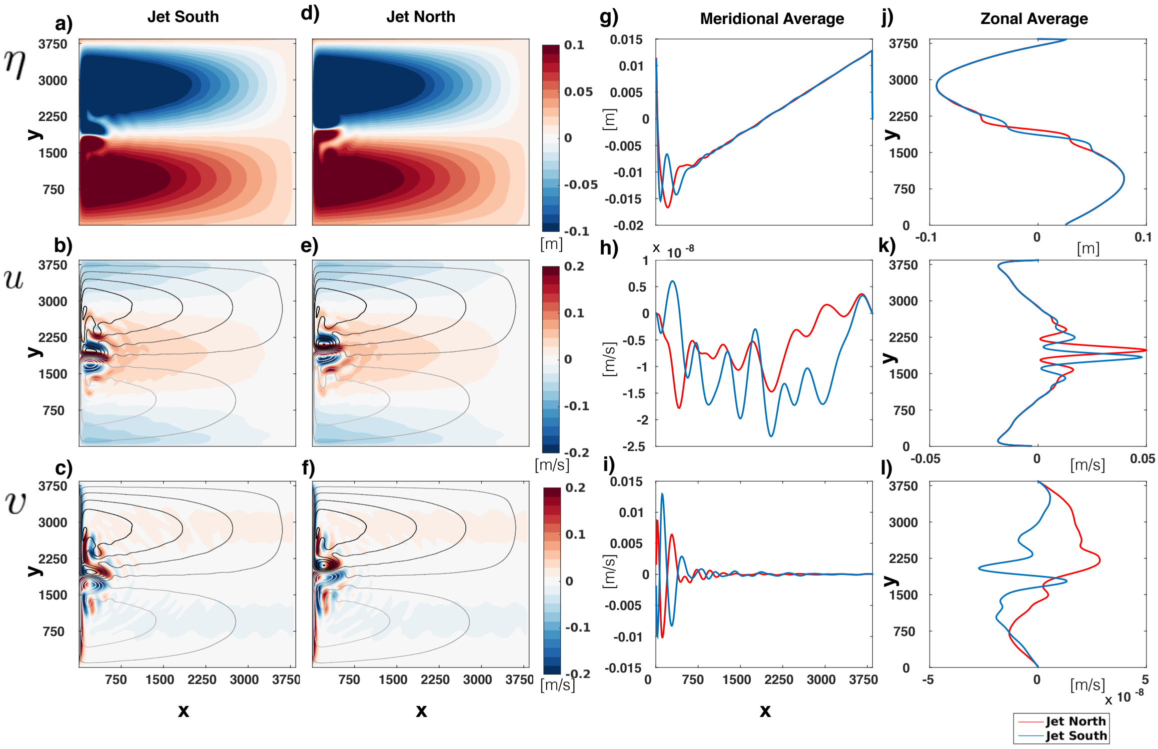

Figure 4.4: Composite means, of the 5 day mean fields of: (a) SSH, (b) u and (c) v taken when the jet is in a southward jet position, and (d) SSH (e) u and (f) v when the jet is in a northward jet position. Meridional (zonal) averages of the composites of, (g) SSH, (h) u and (i) v, ((j) SSH, (k) u and (l) v) at both northward and southward jet positions. The black and grey contours in panels b and c (panels e and f), are 5cm contours of SSH taken in the southward (northward) jet positions.

characterised by its maximum zonally averaged zonal velocity, with a strong (weak) jet corresponding to a zonal velocity greater than 0.5 m/s (less than 0.45 m/s). Although the gap between the two defined states is quite small, Figure 4.2 shows that these limits are clearly separate the variability extremes present. The zonally averaged u (Figure 4.5k) is larger in the core and the flank of the jet in the strong jet states relative to the weak states. A comparison of panels b and e demonstrates that in the strong states there is an intensification of the jet's zonal velocity, as well as intensifications of the zonal return flow in the recirculation gyres. These variations manifest themselves as ≈ 100km fluctuations in the length of the jet, as seen in the SSH (panels a and d). There is also a steepening in the gradient of SSH across the recirculation gyres when the jet is in a strong state (Figure 4.5j) relative to the weak state. This variation is due to geostrophy and is a reflection of the variations in transport. The meridionally averaged v, Figure 4.5i, also demonstrates a change in the zonal extent of the recirculation gyres.

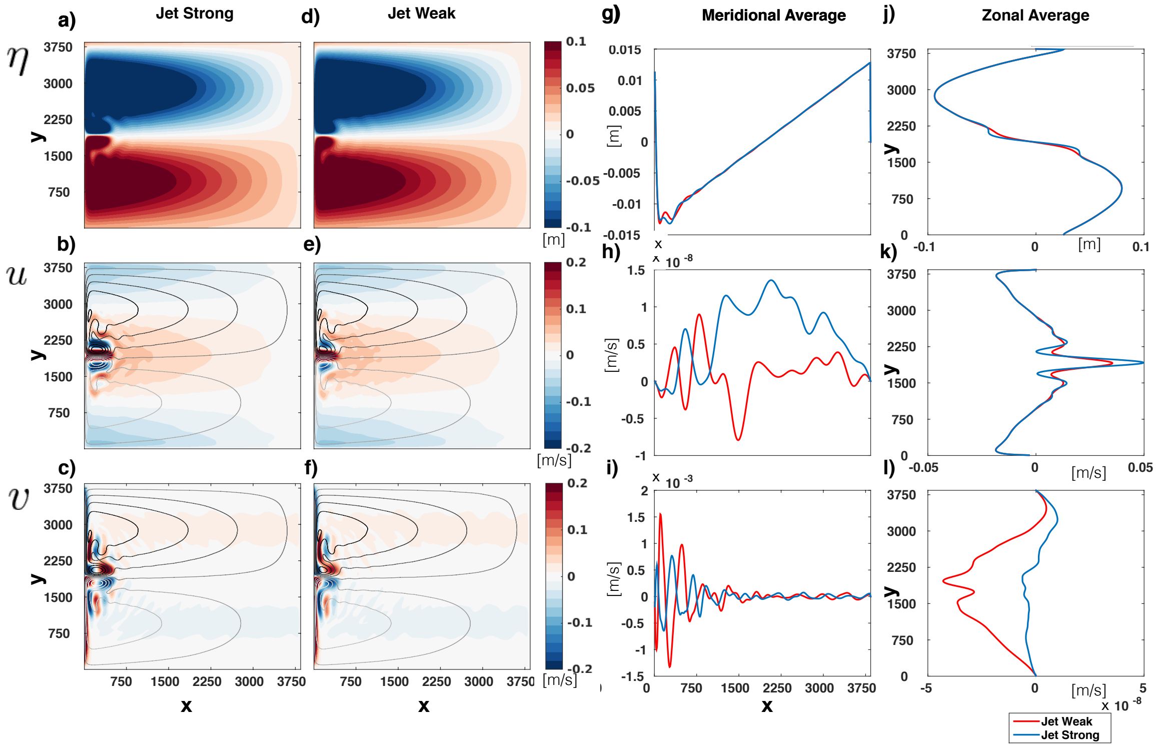

Figure 4.5: Composite means, of the 5-day mean fields of: (a) SSH, (b) u and (c) v taken when the jet is in a strong state, and (d) SSH (e) u and (f) v when the jet is in a weak state. Meridional (zonal) averages of the composites of, (g) SSH, (h) u and (i) v, ((j) SSH, (k) u and (l) v) at both strong and weak jet states.

4.2.3 Jet Position and Strength: Momentum Budget Analysis

A budget decomposition is used to infer variations in the momentum tendencies as the jet changes position and strength. The zonal and meridional momentum equations, are as given in equations 3.1 and 3.2,

$$\underbrace{\frac{\partial u}{\partial t}}_{U_a} = \overbrace{-(\mathbf{u_h}\cdot\nabla_h)u}^{U_b} \underbrace{+fv}_{U_c} \overbrace{-g\frac{\partial \eta}{\partial x}}^{U_d} \underbrace{+\frac{\tau}{\rho h}}_{U_e} \overbrace{-\frac{C_{drag}}{h}u\sqrt{u^2+v^2}+A_h\nabla_h^2 u}^{U_f}, \qquad \text{(3.1 revisited)}$$

and

$$\underbrace{\frac{\partial v}{\partial t}}_{V_a} = \overbrace{-(\mathbf{u_h} \cdot \nabla_h)v}^{V_b} \underbrace{-fu}_{V_c} \overbrace{-g\frac{\partial \eta}{\partial y}}^{V_d} \underbrace{-\frac{C_{drag}}{h}v\sqrt{u^2+v^2} + A_h\nabla_h^2 v}_{V_e}, \qquad \text{(3.2 revisited)}$$

where the variables and parameters as defined in Section 3.1. The under-braced and over-braced quantities include the preceding signs in their definitions.

Composites of the different tendencies are calculated in the same manner as described in the previous section. We then examine the zonal and meridional averages of these composites in the western part of the domain in an area of the domain where jet variability is most prominent (0-2000km in the x-direction, at all y values). Figure 4.6 examines the changes in the budget as the jet shifts meridionally. It is difficult to discern any changes in the momentum budget between the northward (dashed lines) and southward (solid lines) shifted jet states, apart from some discrepancies in the meridionally averaged meridional momentum equation (panel c). This panel shows a balance between the tendency from the Coriolis term and the advective tendencies, with the tendencies changing their sign depending on the meridional position of the jet. The balance occurs mainly near to the western boundary, and in and around the recirculation gyres, which correspond to the regions discussed in the transport analysis. In the other averages (panels a, b and d), geostrophic balance dominates the tendencies, with only small contributions from the ageostrophic terms, except in panel b. In panel b, there is a balance between the steady wind forcing and the differences between the pressure and Coriolis terms. The lack of any noticeable differences in the other averages indicates that the main differences between the two states are contained in the meridional non-linear advective terms.

The composites of the averaged tendencies relevant to the changes in transport are shown in 4.7. Notably, the variations in transport cause changes in the magnitude of the zonally averaged meridional geostrophic balance (panel d). The largest noticeable changes between the two states occurs in the meridionally averaged meridional

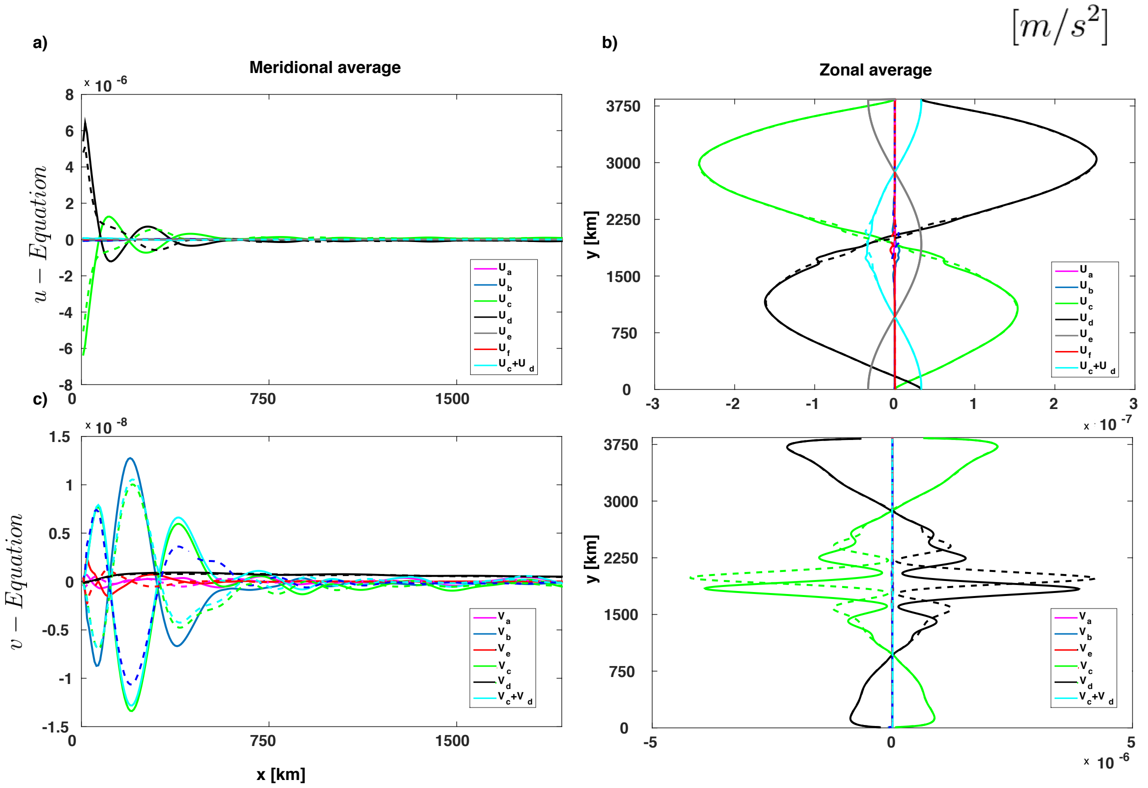

Figure 4.6: Averages of the zonal [meridional] momentum equation in the (a)[(c)] meridional and (b)[(d)] zonal directions. The dashed (solid) lines indicate when the jet is shifted northward (southward).

momentum equation (panel c), but these are of small magnitudes. As these variations are hard to interpret, it motivates an examination of the spatial variations in the Reynolds stresses.

4.2.4 The Reynolds Decomposed Momentum Budget

To assess the impact of the eddy terms on the interannual variability of the jet position and transport, a Reynolds decomposition of the zonal and meridional momentum equations, 3.1 and 3.2, is performed. The derivations of these are detailed in Section 3.1.2 and result in:

$$\begin{aligned}\frac{\partial \bar{u}}{\partial t} = -\nabla_h \cdot (\bar{\mathbf{u}}_{\mathbf{h}}\bar{u}) - \overline{\frac{u}{h}\frac{Dh}{Dt}} - g\frac{\partial \bar{\eta}}{\partial x} + f\bar{v} - \nabla_h \cdot (\overline{\mathbf{u}'_{\mathbf{h}}u'}) - \overline{\frac{u'}{h}\frac{Dh'}{Dt}} \\ + \overline{\frac{\tau}{\rho h}} - \overline{\frac{C_{drag}}{h}u\sqrt{u^2+v^2}} + A_h\nabla_h^2\bar{u},\end{aligned} \tag{3.8 revisited}$$

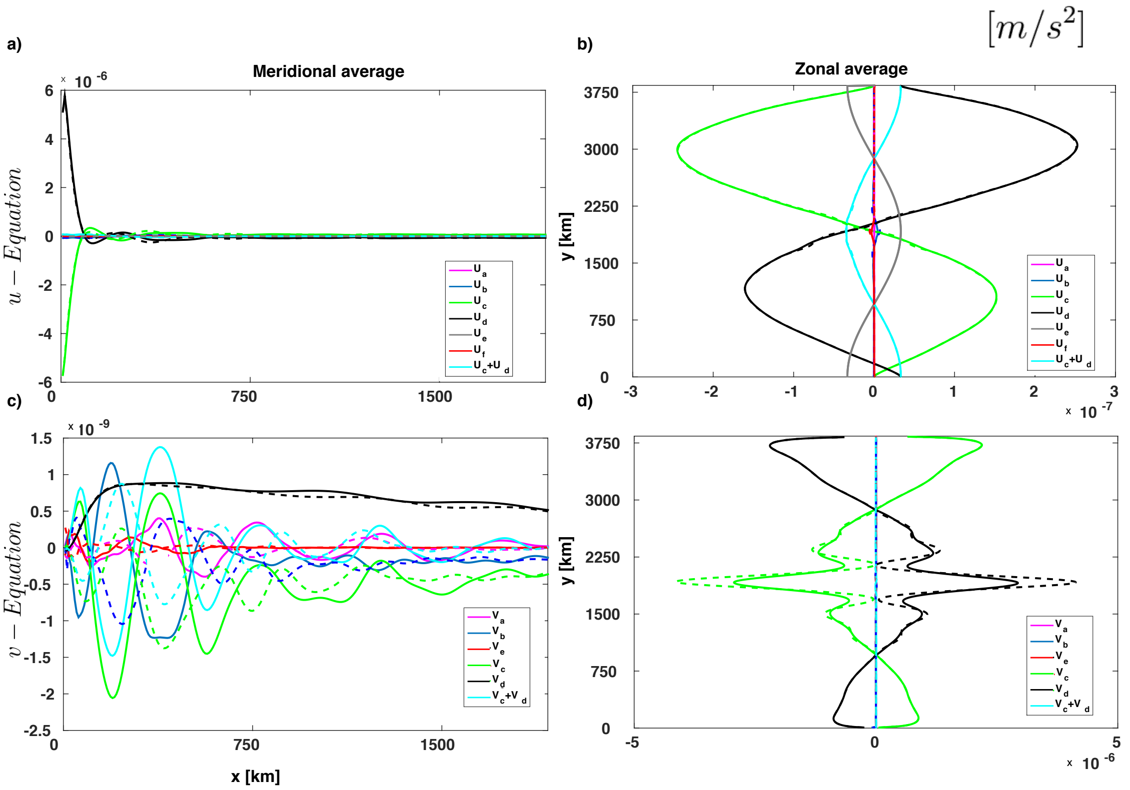

Figure 4.7: a) Averages of the zonal [meridional] momentum equation in the (a)[(c)] meridional and (b)[(d)] zonal directions.The dashed (solid) lines indicate when the jet transport is strong (weak).

and

$$\frac{\partial \bar{v}}{\partial t} = -\nabla_h \cdot (\bar{\mathbf{u}}_{\mathbf{h}}\bar{v}) - \overline{\frac{v}{h}\frac{Dh}{Dt}} - g\frac{\partial \bar{\eta}}{\partial y} - f\bar{u} - \nabla_h \cdot (\overline{\mathbf{u}'_{\mathbf{h}} v'}) - \overline{\frac{v'}{h}\frac{Dh'}{Dt}} \\ - \overline{\frac{C_{drag}}{h} v\sqrt{u^2+v^2}} + A_h \nabla_h^2 \bar{v}. \tag{3.9 revisited}$$

To allow for a comparison with the results of Waterman and Jayne (2011), the divergence of the eddy potential vorticity (PV) flux, or eddy potential vorticity forcing term is also calculated (Waterman and Hoskins, 2013),

$$-\nabla_h \cdot \overline{\mathbf{u_h}' q'} = 2\frac{\partial^2 M}{\partial x \partial y} - \frac{\partial^2 N}{\partial x^2} + \frac{\partial^2 N}{\partial y^2}, \tag{4.3}$$

where, $N = \overline{u'v'}$ and $M = \frac{1}{2}(\overline{u'^2} - \overline{v'^2})$, and q is the potential vorticity. An output formed with 3-month means is used to compose the Reynolds stresses, i.e. the average is defined as a 3 month temporal mean. The timescale of three months is long enough so as to resolve eddy momentum tendencies but not so long that it would act to conceal the intrinsic interannual variability of the system. Repeat experiments conducted with 5-day and 1-month time means give similar results.

Attempts made to temporally correlate the divergence of the Reynolds stresses with metrics relating to the position and strength of the jet proved unfruitful, due to rapidly temporally varying and spatially complex nature of the divergence of the Reynolds stresses. Thus, an alternative approach is employed, whereby the composite mean spatial patterns of the terms in the Reynolds decomposed momentum equations are examined at extreme values of jet strength and position.

To investigate the eddy-mean flow interactions, eddy-driven properties are examined in the recirculation gyres at different jet states corresponding to northward and southward positions of the jet (as in Section 4.2.2). Figure 4.8 demonstrates the variations in the eddy PV forcing term (equation 4.3) and the tendencies related to the horizontal Reynolds stresses, as the jet shifts meridionally. The eddy PV forcing terms (panels a and b) act to decelerate the flow near the western boundary, whereas on the eastward side of the recirculation gyres the eddies act to accelerate the flow (in agreement with Waterman and Jayne (2011)). The eddy tendency terms in the zonal momentum equation (panels e and f) act to accelerate the flow zonally near the western boundary, and decelerate it on the eastward side of the recirculation gyres. The meridional terms (panels i and j) have different signs in each of the recirculation gyres. In the subpolar gyre they accelerate the jet northwards, and in the subpolar gyre, they act to accelerate the jet southwards. In the recirculation gyres' upstream regions, near to the western boundary, these terms act to decelerate meridional currents entering the jet, whereas in the downstream jet regions, the meridional eddy tendencies are seen to accelerate the meridional velocity acting in the direction of the mean flow. In the meridional averages of the three terms, the most prominent differences occur in the meridional momentum eddy terms (panel k). In the northward jet position, the eddies act to accelerate the jet core in a net northward direction, whereas in the southward state the eddies are acting to accelerate the jet core southward. Near to the western boundary, the eddies have the opposite signs, indicating a southward acceleration in the northern state and a northward acceleration in the southern state. This is suggestive that the tendencies of the eddies in the boundary currents could act to restore the jet's position.

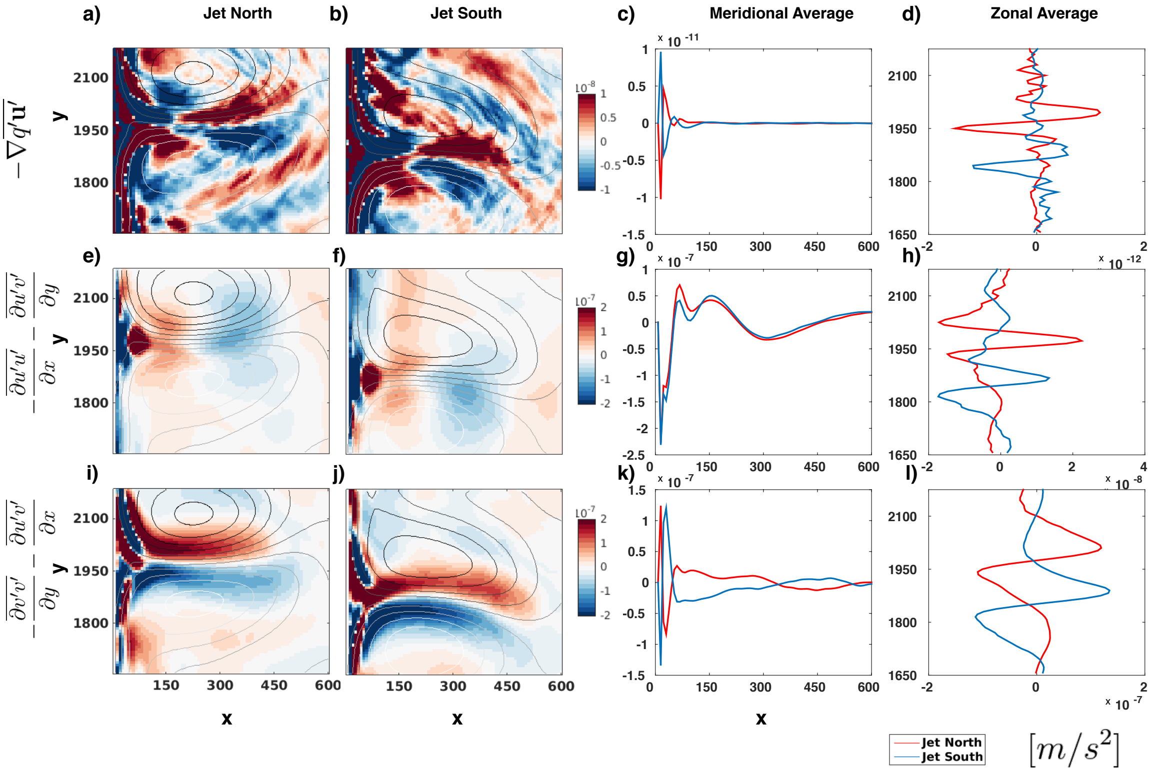

Figure 4.8: Composite means of the (a)[(b)] eddy potential vorticity forcing, (e)[(f)] eddy tendencies in the zonal momentum equation, (i)[(j)] eddy tendencies in the meridional momentum equation, when the jet is in a northward [southward] jet position. Meridional [zonal] averages of the displayed composites of (c)[(d)] eddy potential vorticity forcing, (g)[(h)] eddy tendencies in the zonal momentum equation, (k)[(l)] eddy tendencies in the meridional momentum equation. The grey contours are 20cm contours of SSH.

Similarly, the eddy terms are evaluated for different magnitudes of jet's zonal velocity. In the strong jet state, Figure 4.9a, shows a clear example of the eddy PV forcing observed by Waterman and Jayne (2011). However, the composite in the weaker jet is less spatially coherent than the pattern in the strong jet state, indicating that on average the eddies are less effective in accelerating the jet when the jet has a weaker zonal transport (Figure 4.9b). In the strong jet state, the zonal eddy momentum terms act to accelerate the flow in the upstream region, and decelerate the flow downstream (panel e). There is a decrease in the magnitude of the zonal acceleration in the core of the jet when the jet is weak (panel f). The most marked difference is observed in the meridional eddy components (Figure 4.9i,j). In the strong jet state, the meridional terms act strongly to decelerate the flow in the recirculation gyres, in the upstream region of the jet. In the weak jet state, the deceleration has a smaller magnitude, as the downstream acceleration is more prominent relative to that upstream. The eddy terms are acting to force the mean flow in significantly different ways as the transport varies. Therefore Figure 4.9 demonstrates an example of the eddies acting locally in the recirculation gyres to drive the jet transport.

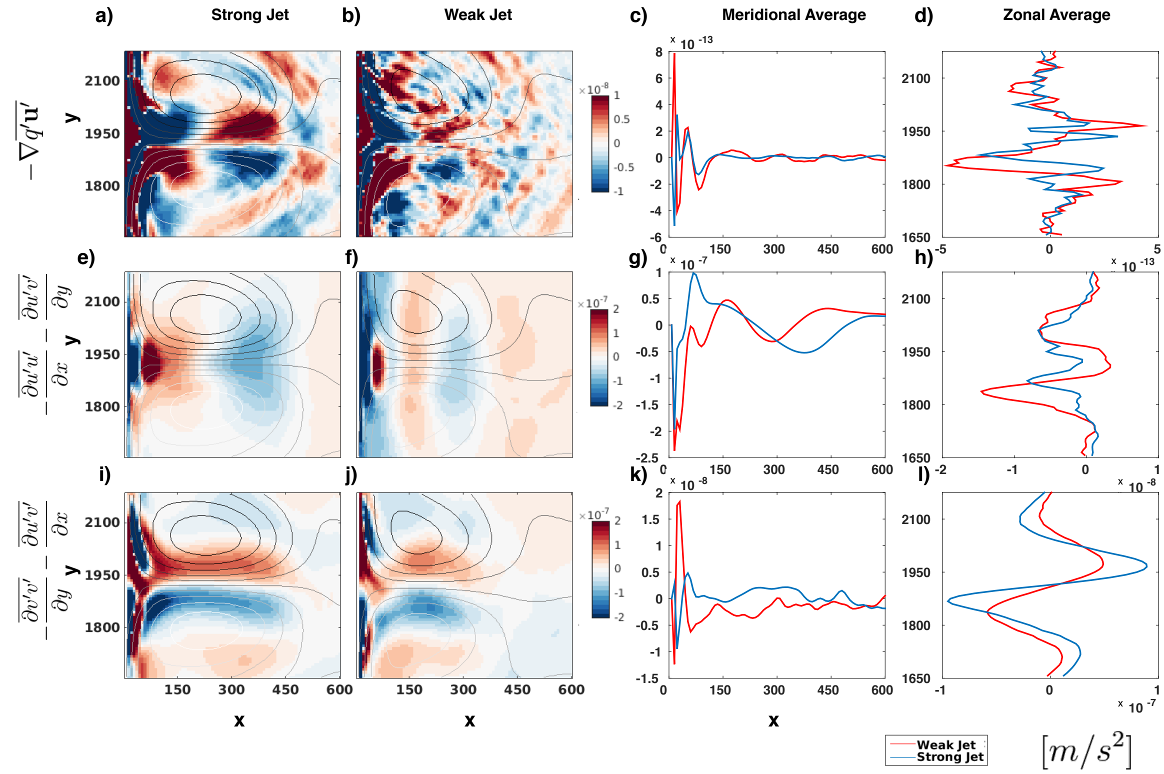

Figure 4.9: Composite means of the (a)[(b)] eddy potential vorticity forcing, (e)[(f)] eddy tendencies in the zonal momentum equation, (i)[(j)] eddy tendencies in the meridional momentum equation, when the jet is in a strong [weak] transport state. Meridional [zonal] averages of the displayed composites of (c)[(d)] eddy potential vorticity forcing, (g)[(h)] eddy tendencies in the zonal momentum equation, (k)[(l)] eddy tendencies in the meridional momentum equation. The grey contours are 20cm contours of SSH.

4.3 Interannual Intrinsic Variability in Mid-Latitude Baroclinic Jets

As discussed in Section 3.2.3, the baroclinic model's mean state exhibits several features that are qualitatively similar to that of the barotropic model and observations. The mean SSH pattern consists of two large-scale gyres, with intensifications in the recirculation regions (Figure 4.10b). However, there are also additional gyres present at higher and lower latitudes. Such structures are common in idealised baroclinic models and are sensitive to the model's boundary conditions, but won't affect the results presented here (Greatbatch and Nadiga, 2000; Wilson and Williams, 2004). The largest values of SSH variability are located in the jet's extension region, as shown in Figure 4.10c. The mean temperature profile also has a multi-gyre pattern (Figure 4.10e), which is similar to that of the mean SSH. In the mid-latitudes, the meridional temperature gradient varies depending on longitude, with a steeper gradient near the west coast, and a flatter gradient in the basin interior.

Several features which are not present in the barotropic model are also evident. The mean zonal velocity profile at 150m, shown in Figure 4.10a, indicates the presence of two zonal jets in the basin's interior. One jet is at 27-28°N, and the other weaker jet is situated just northwards at 30°N. The occurrence of multiple jets is not uncommon in high-resolution primitive equation models when a broad wind forcing is applied (Richards et al., 2006; Chan et al., 2007; Thompson and Richards, 2011), and are also seen in observations (Roden, 2000; Hughes and Ash, 2001; Maximenko et al., 2005). The presence of multiple jets could have important implications for the interannual intrinsic variability of the ocean.

Figure 4.11 shows the time series, and the associated power spectra, of SSH anomalies taken at several different locations (indicated in Figure 4.10b). At all locations the power spectra selected exhibit considerable power on interannual timescales, with the largest values of power spectral density found in the jet regions (Figure 4.11, panels d and h). On periods longer than one year, the power spectral density in these

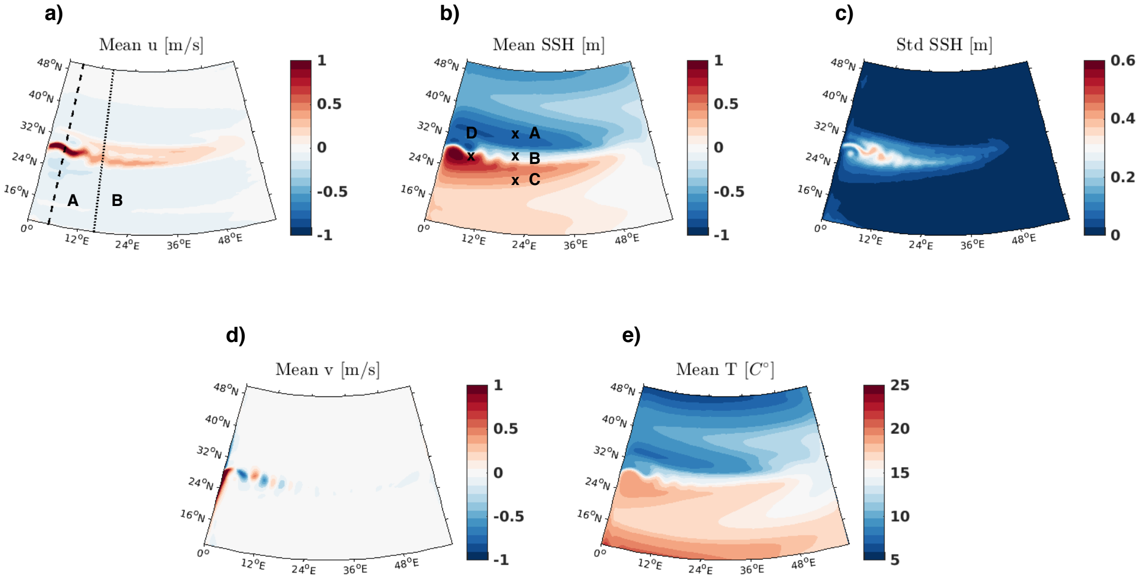

Figure 4.10: Time mean (a) zonal velocity [m/s] and (b) SSH [m]. (c) Standard deviation of SSH [m] (composed from 10-day time means). Time mean (d) meridional velocity [m/s] and (e) Temperature [C°]. Velocity components and temperature are computed at a depth of 150m.

regions is up to an order of magnitude larger than those found in the gyre regions. Multiple profiles of variability are seen to occur in the jet region (Figure 4.11, panels c and g). In the jet extension region, the time series exhibit a very distinctive, almost periodic pattern, occurring on timescales of ≈ 5 years (panel c). In the jet region closer to the western boundary, panel g, the variability is asymmetric with greater magnitude negative anomalies corresponding to southward deflections of the subpolar recirculation gyre on interannual timescales (not shown). In the subpolar gyre, panels a and b, the power spectra are reminiscent of that seen in the gyre region of the barotropic model, with a peak on timescales of $\approx 0.1 - 0.2$ years with flatter spectra on times longer than a year. In the subtropical gyre (Figure 4.11, panels e and f) interannual variability is also present, with a prominent spectral peak occurring on periods between 5-6 years.

Figure 4.12 shows an EOF analysis of SSH. A similar number of EOFs are required to reconstruct the variability of the system as in the barotropic case, as approximately 50 EOFs are needed to reconstruct 85% of the variability. The first and third EOF

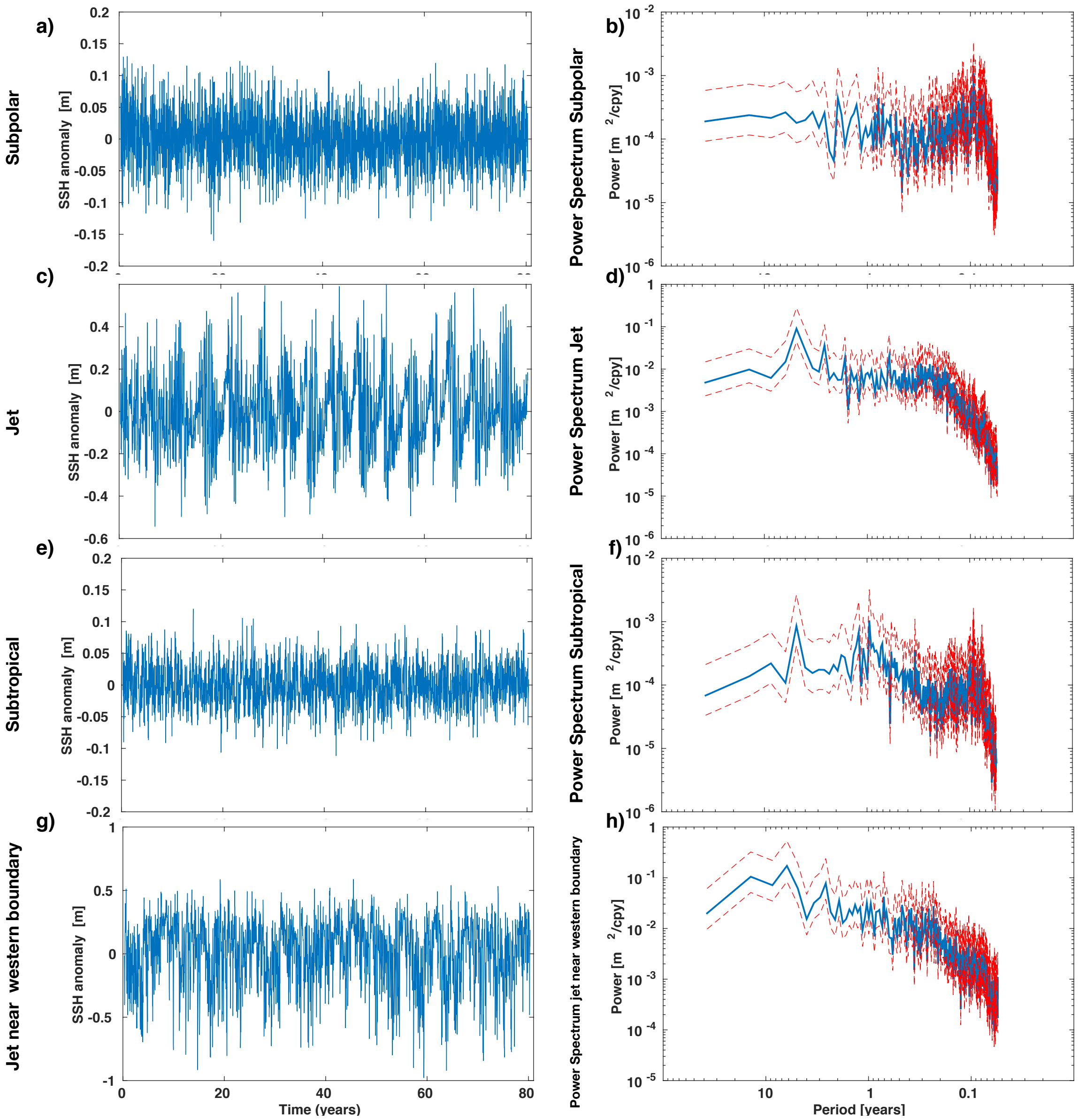

Figure 4.11: Time series created using 80 years of SSH anomaly data taken at locations: (a) A, (c) B, (e) C, (g) D marked in Figure 4.10a. Power spectra of the time series at the locations marked: (b) A, (d) B, (f) C, (h) D. The dashed red lines show the 95%-confidence intervals calculated using an inverse chi-squared distribution.

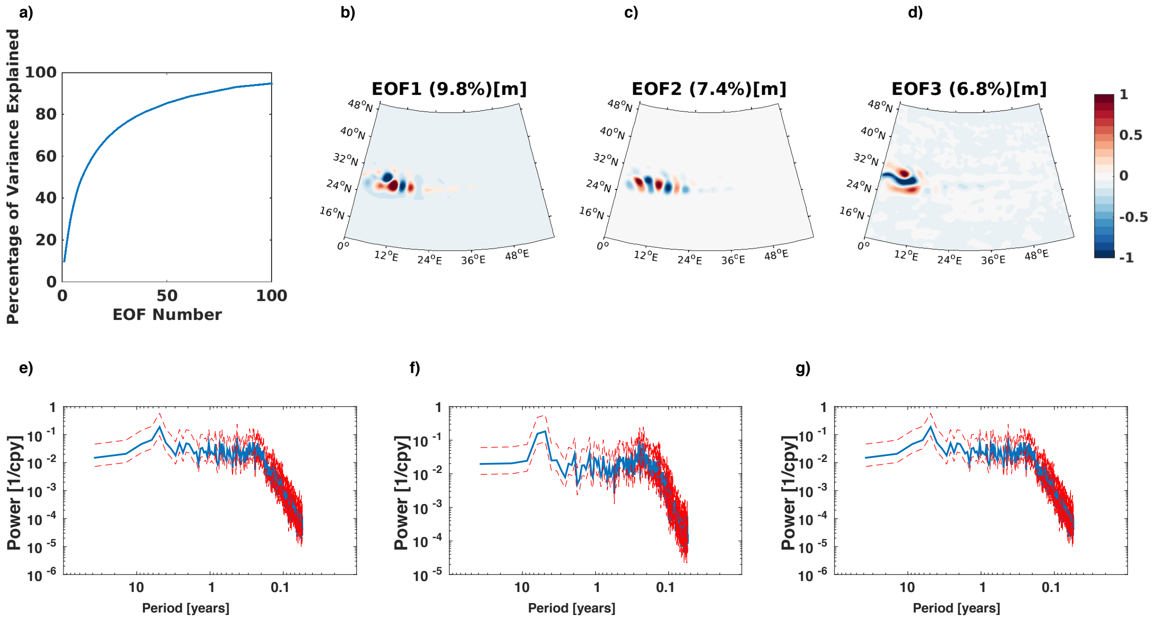

Figure 4.12: (a) The percentage of variance explained by each of the EOFs. The (b) first, (c) second and (d) third EOFs of SSH. The power spectra of the (e) first, (f) second and (g) third principal components. The dashed red lines show the 95%-confidence intervals calculated using an inverse chi-squared distribution.

patterns are reminiscent of those found in the barotropic model. This first EOF pattern (panel b) has a dipolar pattern around 12°E which affects the transport of the jet, as in the barotropic case. The second EOF pattern (panel c), is associated with the meandering of the jet. The third EOF pattern (panel d) has a tripole pattern west of 15°E, corresponding to a meridional jet shift as in the barotropic system. All three principal components display similar power spectra, with white profiles on timescales longer than a year, and a peak at a frequency of approximately 5 years (panels e-g). These variations, in the jet's meridional position and transport, captured by the first and third EOFs, are driven by the barotropic mechanisms previously discussed in Section 4.2.4. However, the corresponding patterns of eddy momentum convergence, are more complicated due to the meandering structure of the jet. Eddies are seen to accelerate and decelerate the mean flow on interannual timescales.

The Hövmoller plots in Figure 4.13, taken along Sections A and B (marked in Figure 4.10a), examine the differences in variability along the path in the jet. The

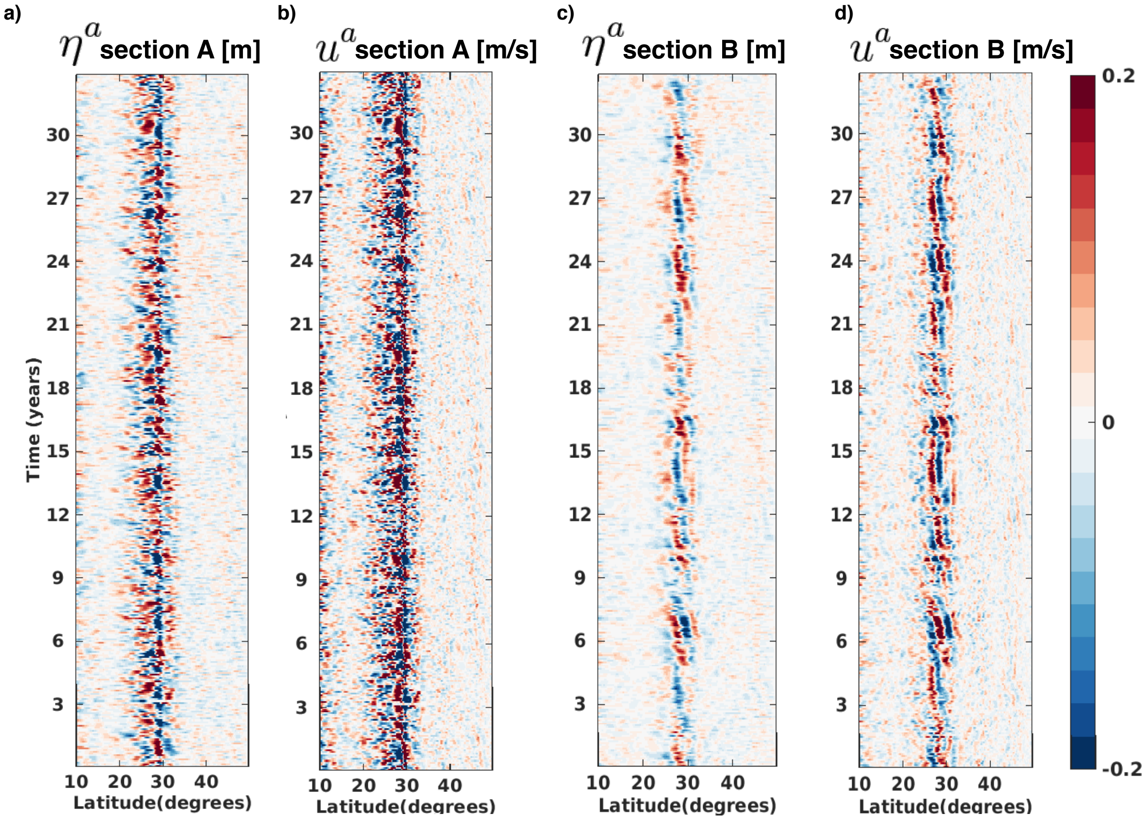

Figure 4.13: Hövmoller plots of zonal velocity and SSH anomalies taken at two different regions in the model domain (shown in Figure 4.10a).

plots show anomalies, where a field X has decomposed into components representing a 35 year time mean ($\widetilde{X}$) and fluctuations to this mean (X^a), i.e., $X = X^a + \widetilde{X}$. In the downstream jet region (Section B), both the SSH anomalies and the anomalous zonal velocities exhibit patterns due to interannual equatorward propagation. These equatorward drifts occur on a timescale of approximately $5 - 6$ years, and are not present in the upstream jet region (Section A). The anomalous meridional migration is only evident between latitudes of 25°N - 31°N. The timescale of this drift is reminiscent of the variability found in both the time series in Figure 4.11c, and in the power spectra of principal components (Figure 4.12).

As the zonal velocity anomalies migrate southwards (4.14a), two zonal jets seen in the zonally averaged monthly mean zonal velocity fields (4.14b), are seen to split and merge (evident in a comparison of the profiles at T1 and T3). Figure 4.14b shows that when the jets have separated, the jet at the higher latitude (29-31°N) is more barotropic than the jet at the lower latitude (26-29°N), as it extends to far deeper depths ($\sim$ 4000m rather than $\sim$ 1000m). However, this distinction is not as apparent when the jets merge, and both jets extend to $\sim$ 3000m. These anomalous jets migrate over the latitude range where there is a strong meridional gradient in the mean temperature (as seen in Figure 4.14c). Panel d shows that on either side of the positive zonally averaged zonal velocity anomalies there are temperature anomalies of differing signs. This resultant meridional temperature gradient across the jet is as expected from thermal wind balance. Therefore there is a baroclinic pressure gradient, across the anomalous jets, which could be important in the mechanism of the observed migration.

4.3.1 Interannual Eddy-Jet Interactions

Previous studies have attributed such low-frequency jet migrations to an asymmetric convergence of eddy momentum fluxes caused by meridional variations of baroclinic instabilities (Chan et al., 2007; Chemke and Kaspi, 2015). To detect such variations the Eady growth rate is often diagnosed. In this study The Eady growth rate is also the chosen measure of baroclinicity due to its simplicity. Although, this measure was developed for use on an f plane, it can also be used on a beta plane as an effective measure of the growth rate of the most unstable waves (Lindzen and Farrell, 1980). The across jet differences arise because of meridional variations in either the Coriolis parameter, the zonal velocity shear, or the static stability (Chan et al., 2007; Chemke and Kaspi, 2015). Using Reynolds decomposition, we can explore the dynamical mechanisms responsible for the jet migration on interannual timescales for both momentum (Figures 4.15 and 4.16) and temperature (Figure 4.17a). The derivation of the Reynolds decomposed HPEs is included in Appendix 3.B and the

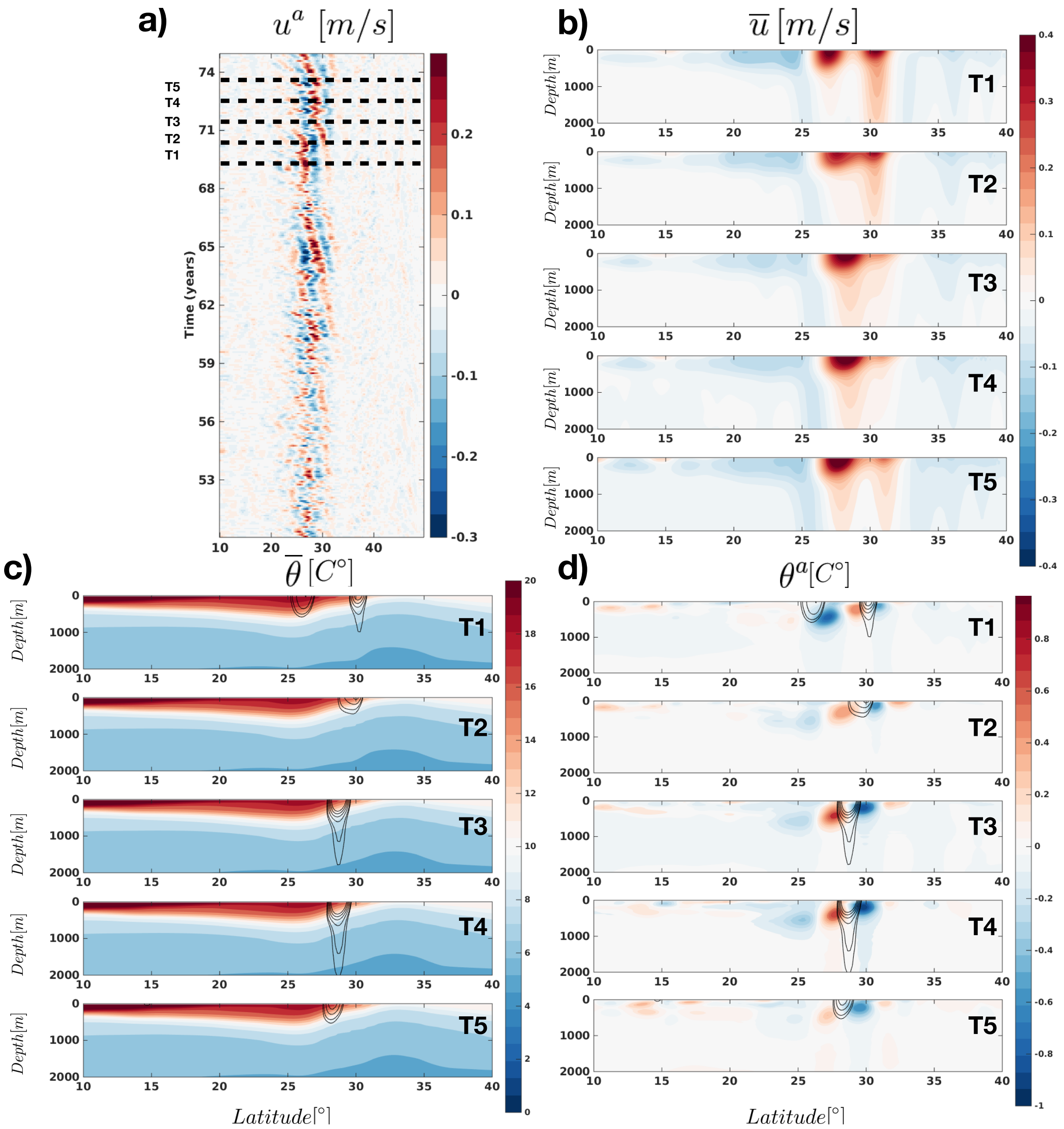

Figure 4.14: (a) Hövmoller plots of zonal velocity anomalies, taken along Section b (as indicated in Figure 4.10c). (b) Monthly mean zonal velocities (indicated by the overbar) zonally averaged between longitudes of 16°-22°E, taken at times indicated in panel a. (c) The monthly mean zonally averaged temperature profiles averaged between longitudes of 16°-22°E. (d) The monthly mean zonally averaged temperature anomalies averaged between longitudes of 16°-22°E. The black contours indicate positive zonally averaged zonal velocity anomalies, with contour intervals of 3cm/s.

resultant equations are: the Reynolds decomposed zonal

$$\underbrace{\frac{\partial \bar{u}}{\partial t}}_{U_a} = \overbrace{-\frac{1}{acos\phi}\frac{\partial \bar{u}\bar{u}}{\partial \lambda}}^{U_b} \underbrace{-\frac{1}{a}\frac{\partial \bar{v}\bar{u}}{\partial \phi}}_{U_c} \overbrace{-\frac{\partial \bar{w}\bar{u}}{\partial z}}^{U_d} \underbrace{-\frac{g}{acos\phi}\frac{\partial \bar{\eta}}{\partial \lambda}}_{U_e} \underbrace{+\frac{g}{acos\phi}\frac{\partial \int_z^0 \alpha_\theta(\bar{\theta}-\theta_{ref})dz}{\partial \lambda}}_{U_f} \underbrace{+f\bar{v}}_{U_g}$$
$$\overbrace{-\frac{1}{acos\phi}\frac{\partial \overline{u'u'}}{\partial \lambda}}^{U_h} \underbrace{-\frac{1}{a}\frac{\partial \overline{v'u'}}{\partial \phi}}_{U_i} \overbrace{-\frac{\partial \overline{w'u'}}{\partial z}}^{U_j} \underbrace{+\overline{F_\lambda}+\overline{D_\lambda}}_{U_k} \overbrace{+uvtan\phi}^{U_l}, \tag{3.34 revisited}$$

and meridional

$$\underbrace{\frac{\partial \bar{v}}{\partial t}}_{V_a} = \overbrace{-\frac{1}{acos\phi}\frac{\partial \bar{u}\bar{v}}{\partial \lambda}}^{V_b} \underbrace{-\frac{1}{a}\frac{\partial \bar{v}\bar{v}}{\partial \phi}}_{V_c} \overbrace{-\frac{\partial \bar{w}\bar{v}}{\partial z}}^{V_d} \underbrace{-\frac{g}{a}\frac{\partial \bar{\eta}}{\partial \phi}}_{V_e} \underbrace{+\frac{g}{a}\frac{\partial \int_z^0 \alpha_\theta(\bar{\theta}-\theta_{ref})dz}{\partial \phi}}_{V_f} \underbrace{-f\bar{u}}_{V_g}$$
$$\overbrace{-\frac{1}{acos\phi}\frac{\partial \overline{u'v'}}{\partial \lambda}}^{V_h} \underbrace{-\frac{1}{a}\frac{\partial \overline{v'v'}}{\partial \phi}}_{V_i} \overbrace{-\frac{\partial \overline{w'v'}}{\partial z}}^{V_j} \underbrace{+\overline{F_\phi}+\overline{D_\phi}}_{V_k} \overbrace{+\frac{u^2tan\phi}{a}}^{V_l}, \tag{3.35 revisited}$$

momentum equations, and the Reynolds decomposed temperature equation

$$\underbrace{\frac{\partial \bar{\theta}}{\partial t}}_{T_a} = \overbrace{-\frac{1}{acos\phi}\frac{\partial \bar{u}\bar{\theta}}{\partial \lambda}}^{T_b} \underbrace{-\frac{1}{a}\frac{\partial \bar{v}\bar{\theta}}{\partial \phi}}_{T_c} \overbrace{-\frac{\partial \bar{w}\bar{\theta}}{\partial z}}^{T_d} \underbrace{-\frac{1}{acos\phi}\frac{\partial \overline{u'\theta'}}{\partial \lambda}}_{T_e} \overbrace{-\frac{1}{a}\frac{\partial \overline{v'\theta'}}{\partial \phi}}^{T_f} \underbrace{-\frac{\partial \overline{w'\theta'}}{\partial z}}_{T_g} \overbrace{+k_h\nabla_h^2\bar{\theta}}^{T_h} \underbrace{+k_z\frac{\partial^2\bar{\theta}}{\partial z^2}}_{T_i}. \tag{3.36 revisited}$$

The over and under bracketed terms include the preceding sign in their definitions. The physical processes associated with all these tendencies are presented in Tables 4.1, 4.2 and 4.3.

We examine the departures of the tendencies from their time means (where the eddy terms are denoted by primes (′) and the monthly mean terms by overbars (¯) as described in Section 3.1.2), to isolate the signal related to the meridional migration. Initially, we concentrate on tendencies with the largest magnitudes to identify those responsible for the meridional migration. The temporal evolution of the anomalous

Tendency	Related physical interpretation
U_a	Tendency of the mean zonal velocity component
U_b	Mean zonal advection of zonal momentum
U_c	Mean meridional advection of zonal momentum
U_d	Mean vertical advection of zonal momentum
U_e	Zonal momentum tendency from the barotropic pressure gradient
U_f	Zonal momentum tendency from the baroclinic pressure gradient
U_g	Zonal momentum tendency from the Coriolis term
U_h	Eddy zonal advection of zonal momentum
U_i	Eddy meridional advection of zonal momentum
U_j	Eddy vertical advection of zonal momentum
U_k	Zonal momentum tendency from forcing and dissipation
U_l	Zonal momentum tendency from a metric term

Table 4.1: The tendencies in the zonal momentum equation and the physical interpretations to which the are related.

Tendency	Related physical interpretation
V_a	Tendency of the mean meridional velocity component
V_b	Mean zonal advection of meridional momentum
V_c	Mean meridional advection of meridional momentum
V_d	Mean vertical advection of meridional momentum
V_e	Meridional momentum tendency from the barotropic pressure gradient
V_f	Meridional momentum tendency from the baroclinic pressure gradient
V_g	Meridional momentum tendency from the Coriolis term
V_h	Eddy zonal advection of meridional momentum
V_i	Eddy meridional advection of meridional momentum
V_j	Eddy vertical advection of meridional momentum
V_k	Meridional momentum tendency from forcing and dissipation
V_l	Meridional momentum tendency from a metric term

Table 4.2: The tendencies in the meridional momentum equation and the physical interpretations to which the are related.

Tendency	Related physical interpretation
T_a	Tendency of the mean potential temperature
T_b	Mean zonal advection of potential temperature
T_c	Mean meridional advection of potential temperature
T_d	Mean vertical advection of potential temperature
T_e	Eddy zonal advection of potential temperature
T_f	Eddy meridional advection of potential temperature
T_g	Eddy vertical advection of potential temperature
T_h	Horizontal diffusion of potential temperature
T_i	Vertical diffusion of potential temperature

Table 4.3: The tendencies in the temperature equation and the physical interpretations to which the are related.

tendencies in the momentum budget are zonally averaged between 16°E and 22°E, and examined at the location of the observed variability, at a latitude of 28°N.

The majority of the tendencies in the the zonal momentum equation (equation 3.34), shown in Figure 4.15a, exhibit variability with a 5 year periods. The largest terms correspond to those tendencies which are in geostrophic balance. The next largest terms are those which relate to the baroclinic pressure gradients U_f $(+\frac{g}{acos\phi}\frac{\partial\int_z^0 \alpha_\theta(\bar{\theta}-\theta_{ref})dz}{\partial\lambda})$, and the vertical component of the divergence of the Reynolds stresses, U_j $(-\frac{\partial\overline{w'u'}}{\partial z})$. Similarly, the largest tendencies in the meridional momentum equation (equation 3.35), shown in Figure 4.16, are the tendencies which are in geostrophic balance: the tendency related to the baroclinic pressure gradient $(V_f, +\frac{g}{a}\frac{\partial\int_z^0 \alpha_\theta(\bar{\theta}-\theta_{ref})dz}{\partial\phi})$, and that due to the vertical Reynolds stress $(V_j, -\frac{\partial\overline{w'v'}}{\partial z})$.

The temperature budget (equation 3.36), shown in Figure 4.17, is dominated by the advective terms, as the terms relating to the diffusion of temperature are several orders of magnitude smaller than the advective terms (not shown). The mean temperature tendency, T_a $(\frac{\partial\bar{\theta}}{\partial t})$, is also negligible. The terms relating to the zonal, $T_{b,e}$ $(-\frac{1}{acos\phi}\frac{\partial\bar{u}\bar{\theta}}{\partial\lambda} - \frac{1}{acos\phi}\frac{\partial\overline{u'\theta'}}{\partial\lambda})$, and meridional, $T_{c,f}$ $(-\frac{1}{a}\frac{\partial\bar{v}\bar{\theta}}{\partial\phi} - \frac{1}{a}\frac{\partial\overline{v'\theta'}}{\partial\phi})$, heat advection are seen to balance each other. The terms related to the vertical advection term $T_{d,g}$, are also significant and show a balance between the mean, T_d $(-\frac{\partial\bar{w}\bar{\theta}}{\partial z})$, and eddy, T_g $(-\frac{\partial\overline{w'\theta'}}{\partial z})$, components. This is potentially related to eddy cancellation, a mechanism proposed in Doddridge et al. (2016). The small temperature anomaly tendency is due to the near cancellation of the lateral and vertical temperature gradients, maintained by both the Eulerian and eddy components.

We will now further investigate how the largest tendencies act to cause an equatorward migration of the anomalous jets. As the anomalous zonal jets seem to move exclusively equatorward, we hypothesise that the migration is due to a meridional imbalance in the momentum tendencies across the jets. For example, if the tendencies related to the eddy momentum fluxes are the largest terms in the momentum equations, and if their contributions are more substantial on the poleward flank of the jet relative to the equatorward flank, the imbalance will lead to the jet moving in the equatorward direction. An approach motivated by Chemke and Kaspi (2015) is adopted to identify the presence of any latitudinal variations in the momentum and temperature tendencies across the northern jet. The northern jet is chosen for this analysis as it displayed the most significant displacement in the meridional direction. Due to the lack of zonal symmetry, the jet positions are defined as the maxima of the zonal average of u between 16°E and 22°E in longitude. The northern jet is defined as the jet at the highest latitude with a zonally averaged u of more than 0.25 m/s. The tendencies are summed separately over the poleward (Σ_p) and equatorward (Σ_e) flanks of the jet. The meridional width of the jet flanks is defined as the distance between the maximum of zonally integrated u, and the latitude of the nearest zero or minimum in zonally integrated u. Such an approach takes into account any meridional migration of the jet and variations in the width of the jet's flanks. This analysis is performed with 35 years of monthly mean model output, enough time for there to be several cycles of the variability. Repeat analysis is also performed with the output on several different depth layers. The plots presented are for the depth layer spanning 350-380m, but the results appear qualitatively similar for any of the layers in the top 1000m of the model.

Figure 4.18 shows the summed tendencies comprising the zonal momentum equa-

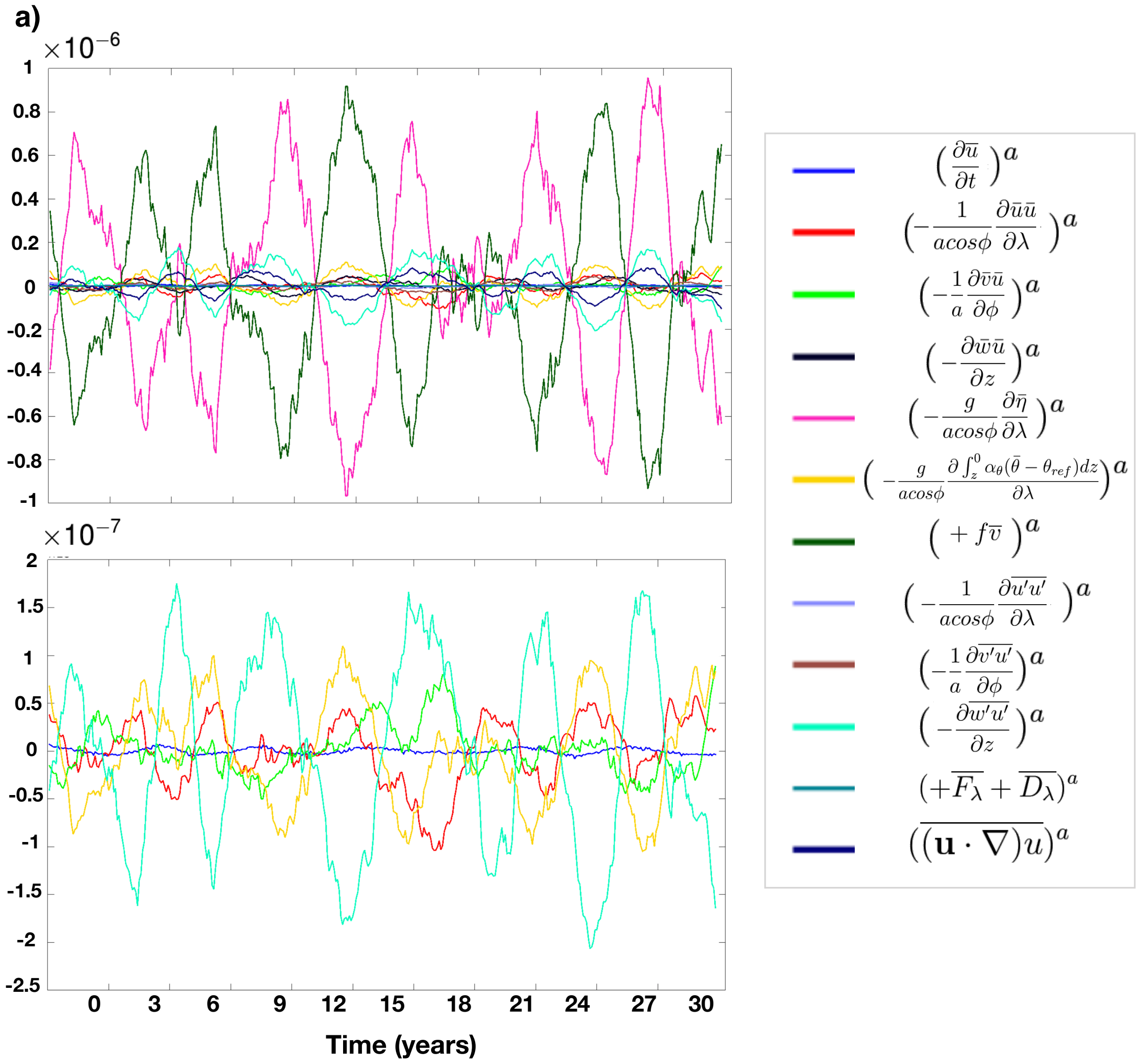

Figure 4.15: All the anomalous momentum tendencies in the (a) zonal (i.e. U_a^a, U_b^a etc) momentum equations zonally averaged between 16° E and 22° E in longitude (all in m/s^2). It also shows the largest magnitude anomalous terms in the (c) zonal momentum equation excluding those in geostrophic balance. In the zonal equations these terms are related to the zonal and meridional mean flow advection (U_b^a, $(-\frac{1}{acos\phi}\frac{\partial\bar{u}\bar{u}}{\partial\lambda})^a$, red and U_c^a, $(-\frac{1}{a}\frac{\partial\bar{v}\bar{u}}{\partial\phi})^a$, light green), the thermosteric part of the pressure gradient (U_f^a, $(+\frac{g}{acos\phi}\frac{\partial\int_z^0\alpha_\theta(\bar\theta-\theta_{ref})dz}{\partial\lambda})^a$, yellow) and the vertical eddy momentum flux (U_j^a, $(-\frac{\partial\overline{w'u'}}{\partial z})^a$, turquoise). All the time series shown are constructed from the zonally averaged anomalous terms in the momentum equations at a latitude of 28° N.

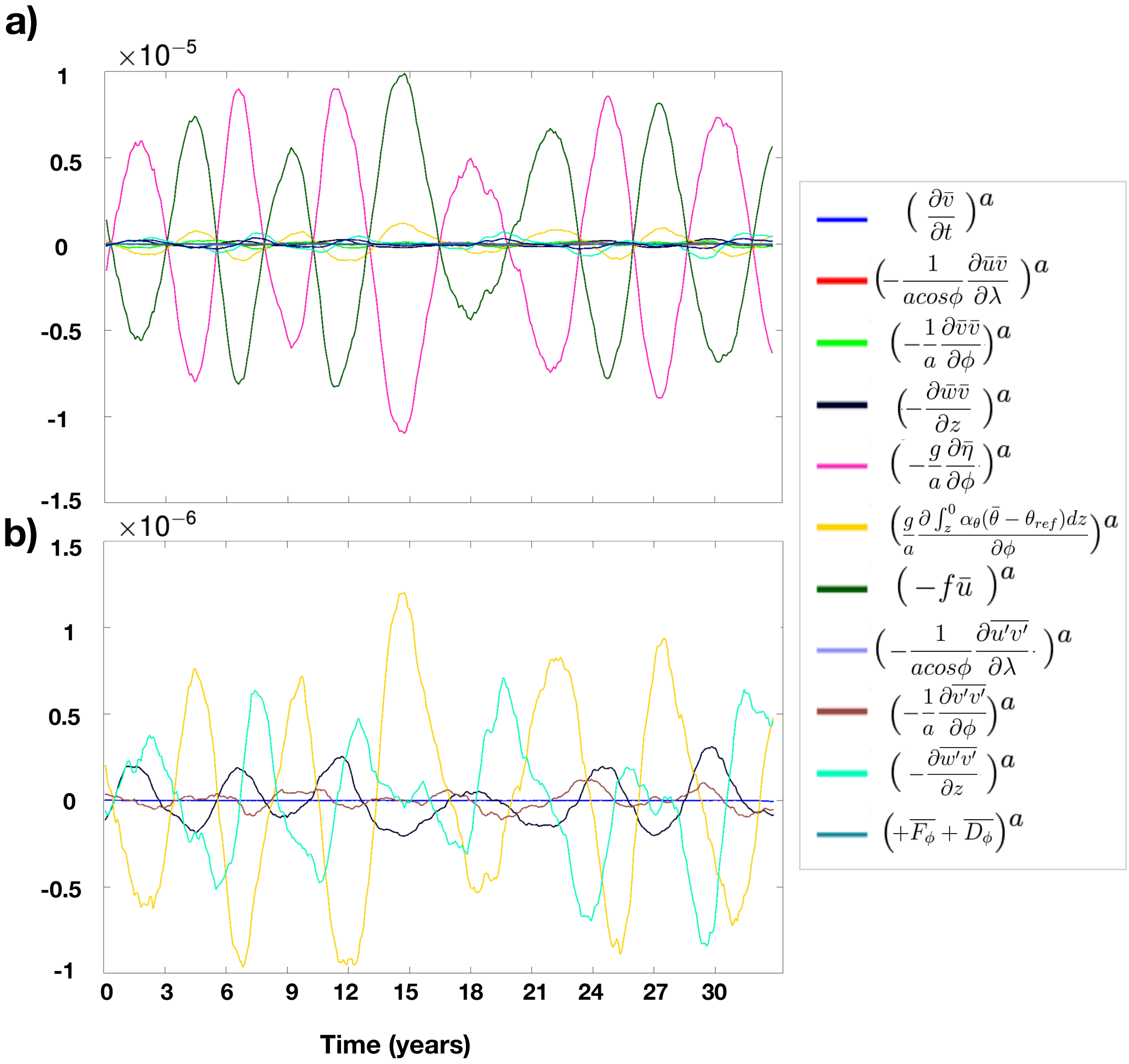

Figure 4.16: All the anomalous momentum tendencies in the (a) meridional (i.e. V_a^a, V_b^a etc) momentum equations zonally averaged between 16° E and 22° E in longitude (all in m/s^2). It also shows the largest magnitude anomalous terms in the (b) meridional momentum equation excluding those in geostrophic balance. In the meridional equation the largest magnitude terms are vertical mean and eddy fluxes (V_d^a, $(-\frac{\partial \bar{w}\bar{v}}{\partial z})^a$, black and V_j^a, $(-\frac{\partial \overline{w'v'}}{\partial z})^a$, turquoise), the meridional eddy flux (V_i^a, $(-\frac{1}{a}\frac{\partial \overline{v'v'}}{\partial \phi})^a$, brown) and the the thermosteric part of the pressure gradient (V_f^a, $(+\frac{g}{a}\frac{\partial \int_z^0 \alpha_\theta(\bar{\theta}-\theta_{ref})dz}{\partial \phi})^a$, yellow). All the time series shown are constructed from the zonally averaged anomalous terms in the momentum equations at a latitude of 28° N.

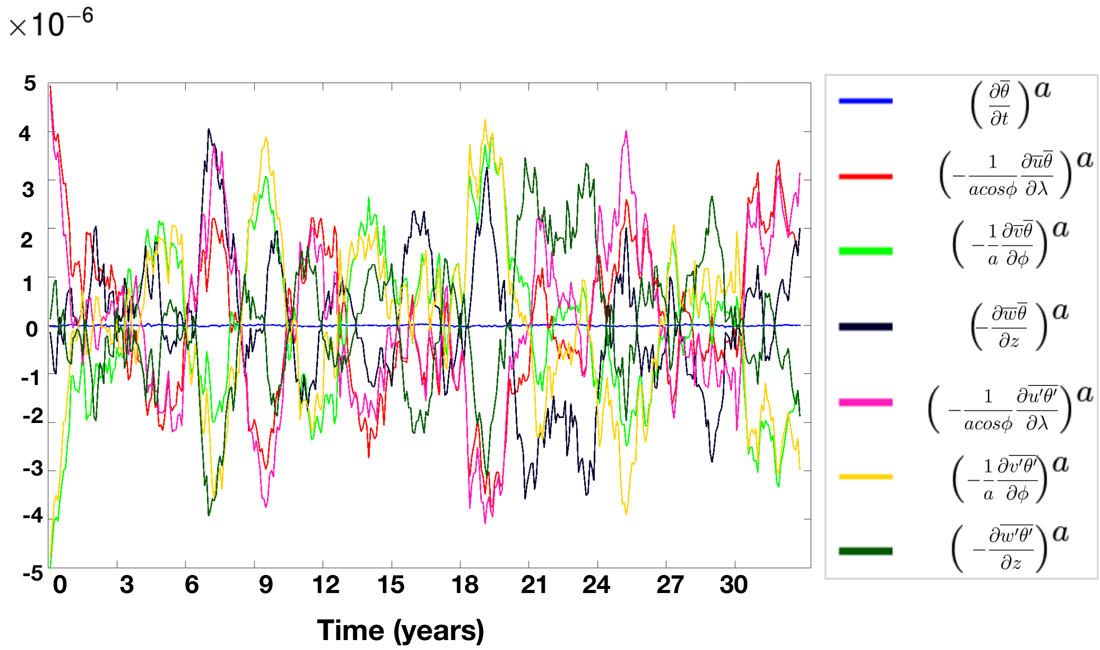

Figure 4.17: All the anomalous terms in the temperature budget zonally averaged between 16°E and 22°E in longitude, at a latitude of 28° N (i.e. T_a^a, T_b^a etc, all in units of C°/s).

tion. Several of the terms are small with no apparent meridional asymmetries. In agreement with the time series analysis, the largest terms are related to the baroclinic pressure gradient (panel f), and the sum of the geostrophic terms (panel e). However, neither of these terms has a clear meridional asymmetry. Most of the tendencies related to the vertical eddy advection (U_j, panel i), are small and close to zero, but there are numerous negative extreme values which decelerate the jet on its equatorward flank. Figure 4.19 shows the summed tendencies of the meridional momentum equation. The largest terms again are those related to geostrophic balance. The ageostrophic components are seen to act to balance the tendency due to the baroclinic pressure gradient. The tendency due to the baroclinic pressure gradient (panel f) acts to accelerate the jet exclusively in the equatorward direction on both flanks of the jet. The tendency associated with the vertical eddy momentum (V_j, panel i), is also seen to mainly accelerate the jet equatorward, in both the jet's poleward and equatorward flanks. The summed temperature tendencies are shown in Figure 4.20. The largest

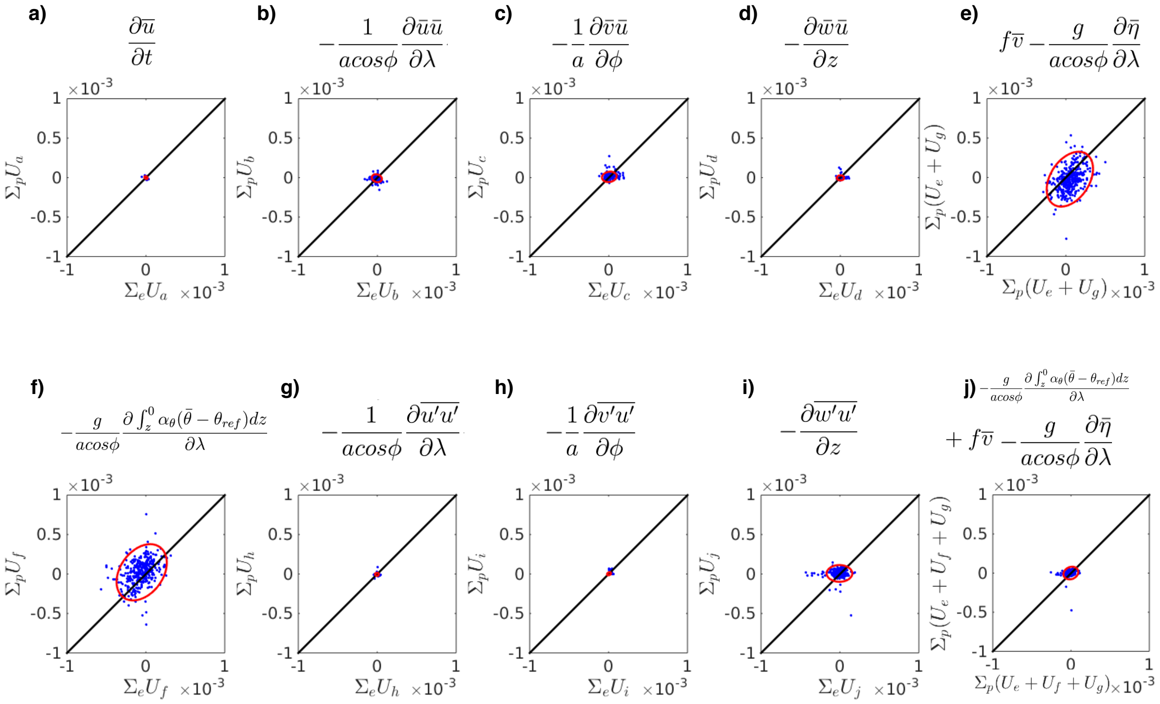

Figure 4.18: The sum over the poleward ($\sum_p$) versus equatorward ($\sum_e$) flanks of the northern meridionally migrating jet of each term in the zonal momentum budget (equation 3.34) $[m/s^2]$. Each dot represents the summations taken of the monthly-mean tendencies, over 35 years. The black line indicates when the tendency summed over the poleward flank and that summed over the equatorward flank are equal.The red ellipses define the 95% confidence interval of the summed quantities.

terms are the those related to the horizontal advection of heat and the vertical eddy temperature fluxes. The tendency T_g ($-\frac{\partial \overline{w'\theta'}}{\partial z}$) displays an evident asymmetry, which causes an increase in the heat in the poleward flank of the jet at all times. Such an increase acts to steepen the meridional temperature gradient across the jet. This steepening leads to a southward directed acceleration in the meridional momentum equations, due to the resultant baroclinic pressure gradient ($V_f, +\frac{g}{a}\frac{\partial \int_z^0 \alpha_\theta(\bar{\theta}-\theta_{ref})dz}{\partial \phi}$). In summary, the scatter plots do not detect any noticeable sizable asymmetries in the tendencies related to eddy momentum flux convergence. Instead, it appears that any asymmetries are due to the vertical eddy temperature fluxes. These temperature fluxes will influence the tendencies related to the meridional temperature gradients, which are the largest tendencies in the meridional momentum equation.

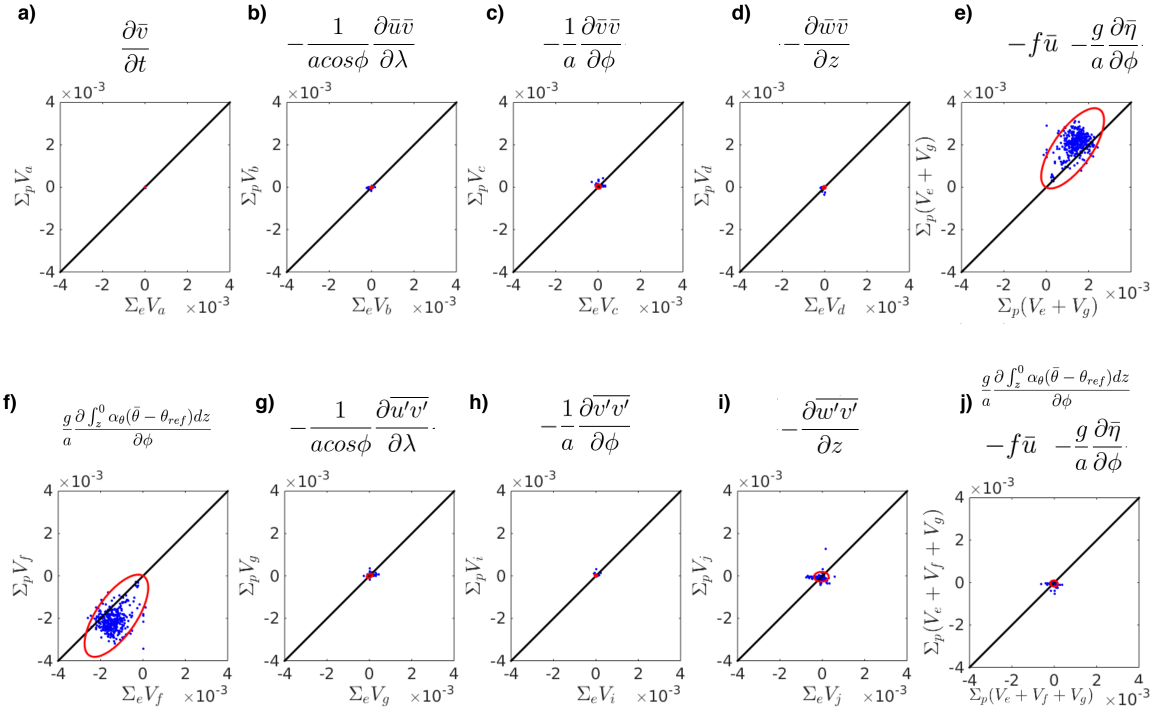

Figure 4.19: The sum over the poleward ($\sum_p$) versus equatorward ($\sum_e$) flanks of the northern meridionally migrating jet of each term in the meridional momentum budget (equation 3.35)$[m/s^2]$. The red ellipses are as in figure 4.18.

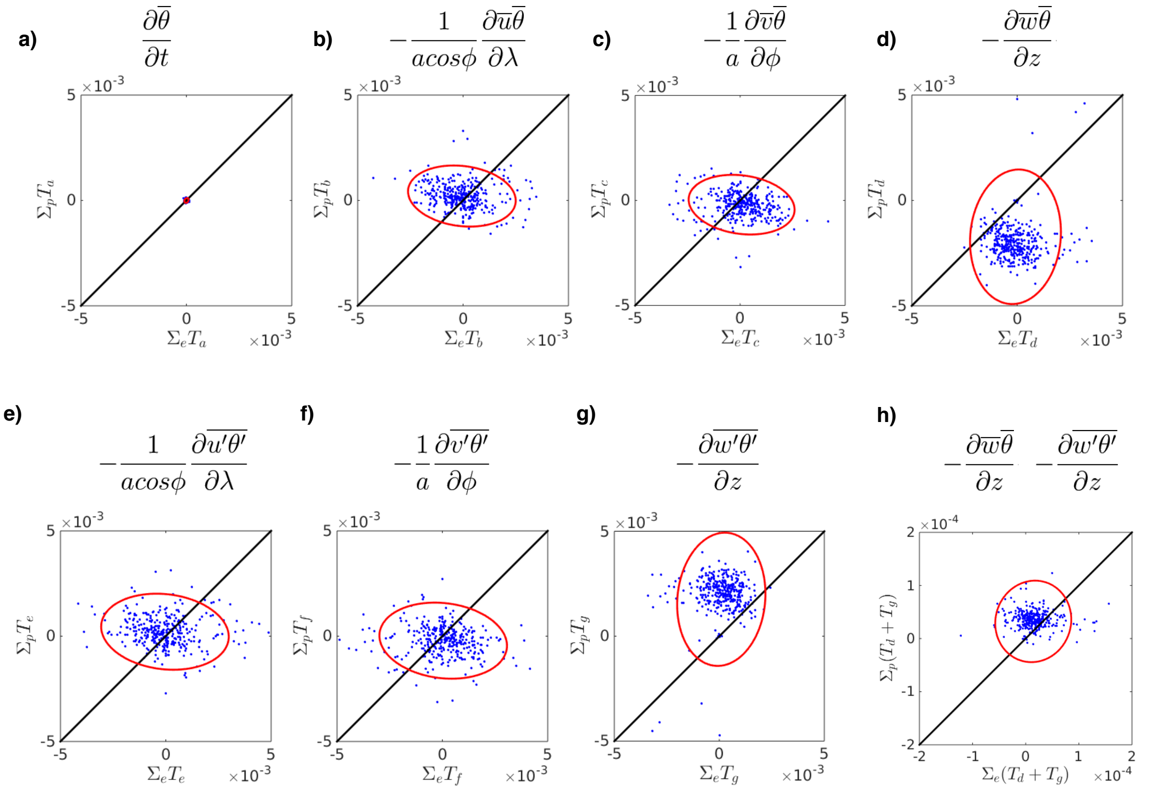

Figure 4.20: The sum over the poleward ($\sum_p$) versus equatorward ($\sum_e$) flanks of the northern meridionally migrating jet of each term in the temperature budget (equation 3.36) $[C^\circ/s]$. The red ellipses are as in figure 4.18.

Previous studies of meridionally propagating jets have attributed such variability to imbalances in the eddy momentum fluxes. These imbalances are caused by meridional asymmetries in the Eady growth rate across the migrating jets (Chan et al., 2007; Chemke and Kaspi, 2015). Chemke and Kaspi (2015) showed such variability to be due to variations in the Coriolis parameter, whereas, Chan et al. (2007) found variations in the static stability to be the dominant effect. In the current study, the positive tendencies due to the vertical eddy heat fluxes on the poleward side of the jet, may be due to variations in the baroclinicity. To diagnose this, meridional asymmetries in the Eady growth rate are examined (Eady, 1949)

$$\sigma \propto \frac{fU_z}{N}, \tag{4.4}$$

where N is the buoyancy frequency given by,

$$N = \sqrt{\frac{g}{\theta}\frac{d\theta}{dz}}, \tag{4.5}$$

as salinity is not included in the equation of state in this model. Figure 4.21 shows that the Eady growth rate is slightly larger on the jet's poleward flank as hypothesised. However, it is uncertain which of the constituent terms leads to such a meridional imbalance, as both the summations of the Coriolis parameter and static stability demonstrate meridional imbalances. Both exhibiting larger values in the jets poleward flank, than in the equatorward flank. However, this asymmetry is less clear in the zonal velocity's vertical shear and thus in the Eady growth rate itself.

A plausible mechanism for the interannual anomalous jet migration is therefore due to a combination several different effects, and appears to be largely related to the temperature tendencies, rather than those tendencies due to eddy momentum convergence. All of the results can be drawn together into the following mechanism, which is summarized in the schematic in Figure 4.22:

1. There is a small asymmetry in the system's Eady growth rate across the migration region, due to meridional differences in both the static stability and the Coriolis parameter.

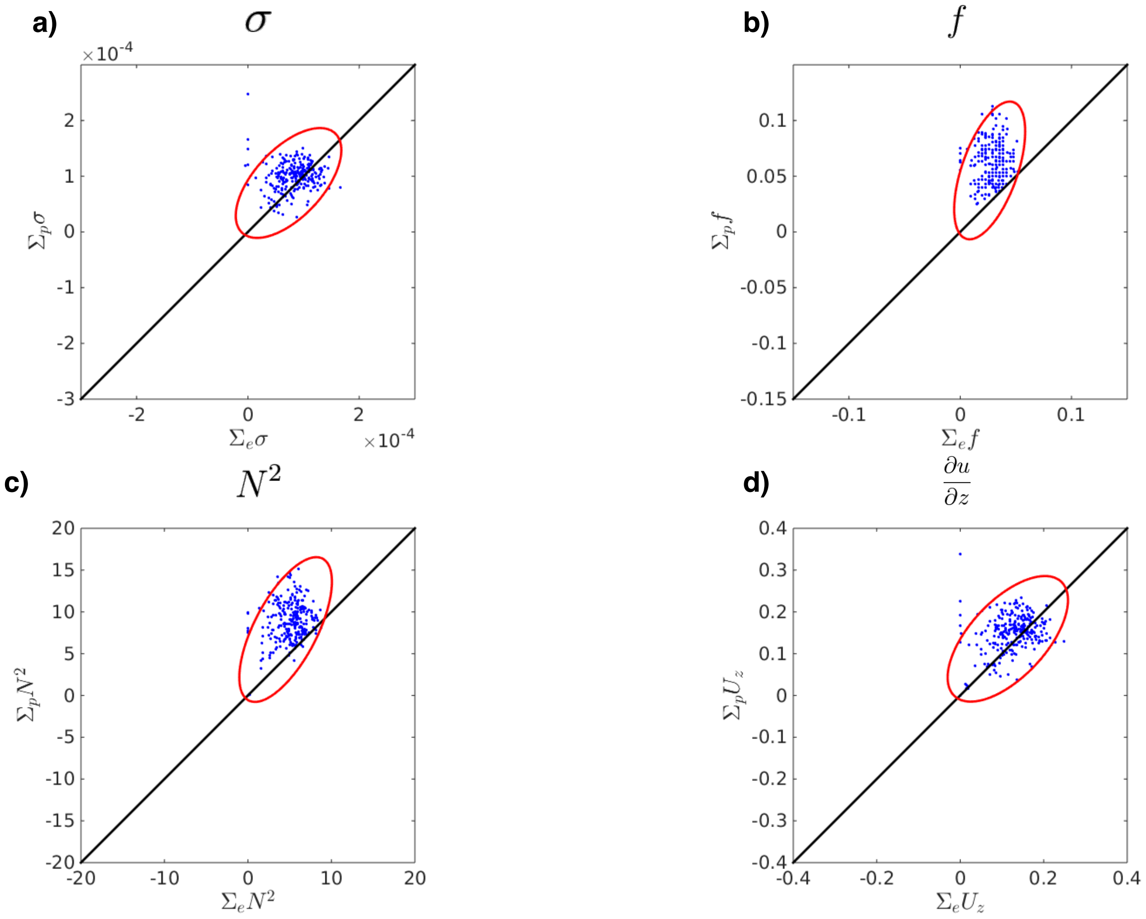

Figure 4.21: The sum over the poleward ($\sum_p$) versus equatorward ($\sum_e$) flanks of the upper meridionally migrating jet of the (a) Eady growth rate, (b) Coriolis parameter, (c) Static stability and (d) the vertical shear in the zonal velocity.

2. The anomalous vertical velocities, shown in Figure 4.23a, indicate that there is a residual circulation with positive vertical velocity anomalies in the core of the jet, and sinking on the flanks.

3. The variations in the eddy temperature tendencies terms, most notably in $-\frac{\partial \overline{w'\theta'}}{\partial z}$, are displaced meridionally from the positions of the temperature anomalies present in the anomalous jets, which are set by the thermal wind (shown in Figure 4.23b).

4. These eddy heat fluxes, change the position of the anomalous jet's baroclinic zone and induce an equatorward migration of the jet. By simultaneously warming the anomalous zonal jet on its equatorward flank and cooling its core.

5. The migration terminates when there is no longer an asymmetry in the Eady growth rate around the jet.

The timescale of the shifting is hypothesised to depend on the anomalous vertical velocities, the related vertical heat advection, and the magnitude of the resultant meridional temperature gradient.

4.4 Conclusions and Discussion

This chapter addressed the emergence of intrinsic interannual variability in both barotropic and baroclinic double-gyre models with a steady wind forcing, at eddy permitting resolutions. The presence of mesoscale eddies can dramatically impact the proportion of interannual variability present in ocean models (Penduff et al., 2011). Moreover, such intrinsic variability, has large implications for interannual variability in the North Atlantic, particularly in the Gulf Stream region (Sérazin et al., 2015). In the barotropic model, both the position of the jet and its zonal transport are seen to vary on interannual timescales. The jet's position varies between approximately 1800-2000km in the meridional direction and its zonally averaged velocity

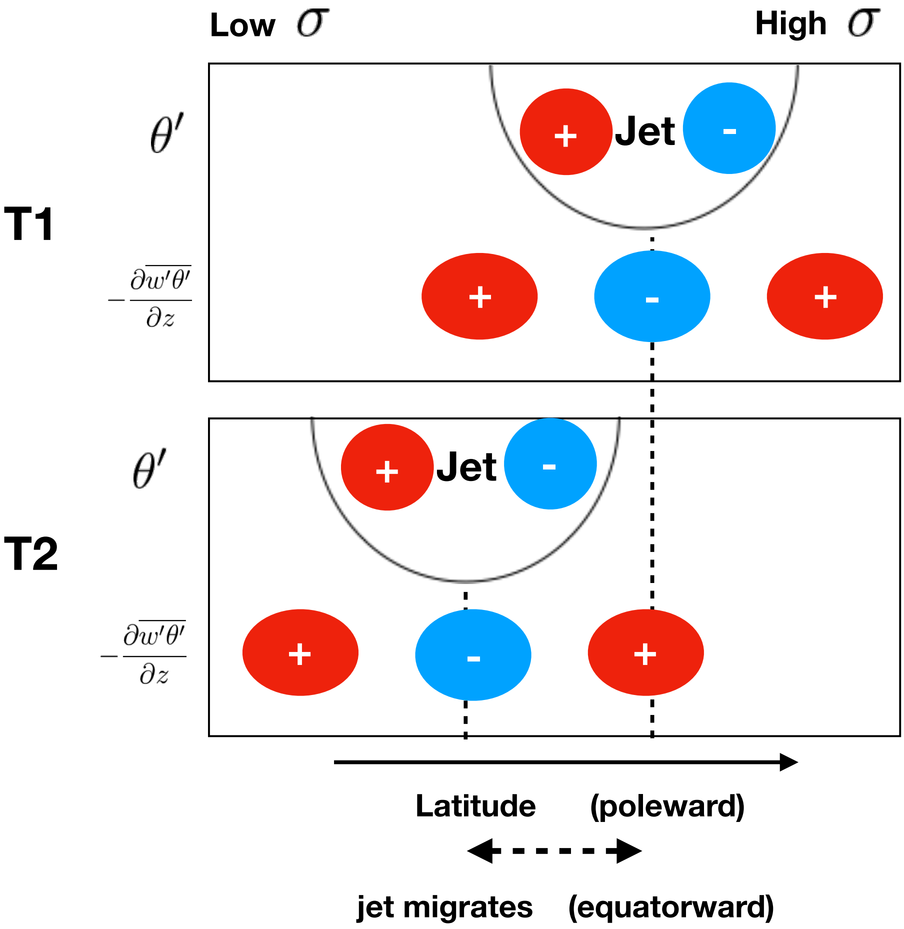

Figure 4.22: Schematic of the eddy-jet interactions responsible for the interannual equatorward migration of the anomalous jets, shown at an initial state (T1) and at a later time (T2). The asymmetric Eady growth rate means that the vertical eddy heat fluxes are shifted meridionally relative to those due to thermal wind balance. This offset causes an equatorward migration of the jet's baroclinic zone.

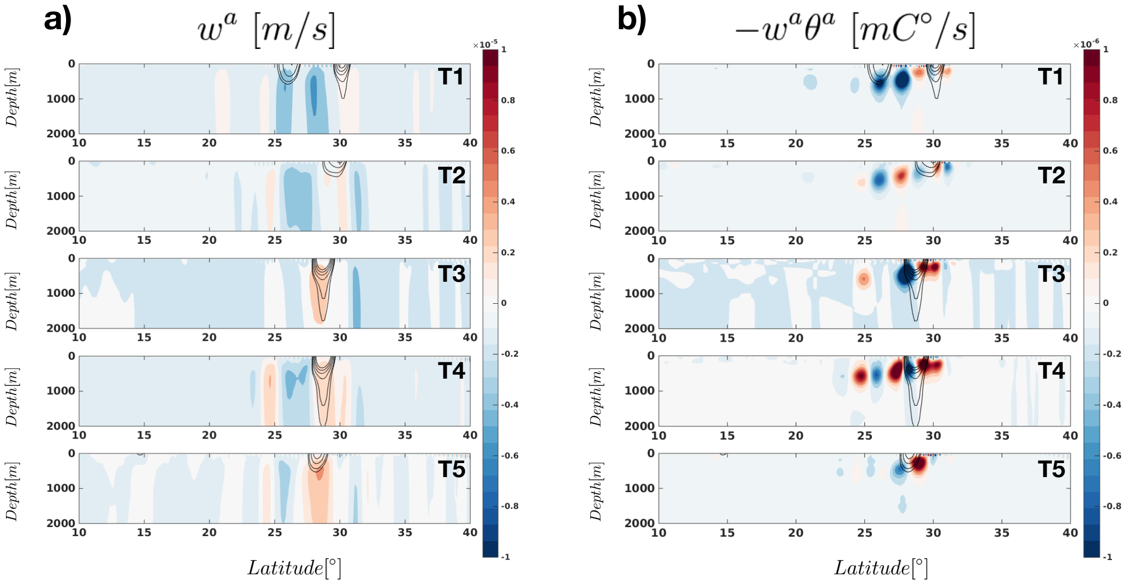

Figure 4.23: (a) The monthly mean vertical velocity anomalies, zonally averaged between longitudes of 16°-22°E. (b) The monthly mean zonally averaged temperature anomalies averaged between longitudes of 16°-22°E. The profiles are taken at the times indicated in Figure 4.14a. The black contours indicate positive zonally averaged zonal velocity anomalies, with contour intervals of 3cm/s.

varies between 0.3-0.55m/s. This variability appears to be similar to that described in numerous other idealised model studies (Jiang et al., 1995; Spall, 1996; Dewar, 2003; Simonnet et al., 2005; Berloff et al., 2007; Quattrocchi et al., 2012). Previously, two approaches have been used to investigate such variability: an approach based on dynamical systems theory (Jiang et al., 1995; Simonnet et al., 2005; Dijkstra and Ghil, 2005; Quattrocchi et al., 2012), and investigations based on examining the statistics of the dynamical processes present (e.g, Berloff et al., 2007). The present study adopts an approach which is similar to the latter, however considering the full momentum and buoyancy budgets (Waterman, 2009) to investigate the eddy-mean flow interactions, which are hypothesised to drive interannual intrinsic variability.

Analysis of the momentum budget determined that two distinct mechanisms induce variability in the jet transport and position. The transport is driven locally by Reynolds stress variations in the recirculation gyres; whereas the meridional position appears to be driven by variations in the strength of the meridional transport in the

WBCs. This mechanism, associated with the meridional position shift is more difficult to discern as the main differences between the northward and southward states are located in the narrow western boundary currents near to the jet's separation point. Such variations are hypothesized to be due to a combination of eddy-boundary current interactions, and variations in the transport of the large-scale gyres (as in McCalpin and Haidvogel, 1996). This results implies that the predictability timescale of a meridional jet shift will be limited, by either the time taken for inter-gyre potential vorticity anomalies to (1) propagate around the gyre circulation (approximately 5 months), or (2) to be advected towards the coast by the recirculation gyres (approximately 1 month). The propagation timescales of inter-gyre potential vorticity anomalies could also be affected by the strength of the jet and therefore the associated cross-frontal potential vorticity mixing as discussed by Berloff et al. (2007). Although in this study no correlation was found between the jet transport and the jet position, perhaps due to the short zonal jet length.

The baroclinic model displayed several features similar to the barotropic model, as the largest amount of interannual SSH variability is again located in the jet region. In the recirculation gyres, the mechanisms of low-frequency variability are similar to those seen in the barotropic case. However, away from the western boundary in the basin's interior, a different form of variability emerged which involved multiple anomalous zonal jets. The existence of multiple zonal jets has previously been reported in the ocean's interior in observations (Maximenko et al., 2005) and eddying models (Thompson and Richards, 2011). In the baroclinic model the anomalous zonal jets are seen to drift meridionally equatorward on interannual timescales between latitudes of 25°N - 31°N. These drifts are also seen in the zonally averaged SSH anomalies (averaged between longitudes of 16°-22°E), with magnitudes of approximately 0.3m.

The jet migration resembled that previously discussed in studies by Chan et al. (2007) and Chemke and Kaspi (2015), which analysed zonally symmetric configurations of oceanic and atmospheric flows, respectively. However, the mechanism of variability is dissimilar to that presented in Chemke and Kaspi (2015), as no significant across jet eddy momentum flux asymmetries are observed. Instead, the mechanism is shown to share similar ingredients to that presented by Chan et al. (2007); it is the tendencies related to eddy temperature fluxes, not those related to the momentum fluxes, which cause the shift in the position of the anomalous jet's baroclinic zone on interannual timescales. This shift could be seen in the larger scale jet features, causing several jets to merge and separate (as seen in Figure 4.14b), thus causing interannual variations in the zonal transport and SSH. The model setup used here and containing gyre structures with strong western boundary currents is distinct to that used by Chan et al. (2007) which used a re-entering zonal channel mimicking the Southern Ocean. However, there are some similarities: the Eady growth rate varies as a function of latitude, there are offsets between the wind stress curl zero line and the middle of the temperature restoring profile, and the models are on spherical polar grids with subsequent meridional variations in the Coriolis parameter. Each of these ingredients introduces potential asymmetries in the system, which can explain why the anomalous jets migrate solely equatorwards. Chan et al. (2007) primarily related the asymmetries in the Eady growth rate to meridional variations in static stability. However, we find that variations in the Coriolis parameter also have a significant contribution.

In both the barotropic and baroclinic model setups intrinsic mechanisms of ocean variability drive SSH variability on interannual timescales. Interestingly, neither model displays any gyre-scale modes of variability. Instead, the interannual variability is particularly prevalent in the jet extension regions. This jet-localised intrinsic variability could have implications on other modes of climate variability, as mid-latitude ocean jets can influence the atmospheric circulation through variations in ocean-atmosphere heat fluxes (Kwon et al., 2010; O'Reilly et al., 2017). However, in both models, the power spectra taken in the jet regions near to the coast have white profiles on interannual timescales (as in observations as demonstrated by Hughes and

Williams (2010)), which is indicative that the intrinsic SSH variability is chaotic and unlikely to be predictable on interannual timescales.

Future studies should consider more dynamically complex models, as it remains unclear how the addition of bathymetry, time-varying wind forcing, or a buoyancy driven overturning circulation, will influence the intrinsic variability. Indeed, it is hypothesised that the introduction of a wind which varies on interannual timescales may introduce mechanisms which dominate over the intrinsic mechanisms discussed here.

Chapter 5

An Evaluation of Intrinsic and Forced Sea Surface Height Predictability in Double Gyres

5.1 Introduction

In the North Atlantic, interannual variability is due to both intrinsic ocean processes and the ocean's response to external forcings. The interannual SSH variability in the CMIP5 AOGCMs displays some differences from that observed by tide gauges (Becker et al., 2016) and altimetry (Landerer et al., 2014), which are particularly prominent in the North Atlantic. These differences are partly because the ocean models used do not generally resolve oceanic eddies, a component which can dramatically alter the spatio-temporal features of SSH variability (Landerer et al., 2014; Penduff et al., 2011; Becker et al., 2016; O'Rourke et al., 2018). Moreover, the presence of eddies can dramatically effect the appearance of WBCs and atmosphere-ocean interactions (Hewitt et al., 2017).

Although idealised models and simplified GCM based studies have shown that eddies contribute to interannual variability, particularly in regions with mid-latitude ocean jets (Dijkstra and Ghil, 2005; Berloff et al., 2007; Giannakis and Majda, 2012; Arbic et al., 2014; Sérazin et al., 2015). It is still uncertain how the introduction of mesoscale eddies will effect SSH forecasts because, although they can contribute to interannual variability, such variability may be chaotic, or masked by other high frequency components of variability which the eddies introduce. The latter seems to be true in observations as SSH power spectra taken in mid-latitude jet regions have white profiles on interannual timescales (Hughes and Williams, 2010; Forget and Ponte, 2015). However, even if the ocean dynamics in the jet regions is unpredictable, the variability present may induce predictable responses in the atmosphere (Kwon et al., 2010; Scaife et al., 2011).

SSH predictability related to intrinsic variability has previously been examined in idealised models and simplified GCMs (Mahadevan et al., 2001; Dijkstra and Ghil, 2005; Giannakis and Majda, 2012; Nonaka et al., 2016). The studies have shown some contrasting results, Giannakis and Majda (2012) investigated the predictability generated by intrinsic ocean variability using an ensemble of eddy-resolving, equivalent barotropic, double gyre systems. The leading EOFs of the system, which were related to the states of the eastward jet, were found to be predictable on timescales in the range of 1000-3000 days. In contrast to this result when Nonaka et al. (2016) investigated the associated predictability of mid-latitude ocean currents using an ensemble of eddy-permitting OGCM experiments, they found substantial uncertainty in the SSH hindcasts in the jet regions, on seasonal timescales, due to the contributions of the mesoscale eddies. Further investigation is required to establish the reason for these differences.

This chapter will address the second aim of the thesis, which is: **to quantify the predictability of SSH due to the sensitivity in ocean initial conditions and surface forcings in the presence of resolved eddies**. The first part of this chapter will address how intrinsic mechanisms set predictable timescales in the models described in Chapter 3. Specifically, I will:

- Evaluate whether intrinsic variability is predictable on interannual timescales.
- Examine the models' sensitivity to perturbation growth.

The second half of the chapter will examine the predictability as a function of the applied surface forcings, and will address:

- The relationship between any interannual predictability and the magnitudes of both the applied steady wind forcings and surface temperature profiles.

A small study at the end of the chapter will examine the impact of time-varying wind forcings (simulating the NAO or another mode of atmospheric variability) on the variability and predictability present in the baroclinic system. Previously, several double-gyre based studies have examined how changes in applied time-dependent external forcings impact such systems' interannual variability (e.g., Simonnet et al., 2005; Shimokawa and Matsuura, 2010; O'Reilly et al., 2012; Sapsis and Dijkstra, 2013). However, it remains unclear how time-dependence in the applied wind and buoyancy forcings impact predictability.

5.2 Ocean Initial Conditions and Sea Surface Height Predictability

5.2.1 Intrinsic Barotropic Timescales of Predictability

In this section, 100 years of 10-day mean SSH output from the barotropic model (described in Section 3.1), are used to examine the initial condition predictability. Before attempting to evaluate interannual predictability, I first identify areas which display interannual variability and determine the ratio between the interannual and high-frequency variability present. This is done by diagnosing the potential predictability, the signal to noise ratio of interannual variability, $\frac{\sigma_N}{\sigma_{10}}$, where σ_N represents the standard deviation of N-day means of SSH (Boer, 2004; Hawkins et al., 2011). Figure 5.1a shows that the variability is within the jet extension region. Moreover, the potential predictability is also predominantly localised to the jet region (panels b and c). Therefore a large proportion ($> 60\%$) of the variability in the jet region is on timescales longer than 180-360 days. However, it has previously been shown that on such timescales the power spectra of SSH anomalies are white (Figure 4.1), and are therefore likely unpredictable.

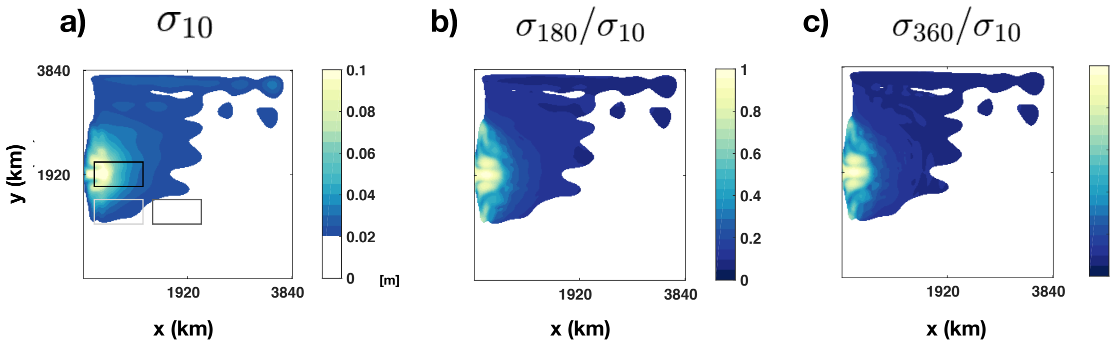

Figure 5.1: a) SSH Standard deviation calculated with 10-day means from the 100 year barotropic control run. Potential predictability- ratio of the standard deviations of the : b) 180 c) 360 day means to the standard deviation calculated with 10-day means. Areas of low standard deviations <0.02m are masked in white. The boxes in panel a indicate the positions (x,y) of three regions: the 'Subtropical Gyre in basin' (1075-2000km, 1520-1720km, Dark Grey), the 'Subtropical Gyre near coast' (75-1000km, 1520-1720km, Light Grey) and the 'Jet' (75-1000km, 1820-2120km, Black).

The non-normal growth of SSH anomalies is now investigated (see Section 2.2.2 for a review of the methods used). The system is found to obey the main criteria necessary to derive a LIM based on SSH alone (detailed in Section 2.2.2). Figure 5.2a shows that the operator **A** is invariant, when constructed using lag times, τ_0, between 30-100 days. In the case where 20 EOFs are retained (representing 70% of the variance), it is possible for the non-normal amplification of SSH variance to occur on timescales of up to 500 days, as shown in Figure 5.2b. This growth timescale can be thought of as the upper limit of the linear predictability of the system. The maximum amplification is found at a lag time of 130-180 days and is insensitive to the number of EOFs used. The initial pattern which results in the maximum amplification of SSH variance is shown in Figure 5.3a. This optimal initial condition is quite intricate and is concentrated near the jet region. Its associated geostrophic velocity anomalies have small asymmetries in the meridional direction, near to the western boundary (blue line in 5.3a). The propagated optimal initial conditions (panels b and c), resemble the leading EOF of the system (Figure 4.2b), corresponding to a meridional deflection of the (small) recirculation gyres (seen previously in Section 4.2.2). This growth also results in variations in the geostrophic velocities. Figure 5.3d shows that the propagated state has increased meridional velocities near the western boundary. Moreover, Figure 5.3e shows that the propagated pattern exhibits increased zonal geostrophic velocities in the recirculation gyres. Therefore it is hypothesised that this evolution can be dynamically explained by one of the two following mechanisms. Either, the optimal initial conditions relate to the shedding of an eddy, which then is advected to the western boundary, resulting in a meridional shift in the jet 180 days later. Alternatively, the initial condition results in a barotropic instability and the creation of a Rossby wave; in response, momentum is asymmetrically fluxed into the jet region, shifting the jet 180 days later. The magnitudes of such SSH amplifications are significant, with initial SSH anomalies of $\mathcal{O}(5\text{cm})$ resulting in SSH anomalies of $\mathcal{O}(1\text{m})$ and anomalous geostrophic velocities of $\mathcal{O}(0.5\text{m/s})$ 180 days after initialisation.

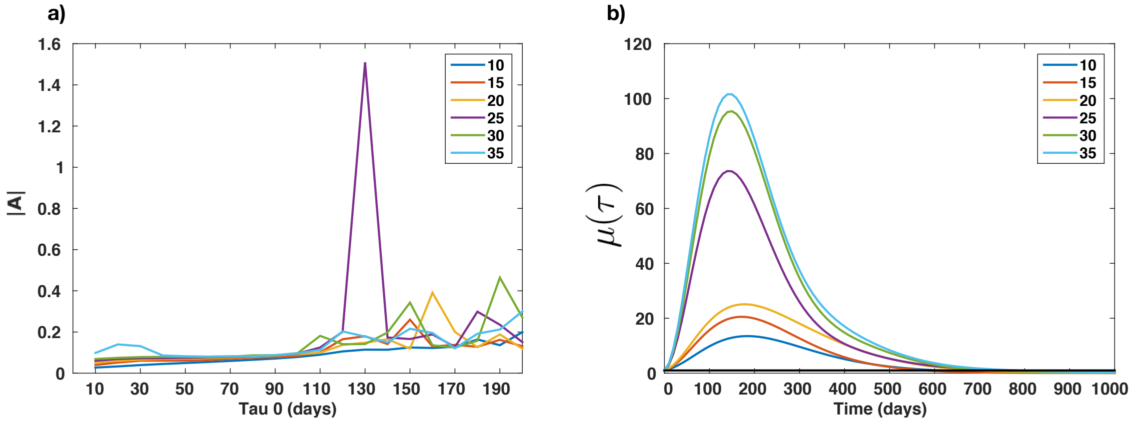

Figure 5.2: a) The Euclidean norm of the operator, **A**, as a function of different lag times τ_0, and with differing number of EOFs used in its calculation (the number of EOFs used is indicated by the colors). b) The maximum amplification curve (eq. 2.33), for differing numbers of EOFs using τ_0 =50 days. The black line indicates the threshold require for growth to occur.

The average predictability time (APT) is calculated using the methodology described in Section 2.2.4.2 and is used to evaluate the predictability of the system over all lag times. This method is also used to decompose the system into its different predictable components. The predictability of the system, measured by the Mahalanobis

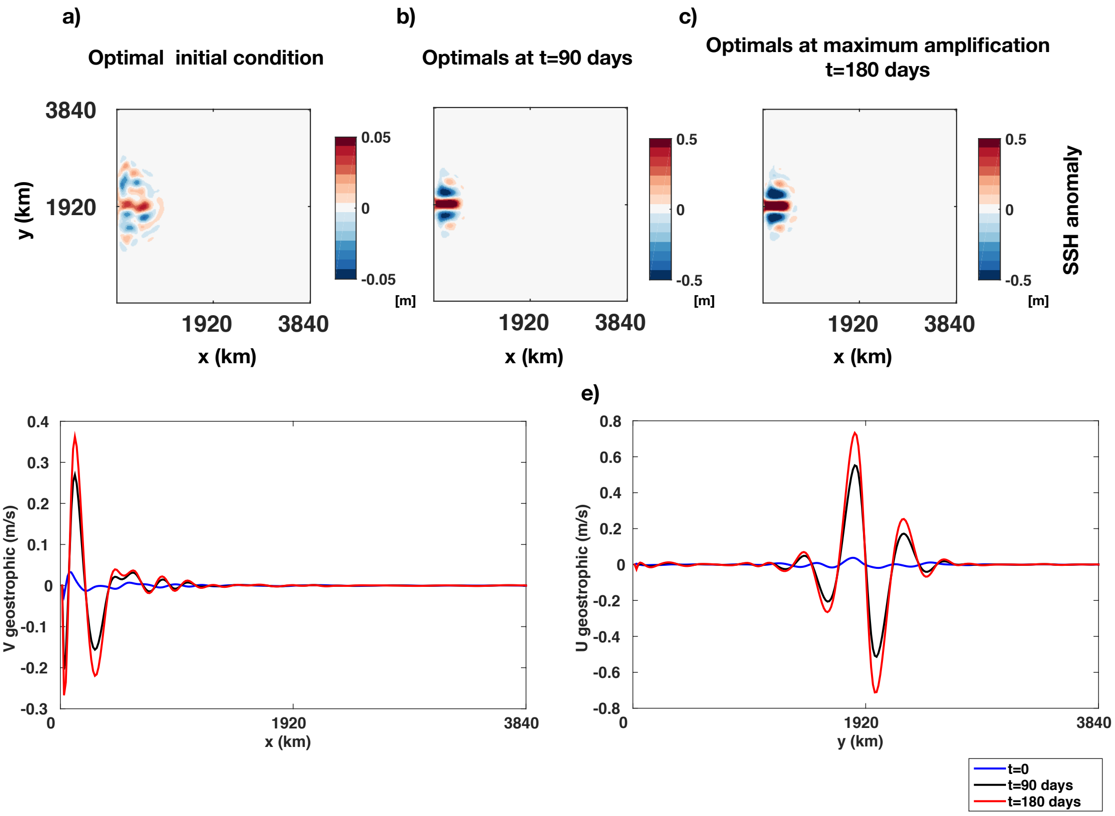

Figure 5.3: Non-normal mode analysis in the case where the propagator, $\mathbf{B}$, is formed with 20 EOFs and τ_0 =50 days. a) The optimal initial condition. b) The optimal at its propagated state 90 days later and (c) at its state of maximal growth at 180 days. Note that the scales in panel a is small when compared to those in panels b and c. d) The meridionally-averaged meridional geostrophic velocities of the initial (blue) and propagated optimals (black and red). e) The zonally-averaged zonal geostrophic velocities of the initial and propagated optimals.

signal, decreases rapidly and reaches low values, < 0.2, after times in the range of 100-200 days (Figure 5.4a), which is similar to the timescale of maximum growth from LIM. The leading predictable components correspond to variations in the jet's latitudinal position and transport (panels d-f) and are predictable on timescales between 150-260 days (Figure 5.4b). The power spectra of the leading three predictable components are white on interannual timescales, signifying a lack of any interannual ($>$ 1 year) predictability (Figure 5.4c).

Therefore both the non-normal mode analysis and the APT calculations are in agreement that there exists linearly predictable patterns on timescales of approximately 200 days. These patterns represent meridional shifts in the position of the jet and variations in its transport. The patterns are largely located near to the western boundary in the vicinity of the jet. The correlation times, τ_i of the leading two principal components of the system are 45 and 39 days ($\tau_i = \int_0^T dt|\rho_i(t)|$, where i is the principal component number, T is the total time of the model run and ρ is the empirical auto-correlation function $\rho_i(t) = \int_0^T dt'\mathbf{P}_i(t')\mathbf{P}_i(t'+t)/T$). Therefore, the results are in agreement with Giannakis and Majda (2012), as the predictability times are significantly longer than the correlation times of the leading principal components. However, despite the model displaying interannual variability, there is no observed predictability on interannual timescales.

5.2.2 Timescales of Predictability in a Baroclinic Model

In this section, 100 years of 10-day SSH mean model output are used to evaluate the baroclinic system's predictability (the baroclinic model forced by a steady external wind, as described in Section 3.2.3). As in the barotropic model, the intrinsic variability is largest in the jet extension region (Figure 5.5 panel a). However, the potential predictability is largest in the jet extension rather than near to the western boundary of the domain (panels b and c). To evaluate the system's predictability a LIM is again trained on the SSH field. The operator $\mathbf{A}$, shown in Figure 5.6a, is invariant to changes in the time lag, τ_0, for lags equal to and longer than 100 days. A time lag of τ_0 =100 days and the leading 30 EOFs of SSH are used to construct the linear model.

The amplification of the variance of the SSH happens on times of up to 600 days (Figure 5.6b). However, the maximum amplification occurs at a timescale of 10-30 days. Since this timescale is below the τ_0 used to construct the operator these patterns are subject to large errors, as timescales shorter than τ_0 are not included in the covariance matrices used to construct the operator. Figure 5.7 shows the initial conditions related to the growth occurring at 240 days (panel a). The initial

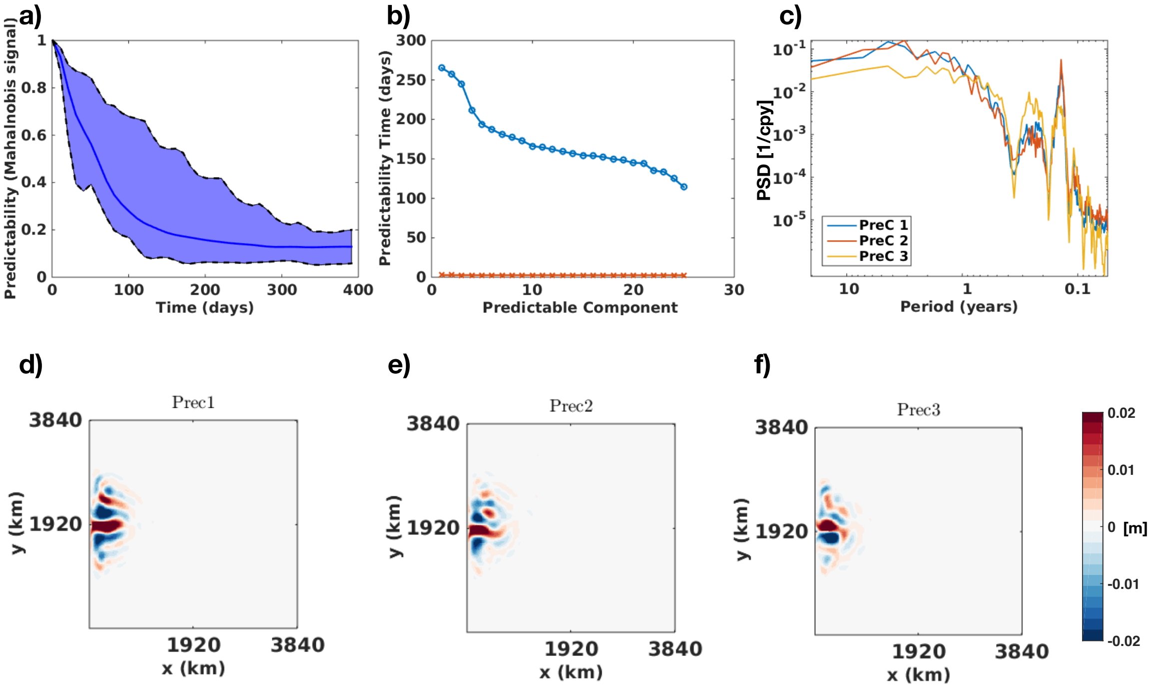

Figure 5.4: a) Predictability measured by the Mahalanobis signal (S_τ as defined in equation 2.35) of the whole system (blue line), created using linear regression models and the leading 25 principal components. The envelope denotes the spread in predictability measured by the Mahalanobis signal (S_τ) for each of the leading predictable components. b) The average predictability time (APT) for the first 25 predictable components (blue) and the 5% significance level (orange) estimated by the Monte Carlo method described in Section 2.2.4.2. c) Power spectra of the time series associated with the three leading predictable components ($\mathbf{q}^{\mathbf{T}}\mathbf{P}$) (in units of [1/cpy], where cpy is 'cycles per year'). The spatial patterns ($\mathbf{p}$) of the (d) first, (e) second and (f) third predictable components, ranked in order of their values of APT.

conditions are tripolar and situated in the jet region. As they evolve, the pattern appears to be stationary in position, only growing in magnitude (panels b and c). The meridionally averaged meridional geostrophic velocities (panel d) show growths in anomalies, which lead to jet meandering as the initial conditions are propagated in time. Moreover, the zonally averaged zonal geostrophic velocities (panel e) exhibit an equatorward shift of the recirculation gyres. The amplification is smaller than in the barotropic gyre case, with SSH anomalies growing by a factor of approximately 1.4, albeit occurring on longer timescales.

The APT is evaluated using 100 years of 10-day mean SSH model output and 25

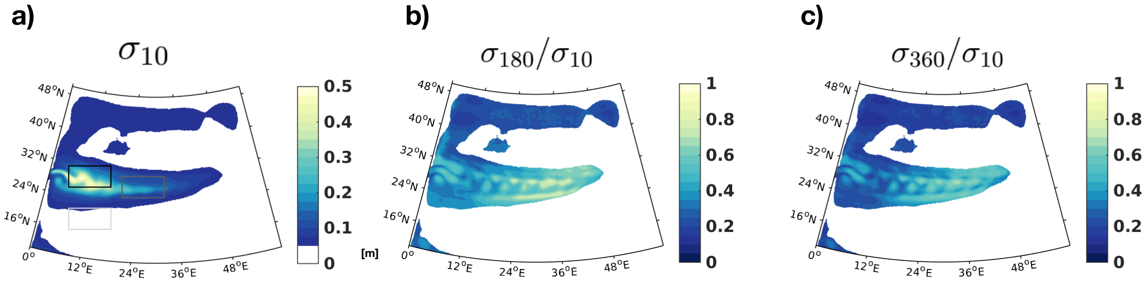

Figure 5.5: a) Standard deviation calculated with 10-day means from the 100 year baroclinic control run. Potential predictability- ratio of the standard deviations of the b) 180 c) 360 day means to the standard deviation calculated with 10-day means. Areas of low standard deviations <0.05m are masked in white. The boxes in panel a show indicate three regions: 'Jet near coast' (1.5-16.5°W, 23.2-31.5°N, Black), 'Jet away from coast' (16.5-24.8°W, 23.2-31.5°N, Dark Grey), 'Subtropical Gyre' (20.6-28.1°W, 18.2-26.5°N, Light Grey)

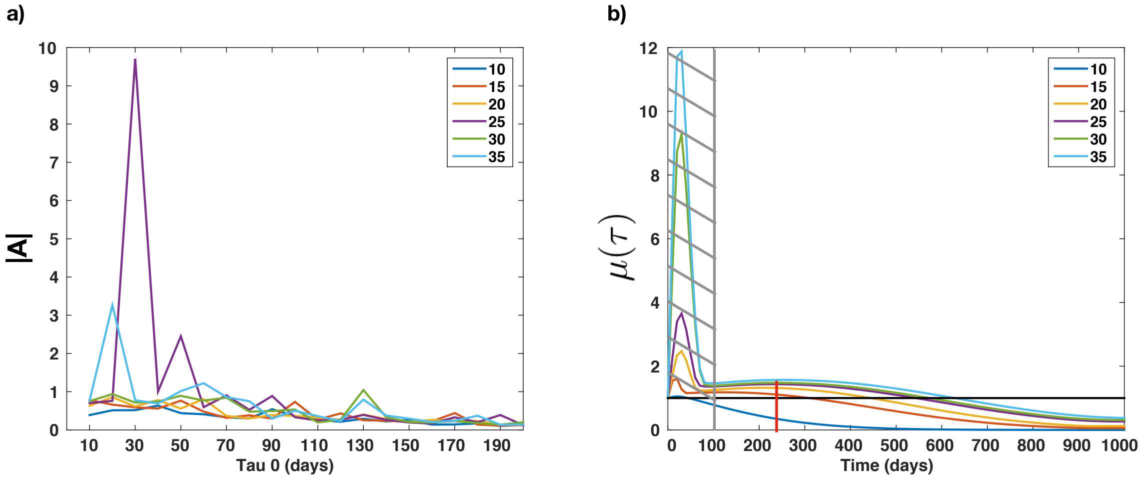

Figure 5.6: a) The Euclidean norm of the operator, **A**, as a function of both different lag times τ_0 and the number of EOFs used in the calculation of the propagator. b) The maximum amplification curve (eq. 2.33), for differing numbers of EOFs and τ_0 =100 days. The black line indicates the threshold required for growth to occur. The red vertical line indicates the growth which is discussed in the text. The grey hashed area which contains the optimal amplifications is not considered as it occurs on times shorter than τ_0.

EOFs. An upper summation limit, which is longer than the timescales of the observed variability, of 10 years is applied when calculating the APT (M in equation 2.45). The APT of the total baroclinic system is seen to decay rapidly on a timescale of 100 days (Figure 5.8 a). However, in contrast to this behaviour, the two leading predictable

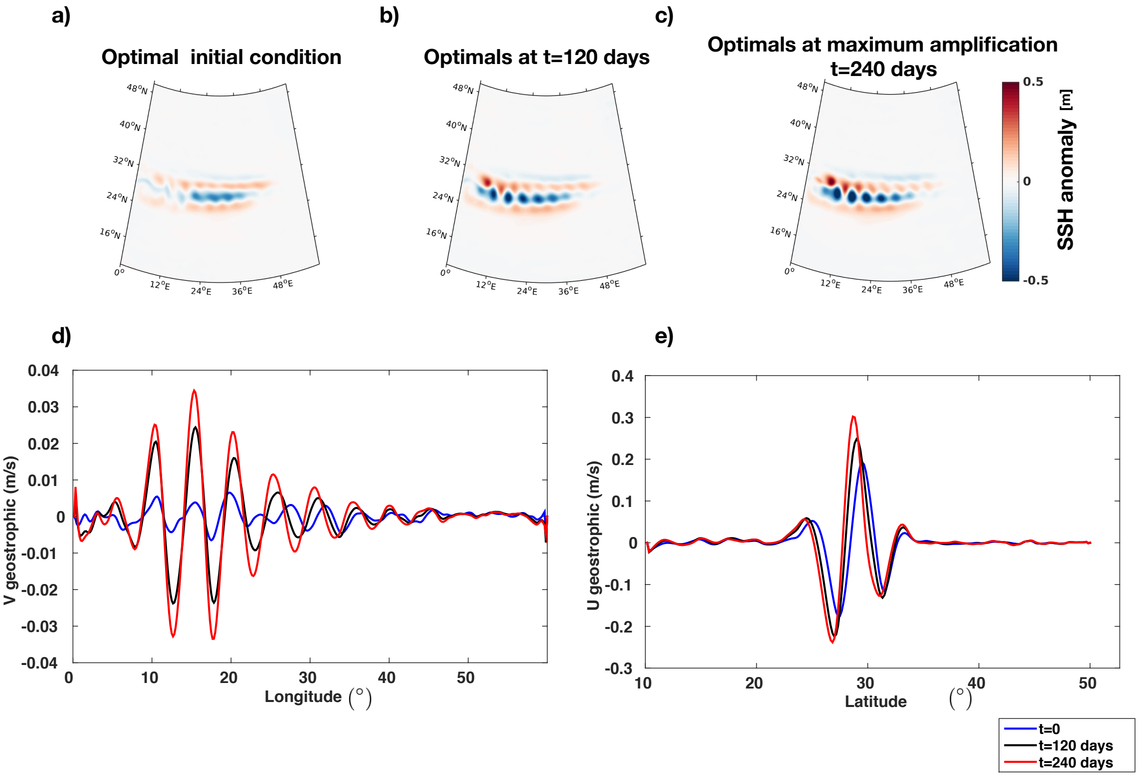

Figure 5.7: An examination of the conditions that lead to a secondary peak at 240 days, using a linear operator created from 30 EOFs and where τ_0 =100. The initial condition (a), at its propagated state 120 days later (b) and at its state of growth at 240 days (c). d) The meridionally-averaged meridional geostrophic velocities of the initial (blue) and propagated optimals (black and red). e) The zonally-averaged zonal geostrophic velocities of the initial and propagated optimals.

components are predictable on far longer times of approximately 4.8 years. These components relate to a meridional propagation of anomalies in the jet and are shown in Figure 5.8 panels d and e. The higher order predictable components correspond to processes acting on shorter time scales such as Rossby waves, examples of which are seen in the third and fourth predictable components (Figure 5.8 panels f and g). Figure 5.8 panel c, shows the power spectra associated with the predictable component time series. The leading two predictable components have red spectra on periods of up to 2 years, and possess distinct peaks at periods of 5-6 years. On shorter timescales the other predictable components can dominate the variability, for example predictable component 4 has a sharp peak at a period of approximately 0.09 years. A plausible explanation for such high frequency peaks is that they are associated with Rossby basin modes. Calculations of the basin-scale Rossby wave periods estimated using the barotropic Rossby wave dispersion relation (equation 2.10) support this explanation as the calculated periods closely matched those observed.

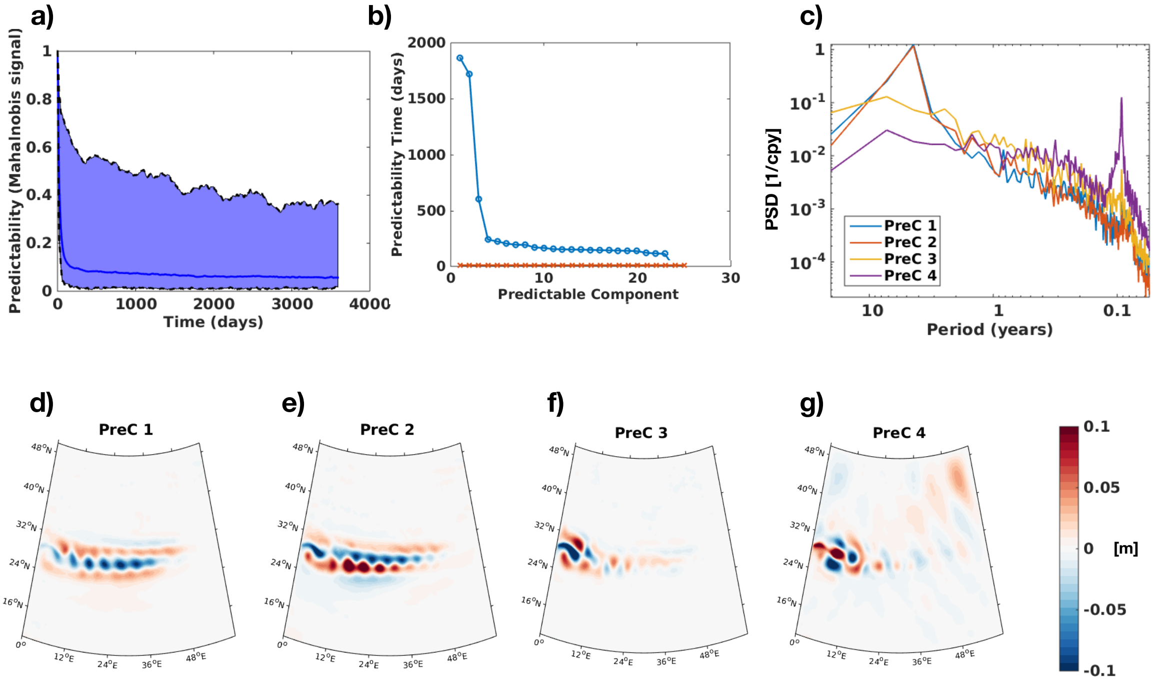

Figure 5.8: a) Predictability measured by the Mahalanobis signal (S_τ as defined in equation 2.35) of the whole system (blue line), created using linear regression models and the leading 25 principal components. The envelope denotes the spread in predictability measured by the Mahalanobis signal (S_τ) for each of the leading predictable components. b) The average predictability time (APT) for the first 25 predictable components (blue) and the 5% significance level (orange) estimated by the Monte Carlo method described in Section 2.2.4.2. c) Power spectra of the time series associated with the three leading predictable components ($\mathbf{q^T P}$) (in units of [1/cpy], where cpy is 'cycles per year'). The spatial patterns ($\mathbf{p}$) of the (d) first, (e) second and (f) third predictable components, ranked in order of their values of APT.

The analysis presented investigated the predictability present in the barotropic and baroclinic model set-ups. The barotropic model displays predictability in the jet region of timescales of approximately 200 days, a timescale which is longer than the correlation times of the leading principal components (in agreement with (Giannakis and Majda, 2012)). Both the most predictable barotropic patterns and the optimal initial conditions are localised to small scale features in the jet region. In comparison to this the baroclinic model's amplification timescales and average predictability times are far longer than in the barotropic model, both measuring approximately 5 years. The spatial patterns associated with these interannually predictable components are jet localised, and are the result of interannual meridional propagation in the jet region, which not present in the barotropic model. In addition to these patterns, the predictable components with shorter predictability times exhibit similar predictability times and spatial structures to those diagnosed in the barotropic experiment. These similarities are suggestive that such patterns occur due to primarily barotropic mechanisms.

5.3 An Analysis of the Effects of Wind and Buoyancy Forcings on Sea Surface Height Interannual Predictability

This section will examine the sensitivity of the predictable timescales due to variations in the applied wind and buoyancy forcings.

5.3.1 Forcing Details

The forcing experiments are divided into three types: variations in the profile of steady wind forcing, variations in the surface temperature restoring profile, and the addition of a time-varying wind forcing.

The applied wind forcing for the barotropic experiment is

$$\tau_x(y) = A\ sin(\frac{\pi y}{L_y}), \tag{3.6 revisited}$$

where A is the magnitude of the wind forcing, y is the meridional displacement and L_y is the meridional extent of the domain. The different experiments involved adjusting the magnitude of the wind forcing, A, as detailed in Table 5.1.

For the forced experiments WN and RN, a time-varying stochastic noise component is added to the steady wind profile. The stochastic wind stress component is represented as a first-order Markov process with zero mean and is chosen to represent the high frequency (WN) and the interannual NAO variability (RN)(Wunsch, 1999; O'Reilly et al., 2012). To simplify the analysis the applied wind forcing only varies in the meridional direction and is of the form

$$\tau_x(y) = A\ sin\left(\frac{\pi y}{L_y}\right) + W_s\ cos\left(\frac{\pi y}{L_y}\right), \tag{5.1}$$

where

$$W_s(t) = \sigma_{ref} M(t), \tag{5.2}$$

σ_{ref} is a constant of magnitude $0.02N/m^2$, which gives a perturbation which is 10% the size of the mean field and

$$M(t) = \gamma\ M(t-1) + a(t) \tag{5.3}$$

is a first order Markov process with zero mean and unit standard variance, where γ is a coefficient setting the persistence timescale of the wind forcing and $a(t)$ is a Gaussian white noise process with unit variance (O'Reilly et al., 2012). In the white noise (WN) experiment $\gamma = 0$ while in the red noise (RN) experiment $\gamma = 0.9$. As before, the profile leads to a double gyre structure with an added single (inter-) gyre stochastic component mimicking a latitudinal jet shift, as in Marshall et al. (2001) and O'Reilly et al. (2012).

The steady wind forcing in the baroclinic experiments, is as described in Section 3.2.3 and given by

$$\tau_x(y) = A\ sech^2(y - \frac{L_{yn}}{2}) - C \tag{3.24 revisited}$$

where L_{yn} is 40°and y is defined in the meridional distance in degrees, from 10°N. Although this wind profile (CB1) generates smaller gyres than a sinusoidal profile, it creates a strong mid-latitude jet with a mean zonal velocity of approximately $2m/s$. This time-independent wind profile is perturbed by varying A in experiments W1 and W2, with magnitudes shown in Table 5.2. In these steady experiments, the surface temperature is restored each month to the profile, C1, shown in Figure 5.10. The surface temperature restoring profile is perturbed in experiments, T1 and T2, shown in Figure 5.10, while the wind forcing is the same as in C1. All three temperature restoring profiles are linear as a function of latitude. The profile in the control experiment, C1, ranges between between 30°C at the equator and 5°C at 50°N. The experiments T1 and T2 relate to variations in the temperatures at the high latitudes. T1 undergoes a high latitude warming (8°C at 50°N) and T2 experiences a cooling (3°C at 50°N).

In the time-dependent forcing experiments with the baroclinic model, two different types of simulations are used. Firstly, a red noise forcing (V1) is employed. This is done as for the barotropic simulation but is applied to a cosine function,

$$\tau_x(y) = A\ cos\left(\frac{\pi y}{L_y}\right)^{10} + W_s\ cos\left(\frac{\pi y}{L_y}\right)^{10}, \tag{5.4}$$

where A and W_s are as defined previously. This mean profile again generates a double-gyre structure with a strong mid-latitude jet of significant magnitude (zonally averaged zonal velocity of 1.5m/s) and gives a mean profile very similar to the experiments forced with the profile given in equation 3.24. This profile is chosen as it creates both a strong jet and large scale gyres. The larger gyres are an improvement from those generated using the wind stress profile in equation 3.24 and also still exhibited the same shifting variability as discussed in Section 4.3. Secondly, there is a wind forcing experiment whereby a perturbation to the mean wind is applied, such that its zero wind stress curl line oscillates between two latitudes separated from the mean state by 5°(V2), i.e,

$$\tau_x(y) = A\ cos\left(\frac{\pi y}{L_{yn}}\right)^{10} + B\ cos\left(\frac{y_0 \pi}{L_{yn}}\right)^{10} \tag{5.5}$$

where A is as defined previously and B is 0.05N/m^2. The meridional position of the perturbation is given by

$$y_0 = \frac{L_{yn}}{8} sgn(cos(\omega_f t)) + \frac{L_{yn}}{2}, \tag{5.6}$$

Identifier	Description	Wind Forcing (A) N/m^2
CB1	Control	0.2
WB1	Weak Wind	0.15
WB2	Strong Wind	0.25
WN	White Noise	0.2 with white noise
RN	Red Noise	0.2 with red noise

Table 5.1: The different parameters used in the barotropic model based forcing experiments.

where ω_f is the frequency of the latitudinal shift with an associated period of 20 months. The profile is an attempt to add a time varying component of variability to the wind stress. Although the step function might appear as unphysical it allowed a clear distinction between the two states: State 1, A strong subpolar gyre and a weak subtropical gyre, and State 2, A weak subpolar gyre and and a strong subtropical gyre. It is hypothesised that the gyre scale adjustment to the changes in state of the wind stress forcing is communicated through Sverdrup balance which leads to predictable adjustments on interannual timescales as the SSH components diverge and converge. The set up with the time dependent stochastic components lacks a spatial coherence in the wind stress structures. Thus, in order to investigate the effect of a time dependent wind stress with large scale spatial variability (an ultra-simplified version of the observed EOF of the wind stress curl with a pattern associated with the NAO (the pattern shown in Fig. 11 of Häkkinen et al. (2011))) we used the time varying component with the step function. The timescale of the wind forcing variability is chosen so as to be separable from the intrinsic variations associated with the anomalous jet migrations.

5.3.2 Barotropic Gyre Response

Figure 5.11 shows the changes in SSH variability, as a result of variations in wind forcing. In all experiments, there are several orders of magnitude more spectral power on interannual timescales (periods > 1 year) in the jet region (panel c), than in the

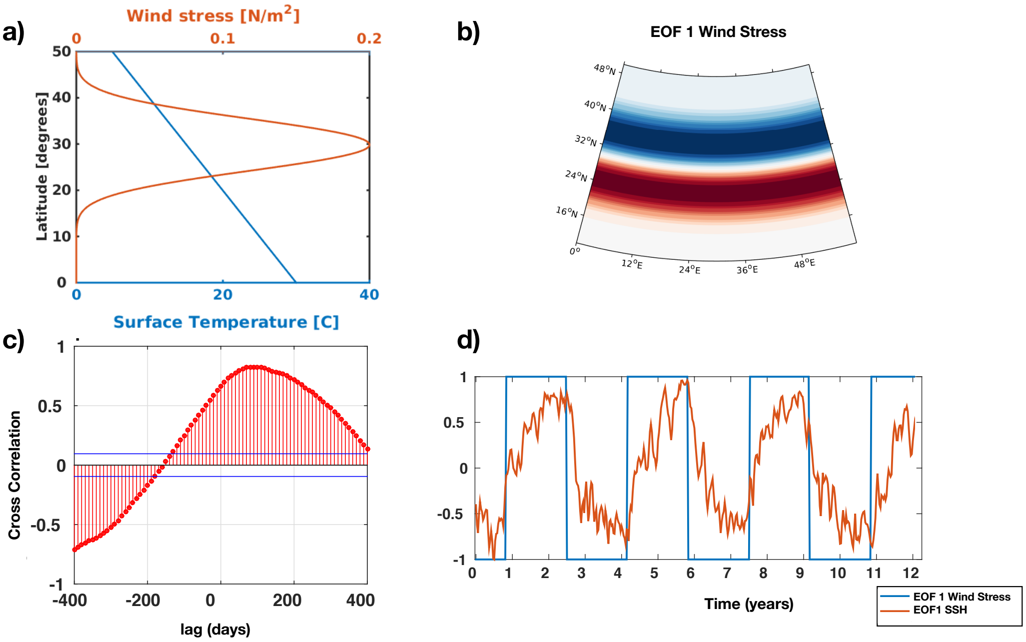

Figure 5.9: a) The surface restoring of temperature profile and the profile of the steady, zonal wind stress used in experiment V2 (if B were zero) . b) The EOF of the zonal wind stress associated with the time-varying forcing in V2. c) The time-lagged cross-correlation of the leading EOF of the zonal wind stress and the leading EOF of the SSH. d) Time series of the leading principal component of the zonal wind stress and the leading principal component of the SSH. Positive lag times indicate the SSH EOF is lagging the EOF of the wind stress.

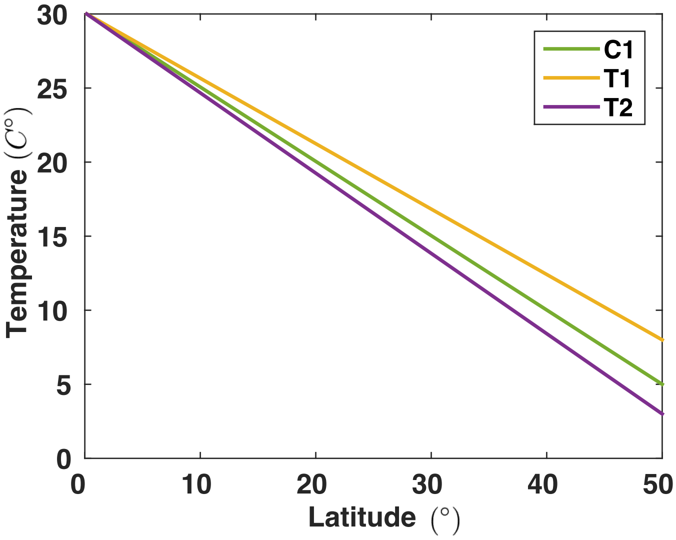

Figure 5.10: The steady temperature profiles which the models are restored to at the surface each month.

Identifier	Description	Temperature Range C°	Wind Forcing(A) N/m^2
C1	Control	5-30	0.2
T1	Cold Pole	3-30	0.2
T2	Warm Pole	8-30	0.2
W1	Weak Wind	5-30	0.15
W2	Strong Wind	5-30	0.25
V1	Red noise	5-30	0.2
V2	Periodic Wind	5-30	0.2

Table 5.2: The different parameters used in the baroclinic model based forcing experiments.

gyre regions (panels a and b). Moreover, in all regions, the spectra are white on interannual timescales. However, there are some important differences between the different forcing experiments. The time series of SSH anomalies in the jet region of the weak wind forcing experiment (WB1) has lower spectral power on interannual timescales than in the other experiments. There are also some differences in the amount of power in the subtropical gyre region near to the coast, with the red noise experiment (RN) displaying a higher proportion of power, than is seen in the control experiment (CB1). Conversely, the weaker magnitude forcing experiment (WB1) displays a lower spectral power on interannual timescales than is seen in the control experiment. However, in this region, the interannual variability only represents a small amount of the total power and therefore will likely have a modest impact on the system's total predictability.

The auto-correlations of the averaged SSH in the subtropical gyre regions in panels d and e show that the time series decorrelate rapidly (the time taken for the auto-correlation to reach a threshold value of 0.5), on time scales of only 20 days. However, in the jet region, the decorrelation times are longer, in the range of 50-100 days. This is to be expected as there is a more substantial proportion of spectral power on interannual timescales in the jet region.

The APTs of the system under different forcings is evaluated using 65 years of 10-day mean SSH model output. An upper summation limit of 500 days is used

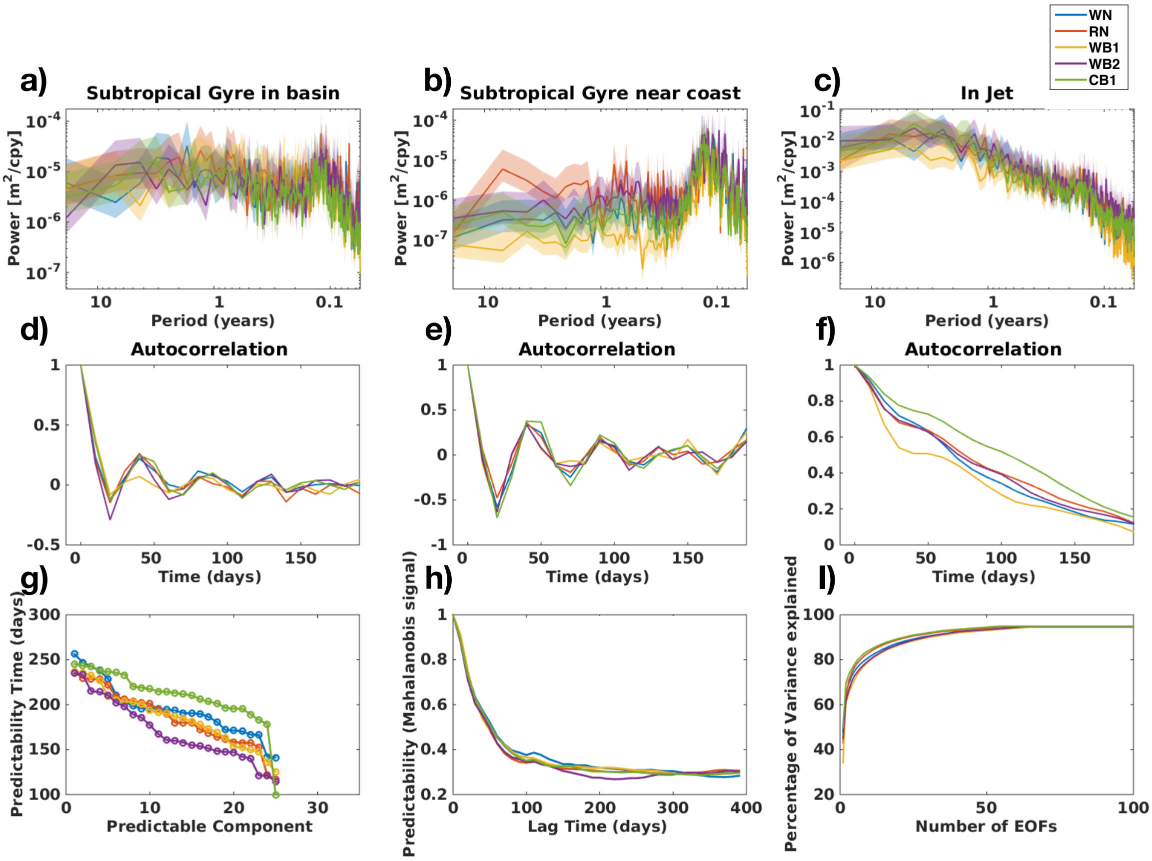

Figure 5.11: Power Spectra of the spatially averaged taken in the: a) subtropical gyre in the basin (dark grey), b) subtropical gyre near the coast (light grey), c) in the jet region (black), as shown in Figure 5.1a. The translucent regions show the 95%-confidence intervals of the power spectra, calculated using an inverse chi-squared distribution. The auto-correlation functions of the time series in the: d) subtropical gyre in the basin, e) subtropical gyre near the coast, f) in the jet region. g) The average predictability time (APT) for the first 25 predictable components. h) Predictability measured by the Mahalanobis signal (S_τ as defined in 2.35) of the whole system (blue line), created using linear regression models and the leading principal components required to explain 90% of the variance. i) The percentage of variance explained as a function of the number of EOFs.

to evaluate the predictability times (M in equation 2.45). In each evaluation, the number of EOFs retained corresponds to the number required to explain 90% of the variance in each experiment. The predictability times of the leading predictable components for each experiment, shown in Figure 5.11g, are in the range of 150-260 days. The leading predictable patterns in each experiment resemble the leading EOFs and represent variability in the meridional position of the zonal jet and variations in the zonal jet transport. These timescales are slightly longer than the decorrelation timescales of SSH in the jet region, which is indicative that non-local processes may play a role in forming the predictable components. The other predictable components have predictability times of < 100 days. These results show that even though interannual variability is present in the barotropic model experiments, it does not result in predictability on interannual timescales. Furthermore, each of the different external forcings results in only minor variations in the predictable components spatial patterns (not shown) and timescales. This is likely because of the fast adjustment timescales present in the barotropic model.

5.3.3 Baroclinic Gyre Response

Figure 5.12 panels a-c show that, in the baroclinic model, variations in the piecewise-steady wind and steady temperature forcings lead to changes in the variability of the system. The differences between the experiments are most apparent in the subtropical gyre (panel c), where there are different values of the spectral peak on periods of 2-10 years. The separations between the peaks on interannual timescales in the 'strong wind' (W2), control (C1) and 'hot pole' (T2) experiments is statistically significant. These spectral peaks correspond to the meridional shifting of the jets, as discussed in Section 4.3. The timescale of this shifting is longest in the 'weak wind' experiment (W1) with a timescale of of approximately 9 years. Conversely, this timescale is much shorter in the 'strong wind' experiment (W2) which has a spectral peak with a timescale of approximately 4 years. In the subtropical gyre region, there are notable differences in the amount of power displayed. The weak wind experiment has $< 10\%$ of the power contained in its peak as some of the other spectra, moreover, the power is lower on timescales with periods of $1 - 10$ years. In the jet regions, 5.12 panels a and b, the 'weak wind' experiment (W1) again has lower spectral power than the other experiments over the majority of frequencies. Moreover, the 'hot pole' experiment (T2) displays a higher amount of power in the jet region on timescales with periods of $1 - 10$ years. Subsequently, there are related differences in the autocorrelation timescales of these time series. Most of these decorrelate rapidly on times of less than 100 days. However, in the subtropical gyre and 'jet near coast' regions, the 'weak wind' experiment (W1) has shorter decorrelation timescales, decorrelating approximately 50 days faster than in the other experiments. The 'hot pole' experiment (T2) is seen to decorrelate in the jet regions on slightly longer timescales than those seen in the other experiments.

The APT is evaluated for each of the experiments using 65 years of 10 day mean SSH model outputs. The number of EOFs retained in each case are the minimum required to explain 70 percent of the variance. Moreover, an upper summation limit of 10 years is applied, when calculating the APT (M in equation 2.45). The predictable patterns found, are insensitive to this upper limit and in every experiment they resembled those seen in the control experiment (as seen in Figure 5.8), with the leading two predictable components in each experiment corresponding to the meridional shifting of the anomalous zonal jet. However, varying this limit did cause small changes in the APT of the predictable components of $\mathcal{O}(100 \text{ days})$. The average predictability times for the different forcing experiments are shown in Figure 5.12g. Although the weak wind experiment (W1) has a spectral peak occurring on the longest timescales, the predictability time of its leading predictable components are the shortest of all the experiments. This is because APT is a measure of the ratio of the forecast covariance matrix to the climatological covariance matrix. Even though the shifting occurs on longer timescales, it is less distinguishable from the climatology than in other experiments and therefore has a lower associated APT. This is seen in the power spectra in Figure 5.12c where the peak at 9 years is barely larger than the power on the nearby timescales. An entirely different behaviour is seen in the 'hot pole' experiment (T2). Here the majority of predictable components (1-10) all have longer predictability times than in the other experiments. In this experiment, the variability related to the Rossby wave type patterns are more separable from the systems climatology. Figure 5.12g shows the leading predictable timescales of the shifting are approximately 4-5 years. In all the experiments, apart from in T2, the other predictable components have far smaller predictability times (< 400 days). Figure 5.12h shows that the 'hot pole' system has the longest predictability times but there are only marginal differences in these predictability times between experiments, as the predictability of each system is dominated by the less predictable components, which have similar predictability times in each experiment (Figure 5.12g).

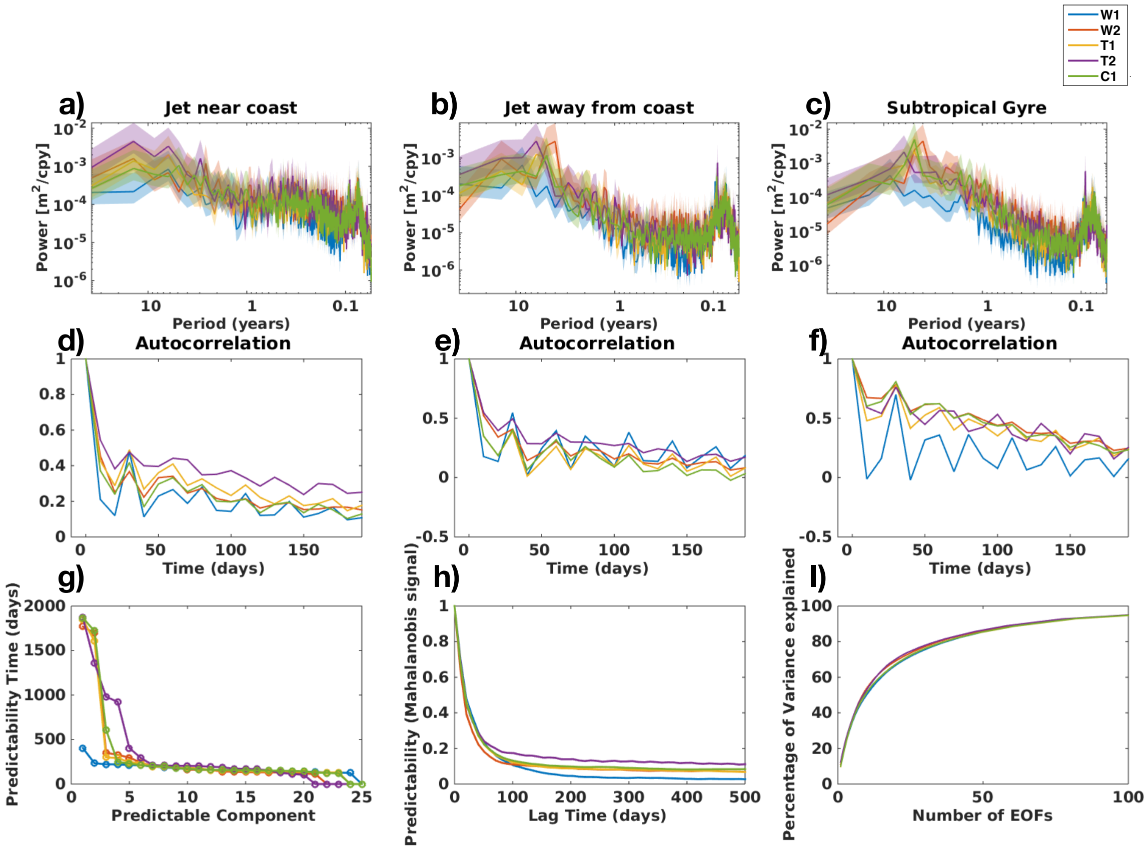

Figure 5.12: Power Spectra of the spatially averaged SSH taken in the: a) jet near the coast (black), b) jet in the basin (dark grey), c) the subtropical gyre (light grey), as shown in Figure 5.5a. The translucent regions show the 95%-confidence intervals of the power spectra, calculated using an inverse chi-squared distribution. The autocorrelation functions of the time series in the: d) jet near the coast, e) jet in the basin, f) in the subtropical gyre. g) The average predictability time (APT) for the first 25 predictable components. h) Predictability measured by the Mahalanobis signal (S_τ as defined in 2.35) of the whole system (blue line), created using linear regression models and the leading 25 principal components. i) The percentage of variance explained as a function of the number of EOFs.

5.3.4 Timescale Variation of the Meridional Migration of Zonal Jets

I will now explore why the timescales associated with the meridional jet migrations vary in the different forcing experiments. The anomalous jets migrate in the narrow latitude band, determined between 25°N, which corresponds to the midpoint of the restoring temperature profile, and 30 °N which corresponds to the zero wind stress curl zero line (Figure 4.13a). The meridional southward acceleration of anomalous jets in the mid-latitude regions is dominated by the tendency related to the baroclinic pressure gradient, as described in equation 3.35 given by

$$V_f = \frac{g}{r}\frac{\partial \int_z^0 \alpha_\theta(\overline{\theta} - \theta_r)dz}{\partial \phi}, \tag{5.7}$$

where α_θ is the thermal expansion coefficient and θ_r is a depth-dependent reference temperature. This term was previously found to be the largest tendency in the meridional momentum equation and always directed southwards, in the region of the observed meridional jet shifting (Section 4.3.1). Therefore if we assume it is the term which leads to the southward migration, we can write:

$$\frac{\partial \overline{v}}{\partial t} \propto \frac{g}{r}\frac{\partial \int_z^0 \alpha_\theta(\overline{\theta} - \theta_r)dz}{\partial \phi}. \tag{5.8}$$

An attempt will now be made to relate variations in V_f to variations in the time periods of the observed jet migrations. To do this, it is assumed that the meridional acceleration is a constant for a given experiment in the region of jet migration. Therefore it is possible to relate the timescale of meridional migration of the jet to the meridional acceleration using

$$S = v_0 t + \frac{1}{2}\frac{\partial \overline{v}}{\partial t}t^2 \simeq v_0 t + \frac{1}{2}A_0 V_f t^2, \tag{5.9}$$

where S is the meridional distance which the jet migrates over, v_0 is the initial meridional velocity of the jet (assumed to be zero), and A_0 is a constant. The acceleration is chosen to be the maximum of the modulus of the zonally averaged V_f in the latitudinal ranges of the jet migrations, which are shown in Figure 5.13a for the different experiments. The square root of the maximum jet acceleration should be inversely proportional to the timescales of the jet shifting as,

$$t \simeq \sqrt{\frac{2S}{A_0}\frac{1}{V_f}}. \tag{5.10}$$

The periods directly diagnosed from the model output (based on Hövmollers of SSH zonally averaged between 16°E-22 °E, at a latitude of 28°N) are compared to the timescales calculated from equation 5.10 and are shown in Figure 5.13b. The changes in timescales across experiment are in agreement by using the different methods. This suggests that the change in temperature gradients set the meridional migration timescales between experiments, driven by eddies as described in Section 4.3.1.

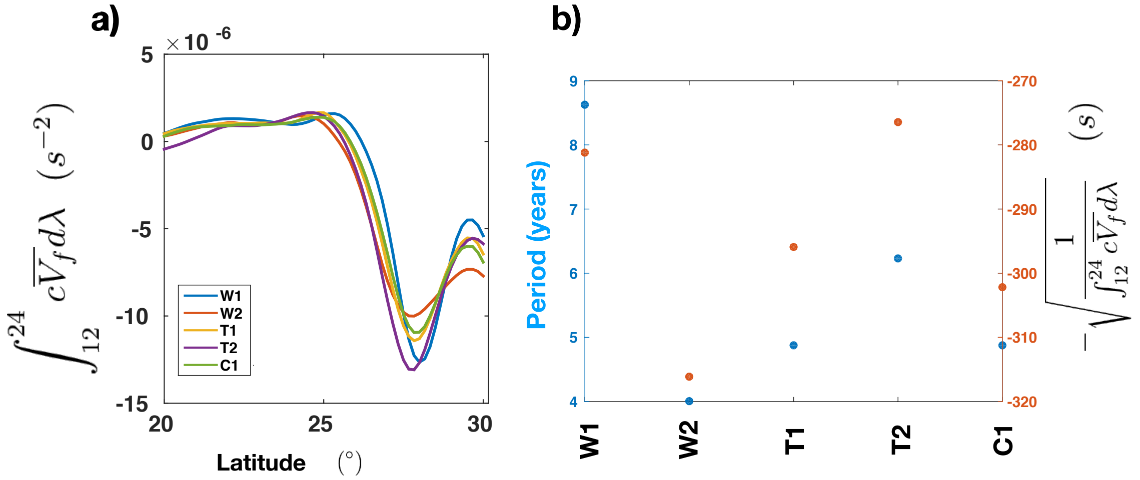

Figure 5.13: a) The spatially averaged time mean tendency due to the baroclinic pressure gradient V_f, zonally integrated between 12°-24°W (at 500m depth). b) The reciprocal of the square root of the maximum values of the modulus of zonally integrated V_f and the diagnosed timescales of the latitudinal migration of the jet. In these plots, c is a geometric factor corresponding to the reciprocal of the area of each grid box.

5.3.5 Interannual Timescales in Wind Forcing

Figure 5.14 shows the predictable component analysis of experiment V2, where the wind is forcing is given a perturbation which varies in latitude with a 20 month timescale. Such a variation acts to spin up/down the subpolar/subtropical gyres

(Häkkinen et al., 2011). These variations result in the large-scale predictable patterns (panels d-f). The leading predictable component (panel d) has a tripolar pattern which corresponds to a weakening or strengthening of jet and the two gyres. Interestingly, this gyre scale adjustment to a change in wind forcing is predictable on timescales of approximately 1500 days. A ocean adjustment timescale can also be diagnosed from the lead-lag relationship between the leading EOFs of the applied wind stress and the SSH (which resembles the leading predictable component shown in Figure 5.14d). This timescale is seen in Figure 5.9c, as the leading EOF of the SSH lags the leading EOF of the wind stress by approximately 100 days.

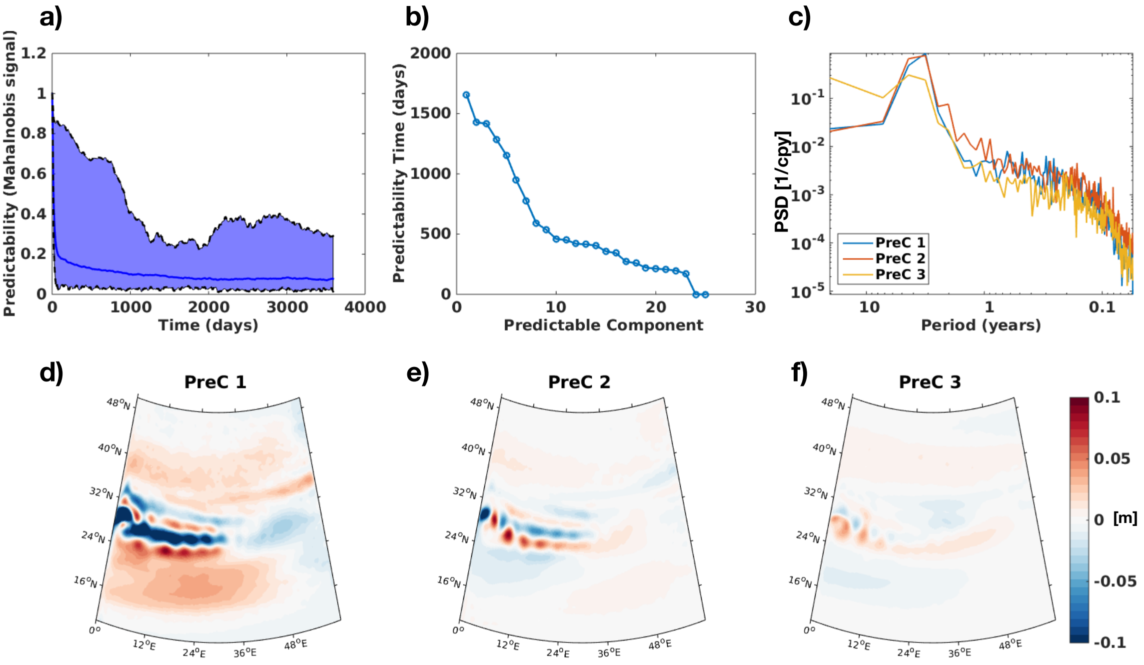

Figure 5.14: As in Figure 5.8 but for experiment V2.

The real NAO is not periodic and is almost white on interannual timescales. As a result, the form of the forcing used in experiment V1 is more similar to observations of wind stress than that used in V2. Figure 5.15 shows the predictable components of experiment V1. The results are similar to those found in the control experiment. However, several of the leading predictable component patterns are complex with multiple jet like anomalies and some features in the subpolar gyre. These variable forcing experiments are therefore indicative that low frequency variations in the wind forcings can lead to predictable interannual oceanic adjustments, which contribute to gyre-scale variations in SSH. The large-scale spatial structure of the applied wind forcing variability also significantly impacts the predictable patterns of SSH. Moreover, both experiments, V1 and V2, still display patterns which relate to the meridional jet shifting, therefore the inclusion of a time varying wind forcing does not prohibit such variability.

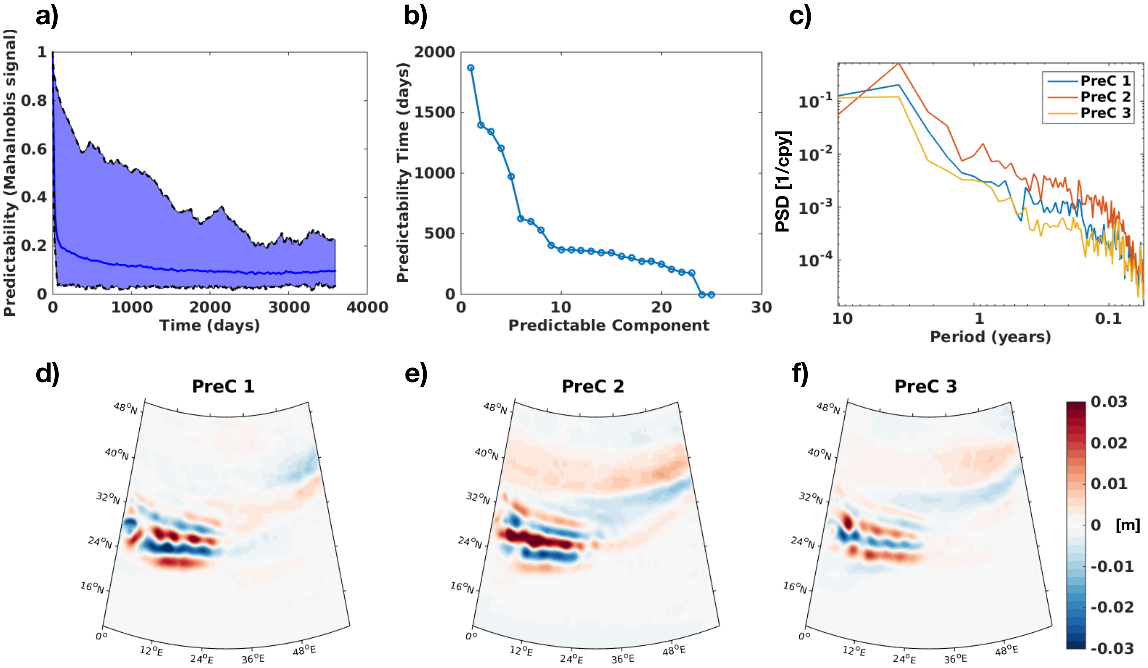

Figure 5.15: As in Figure 5.8 but for experiment V1.

5.4 Discussion and Conclusions

A combination of non-normal mode analysis and an assessment of average predictability time have been used to evaluate the intrinsic predictability related to the barotropic and baroclinic gyre systems. Despite the barotropic model, with a steady wind forcing, displaying interannual variability, the predictability associated with intrinsic mechanisms is relatively short, on the order of 200 days. The predictable patterns found are associated with variations in the meridional position of the jet and variations in the jet's transport. These results are in agreement with those presented by Giannakis and Majda (2012) as the predictable timescales of the system are longer than the correlation times of the leading principal components. The optimal initial conditions associated with the barotropic intrinsic variability are localised to the jet region and are spatially complex. It is hypothesised that this pattern is related to the onset of barotropic instability, triggering a flux of eddy momentum and a resultant shift in the jet's position 180 days later. This mechanism could be examined by initializing the model with the optimal initial condition and inspecting the eddy momentum budget through the subsequent amplification. Although this barotropic mechanism may be predictable, it is foreseen that it will be inherently difficult to observe and detect such small-scale complex structure in a highly eddy active region. This non-normal amplification could potentially aid forecasts of the state of the Gulf Stream, and is reminiscent of the optimal initial conditions calculated in studies which investigate transitions in the state of the Kuroshio (Wang et al., 2017; Zhang et al., 2017).

The baroclinic model, with a steady wind forcing, displays predictable components that act on interannual timescales (approximately 4-5 years). These components are related to the meridional shifting of anomalous zonal jets and the corresponding variability found in Section 4.3. Again, it may be difficult to observe such structures in observations, as they might be obscured by chaotic intrinsic variability. Several of the less predictable components (3 and 4) had structures and predictable timescales, similar to those of the leading predictable components in the barotropic model, indicating the importance of barotropic dynamics in the recirculation gyres (Waterman and Jayne, 2011). Neither of the models, with steady wind forcings, displayed any gyre-scale patterns of predictability. On the contrary, the interannual variability is localised mainly to the jet regions. Forecasts of intrinsic variability will therefore will most likely be affected significantly by initialization errors of small scale features occurring in a small area, near to the jet.

Irrespective of the applied steady external forcings, there are only modest changes in the variability present in the barotropic system. Therefore I hypothesize that the barotropic intrinsic mechanisms are only weakly affected by variations in the wind forcings, this again could be tested by diagnosing the eddy momentum fluxes in each experiment. In response to changes in the steady external forcings, the baroclinic experiments displayed variations in the timescales of the variability associated with the equatorward migration of the anomalous jets. This variation is attributed to changes in the baroclinic pressure gradient associated with the vertical eddy temperature fluxes. The introduction of a time-dependent wind forcing in the baroclinic model leads to gyre-scale predictable adjustments. It also resulted in a greater number of predictable components exhibiting interannual predictability. This alludes to the possibility that in a more complex model, with time-varying wind and buoyancy forcing, the ocean's predictable response may be on interannual timescales and possess gyre- or basin-scale predictable components. These potentially predictable baroclinic adjustments in the idealised model are shown to be sensitive to the spatial pattern of the wind forcing variability. This problem is complicated further as forced variability, superimposed on intrinsic variability, can display very different behaviour in response to seemingly small changes in the applied stochastic forcings timescales (Sura and Penland, 2002). These large scale forced components may also act to drive modes of intrinsic variability in the jet, as several studies have linked variability in the Kuroshio to impinging SSH anomalies influenced by large scale atmospheric modes of variability (Taguchi et al., 2007; Pierini et al., 2014). Moreover, such adjustments may lead to predictable changes in components of the jet's variability on interannual timescales (Qiu et al., 2014). Therefore this motivates the use of a more complex AOGCM in future predictability studies.

Chapter 6

Predictability and Variability of North Atlantic Sea Surface Height

6.1 Introduction

Increased understanding of the internal climate processes which drive interannual sea level variability, could lead to improved forecasts of sea surface height (SSH). Based on observations, Cabanes et al. (2006) found that the mechanisms which contribute to interannual SSH variability are regionally dependent, with the majority of the interannual variability controlled by both the local steric response to heat fluxes, and the large-scale oceanic adjustments to variations in the wind stress forcing. In previous model-based studies the SSH interannual variability in subpolar gyre has been found to be mostly buoyancy driven through variations in both thermosteric and halosteric SSH components, whereas in the subtropical gyre, variability is primarily driven by the momentum forcing and variations in the thermosteric SSH component (e.g., Roberts et al., 2016). In the Gulf Stream region, intrinsic ocean processes, including the effects of mesoscale eddies, are responsible for the majority of the SSH interannual variability present (Penduff et al., 2011). It remains uncertain on which timescales such intrinsic variability is predictable (Nonaka et al., 2016).

On interannual and decadal timescales, studies of the predictability of climate variables, such as sea level, can be separated into two distinct types. Studies of the first kind examine the predictability associated with internally generated components of the climate system. Such predictability is referred to as initial condition predictability. Studies of the second kind concern themselves with the externally forced components of the climate system, those which change due to variation in boundary conditions (such as variation in greenhouse gases, aerosols, and volcanic activity). As both of these distinct components act simultaneously in the Earth's climate system, it can be difficult to separate their relative contributions to predictability (DelSole, 2017). Moreover, the relatively short length of the observational record further inhibits the quantification of predictably on interannual timescales. These problems are simplified in the current study as we will make use of an extended model control run, without interannual variations in the model's boundary conditions. This should enable us to isolate any interannual predictability related to the model's internal variability.

Some key mechanisms, responsible for SSH predictability on interannual timescales, have been previously identified in both GCMs (Roberts et al., 2016) and observations (Cabanes et al., 2006). Roberts et al. (2016) looked at SSH variability using the Hadley Centre Global Environment Model version 3, HadGEM3 and found predictive skill in the Tropics on timescales of several years with a lack of skill in jet regions. Ensemble forecasts did not exhibit skill on 2-5 years that could beat persistence forecasts. The current study looks to build on the work of Roberts et al. (2016), by examining the sensitivity of forecasts to initial conditions and evaluating the most predictable components of SSH forecasts.

In this study, statistical methods are used to evaluate predictability generated through internal variability in a fully coupled climate model. A perfect model approach and a combination of LIM, non-normal mode analysis, and APT are used to evaluate how initial conditions influence error growth (Penland, 1989; Farrell and Ioannou, 1996; Hawkins et al., 2011; Zanna, 2012; Newman, 2013; DelSole et al., 2015).

The aims of this study are:

- To establish the timescales of predictability due to internal climate variability of SSH in the North Atlantic.
- To identify the regions where forecasts are most sensitive to perturbations in the initial conditions. Thereby, examining where it may be most constructive to take measurements to improve predictions.
- To relate any internally generated predictability to large-scale ocean characteristics, with an emphasis on both mid-latitude jets and the gyre circulations.

The predictability of SSH dynamics in the North Atlantic is investigated on interannual timescales using 150 years of output from a HadGEM3 control run. Based on experiments using Linear inverse modeling (LIM) and Average Predictability Time (APT), the SSH is shown to exhibit predictability on interannual timescales on the order of 1-2 years. Forecast skill is found to be highest in both the subtropical and subpolar gyres but reduced in the Gulf Stream extension region. The optimal initial conditions of SSH forecasts involve a tripolar anomaly off Cape Hatteras with the maximum growth in SSH occurring 20 months later. At this time, there is a meridional shift in the Gulf Stream position on the order of 0.5-1.5° in latitude, coupled with a change in SSH along the US east coast. The predictable components, calculated using the APT analysis, are responsible for changes in SSH, on the order of 10cm, along the US east Coast and meridional variations in the Gulf Stream's position. The dynamical mechanisms behind such predictability involve the interannual oceanic adjustment to both variations in the wind stress and the surface heat fluxes. The implications are that skillful interannual SSH forecasts are possible and are primarily dependent on the ocean's response to large-scale wind stress variability.

This chapter is organised as follows, Section 2 details the model set up and the interannual SSH variability present. Section 3 contains information on the statistical methods used to evaluate predictability and an investigation into the influence of eddy-mean flow interactions on forecast skill. Section 4 examines the predictability related to the initial conditions of the ocean model through both the optimal initial conditions of SSH and the predictable components. The final section contains a discussion of the results.

6.2 Interannual Sea Surface Height Variability in the North Atlantic in HadGEM3

6.2.1 Model characteristics

We use the output from a 150-year free-running control simulation of a coupled climate model, HadGEM3 (Williams et al., 2015). This control simulation has repeated-year radiative forcings (e.g., aerosols and greenhouse gases) taken from the year 2000 (identical to experiment 2 in the Coupled Model Inter-comparison Project 3, CMIP3). The ocean component of HadGEM3, GO5.0 is based on version 3.4 of NEMO and is on an ORCA025 horizontal grid, which uses an eddy-permitting 1/4° horizontal resolution and 75 vertical levels, with thicknesses increasing from 1m at the surface to 200m at depth (Megann et al., 2014). The North Atlantic domain analysed in this study is shown in Figure 6.1a. Monthly mean fields of SSH are used to define SSH anomalies, which are then used to create the statistical forecast models in Sections 6.3 and 6.4. In addition to these monthly mean fields, net heat fluxes and both the zonal and meridional wind stresses are used in Section 6.4.4 in the analysis of the mechanisms responsible for the predictable components. All the fields are detrended and have their seasonal cycles removed before being used.

6.2.2 Interannual Sea Surface Height Variability

Figure 6.1a shows the time-mean SSH of the control run. The characteristic double-gyre structure is evident, and the strong SSH gradient is indicative of the location of the Gulf Stream and its extension. The power spectra of SSH anomalies at several locations in the domain are shown in Figure 6.1b. The spectral power measured along the Gulf Stream (black and blue lines) is larger at all timescales than that within the gyre regions (red and green lines). The largest spectral power at interannual frequencies is near Gulf Stream's detachment point (blue line). The spectra taken in the vicinity of the Gulf Stream, display approximately red noise profiles up to timescales of 2-3 years with white noise profiles on longer timescales. This whitening indicates that the predictability of SSH in the Gulf Stream will be limited to timescales shorter than roughly 3 years. In contrast, the profiles taken in the subpolar and subtropical gyres (red and green lines), are red on all frequencies. This is indicative that skillful interannual SSH forecasts can potentially be made in these regions.

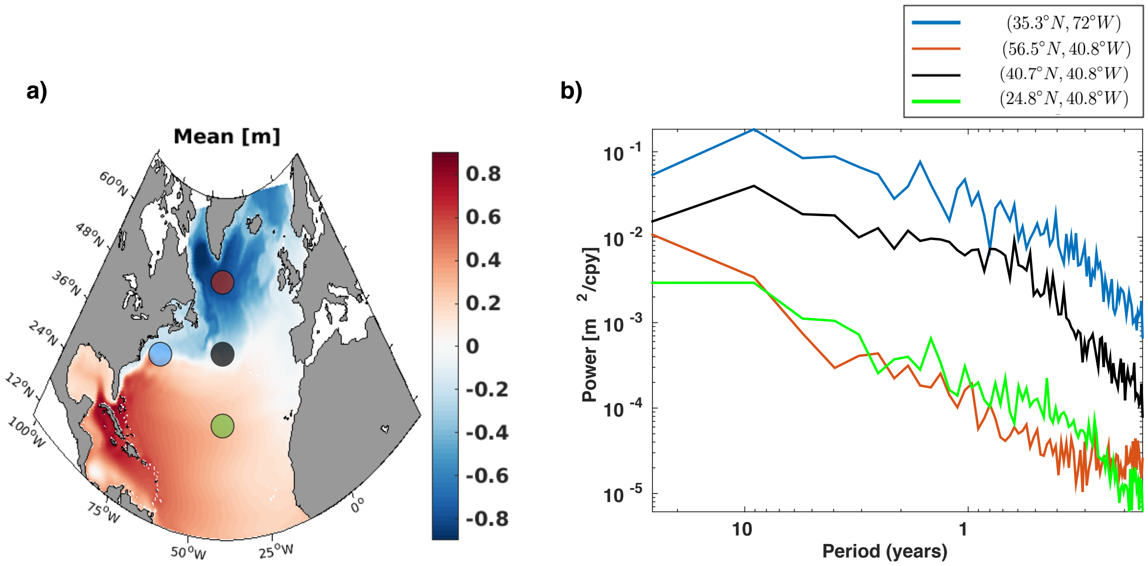

Figure 6.1: HadGEM3 150-year control run: a) Time mean SSH; b) Power spectra of SSH anomalies taken at the 4 locations in the North Atlantic as indicated in panel a: near the detachment point of the Gulf Stream (blue, 35.3°N,72.0°W), in the subtropical gyre (green, 24.8°N,40.8°W), in the Gulf Stream extension region (black, 40.7°N,40.8°W) and in the subpolar gyre (red, 56.5°N,40.8°W). The spectral power is in units of (m^2/cpy) where cpy denotes cycles per year.

Figure 6.2a shows the standard deviation of annual mean SSH anomalies. This again shows that most of the interannual variability is located in the vicinity of the Gulf Stream's extension and in the subpolar gyre. There are several potential mechanisms for such interannual variability in the Gulf Stream's extension, including: baroclinic Rossby waves directly interacting with the jet extension (Sasaki and Schneider, 2011; Qiu et al., 2014); variations in the western boundary currents due to changes in wind forcing (Andres, 2016); and interactions with the mesoscale eddy field (Spall, 1996; Berloff et al., 2007).

The signal to noise ratio of interannual variability in the North Atlantic is investigated by diagnosing the potential predictability (as introduced in section 5.2.1) $\frac{\sigma_N}{\sigma_1}$, where σ_N represents the standard deviation of N-year means of SSH. Regions with weak interannual variability (standard deviations < 0.02m) are masked (white regions in Figure 6.2 panels b and c). These regions of low variability are located along the western edge of the basin. The US east coast south of 45°N stands out as the only portion of coastline where any potential interannual predictability is present (Figure 6.2b-c). The largest potential predictability is located in the subpolar gyre. The dynamics of this region are likely to be relatively linear; dominated by mixed layer's response to forcing and mean advection, and not heavily influenced by the effects of turbulent mesoscale eddies. Figure 6.2a shows large values of interannual variability in the Gulf Stream extension, however, Figures 6.2b-c demonstrate that this considerable variability does not translate into potential predictability. This is indicative that most of the interannual variability along the Gulf Stream is likely chaotic, and therefore maybe unpredictable as suggested by the white profiles on interannual timescales in Figure 6.1b (black and blue curves).

6.3 LIM Forecast Analysis: Influence of Eddy Field Initialisation on Interannual Forecasts

An investigation of SSH forecasts is needed to evaluate the interannual SSH predictability. To do this, a Linear Inverse Model (LIM) is created using the method described in Section 2.2.2. The EOFs are constructed using monthly mean SSH model output. The EOFs are also weighted by the area of their grid boxes (as in Chung and Nigam (1999)). As this study focuses on the large-scale SSH predictability in the basin, the Gulf of Mexico is not included in this analysis. However, in analysis not shown, a large fraction of SSH in the variability in the Gulf of Mexico is related to the

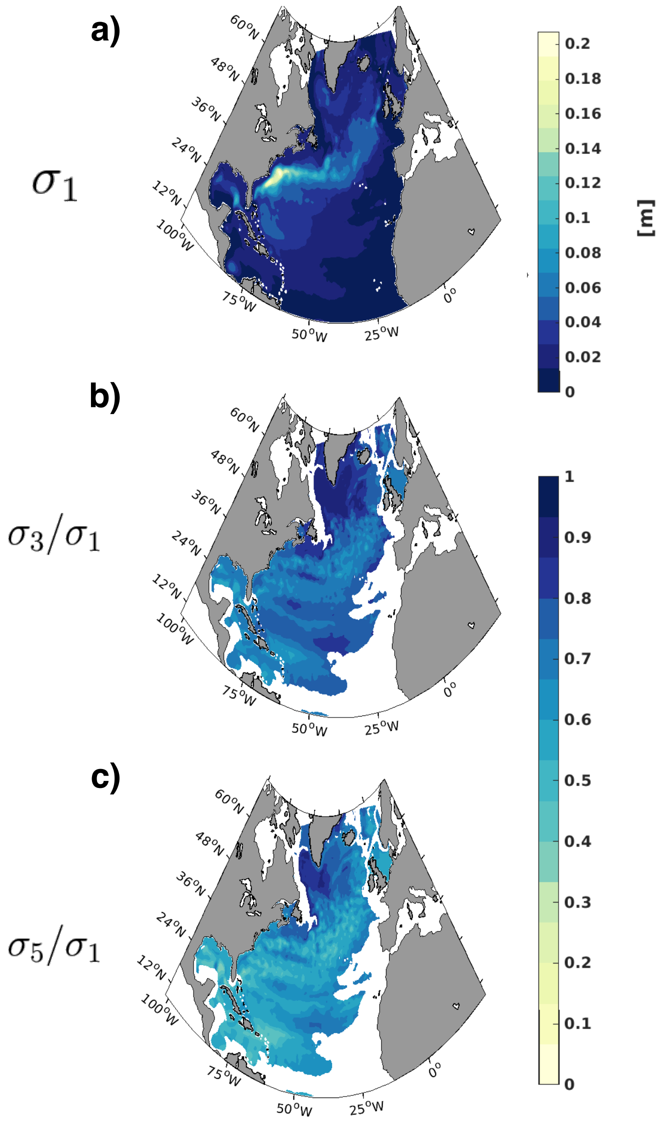

Figure 6.2: a) Standard deviation of SSH anomalies of the control run created with 1 year means. Ratio of standard deviations of the (b) 3 and (c) 5 year means to the interannual standard deviation.

separation of the Loop current.Moreover, the westward migration of eddies emanating from the loop current is seen to be a highly predictable event on timescales of ≈ 10 months.

In the following analysis we use 25 EOFs explaining 63% of the variance; the leading three EOFs (responsible for 9.9%, 5.2% and 5.0% of the variance, respectively) are shown in Figure 6.3. This ensures **A** (introduced in Section 2.2.2, equation 2.27) is representative of the variability of the system. The leading EOF has a spatial structure reminiscent to that calculated using observations (Hatun et al., 2005; Häkkinen et al., 2013). Häkkinen et al. (2011) attributed this pattern of SSH variability to variability in the wind stress curl. As the wind stress curl varies, there are associated variations in the strength and sizes of the subpolar and subtropical gyres and a resultant change in SSH. This 'gyre mode' varies between a state with a small subpolar gyre with a large eastward extended subtropical gyre and a state with a large eastward extended subpolar gyre with a small contracted subtropical gyre (Häkkinen et al., 2011). A similar variation and associated dependence on the wind stress curl has been identified in this model. Moreover, there is a lagged response of the first principal component of SSH to a leading principal component of the wind stress, again in agreement with Häkkinen et al. (2011).

The LIM models are constructed using only the SSH. For LIM to be applied, the system being examined has to possess several characteristics (Penland and Sardeshmukh, 1995):

- it can be described by Gaussian statistics;
- $\mathbf{A}$ is independent of the time lag, τ_0, used to calculate it;
- all real parts of the eigenvalues of $\mathbf{A}$ must be negative and therefore decay.

Tests to assess how well these conditions are met for SSH anomalies in the North Atlantic and are shown in Figure 6.4. Panel a shows a comparison of the cumulative density function of the 150 years of SSH anomalies with that of an idealised Gaussian distribution with the mean and variance of the model output. The agreement between the two profiles demonstrates that the system is well described by Gaussian statistics. To examine the influence of mesoscale eddies on the skill of the forecasts two different linear operators are constructed. In each experiment, the same reduced basis, consisting of 25 EOFs and PCs, is used to create each propagator. The first

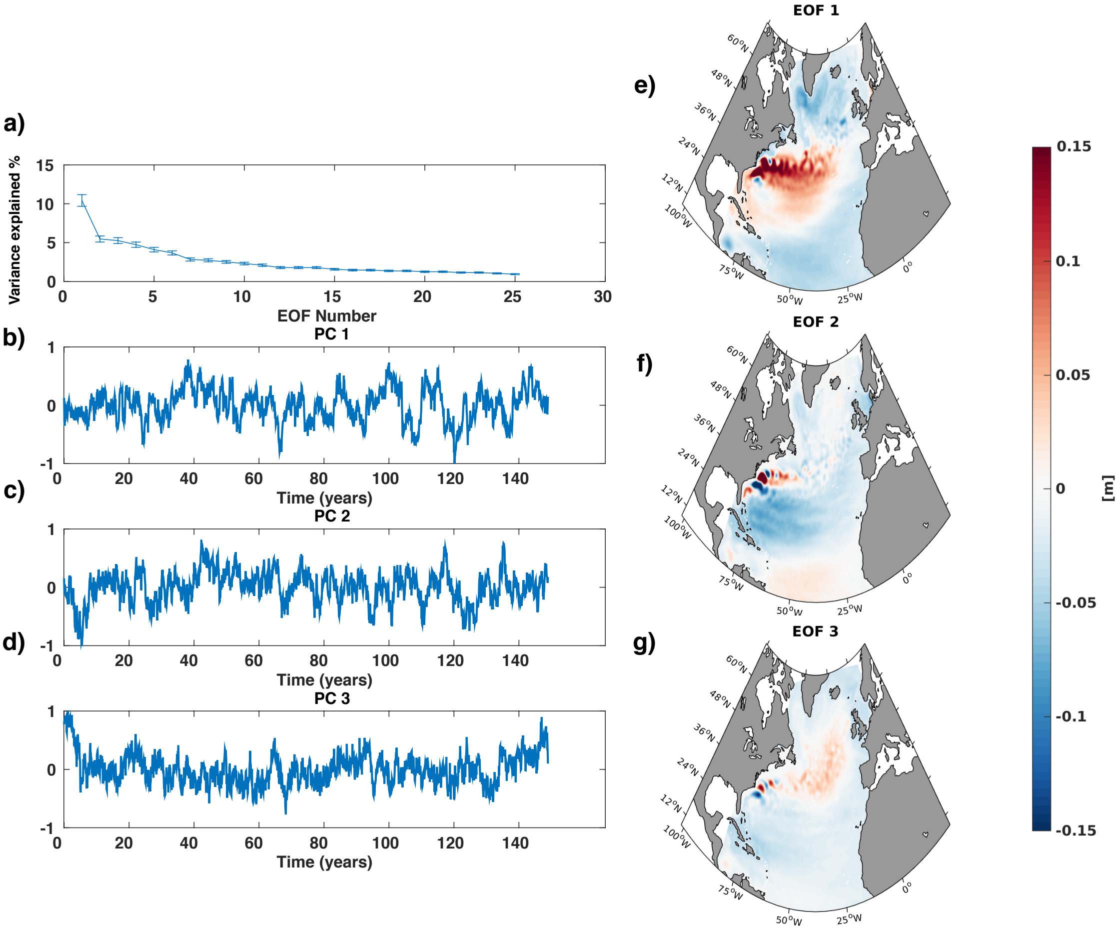

Figure 6.3: a) The fraction of variance each of the leading 25 EOFs explains, calculated from 150 years of monthly mean SSH model output. The error bars represent the one standard deviation error related to sampling (calculated using equation 24 in North et al. (1982)). Timeseries of the: (e) first, (f) second and (g) third principal components. The spatial components of the: (e) first, (f) second and (g) third EOFs.

propagator contains all available frequencies. A second temporally smoothed propagator is constructed by applying an 18-month running mean filter to the PCs. Figure 6.4b shows the Euclidean norm of **A** as a function of different lag times, τ_0, for these two operators. Both operators possess regions where the norm of **A** only varies by a small amount as a function of τ_0. When using the operator constructed with monthly means a τ_0 of 6 months is chosen and when using the smoothed operator a τ_0 of 2 months is used. In both cases, all the real parts of the eigenvalues of **A** are negative and thus satisfy the final necessary condition.

Using the successful LIMs, we can now create forecasts of SSH anomalies. En-

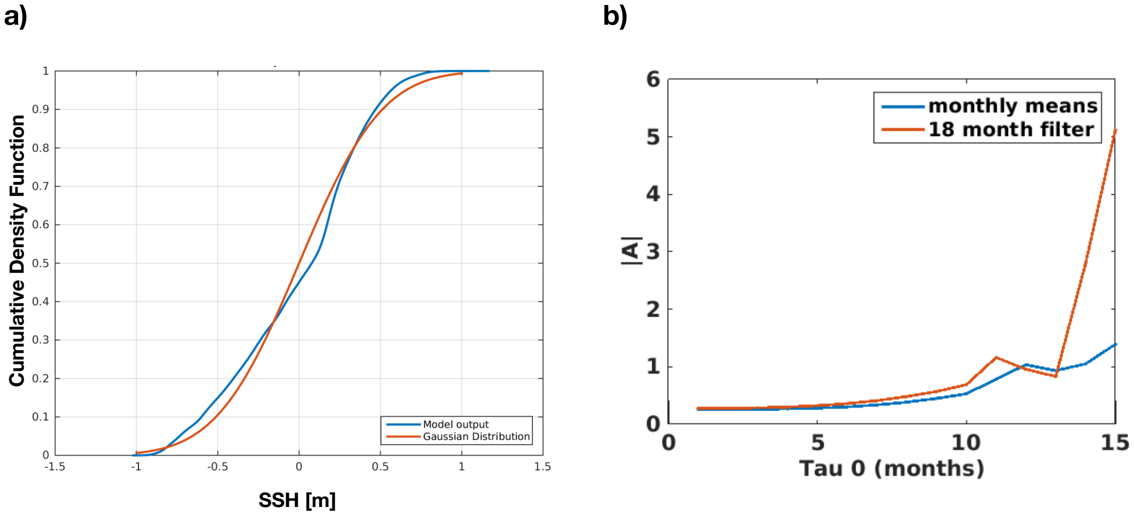

Figure 6.4: a) A comparison of the cumulative distribution functions of the monthly mean SSH model output and an idealised Gaussian distribution constructed using the mean and standard deviation of the SSH model output. b) The Euclidean norm of the operator **A** as a function of different lag times, τ_0. The two operators are constructed with monthly mean and 18 month filtered principal components respectively.

suring a difference between the training and test data sets is crucial. To do this, the LIM propagators are trained with the 140 years of model output, which is not within a ten-year window centered on the forecast initialisation date. Each model is then initialised every 6 months, to create sets of 300 forecasts. Lagged correlation forecasts are also made, using the method described in Section 2.2.2.1 (equation (2.20)), to create a benchmark for the forecasts made using the LIM models (Lorenz, 1963). The output used to construct these damped persistence forecasts is the same as that used to construct the LIM models. To evaluate the skill of the statistical models relative to climatological forecasts, we use a root mean square error metric ($RMSE_{Relative}$) defined as in Section 2.2.4 (equation (2.34), where the root mean square error of the climatology is constructed using the relevant EOFs and PCs). A value greater than unity indicates that the model's forecasts are inferior to those generated using the climatology, and a value of less than unity demonstrates forecast skill.

The forecast error maps for the LIM model trained on monthly data are shown in Figure 6.5 panels d, e and f. Errors emerge rapidly in the subpolar and subtropical

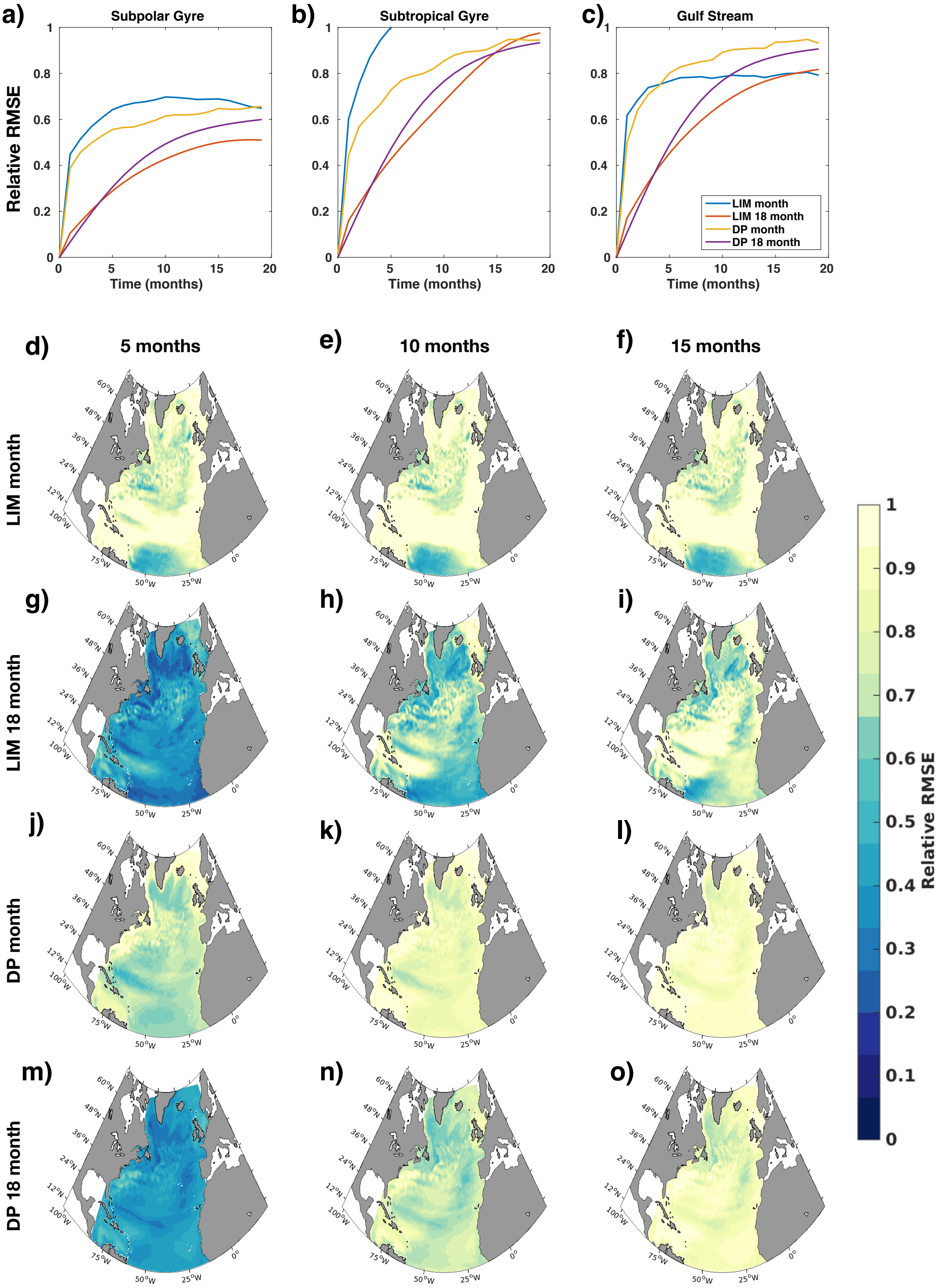

Figure 6.5: RMSEs relative to the climatology in three different regions all with longitudes $18-74^{\circ}W$: a) ‘Subpolar Gyre’, $46-65^{\circ}N$, b) ‘Subtropical Gyre’, $18-37^{\circ}N$, c) ‘Gulf Stream region’, $37-42^{\circ}N$ created using both LIM and damped persistence models. Two differing temporal smoothings are used to construct these models shown, monthly mean (blue and yellow), and monthly means with an 18-month running mean applied (red and purple). The remaining panels show maps of relative RMSE at given lead times. Forecasts made using the LIM model trained on: (d,e,f) monthly means and (g,h,i) 18 month temporally smoothed principal components. Forecasts made with damped persistence models constructed with: (j,k,l) monthly means and (m,n,o) an EOF reconstruction made with 18 month temporally smoothed principal components.

gyres. Only in the Gulf Stream region and southern part of the domain are any areas of skillful forecasts seen. The damped persistence forecasts created with the monthly mean model output (panels j, k, and l) exhibit small errors in the subpolar gyre and parts of the subtropical gyre, coinciding with regions of large potential predictabilities (Figure 6.2). The forecasts created with the LIM model trained on monthly mean SSH anomalies are less skillful than those produced with the damped persistence model. The inclusion of the high-frequency components of the SSH in the construction of the LIM model means that predictably is not exhibited on timescales longer than a year.

The error maps which are subject to 18-month filtering produce smaller errors in all regions (Figure 6.5, panels g-i, and m-o). These models again display the smallest relative RMSEs in the subpolar and subtropical gyres, with more substantial errors in the Gulf Stream region. The LIM model outperforms the damped persistence forecasts in the majority of areas and timescales (the exception being in the subtropical gyre). The subpolar gyre emerges as the region with the largest amount of predictability, on timescales longer than a year (panel i). The US east coast stands out as the only section of coastline which borders a region with forecast errors of less than 0.8 on interannual timescales. On lead times more that five months the 18-month filtered LIM provides more skillful forecasts relative to the damped persistence forecasts. This is indicative that the information retained in the cross correlation matrices used to construct the LIM model aided in creating skillful forecasts. As the removal of the high-frequency SSH anomalies reduces the errors in interannual forecasts, it is hypothesised that future modeling studies, at higher spatial resolutions, are unlikely to exhibit improved skill in the mid-latitude Gulf stream region. These results are in agreement to those found by Nonaka et al. (2016), where a lack of any predictability, on timescales longer than a few months, was also found in the Kuroshio.

6.4 Predictable Patterns: Optimal Initial Conditions and Average Predictability Time

The spatiotemporal structure of the predictability can also be analysed by explicitly identifying any patterns which are predictable on interannual timescales. Two methods are now used: (1) an examination of the growth of optimal initial conditions leading to a maximum increase of variance and (2) a decomposition of the system into predictable components, ranked by their relative contributions to the total average predictability time present.

6.4.1 Optimal Initial Conditions

When the operator $\mathbf{A}$ is non-normal, i.e. $\mathbf{A}\mathbf{A}^{\mathbf{T}} \neq \mathbf{A}^{\mathbf{T}}\mathbf{A}$, it is possible for the eigenmodes of the system to interact and give a large amplification of variance at a finite-time (Farrell and Ioannou, 1996). The SSH anomaly growth at time τ by non-normal eigenmode interference is given by equation (2.33) in Section 2.2.2. The longest timescale on which this growth occurs can be thought of as an optimistic upper bound on the predictability of linear events without forcing. In this section, the LIM constructed using 18 month temporally smoothed principal components is used as it exhibits skillful forecasts on interannual timescales.

The curve depicting the growth of SSH anomalies, $\mu(\tau)$, is shown in Figure 6.6a. The perturbations can grow through non-normal interactions on time scales of up to 100 months, with the maximum growth occurring at 20 months. The optimal initial condition pattern in SSH, which leads to the largest growth in SSH anomalies after 20 months, is shown in Figure 6.6b. This pattern has a very weak gyre scale tripolar pattern, reminiscent of EOF 1 (shown in Figure 6.3e). The pattern has two main notable features, a smaller scale tripolar structure off Cape Hatteras (situated at 32.5°-42.5°N, 67°-74.55°W, shown by the green ellipsoid in panel e) and a single sign SSH anomaly along the US east coast (black ellipsoid, panel e). The propagated optimal initial condition is shown in Figure 6.6, panels c and d, at 10 and 20 months,

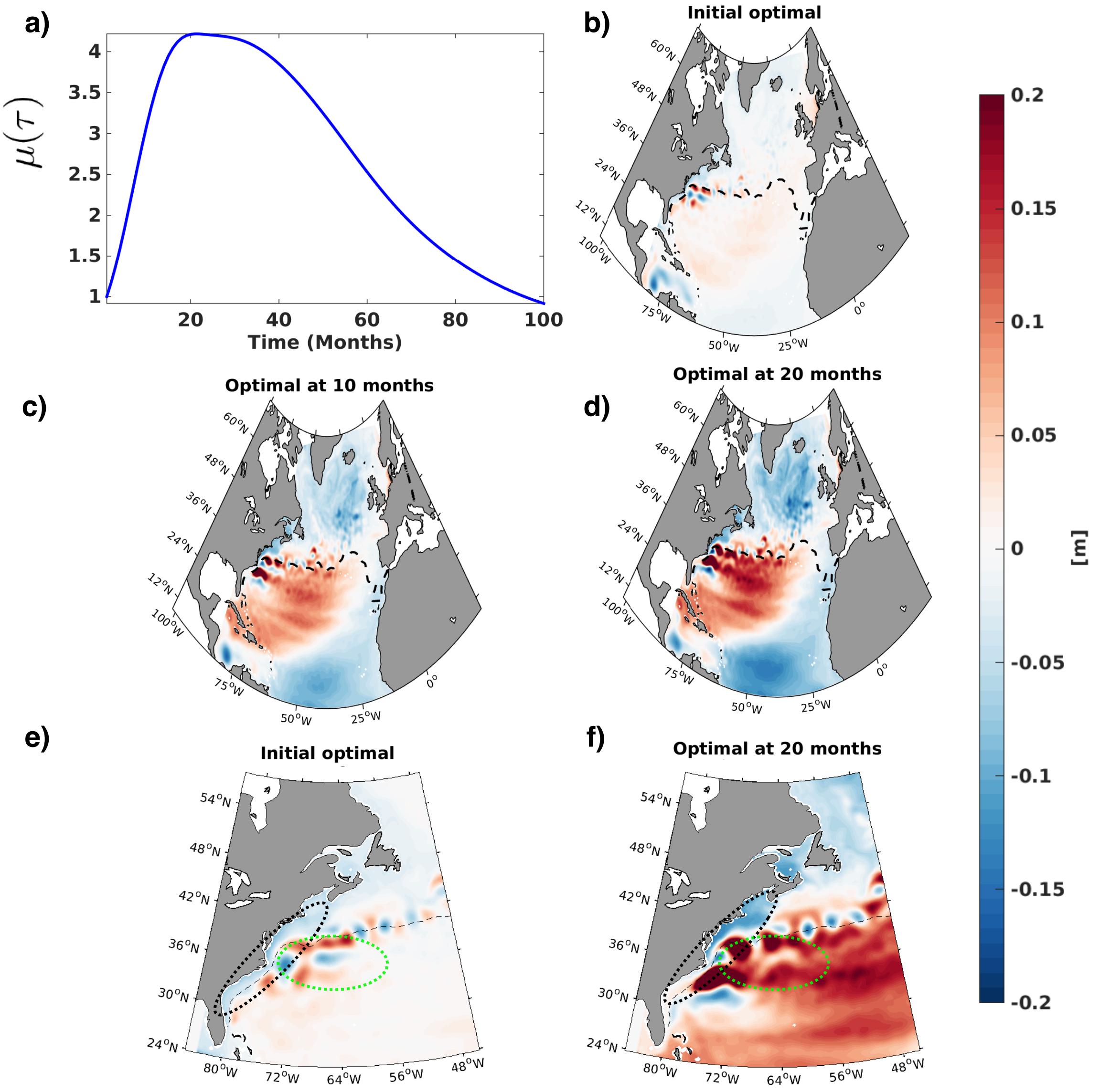

Figure 6.6: a) The maximum amplification curve (eq. 2.33). b) The optimal initial condition with a tripolar pattern. c) The optimal at 10 months. d) The optimal at 20 months, it's state of maximal growth. e) The initial optimal in just the area bordering the US east coast. f) The optimal at 20 months in just the area bordering the US east coast. The black and green dotted ellipsoids indicate regions which were correlated with monthly means from the model output. The ellipsoids are characteristic anomalies described in the text. The black dotted lines indicate the 0m contour in the time mean SSH.

respectively. After 10 months, the SSH anomaly along the boundary no longer has a single sign. There is also an increase in SSH along the path of the Gulf Stream and in the subtropical recirculation gyre. After 20 months, an SSH anomaly grows

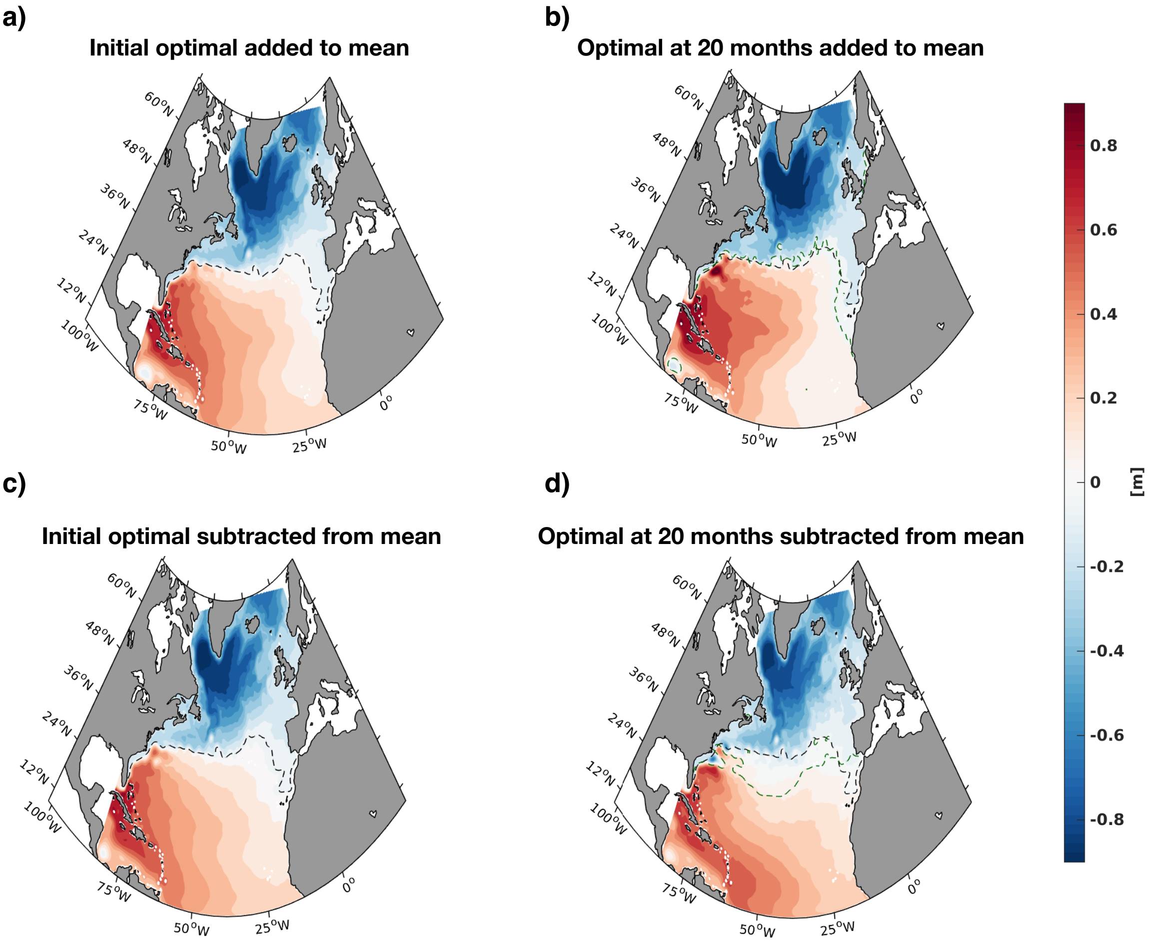

Figure 6.7: a) The initial optimal added to the mean field. b) The initial optimal propagated forward in time by 20 months added to the mean field. c) The negative version of the initial optimal added to the mean field. d) The negative version of the initial optimal propagated forward in time by 20 months added to the mean field. The black dotted lines indicate the 0m contour in the time mean SSH. The green lines denote the SSH 0m contour when the optimal initial condition of double the magnitude of that shown in Figure 6.6b evolves, after 20 months.

along the Gulf Stream path, and its magnitude is seen to double. The magnitude of SSH in the subpolar and subtropical gyres is also seen to increase significantly. The SSH anomaly along the US east coast (black ellipsoid) approximately doubles in magnitude, in 20 months, as the as the optimal initial conditions are propagated. This growth is approximately 5cm in magnitude for an initial condition of the magnitude shown in Figure 6.6b. One interpretation of these optimal initial conditions is that it is especially important to constrain the position of the Gulf Stream separation in the

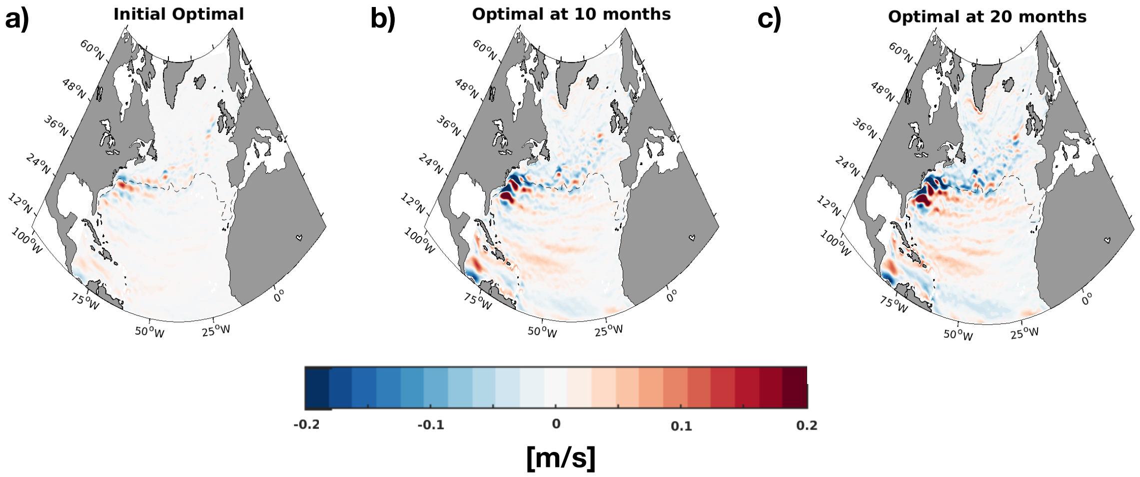

Figure 6.8: Anomalies in the zonal geostophic velocities calculated from the SSH of: a) the initial optimal, b) the initial optimal propagated 10 months forward in time, c) the initial optimal propagated 20 months forward in time (All with the same magnitudes as the patterns shown in Figure 6.6).

initial conditions as initial errors in this region lead to gyre-scale errors within 10-20 months. However, it is also possible that it is the weaker gyre-scale pattern present in the optimal initial conditions which leads to this growth, as SSH anomalies can be integrated by the gyre circulation on interannual timescales.

Figure 6.7 shows the positive optimal initial condition (of the same magnitude as that shown in Figure 6.6b) and its evolution after 20 months when it is added to the mean SSH field. It also shows the negative version of the optimal initial condition added to mean field, which is an equally valid solution since the evolution is linear. The initial and propagated version of the positive optimal initial condition, Figure 6.7, panels a and b, demonstrates an increase in strength of the subpolar gyre, as well as an increase in the SSH gradient across the Gulf Stream. The change in the SSH gradient is linked to variations in the geostrophic transport along the Gulf Stream path, shown in Figure 6.8. The resultant geostrophic velocity anomalies act in different directions in the two gyres and are particularly evident in the subtropical gyre. The SSH 0m contour is also seen to be shifted to a higher latitude. However, this is a marginal effect as shown by the contours in panel b (less than a degree in latitude, for an initial perturbation with double the magnitude of that shown in Figure

6.6a). The evolution of the negative optimal initial conditions, shown in Figure 6.7c-d, demonstrates an increase in SSH along the US east coast North of Cape Hatteras, as well as a southward shifted Gulf Stream detachment point. The SSH gradient across the Gulf Stream is also lower, indicating a decrease in Gulf Stream transport. Panel d shows that the SSH 0m contour's position can move significantly southward (approximately 5°in latitude, for an initial perturbation with double the magnitude of that shown in Figure 6.6a) and that the subtropical gyre contracts to the west of the basin. The initial conditions associated with timescales (τ) ranging from 10 to 30 months are also calculated and compared to the optimal calculated at the maximum amplification time. The spatial correlation between these initial patterns are found to be at least 0.8, and the patterns behave in a qualitatively similar manner when propagated in time. The optimal initial conditions, calculated from similar models with differing numbers of EOFs, exhibited small-scale (1/2°) spatial differences in the Gulf Stream's extension, however the signal along the US east coast and the tripolar pattern appear robust. Moreover, the propagated optimals all resemble that shown in Figure 6.6d.

6.4.2 Optimal Initial Conditions Occurring in the Model Output

It is important to determine how often the optimal initial conditions and their evolved patterns are realised in the model output. Figure 6.9a, shows the projections of the initial states on the model output, as well as the projections of the evolved initial conditions 20 months later. Projection here refers to either the product of the principal component values of the EOF reconstruction of the model output with the principal component values of the initial states or the product of the principal component values of the propagated states with the principal component values of the EOF reconstruction 20 months later. The growth in these projections is seen to be close to that predicted by the maximum amplification curve (Figure 6.6a). Monthly mean anomalies which exhibit the tripolar feature, seen in the optimal initial condition, are identified by calculating the spatial correlation of the tripolar feature and the SSH anomalies in that region (the green ellipsoid in 6.6e). Spatial correlations which were greater than 0.8 were retained. Out of the 1800 SSH anomaly monthly means comprising the model output, 404 were found to display a tripolar anomaly structure off Cape Hatteras. After 15-20 months from those 404 tripolar anomaly patterns, 310 (≈ 77%) lead to SSH anomaly growth along the US east coast (as in Figure 6.6f, green ellipsoid). About 140 (out of 310) also display a change in sign of SSH along the coast (as in Figure 6.6f, black ellipsoid). Therefore 103 SSH anomaly growths result from the 404 tripolar initial states (≈35%). This suggests that there is some skill in the prediction of such growth events from the Gulf Stream characteristics, however, it is also indicative that SSH anomaly growth along the US east coast depends on signals other than just SSH in the Gulf Stream.

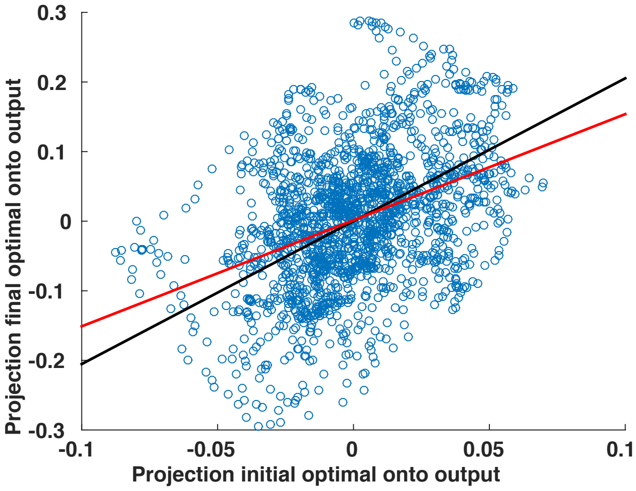

Figure 6.9: Projections of the initial and final states on the model output. The black line is a linear fit to these projections, and the red line is a line with a slope corresponding to $\mu^{1/2}$ ($\tau = 20$ months).

6.4.3 Average Predictability Time

We complement the analysis of the optimal patterns, which depends on the target timescale, by examining predictable patterns that persist over all timescales, and are therefore the most predictable over a range of target times (DelSole and Tippett, 2007). This is done by calculating the APT with the method described in Section 2.2.4.2.

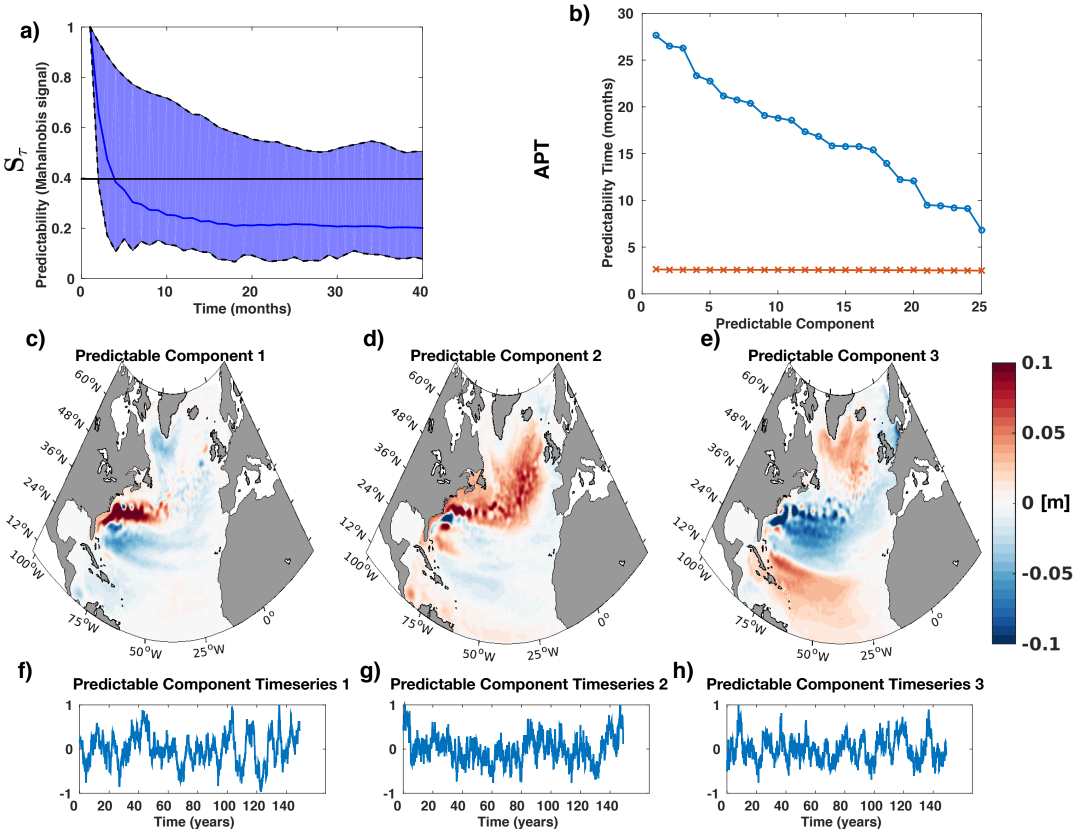

Figure 6.10: a) Predictability measured by the Mahalanobis signal (S_τ as defined in equation 2.35) of the whole system (blue line), created using linear regression models and the leading 25 principal components. The envelope denotes the spread in predictability measured by the Mahalanobis signal (S_τ) for each of the leading predictable components. The solid black line is representative of 5% significance level calculated using a student's t-test. b) The average predictability time (APT) for the first 25 predictable components. The orange line indicates the 5 % significance level estimated using the Monte Carlo method discussed in Section 2.2.4.2. The spatial patterns of the (c) first, (d) second and (e) third predictable components ($\mathbf{p}$), ranked in order of their values of APT. The associated time series for the (f) first, (g) second and (h) third predictable components ($\mathbf{q^T P}$).

Figure 6.10a shows that the predictability of the SSH of the whole system, measured by the Mahalanobis signal (solid blue line), diminishes rapidly, reaching a value of approximately 0.2 after 10 months. This is in approximate agreement with the timescale found in the LIM study. However, Figure 6.10a (blue shaded region) also shows that several of the individual components of the system have Mahalanobis signals which decay on longer timescales. The APT of the leading 25 predictable components shown in panel b, confirms that several components demonstrate predictability on timescales longer than 2 years. The three leading predictable components (those which have the largest values of APT) have average predictability times of 26-28 months. The corresponding spatial patterns of the leading three components are shown in panels c, d, and e. The pattern which is associated with the largest value of APT (panel c) has large values in SSH in both the subpolar gyre and jet extension region. The second pattern (panel d) is localised mainly to the US east coast and Gulf Stream extension region, whereas, the third pattern (panel e) is similar to the evolved optimal initial conditions (Figure 6.6), and EOF1. The time series related to each of these spatial patterns, shown in panels f, g and h, all display interannual variability and have autocorrelation times of 30-60 months.

The similarities between the third leading predictable component, the evolved optimal initial conditions, and EOF1 indicate some robustness of the constructed predictability patterns. The time series associated with the third predictable component correlates strongly with the leading principal component at zero lag. The leading predictable patterns (1 and 2) are not merely EOF1, highlighting that the mode capturing most of the variance is not necessarily the most predictable.

6.4.4 The Influence of Atmospheric Forcings on the Predictable Components

The steric component dominates interannual variability in SSH in the North Atlantic. Roberts et al. (2016) confirmed that this is also the case in HadGEM3 and that it is the thermosteric and wind-driven components which contribute most to the interannual variability in the subtropical gyre. In the subpolar gyre, the variability is caused by both the thermosteric and halosteric components and is dominated the response of the ocean to variations in the buoyancy forcings. Furthermore, in the Gulf Stream region, the intrinsic effects are also important.

Attempts are now made to establish the dynamical origin of the predictable patterns by examining their relationships with fields relating to the wind and buoyancy driven circulations, namely the Ekman components of SSH and the net heat fluxes. The interannual variability detected is likely related to the oceanic adjustment to variations in these forcings. The wind-driven turbulent heat fluxes dominate the net heat fluxes, so the effects of these forcings are closely linked. The net heat fluxes contribute to the thermosteric buoyancy forced component of SSH, and the wind stresses contribute to the steric advective components.

The SSH, meridional and zonal wind stress fields are used to decompose the ocean currents into the associated geostrophic $\mathbf{u_g} = (u_g, v_g)$ and Ekman components $\mathbf{u_e} = (u_e, v_e)$,

$$\mathbf{u} = \mathbf{u_g} + \mathbf{u_e}. \tag{6.1}$$

The Ekman components are calculated from,

$$v_e = -\frac{\tau_s^x}{f\rho_0 d_{Ek}} \quad \text{and} \quad u_e = \frac{\tau_s^y}{f\rho_0 d_{Ek}}, \tag{6.2}$$

where f is the Coriolis parameter, τ_s^x and τ_s^y are the zonal and meridional components of the wind stress, $\boldsymbol{\tau_s}$, at the ocean's surface. The density, ρ_0, and the Ekman depth, d_{Ek}, are taken to be constants of $1000 kg/m^3$ and 100m (a typical value in the Subtropical gyre in the winter (Stommel, 1979)), as most of the variability in the Ekman velocity component is due to variations in the wind stress. The Ekman pumping velocity is also calculated as

$$w_e = \frac{1}{f\rho_0}(\nabla \times \boldsymbol{\tau_s}), \tag{6.3}$$

and the geostrophic currents are calculated as

$$v_g = \frac{g}{af cos\phi}\frac{\partial\eta}{\partial\lambda} \quad \text{and} \quad u_g = -\frac{g}{af}\frac{\partial\eta}{\partial\phi}, \tag{6.4}$$

where η is the monthly mean SSH, a is the radius of Earth, ϕ is latitude, λ is longitude and g is gravity.

These fields and the net heat fluxes are then regressed against the normalized time series of the three leading predictable components (Figure 6.10). The fields are smoothed with 6 months running mean before regression, to focus on the interannual variability. The regression coefficients of the geostrophic currents and the first predictable component are shown in Figure 6.11. The regression coefficients with SSH are also shown as contours. These show a westward propagation of SSH in the subtropical gyre. The meridional geostrophic velocities have large regression coefficients with the leading predictable component, in the subpolar gyre along the Canadian east coast. At times where the current is leading the predictable component time series, there is also a positive signal at the Gulf Stream's detachment point. The lack of a clear lead-lag relationship here makes causality hard to distinguish. However, from these strong correlations, it is apparent that there is significant interannual predictability present in the western boundary current in the subpolar gyre. There is a lack of any apparent changes in the large-scale patterns of the zonal geostrophic current regression coefficients. These coefficients are large in the subtropical gyre and in the Gulf Stream region. The regression coefficients relating to the net heat fluxes have a sizeable dipolar pattern in the Gulf Stream region at all times. However, in the east of the Subpolar gyre, a signal appears only at lead times.

The regression coefficients of the leading predictable component with the Ekman currents are shown in Figure 6.12. There is an apparent time-lagged relationship present, with variations in the Ekman currents leading the predictable component strongly on timescales of up to 15 months. The Ekman currents are associated with the large-scale Sverdrup transport, within the wind-driven gyres. These regression coefficients imply that wind-driven variations in the gyre circulations lead to a predictable change in SSH on interannual timescales. The associated changes in gyre scale variations of the Ekman currents translate to variations in SSH in the Gulf

Stream extension and subpolar gyre regions. Such adjustments may happen at low latitudes via baroclinic Rossby basin modes. This result is also indicative that interannual forecasts of SSH can be improved by better representing the zonal and meridional wind stress fields, on longer than monthly timescales.

It is difficult to discern anything about the variability of the time-lagged geostrophic regression coefficients and predictable component 2 (Figure 6.13). However, there is a signal in the regression coefficients of the net heat fluxes which leads the predictable component by 8-15 months. This signal is located in the Gulf Stream extension region. The regression coefficients relating to the zonal and meridional Ekman components (Figure 6.14 top and middle rows) also strongly lead the predictable component and are related to changes in the wind stress in the east of the North Atlantic and the subpolar gyre.

The third predictable components regression with the Ekman components demonstrate a clear lead-lag relationship (Figure 6.16). The Ekman components are seen to lead variations in the predictable component. The patterns of the regression coefficients are large scale and sizeable in the west of the basin. The meridional components of the Ekman currents can be interpreted as causing a convergence or divergence of SSH in the Gulf Stream region as the gyres react to changes in the wind stress. There are also variations in the net heat fluxes in the subpolar gyre, which lead a change in the predictable component (Figure 6.15).

Therefore it is concluded that predictable component one is largely a response to variations in the wind in at the latitudes of the Gulf Stream. Predictable component two is due to variations in both the net heat fluxes and the wind stress in the subpolar gyre and in the Gulf Stream Extension region. Finally, predictable component three is due to the oceanic adjustment resulting from a combination of both variations in the wind stress in the subpolar gyre and east of the ocean basin, and the response to variations in the net heat fluxes in the subpolar gyre. All three patterns show that changes in the atmospheric forcings lead large-scale predictable patterns of SSH.

Even though the variations in the wind stress and net heat fluxes are unpredictable at times longer than a few months, the oceans adjustment to them appears to be predictable on timescales of approximately 1-2 years.

6.5 Discussion and Conclusions

This chapter has presented an investigation into the predictability of the interannual SSH variability in the North Atlantic, using the eddy-permitting coupled climate model HadGEM3. This interannual variability is mainly located in the Gulf Stream extension region, which is consistent with other modeling (Penduff et al., 2011) and observational studies (Fu, 2004). The timescales of predictability of SSH in the North Atlantic were derived using linear statistical forecasts trained on output from the HadGEM3 control run. The statistical linear inverse model (LIM) provides a computationally inexpensive way of quantifying the linear predictability of the system. The forecasts displayed skill in both the subpolar gyre and along the west coast of the Atlantic basin on times of up to 20 months. However, the forecasts were less skillful in the Gulf Stream extension region. Temporal filtering was used to isolate the effects of the mesoscale eddies on the forecast errors. The eddies were seen to degrade forecast skill, the hypothesised improvement due to the potential for mesoscale eddies to drive variability on interannual timescales is not observed. The results were in agreement with previous modeling studies, which have found timescales of SSH predictability in the Gulf Stream region of the North Atlantic to be limited to a few months, due to the nonlinearities present (Nonaka et al., 2016; Roberts et al., 2016). However, in the subpolar gyre and in areas of the subtropical gyre significant predictive skill was found on timescales over a year.

The patterns of predictability present in the system were then calculated using two separate methods. Non-normal mode analysis was used to identify the optimal initial conditions leading to the largest future growth of SSH anomalies. The optimal initial condition had two major features, a tripolar pattern occurring where the Gulf

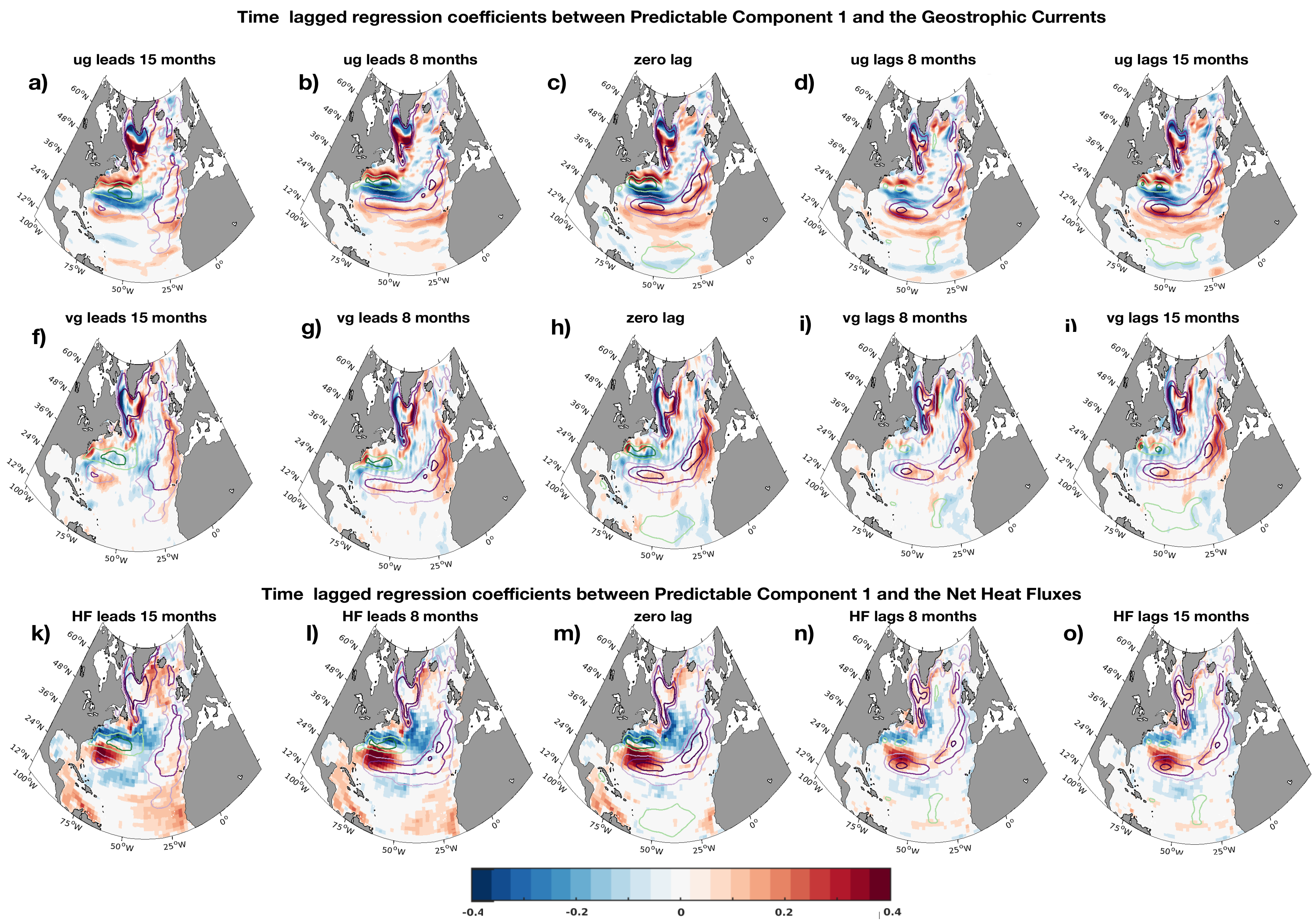

Figure 6.11: Time lagged linear regression coefficients between the time series of the first predictable component and monthly mean zonal and meridional geostrophic currents, created using 150 years of control run output. Only regression coefficients with p values of < 0.05 are retained. Units of the regression are m/s for those involving the geostrophic components and W/m^2 for those investigating the net heat fluxes. The contours show the time-lagged regression coefficients of the predictable component and SSH at 0.1m intervals.

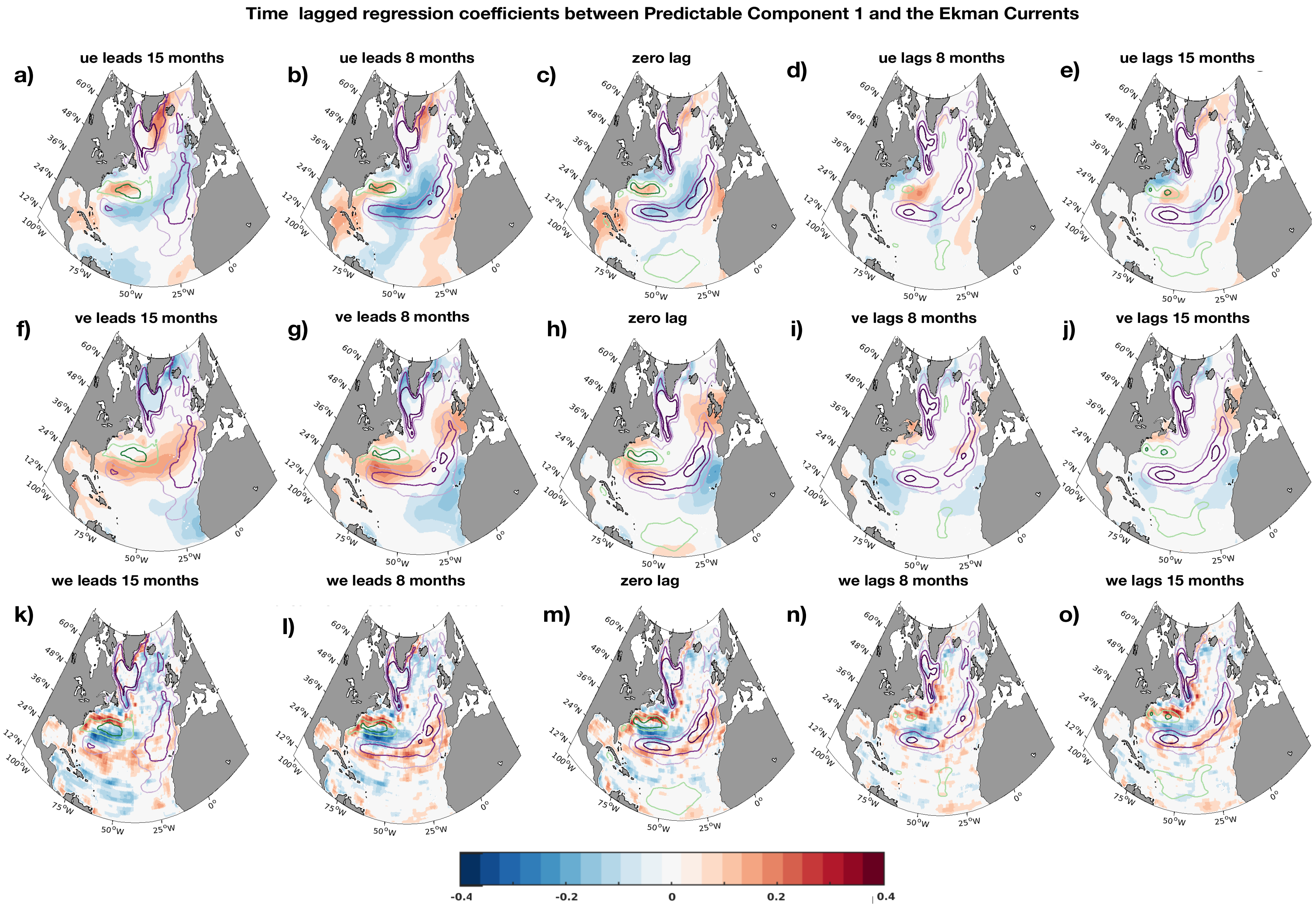

Figure 6.12: Time lagged linear regression coefficients between the time series of the first predictable component and monthly mean zonal and meridional Ekman currents and the Ekman pumping/suction velocity, created using 150 years of control run output. Only regression coefficients with p values of < 0.05 are retained. Units of the regression are m/s. The contours show the time-lagged regression coefficients of the predictable component and SSH at 0.1m intervals.

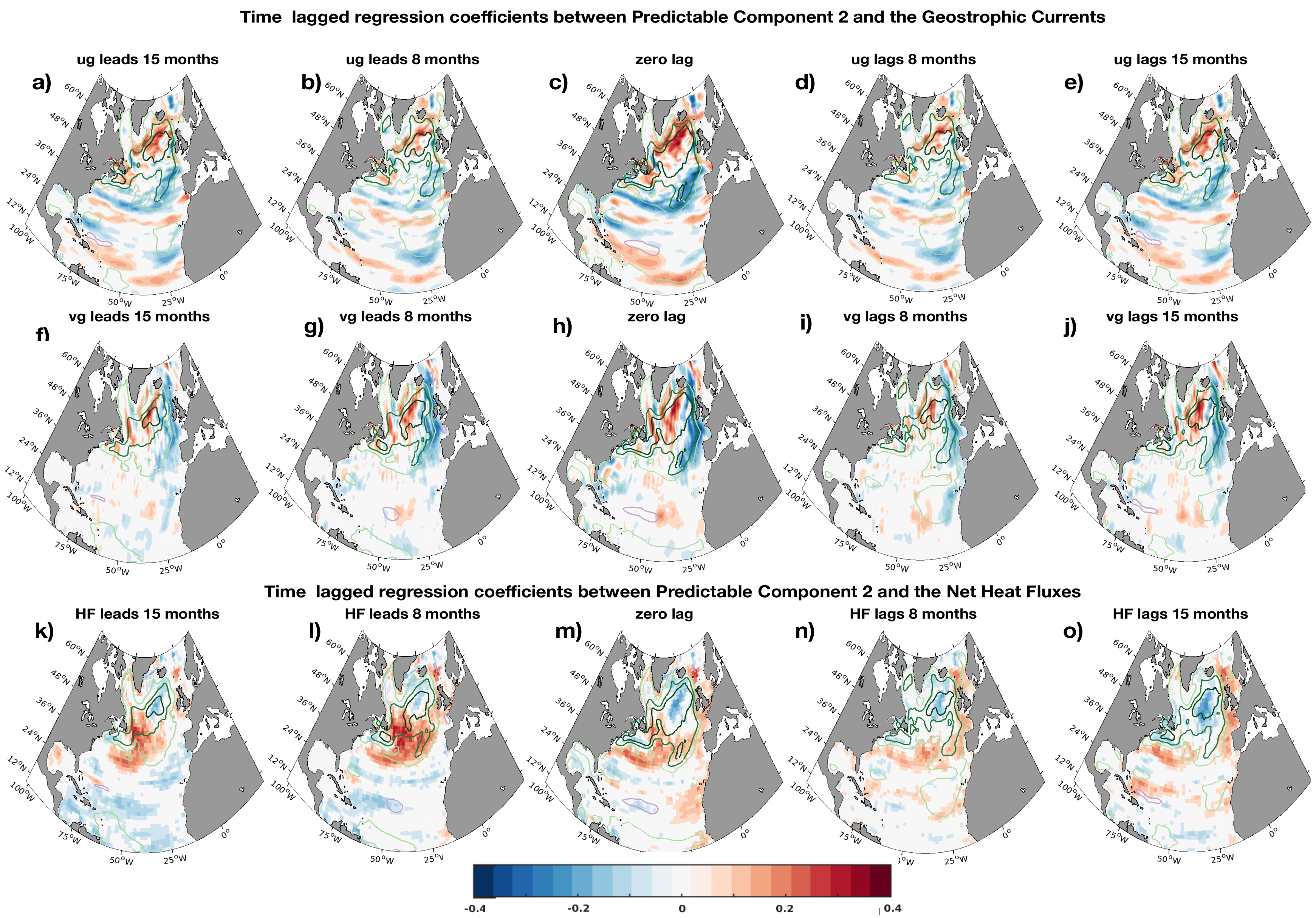

Figure 6.13: Time lagged linear regression coefficients between the time series of the second predictable component and monthly mean zonal and meridional geostrophic currents, created using 150 years of control run output. Only regression coefficients with p values of < 0.05 are retained. Units of the regression are m/s for those involving the geostrophic components and W/m^2 for those investigating the net heat fluxes. The contours show the time-lagged regression coefficients of the predictable component and SSH at 0.1m intervals.

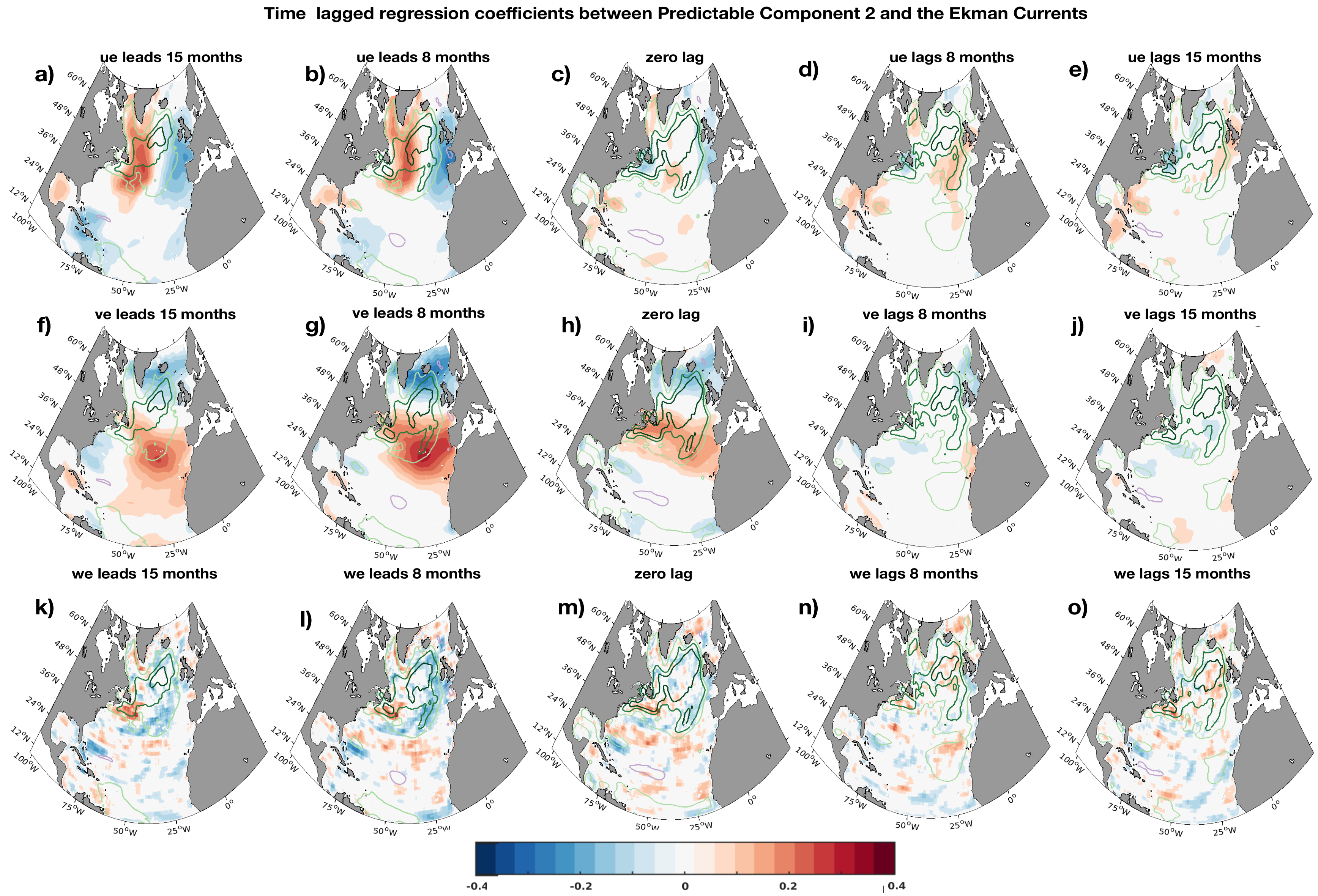

Figure 6.14: Time lagged linear regression coefficients between the time series of the second predictable component and monthly mean zonal and meridional Ekman currents and the Ekman pumping/suction velocity, created using 150 years of control run output. Only regression coefficients with p values of < 0.05 are retained. Units of the regression are m/s. The contours show the time-lagged regression coefficients of the predictable component and SSH at 0.1m intervals.

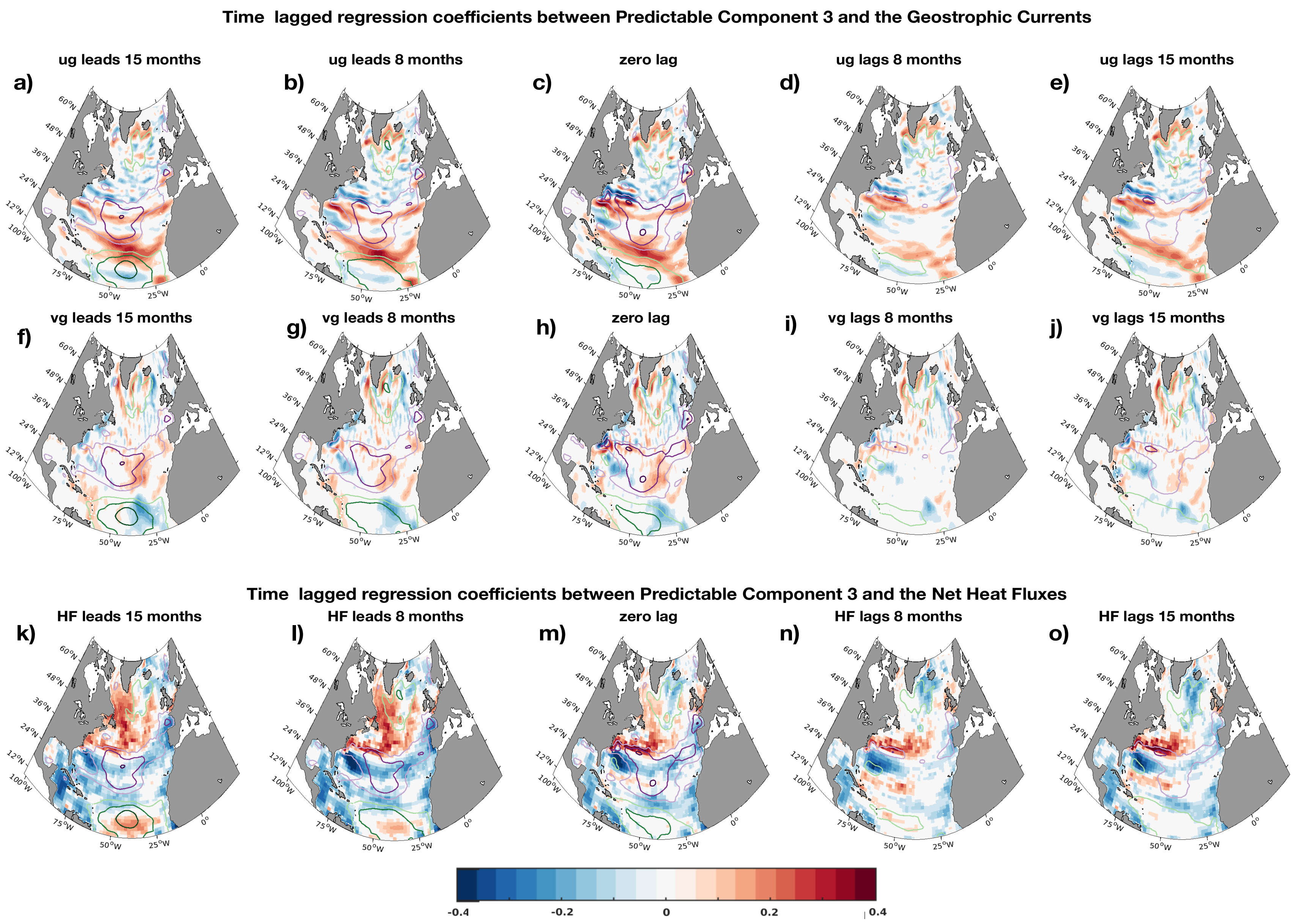

Figure 6.15: Time lagged linear regression coefficients between the time series of the third predictable component and monthly mean zonal and meridional geostrophic currents, created using 150 years of control run output. Only regression coefficients with p values of < 0.05 are retained. Units of the regression are m/s for those involving the geostrophic components and W/m^2 for those investigating the net heat fluxes. The contours show the time-lagged regression coefficients of the predictable component and SSH at 0.1m intervals.

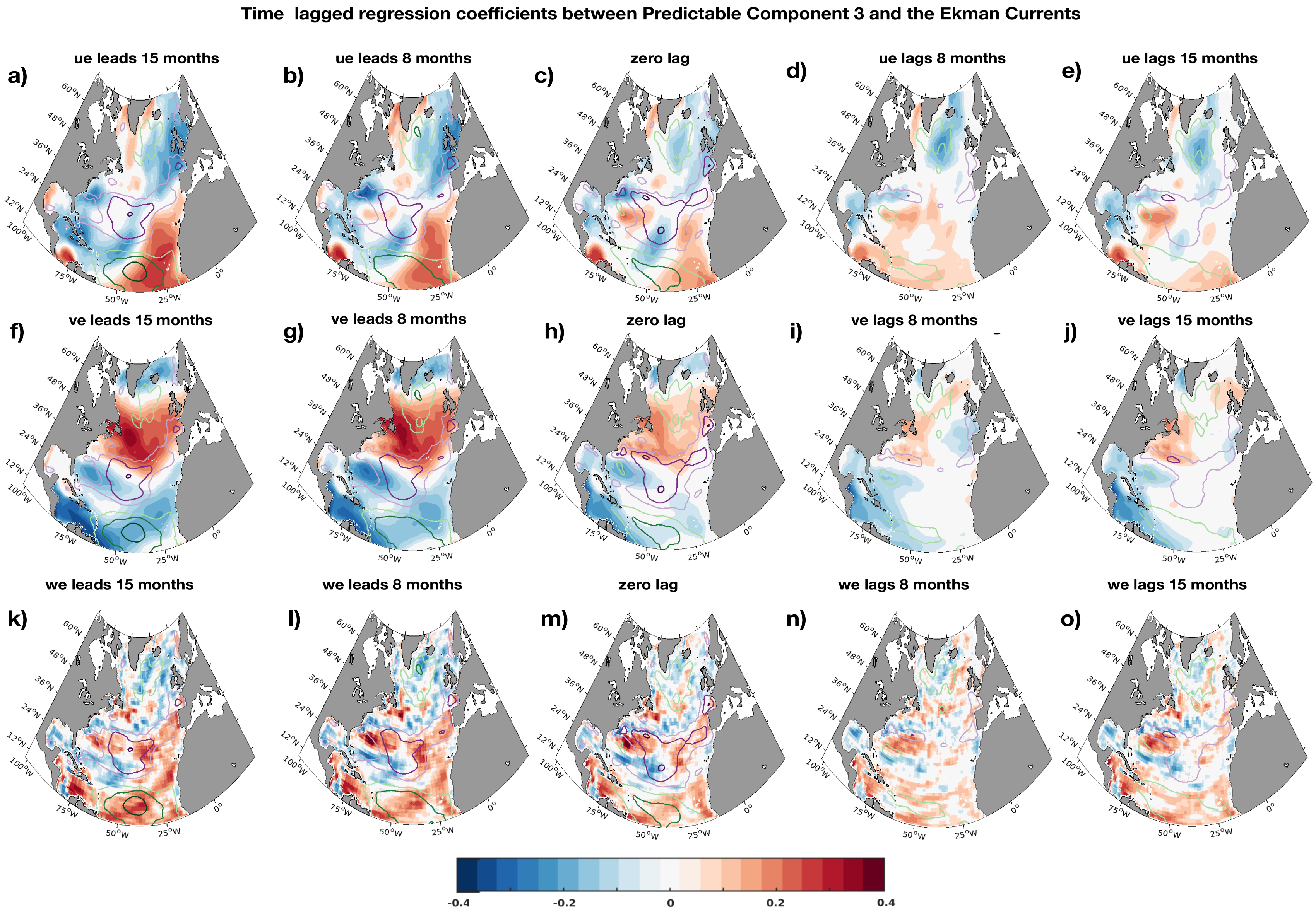

Figure 6.16: Time lagged linear regression coefficients between the time series of the third predictable component and monthly mean zonal and meridional Ekman currents and the Ekman pumping/suction velocity, created using 150 years of control run output. Only regression coefficients with p values of < 0.05 are retained. Units of the regression are m/s. The contours show the time-lagged regression coefficients of the predictable component and SSH at 0.1m intervals.

Stream detaches from Cape Hatteras, and an SSH signal along the US east coast. The maximum amplification of these initial conditions occurs 20 months after initialisation and results in several different effects. Firstly, the amplification can lead to a doubling in the magnitude of the initial SSH anomalies in the Gulf Stream region (i.e., an optimal initial condition with a tripolar anomaly of size 3cm can propagate to give anomalies of 6cm along the Gulf Stream path). Secondly, the amplification acts to increase (or decrease depending on the sign) the SSH gradient across the Gulf Stream, leading to a geostrophic transport anomaly of the order of 10 cm/s (for an optimal perturbation with the magnitudes shown in Figure 6.6b). Moreover, these changes can lead to a meridional shift of an SSH contour of 0 m by several degrees in latitude (a southward shift of approximately 5° for an optimal perturbation with double the magnitude, and the opposite sign of that shown in Figure 6.6b). Finally, this growth results in a 5cm change in SSH along the US east coast at latitudes of 30°- 40°N (for an optimal perturbation with the magnitudes shown in Figure 6.6b, the negative optimal initial condition leads to a increase of SSH in this region).

The optimal initial conditions consist of both small-scale, large amplitude, anomalies in the vicinity of the Gulf Stream's detachment point and smaller amplitude, gyre-scale SSH anomalies. It is uncertain how these features generate the amplification, and whether one feature is more important than the other or whether both are required. In order to investigate this problem the climate model could be restarted with the optimal initial conditions, and with parts of the optimal initial conditions masked (however, restarting the climate model with optimal initial conditions would require multivariate 3D restarts). This would determine which of these features the amplification is most sensitive to and which dynamical mechanisms are responsible for the amplification. Furthermore, it would help elucidate the mechanisms which cause variations in the state of the Gulf Stream, and determine whether it is driven by intrinsic mechanisms, responses to external forcings or a combination of the two. It would also be interesting to compare these effects to those observed in the Kuroshio, where variability is thought to be intrinsically generated, but influenced by adjustments to external forcings (Pierini, 2014). A comparison of the diagnosed optimal initial conditions in the two regions could also be constructive, as those calculated by Wang et al. (2017) (using a shallow water model simulating the intrinsic variability in the Kuroshio), have several similarities to those diagnosed in this study including SSH anomalies near to the mid-latitude jets detachment point and amplification timescales on the order of months.

The optimal initial conditions also have implications for observations. The initial conditions found are indicative that to better constrain interannual predictions of SSH, in the North Atlantic, it would be beneficial to incorporate a higher number of ocean observations (SSH, temperature and velocity fields) in the region near to the Gulf Stream's detachment point. This area has already been the subject of many observational studies and is well observed by altimetry (several of these studies are discussed by Lillibridge and Mariano (2013). Moreover, a mooring array called Line W has recently been established in the region (Toole et al., 2011). Furthermore, the optimal initial conditions could aid in the design of more efficient perturbations in GCM ensemble forecasts. Forecasts using such perturbations may better evaluate the uncertainties related to the initial conditions, and therefore provide more accurate forecast uncertainties (Hawkins and Sutton, 2009).

An evaluation of the control run's APT found three large-scale leading predictable components, which exhibit predictability at times of over 2 years. The leading predictable components were related to changes in SSH in the recirculation gyres, as well as variations in both the position and state of the Gulf Stream. The third predictable component resembled the evolved state of the optimal initial conditions, occurring 20 months after initialisation. The agreement of these results indicates the potential for large-scale predictable patterns of SSH anomalies to exist in the North Atlantic. The relationship between the leading predictable components and the geostrophic and Ekman driven currents was probed using linear regression analysis. The Ekman velocity components were seen to lead the first three predictable components strongly, demonstrating the potential for interannual predictability of large-scale SSH patterns due to the oceanic adjustment to wind stress. Moreover, this eludes to the possibility that improvements in the large-scale wind forcing may lead to improved interannual forecasts of SSH in the North Atlantic.

This study did not entirely decouple the effects of applying interannual external forcings from the intrinsic variability due to the mesoscale eddy fields. It also made use of a single model, and therefore the optimal initial conditions presented may be model specific. It would therefore be beneficial to examine the SSH predictability with a more extensive ensemble of model simulations, including those which isolate the effects of intrinsic processes (such as the experiments described by Sérazin et al. (2015)). Moreover, a comparison with altimetry or higher resolution model output may further elucidate the effects of the eddy field on interannual variability. Finally, a series of idealised simulations, with selective timescales of the wind and buoyancy forcings, may aid in explaining the dynamical origin of the predictable components (Ensembles of the type used by Roberts et al. (2016) would be appropriate for this task). Moreover, such studies could better evaluate the thermosteric and halosteric contributions of the predictable components of SSH.

This study demonstrates the presence of large-scale SSH patterns, which are linearly predictable on interannual timescales (approximately 1-2 years). These patterns appear to significantly lag changes in atmospheric forcings, on times of up to 15 months, indicating the presence of an interannually predictable ocean dynamical adjustment to external forcings. The patterns could have particular relevance when considering interannual predictions of the state of the Gulf Stream and the magnitude of SSH along the US east coast.

Chapter 7

Conclusions and Discussion

Motivated by uncertainties in North Atlantic SSH dynamical forecasts (Nonaka et al., 2016; Roberts et al., 2016), this thesis has examined the oceanic origin of interannual SSH variability and evaluates the associated predictability. A hierarchy of models have been used at eddy-permitting resolution ranging from a barotropic model, with both idealised geometry and forcing to a state-of-the-art AOGCM, all with dynamics relevant to the North Atlantic Ocean. Chapter 4 primarily investigated the role of intrinsic ocean processes in driving interannual SSH variability, whilst the later chapters (5 and 6) considered how the amplitude, pattern and temporal variability in forcings alters such variability and influences the associated predictability. The results presented shed some new light on the mechanisms giving rise to interannual intrinsic ocean variability in the oceans and in models. In addition, this work has important implications for how such mechanisms may influence the predictability of SSH on a range of timescales in the North Atlantic.

7.1 Summary of Results

The study of intrinsically generated SSH variability (Chapter 4) has extended our understanding of how eddy-mean flow interactions can drive interannual variability in mid-latitude ocean jets. The main contributions are:

- The quantification of intrinsically generated interannual SSH variability in the jet regions, in both double-gyre barotropic and baroclinic primitive equation models.

- New insights into jet variability mechanisms, by demonstrating that the interannual variations in both the jet's zonal transport and its position are concurrent with changes in the eddy-mean flow interactions in the recirculation gyres.
- The identification of a mechanism of baroclinic eddy-driven interannual variability associated with equatorward migration of zonal velocity anomalies. The origin of such variability is attributed to an asymmetry in the Eady growth rate, arising from the meridional surface wind and temperature forcing profiles.

This study shows that mesoscale eddies can drive interannual variability in zonal jets, by introducing asymmetries in momentum and temperature. The emergent variability is generated through several different mechanisms including, eddy momentum flux-related jet rectifications, and jet migrations due to variations in eddy heat fluxes in the mid-latitudes.

The examination of the predictability related to both the intrinsic SSH variability and that generated in response to changes in temperature and wind forcings (Chapter 5), demonstrated that:

- In the jet region, the intrinsic barotropic component of SSH variability exhibits predictability on monthly timescales. Whilst the baroclinic component, here associated with meridional migrations of anomalous zonal jets, can be predictable on timescales longer than a year (12-16 months, based on the optimal initial condition analysis).
- Double-gyre primitive equation systems with steady atmospheric forcings do not exhibit gyre-scale patterns of predictable SSH variability.
- Interannually predictable large-scale SSH patterns can emerge with time-dependent forcings (e.g., low-frequency atmospheric modes of variability).

Overall, these results are indicative that the intrinsic ocean variability is largely unpredictable on interannual timescales, and acts to degrade forecast skill in turbulent regions. Moreover, the eddy-mean flow interactions which affect the jet's meridional position and the jet rectification processes seem relatively insensitive to changes in the applied forcings tested. Only the introduction of a low-frequency, large-scale wind forcing generated any large-scale interannual SSH variability. It is the large spatial scale present in the atmospheric forcings, which appear to be responsible for any gyre-scale interannually predictable SSH components.

Finally, the predictability of SSH in the North Atlantic in a control run of a fully coupled model (HadGEM3), was evaluated using methods based on linear inverse modeling and average predictability time (Chapter 6). The contributions from this study include:

- The evaluation of SSH predictability in the subpolar gyre and along the west coast of the basin on timescales of up to 20 months.
- Demonstrating that SSH predictability times are relatively short in the Gulf Stream extension region (5-10 months), as the presence of mesoscale eddies acts to degrade forecast skill.
- Calculating the optimal initial SSH conditions, which consist of a weak large-scale SSH tripole, with a stronger signal at the Gulf Stream's detachment point. The evolution of these optimal initial conditions results in regional SSH changes in the subpolar and subtropical gyres and a change in SSH gradient along the Gulf Stream's extension.
- The identification of large-scale predictable components, which result in SSH variations of 5-10 cm along the US east coast are predictable on timescales longer than 2 years.

- Demonstrating that the diagnosed predictable components contribute to large-scale variations in SSH, and appear to be induced by wind and heat flux forcing in the preceding 8-15 months.

In the coupled model, the interannual variability is still primarily located in the Gulf Stream region. However, in agreement with Nonaka et al. (2016) and Roberts et al. (2016), SSH predictability in the turbulent jet extension regions is limited to less than 5 months. Large-scale predictable SSH patterns correspond to oceanic adjustments to variations in the interannual wind forcings and heat fluxes.

7.2 Discussion

7.2.1 Interannual Sea Surface Height Variability Driven by Intrinsic Processes

It has long been established that the ocean can act to integrate the chaotic, unpredictable fluctuations of the atmosphere, reddening the spectrum of climate variability (Frankignoul and Hasselmann, 1977). However, several studies have shown that the ocean can also produce low-frequency variability through intrinsic mechanisms in the absence of any interannual atmospheric variability (e.g., Spall, 1996; Dijkstra and Ghil, 2005; Berloff et al., 2007; Penduff et al., 2011). Using a global ocean–sea ice general circulation model, Penduff et al. (2011) argued that such interannual intrinsic variability could be comparable in magnitude to that generated in response to variations in atmospheric forcing. This intrinsic variability emerges in the presence of nonlinear mesoscale eddies, as these can enable a temporal inverse cascade of kinetic energy (Arbic et al., 2012, 2014) (believed to be associated with the spatial inverse cascades - since small and fast processes interactions can lead to large-scale and long timescales processes). However, the exact mechanisms by which eddies act to influence low-frequency variability remain poorly understood and rather uncertain. This was the subject of the first thesis aim: **to examine the role of mesoscale eddies in driving interannual SSH variability**.

The idealised model-based studies, presented in this thesis, introduce new perspectives on the mechanisms by which mesoscale eddies act to influence interannual intrinsic ocean variability. Variations in the mid-latitude jet's position and transport are driven by eddy momentum fluxes in the recirculation gyres and WBCs. In addition, the effect of eddy heat fluxes on intrinsic interannual variability, which have been investigated in only a few studies before (Chan et al., 2007; Taguchi et al., 2010; Thompson and Richards, 2011), can generate eddy-modulated interannual quasi-periodic variability in the vicinity of the mid-latitude jet.

The results also yield insights into the contributions of intrinsic processes to SSH spectra. Such contributions are important when considering the uncertainties in sea level trends in eddy-active regions (Sérazin et al., 2016). In both idealized models the variability in the jet regions near to the western boundary appears to be chaotic, in agreement with the dynamical interpretation presented by Berloff et al. (2007) (and indicated by power spectral density plots with white profiles on timescales longer than 2 years). However, the buoyancy-driven variability has a well defined spectral peak on interannual timescales (Chapter 4, Section 4.3). Therefore, there exists intrinsic eddy-modulated variability which may potentially be predictable on interannual timescales. However, power spectra of SSH altimeter data exhibit white noise profiles on interannual timescales (Hughes and Williams, 2010). This result indicates that the chaotic variability constitutes the largest component of the interannual SSH variability in the mid-latitude jet regions, potentially masking the variability related to the meridionally shifting jets. Although, such migrating jets have been observed in the North Pacific Ocean interior (Chen et al., 2016), and may be driven by the mechanisms discussed in this thesis. Alternatively, the migration related variability may not appear in the real climate system, perhaps due to cancelling effects from time-varying salinity and temperature influences or that of bathymetry. It is also conceivable that such interannual variability could be poorly sampled by currently available observations.

Different responses are seen in the studies investigating the changes in variability associated with the wind forcing (Chapter 5). Variations in the magnitudes of the time-invariant surface wind forcings only introduced minor changes in variability and predictability timescales in the barotropic experiment. However, further work is required to determine how such intrinsic variability will vary in coupled models under future climate scenarios. As internal ocean-atmosphere modes of variability could respond in a different manner to the intrinsic ocean modes. Moreover, it is also uncertain how important such variations will be as it is hypothesised that the forced component of SSH variability will constitute a larger amount of the total SSH variability in future climate scenarios (Lyu et al., 2015). The introduction of time-dependent wind forcings, while not dramatically altering the timescales of variability in the barotropic experiments, had more prevalent effects in the baroclinic experiments (Chapter 5, Section 5.3.3). In order to probe the interaction between the forced and intrinsic variability, it would be insightful to investigate the oceans dynamical responses to wind and buoyancy forcings in more detail, using an extensive range of spatial and temporal forcing profiles. The eddy momentum and buoyancy tendencies could then be examined and compared to cases with steady forcing, thus isolating the variations due to the mean and variability of the atmospheric forcing. It could also be insightful to examine the forcing perturbations which have the greatest impact on forecast spread, especially in a primitive equation double-gyre model. This could be addressed by calculating the stochastic optimals of the system, as described in Moore et al. (2002). However, such experiments can be computationally expensive. One could examine the SSH variability in response to variations in the heat fluxes. This is relevant as local steric changes, driven by air-sea buoyancy fluxes have a large contribution to the total interannual SSH variability, particularly in the east of the North Atlantic (Cabanes et al., 2006). Therefore their addition may considerably impact SSH predictability in these regions. The addition of stochastic heat fluxes should be relatively straightforward to implement, and the related SSH variability is less well studied than those due to changes in the wind forcing, and will potentially become more important as the anomalous heat fluxes vary under climate change.

7.2.2 Sea Surface Height Predictability and Its Limits

The second thesis aim is **to quantify the predictability of SSH due to the sensitivity in ocean initial conditions and surface forcings in the presence of resolved eddies**, and is related to understanding the dynamical origins of uncertainties in interannual SSH forecasts. The impact of eddies on interannual SSH forecasts is complicated due to the contrasting effects on variability their inclusion introduces. On the one hand, the presence of eddies can lead to their interaction with the mean flow driving interannual variability. On the other hand, they also introduce chaotic signals which can impact the interannual SSH signal, therefore reducing the memory of the system. The barotropic eddy-mean flow interactions result in predictable components of SSH relating to the position and the strength of the mid-latitude jet, with predictable timescales of approximately 150-250 days (Chapter 5, Section 5.2.1). These results agree with those concerning the optimal initial conditions, which demonstrate that the largest amplification of SSH variance is related to small-scale initial conditions in the vicinity of the WBCs. Similar behaviour is also detected in the baroclinic model (Chapter 5, Section 5.3.3). I therefore conclude that interannual intrinsic variability is inherently difficult to predict, as it is sensitive to small-scale features of the eddy field, which are difficult to observe and cannot be used as part of initialised forecasts, for dynamical and numerical reasons. However, the variability due to the interaction between eddy temperature fluxes and zonal jets is predictable on far longer timescales, of almost 5 years. These patterns of interannual variability exhibit sensitivity to large-scale, jet localized SSH initial conditions, and therefore could conceivably be detected in ocean observations. One important caveat in my analysis is the assumption of linearity. The amplitude of the perturbations is usually small enough to warrant the use of linear methods. An alternative approach would be to calculate the conditional nonlinear optimal perturbations or evaluate the predictability using an ensemble of nonlinear model runs. Both of these methods are computationally expensive (Mu et al., 2003) and would complement the linear results. However, despite their shortcomings, linear models are useful as a benchmark for more complex dynamical models (Sonnewald et al., 2018).

The predictable components and analysis contained in Chapter 6 may be model specific, and therefore it is instructive to calculate the predictable patterns of SSH from observational data rather than from climate model output. Despite the relatively short altimeter record, preliminary analysis indicates that the predictable components estimated from observations are similar to those presented in Chapter 6. Figure 7.1 shows the first three EOFs of North Atlantic SSH calculated from 21 years of monthly mean SSH satellite altimeter data between 1 Jan 1993 – 31 May 2014 (AVISO, 2012). The leading EOF pattern resembles that calculated by Häkkinen et al. (2011), which is seen to correlate with changes in the leading EOF of wind stress curl, and with the NAO index (Häkkinen et al., 2013; Esselborn and Eden, 2001; Han et al., 2017). The relationship between SSH variability and NAO is hypothesised to be closely linked to variability in the thermosteric component of the dynamical SSH (Lombard et al., 2005); however, this is yet to be verified. Figure 7.1, panels d and e, demonstrate that the leading principal component of SSH has a significant lagged correlation with the NAO index, with a maximum correlation occurring at a lag time of 9 months.

Figure 7.2 shows the predictable components calculated from the same monthly mean SSH altimeter data (using the method described as in Section 2.2.4.2). The predictability of the system is seen to decay rapidly after approximately 100 days. However, the leading predictable components exhibit predictable timescales of approximately one year (panel b). The leading predictable component (panel c) resembles the leading SSH EOF and predictable component 3 described in Chapter 6. As in the coupled climate model, large-scale predictable patterns of SSH exist in observations, and lag the variations in the low-frequency patterns of wind stress forcings.

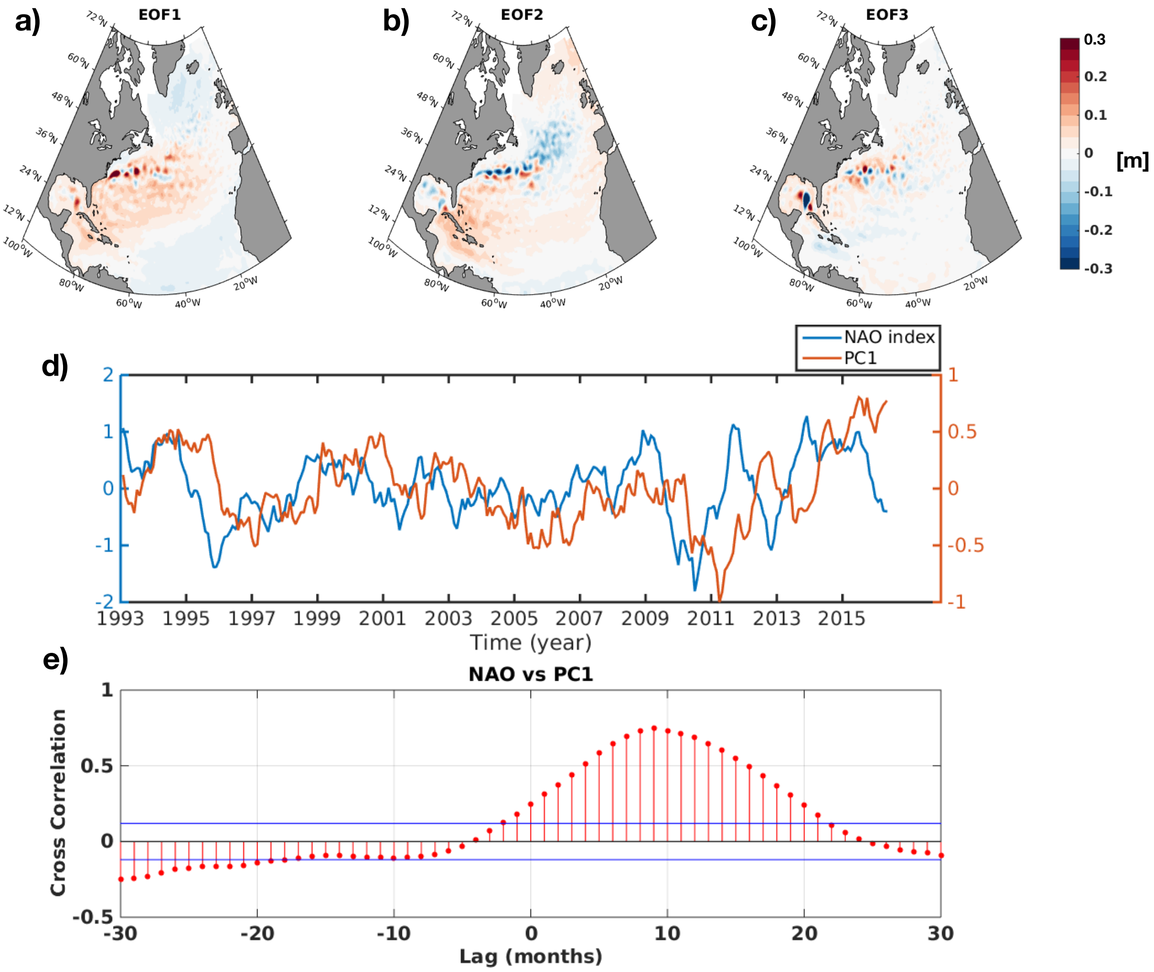

Figure 7.1: The (a) first, (b) second and (c) third EOFs of SSH calculated from monthly mean SSH altimeter data (AVISO, 2012) (representing 6.1%, 3.7% and 3.1% of the variance respectively). (d) Time series of SSH principal component 1 and the NAO index. (e) Time-lagged cross-correlation of SSH principal component 1 and the NAO index (Hurrell and National Center for Atmospheric Research Staff (Eds), 2017). Where a positive lag signifies the leading SSH principal component is lagging the NAO index. The blue lines are the upper and lower 95% confidence bounds for a normal distribution, N(0,1/L) with a standard deviation of $1/\sqrt(L)$, where L is the number of time means used in the analysis.

The observed predictable patterns have signals along the US east coast, indicating their relevance to predicting future coastal flooding in these regions. The presence of these predictable signals, near to the US east coast, may potentially be attributed to a decrease in eddy energy near to the western boundary (Kanzow et al., 2009; Zhai et al., 2010). Further analysis is required to investigate the dynamical origins of the predictable patterns, although I hypothesize that they are due to wind-induced ocean circulation anomalies, and the subsequent convergence and divergence of steric SSH anomalies - potentially influenced by low-pass filtering along the shelves. Finally, the patterns indicate that there are skillful components of SSH forecasts even in regions with large eddy activity.

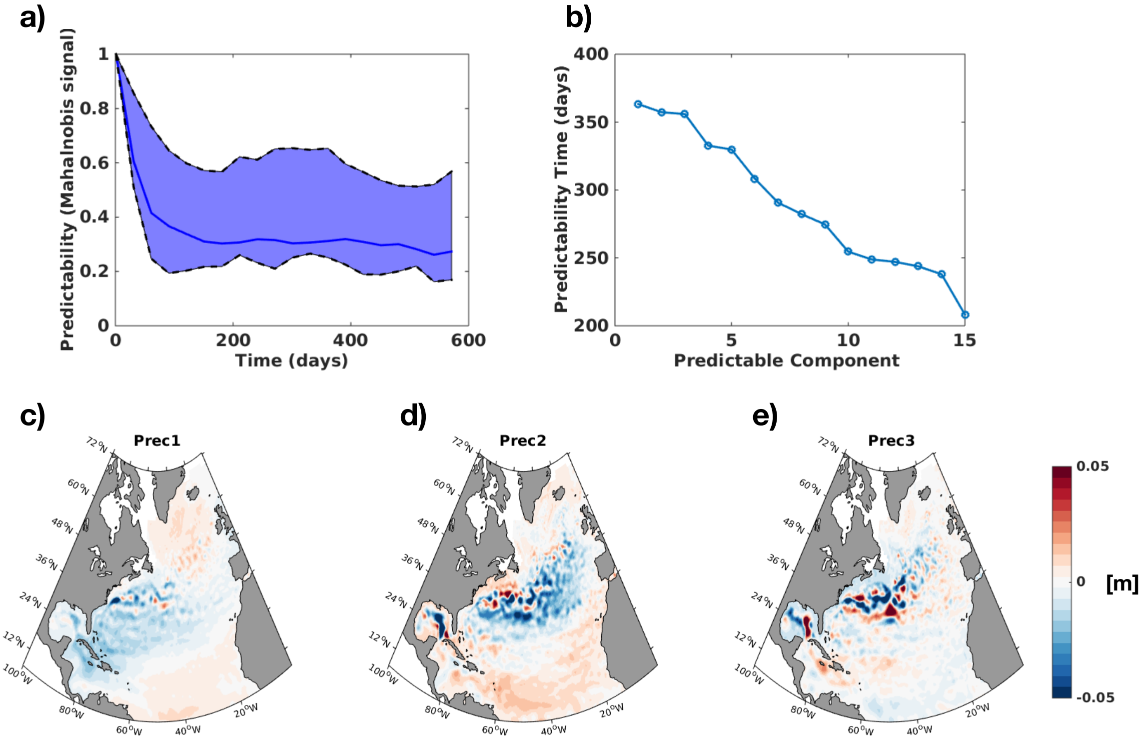

Figure 7.2: (a) Predictability measured by the Mahalanobis signal (S_τ as defined in equation 2.35) of the whole system (blue line), created using linear regression models and the leading 15 principal components. The envelope denotes the spread in predictability measured by the Mahalanobis signal (S_τ) for each of the leading predictable components. (b) The average predictability time (APT) for the first 15 predictable components, ranked in order of their values of APT. The spatial patterns of the (c) first, (d) second and (e) third predictable components. The analysis uses monthly mean SSH altimeter data, between 1 Jan 1993 – 31 May 2014 (AVISO, 2012). The first 13 years of the monthly means are used as the training data and the remaining 10 years is used to verify the predictable components.

Interannual model forecasts are also subject to other uncertainties including those related to unresolved ocean processes, model uncertainties, observational uncertainties and model initialisation. New methods are being developed to better represent these uncertainties including the use of perturbed parameter ensembles and stochastic physics (Brankart, 2013; Andrejczuk et al., 2016; Williams et al., 2016; Juricke et al., 2017). Juricke et al. (2017) showed an increase of 20-25% in interannual SSH variability, in a coarse ocean model when several sub-grid scale parameterisations are stochastically perturbed. Andrejczuk et al. (2016) examined model uncertainty in a coarse GCM using several different stochastic schemes, finding that they could act to increase the spread of the ensemble in eddy-active regions. Such approaches may be useful in future studies which aim to quantify or constrain uncertainties in interannual SSH forecasts.

7.2.3 Intrinsic vs. Forced Sea Surface Height Variability and Predictability

The final thesis aim: **to investigate the relative contributions of the intrinsic and externally forced SSH components, to both the total interannual SSH variability and any associated predictability**, was considered in Chapters 5 and 6. In the presence of a steady wind forcing, the ocean generates interannual intrinsic variability, primarily in regions with mid-latitude jets. Such variability is not generally predictable on interannual timescales. In contrast to this, the ocean's adjustment to fluctuations in the interannual components of the external forcings appears to be the primary cause of large-scale interannual predictable SSH patterns. Such predictable behaviour depends on the ocean's interannual dynamical adjustment mechanisms, including: Rossby waves, locally forced Ekman pumping and buoyancy forced circulation changes. Therefore, interannual SSH predictions are reliant on ocean-atmosphere interactions.

Several of my results have implications related to interannual SSH forecasts. The jet region forecasts, relating to the meridional jet position and the jet's transport, are very sensitive to the state of the eddy field, and exhibit sub-annual predictability times (Chapter 5). However, it has also been shown that in the coupled climate system there are patterns of interannual SSH variability which are predictable on timescales greater than a year (Chapter 6). Some of these predictable patterns contain signals relating to the state and position of the Gulf Stream, including the position of its detachment point. Therefore, the presence of eddies does not completely obscure predictable SSH components related to oceanic adjustments to large-scale external forcings, even in regions where the majority of the variability is intrinsically generated.

Large-scale predictable patterns of SSH are seen to lag large-scale changes in the external forcings, on timescales of up to a year. Therefore I hypothesise that LIM models constructed using not only the SSH field, but also the time-varying wind forcings and surface heat fluxes will display improved forecasts of SSH anomalies, relative to those generated by a LIM trained on SSH alone. This analysis could be extended to give insights into the sensitivities of SSH forecasts to different temporal and spatial timescales of atmospheric forcings.

Given sufficient resources, several further GCM based studies could be undertaken to compliment the analysis presented in this thesis. Firstly, this thesis did not entirely decouple the effects of the intrinsic and forced variability in GCM experiments. It would be informative to examine the predictability in a GCM which intrinsic ocean variability were isolated, i.e., the GCM is run with no interannual variability in its external atmospheric forcings, similar to the experiments by Sérazin et al. (2015). This approach would enable us to investigate whether the intrinsic variability is unpredictable on timescales longer than a few months, in agreement with the idealised experiments. Alternatively, longer timescale predictable intrinsic behaviours may emerge, such as the meridional anomalous jet migration discussed in Chapter 4. Secondly, idealized forcing experiments, where the applied wind and buoyancy forcings are restricted in their timescales could also be used to further examine the oceanic adjustment mechanisms responsible for the diagnosed interannual SSH predictability. Such ensembles already exist for a range of applications (Gregory et al., 2016; Roberts et al., 2016; Meyssignac et al., 2017). For example, the HadGEM3 ensemble presented by Roberts et al. (2016) could be used to infer the optimal initial conditions, and predictable patterns associated with the intrinsic ocean variability, the interannual wind forcings and the interannual buoyancy forcings. Alternatively, a probabilistic approach as described by Bessières et al. (2017) could be used to disentangle the forced and intrinsic variability components, thus, better explaining the dynamical origin of the patterns shown in Chapter 6. Finally, it would be interesting to be able to restart the GCM using the optimal initial conditions found in Chapter 6. Such experiments would be able to deduce whether it is the oceanic dynamical adjustments which lead to the growth of the initial conditions, or whether it is the state of the atmosphere that is the most important factor in the optimal evolution of variability and errors in models.

Bibliography

AMS
2012. *AMS Glossary of Meteorology, 2nd Edition*. American Meteorological Society.

Andrejczuk, M., F. C. Cooper, S. Juricke, T. N. Palmer, A. Weisheimer, and L. Zanna
2016. Oceanic stochastic parameterizations in a seasonal forecast system. *Monthly Weather Review*, 144(5):1867–1875.

Andres, M.
2016. On the recent destabilization of the gulf stream path downstream of cape hatteras. *Geophysical Research Letters*, 43(18):9836–9842.

Arbic, B. K., M. Müller, J. G. Richman, J. F. Shriver, A. J. Morten, R. B. Scott, G. Sérazin, and T. Penduff
2014. Geostrophic turbulence in the frequency–wavenumber domain: Eddy-driven low-frequency variability. *Journal of Physical Oceanography*, 44(8):2050–2069.

Arbic, B. K., R. B. Scott, G. R. Flierl, A. J. Morten, J. G. Richman, and J. F. Shriver
2012. Nonlinear cascades of surface oceanic geostrophic kinetic energy in the frequency domain. *Journal of Physical Oceanography*, 42(9):1577–1600.

AVISO
2012. (Archiving, Validation and Interpretation of Satellite Oceanographic data), available at www.aviso. oceanobs.com.

Bamber, J., M. van den Broeke, J. Ettema, J. Lenaerts, and E. Rignot
2012. Recent large increases in freshwater fluxes from Greenland into the North Atlantic. *Geophys. Res. Lett.*, 39:L19501.

Becker, M., M. Karpytchev, M. Marcos, S. Jevrejeva, and S. Lennartz-Sassinek
2016. Do climate models reproduce complexity of observed sea level changes? *Geophysical Research Letters*, 43(10):5176–5184.

Berloff, P., A. Hogg, and W. Dewar
2007. The Turbulent Oscillator: A Mechanism of Low-Frequency Variability of the Wind-Driven Ocean Gyres. *Journal of Physical Oceanography*, 37(9):2363–2386.

Bessières, L., S. Leroux, J.-M. Brankart, J.-M. Molines, M.-P. Moine, P.-A. Bouttier, T. Penduff, L. Terray, B. Barnier, and G. Sérazin
2017. Development of a probabilistic ocean modelling system based on nemo 3.5: application at eddying resolution. *Geoscientific Model Development*, 10(3):1091–1106.

Bindoff, N. L., J. Willebrand, V. Artale, A. Cazenave, J. Gregory, S. Gulev, K. Hanawa, C. Le Quéré, S. Levitus, Y. Nojiri, C. K. Shum, L. D. Talley, and A. Unnikrishnan
2007. *Observations: Oceanic Climate Change and Sea Level. In: Climate Change 2007: The Physical Science Basis. Contribution of Working Group I to the Fourth Assessment Report of the Intergovernmental Panel on Climate Change [Solomon, S., D. Qin, M. Manning, Z. Chen, M. Marquis, K.B. Averyt, M. Tignor and H.L. Miller (eds.)].* Cambridge University Press.

Bingham, R. J. and C. W. Hughes
2009. Signature of the Atlantic meridional overturning circulation in sea level along the east coast of North America. *Geophys. Res. Lett.*, 36:L02603.

Bjornsson, H. and S. A. Venegas
1997. A manual for EOF and SVD analyses of climate data. *McGill University Montreal*, P. 52.

Boer, G. J.
2004. Long time-scale potential predictability in an ensemble of coupled climate models. *Climate dynamics*, 23(1):29–44.

Bouttes, N., J. M. Gregory, T. Kuhlbrodt, and R. S. Smith
2013. The drivers of projected North Atlantic sea level change. *Climate Dynamics*, 43(5-6):1531–1544.

Brankart, J.-M.
2013. Impact of uncertainties in the horizontal density gradient upon low resolution global ocean modelling. *Ocean Modelling*, 66:64 – 76.

Branstator, G. and H. Teng
2014. Is AMOC More Predictable than North Atlantic Heat Content?. *Journal of Climate*, 27(10):3537–3550.

Branstator, G., H. Teng, G. A. Meehl, M. Kimoto, J. R. Knight, M. Latif, and A. Rosati
2012. Systematic Estimates of Initial-Value Decadal Predictability for Six AOGCMs. *Journal of Climate*, 25:1827–1846.

Cabanes, C., T. Huck, and A. Colin de Verdière
2006. Contributions of wind forcing and surface heating to interannual sea level variations in the Atlantic Ocean. *Journal of physical oceanography*, 36(9):1739–1750.

Cazenave, A. and W. Llovel
2010. Contemporary sea level rise. *Annual review of marine science*, 2:145–73.

Cessi, P. and F. Paparella
2001. Excitation of basin modes by ocean-atmosphere coupling. *Geophysical Research Letters*, 28(12):2437–2440.

Chan, C. J., R. A. Plumb, and I. Cerovecki
2007. Annular modes in a multiple migrating zonal jet regime. *Journal of the Atmospheric Sciences*, 64(11):4053–4068.

Chemke, R. and Y. Kaspi
2015. Poleward migration of eddy-driven jets. *Journal of Advances in Modeling Earth Systems*, 7(3):1457–1471.

Chen, C., I. Kamenkovich, and P. Berloff
2016. Eddy trains and striations in quasigeostrophic simulations and the ocean. *Journal of Physical Oceanography*, 46(9):2807–2825.

Chowdhury, M., P.-S. Chu, T. Schroeder, and N. Colasacco
2007. Seasonal sea-level forecasts by canonical correlation analysis—an operational scheme for the us-affiliated pacific islands. *International journal of climatology*, 27(10):1389–1402.

Chung, C. and S. Nigam
1999. Weighting of geophysical data in principal component analysis. *Journal of Geophysical Research: Atmospheres*, 104(D14):16925–16928.

Church, J. A., P. U. Clark, A. Cazenave, J. M. Gregory, S. Jevrejeva, A. Levermann, M. A. Merrifield, G. A. Milne, R. S. Nerem, P. D. Nunn, A. J. Payne, W. T. Pfeffer, D. Stammer, and A. S. Unnikrishnan
2013. *2013: Sea Level Change. In:Climate Change 2013: The Physical Science Basis. Contribution of Working Group I to the Fifth Assessment Report of the Intergovernmental Panel on Climate Change [Stocker, T.F., D. Qin, G.-K. Plattner, M. Tignor, S.K. Allen, J. B.* Cambridge University Press.

Church, J. A. and N. J. White
2006. A 20th century acceleration in global sea-level rise. *Geophysical Research Letters*, 33:L01602.

Church, J. A. and N. J. White
2011. Sea-level rise from the late 19th to the early 21st century. *Surveys in Geophysics*, 32(4-5):585–602.

Church, J. A., P. L. Woodworth, A. Thorkild, and W. Stanley Wilson
2010. *Understanding Sea Level Rise and Variability.* Blackwell Publishing Limited.

Collins, M., M. Botzet, A. F. Carril, H. Drange, A. Jouzeau, M. Latif, S. Masina, O. H. Otteraa, H. Pohlmann, A. Sorteberg, R. Sutton, and L. Terray
2006. Interannual to Decadal Climate Predictability in the North Atlantic : A Multimodel-Ensemble Study. *Journal of Climate*, 19:1195–1203.

DelSole, T.
2004. Predictability and Information Theory . Part I : Measures of Predictability. *Studies, Atmosphere*, 61:2425–2440.

DelSole, T.
2017. Decadal prediction of temperature: Achievements and future prospects. *Current Climate Change Reports*, 3(2):99–111.

DelSole, T. and M. K. Tippett
2007. Predictability: Recent insights from information theory. *Reviews of Geophysics*, 45.4:1188–1204.

DelSole, T. and M. K. Tippett
2009a. Average Predictability Time. Part I: Theory. *Journal of Atmospheric Science*, 66:1172–1187.

DelSole, T. and M. K. Tippett

2009b. Average predictability time. Part II: Seamless diagnoses of predictability on multiple time scales. *Journal of the Atmospheric Sciences*, 66:1188–1204.

DelSole, T., M. K. Tippett, and L. Jia

2015. *Multi-year Prediction and Predictability*, chapter Chapter 14, Pp. 219–233. World Scientific.

Dewar, W. K.

2003. Nonlinear Midlatitude Ocean Adjustment. *Journal of Physical Oceanography*, 33(5):1057–1082.

Dijkstra, H. A. and M. Ghil

2005. Low-Frequency Variability of the Large-scale Ocean Circulation: A Dynamical Systems Approach. *Reviews of Geophysics*, 43(3):1–38.

Doddridge, E. W., D. P. Marshall, and A. M. Hogg

2016. Eddy cancellation of the ekman cell in subtropical gyres. *Journal of Physical Oceanography*, 46(10):2995–3010.

Douglass, E., S. Jayne, S. Peacock, F. Bryan, and M. Maltrud

2012. Subtropical mode water variability in a climatologically forced model in the northwestern pacific ocean. *Journal of Physical Oceanography*, 42(1):126–140. cited By 6.

Douglass, E. M., Y.-O. Kwon, and S. R. Jayne

2013. A comparison of north pacific and north atlantic subtropical mode waters in a climatologically-forced model. *Deep Sea Research Part II: Topical Studies in Oceanography*, 91:139 – 151. Subtropical Mode Water in the North Atlantic Ocean.

Eady, E. T.

1949. Long waves and cyclone waves. *Tellus*, 1(3):33–52.

Enfield, D. B. and J. S. Allen

1980. On the structure and dynamics of monthly mean sea level anomalies along the pacific coast of north and south america. *Journal of Physical Oceanography*, 10(4):557–578.

Esselborn, S. and C. Eden

2001. Sea surface height changes in the north atlantic ocean related to the north atlantic oscillation. *Geophysical Research Letters*, 28(18):3473–3476.

Farrell, B. and P. J. Ioannou

1996. Generalized Stability Theory. Part I: Autonomous Operators. *Journal of Atmospheric Science*, 53:2025–2040.

Farrell, B. F.

1982. The initial growth of disturbances in a baroclinic flow. *Journal of the Atmospheric Sciences*, 39(8):1663–1686.

Farrell, B. F.

1990. Small error dynamics and the predictability of atmospheric flows. *Journal of the Atmospheric Sciences*, 47(20):2409–2416.

Farrell, B. F. and P. J. Ioannou

1995. Stochastic dynamics of the midlatitude atmospheric jet. *Journal of the Atmospheric Sciences*, 52(10):1642–1656.

Farrell, B. F. and A. M. Moore

1992. An adjoint method for obtaining the most rapidly growing perturbation to oceanic flows. *Journal of Physical Oceanography*, 22(4):338–349.

Forget, G. and R. M. Ponte

2015. The partition of regional sea level variability. *Progress in Oceanography*, 137:173 – 195.

Frankignoul, C. and K. Hasselmann

1977. Stochastic climate models, part ii application to sea-surface temperature anomalies and thermocline variability. *Tellus*, 29(4):289–305.

Frankignoul, C., P. Müller, and E. Zorita

1997. A simple model of the decadal response of the ocean to stochastic wind forcing*. *Journal of Physical Oceanography*, 27(8):1533–1546.

Fu, L.-L.

2004. The interannual variability of the North Atlantic Ocean revealed by combined data from TOPEX/Poseidon and Jason altimetric measurements. *Geophysical Research Letters*, 31(23):L23303.

Fukumori, I., R. Raghunath, and L.-l. Fu

1998. Nature of global large-scale sea level variability in relation to atmospheric forcing : A modeling study Ichiro by daily winds and climatological heat fluxes corresponding to the period from January. *Journal of Geophysical Research: Oceans*, 103:5493–5512.

Fukuoka, A.
1951. A Study of 10-day Forecast (A Synthetic Report). *The Geophysical Magazine: Tokyo*, XXII:177 218.

Giannakis, D. and A. J. Majda
2012. Quantifying the Predictive Skill in Long-Range Forecasting. Part I: Coarse-Grained Predictions in a Simple Ocean Model. *Journal of Climate*, 25(6):1793–1813.

Gill, A. and P. Niller
1973. The theory of the seasonal variability in the ocean. In *Deep Sea Research and Oceanographic Abstracts*, Pp. 141–177. Elsevier.

Greatbatch, R. J. and B. T. Nadiga
2000. Four-gyre circulation in a barotropic model with double-gyre wind forcing. *Journal of Physical Oceanography*, 30(6):1461–1471.

Gregory, J. M., N. Bouttes, S. M. Griffies, H. Haak, W. J. Hurlin, J. Jungclaus, M. Kelley, W. G. Lee, J. Marshall, A. Romanou, O. A. Saenko, D. Stammer, and M. Winton
2016. The flux-anomaly-forced model intercomparison project (fafmip) contribution to cmip6: investigation of sea-level and ocean climate change in response to co$_2$ forcing. *Geoscientific Model Development*, 9(11):3993–4017.

Gregory, J. M. and J. A. Lowe
2000. Predictions of global and regional sea-level rise using AOGCMs with and without flux adjustments. *Geophysical Research Letters*, 27:3069–3072.

Griffies, S. M. and K. Bryan
1997. A predictability study of simulated North Atlantic multidecadal variability. *Climate dynamics*, 13:459 487.

Griffies, S. M. and R. W. Hallberg
2000. Biharmonic friction with a smagorinsky-like viscosity for use in large-scale eddy-permitting ocean models. *Monthly Weather Review*, 128(8):2935–2946.

Haidvogel, D. B. and P. B. Rhines
1983. Waves and circulation driven by oscillatory winds in an idealized ocean basin. *Geophysical & Astrophysical Fluid Dynamics*, 25(1-2):1–63.

Häkkinen, S.
2001. Variability in sea surface height: A qualitative measure for the meridional overturning in the North Atlantic. *Journal of Geophysical Research*, 106(C7):13837.

Häkkinen, S., P. B. Rhines, and D. L. Worthen
2011. Warm and saline events embedded in the meridional circulation of the northern north atlantic. *Journal of Geophysical Research: Oceans*, 116(C3):0148–0227.

Häkkinen, S., P. B. Rhines, and D. L. Worthen
2013. Northern North Atlantic sea surface height and ocean heat content variability. *Journal of Geophysical Research: Oceans*, 118(7):3670–3678.

Han, W., G. A. Meehl, D. Stammer, A. Hu, B. Hamlington, J. Kenigson, H. Palanisamy, and P. Thompson
2017. Spatial patterns of sea level variability associated with natural internal climate modes. *Surveys in Geophysics*, 38(1):217–250.

Hatun, H., A. B. Sando, H. Drange, and B. Hansen
2005. Influence of the Atlantic Subpolar Gyre on the Thermohaline Circulation. *Science*, 309:1841–1844.

Hawkins, E., J. Robson, R. Sutton, D. Smith, and N. Keenlyside
2011. Evaluating the potential for statistical decadal predictions of sea surface temperatures with a perfect model approach. *Climate dynamics*, 37:2495 2509.

Hawkins, E. and R. Sutton
2009. Decadal Predictability of the Atlantic Ocean in a Coupled GCM: Forecast Skill and Optimal Perturbations Using Linear Inverse Modeling. *J. Climate*, 22:3960–3978.

Hazeleger, W. and S. S. Drijfhout
2000. A model study on internally generated variability in subtropical mode water formation. *Journal of Geophysical Research: Oceans*, 105(C6):13965–13979.

Hewitt, H. T., M. J. Bell, E. P. Chassignet, A. Czaja, D. Ferreira, S. M. Griffies, P. Hyder, J. L. McClean, A. L. New, and M. J. Roberts
2017. Will high-resolution global ocean models benefit coupled predictions on short-range to climate timescales? *Ocean Modelling*, 120:120 – 136.

Hinkel, J., D. Lincke, A. T. Vafeidis, M. Perrette, R. J. Nicholls, R. S. J. Tol, B. Marzeion, X. Fettweis, C. Ionescu, and A. Levermann
2014. Coastal flood damage and adaptation costs under 21st century sea-level rise. *Proceedings of the National Academy of Sciences of the United States of America*, 111.9:3292–3297.

Hogg, N. G.
1992. On the transport of the gulf stream between cape hatteras and the grand banks. *Deep Sea Research Part A. Oceanographic Research Papers*, 39(7):1231 – 1246.

Hsieh, W. W. and K. Bryan
1996. Redistribution of sea level rise associated with enhanced greenhouse warming: a simple model study. *Climate Dynamics*, 12(8):535–544.

Hu, A. and C. Deser
2013. Uncertainty in future regional sea level rise due to internal climate variability. *Geophysical Research Letters*, 40(11):2768–2772.

Huck, T., O. Arzel, and F. Sèvellec
2015. Multidecadal variability of the overturning circulation in presence of eddy turbulence. *Journal of Physical Oceanography*, 45(1):157–173.

Hughes, C. W. and E. R. Ash
2001. Eddy forcing of the mean flow in the Southern Ocean. *Journal of Geophysical Research*, 106(C2):2713.

Hughes, C. W. and S. D. P. Williams
2010. The color of sea level: Importance of spatial variations in spectral shape for assessing the significance of trends. *Journal of Geophysical Research: Oceans 1978-2012*, 115(C10048):18.

Hurrell, J. and National Center for Atmospheric Research Staff (Eds)
2017. The climate data guide: Hurrell north atlantic oscillation (nao) index (station-based). `https://climatedataguide.ucar.edu/climate-data/`

`hurrell-north-atlantic-oscillation-nao-index-station-based.`
Accessed:2018-01-5.

Huthnance, J. M.
1989. Internal tides and waves near the continental shelf edge. *Geophysical & Astrophysical Fluid Dynamics*, 48(1-3):81–106.

Isachsen, P. E., J. H. LaCasce, and J. Pedlosky
2007. Rossby wave instability and apparent phase speeds in large ocean basins. *Journal of Physical Oceanography*, 37(5):1177–1191.

Jayne, S. R., N. G. Hogg, and P. Malanotte-Rizzoli
1996. Recirculation gyres forced by a beta-plane jet. *Journal of Physical Oceanography*, 26(4):492–504.

Jia, L. and T. DelSole
2011. Diagnosis of multiyear predictability on continental scales. *Journal of Climate*, 24(19):5108–5124.

Jiang, S., F.-F. Jin, and M. Ghil
1995. Multiple equilibria, periodic, and aperiodic solutions in a wind-driven, double-gyre, shallow-water model. *Journal of Physical Oceanography*, 25(5):764–786.

Johnson, H. L. and D. P. Marshall
2002. A theory for the surface atlantic response to thermohaline variability. *Journal of Physical Oceanography*, 32(4):1121–1132.

Juricke, S., T. N. Palmer, and L. Zanna
2017. Stochastic subgrid-scale ocean mixing: Impacts on low-frequency variability. *Journal of Climate*, 30(13):4997–5019.

Kanzow, T., H. L. Johnson, D. P. Marshall, S. A. Cunningham, J. J.-M. Hirschi, A. Mujahid, H. L. Bryden, and W. E. Johns
2009. Basinwide integrated volume transports in an eddy-filled ocean. *Journal of Physical Oceanography*, 39(12):3091–3110.

Katsman, C. A., S. S. Drijfhout, and H. A. Dijkstra
2001. The interaction of a deep western boundary current and the wind-driven gyres as a cause for low-frequency variability. *Journal of Physical Oceanography*, 31(8):2321–2339.

Kleeman, R.

2002. Measuring dynamical prediction utility using relative entropy. *Journal of the atmospheric sciences*, 59.13.

Kwon, Y.-O., M. A. Alexander, N. A. Bond, C. Frankignoul, H. Nakamura, B. Qiu, and L. A. Thompson

2010. Role of the gulf stream and kuroshio-oyashio systems in large-scale atmosphere-ocean interaction: A review. *Journal of Climate*, 23(12):3249–3281.

Köhl, A.

2014. Detecting processes contributing to interannual halosteric and thermosteric sea level variability. *Journal of Climate*, 27(6):2417–2426.

Landerer, F. W., P. J. Gleckler, and T. Lee

2014. Evaluation of cmip5 dynamic sea surface height multi-model simulations against satellite observations. *Climate Dynamics*, 43(5):1271–1283.

Latif, M., M. Collins, H. Pohlmann, and N. Keenlyside

2006. A review of predictability studies of atlantic sector climate on decadal time scales. *Journal of Climate*, 19(23):5971–5987.

Lillibridge, J. L. and A. J. Mariano

2013. A statistical analysis of gulf stream variability from 18+ years of altimetry data. *Deep Sea Research Part II: Topical Studies in Oceanography*, 85:127 – 146. Modern Physical Oceanography and Professor H.T. Rossby.

Lindzen, R. S. and B. Farrell

1980. A simple approximate result for the maximum growth rate of baroclinic instabilities. *Journal of the Atmospheric Sciences*, 37(7):1648–1654.

Lombard, A., A. Cazenave, P. Y. Le Traon, and M. Ishii

2005. Contribution of thermal expansion to present-day sea level rise revisited. *Glob. Planet. Change*, 47:1–16.

Lorenz, E.

1993. *The Essence of Chaos.* Seattle, WA: University of Washington Press.

Lorenz, E. N.

1956. Empirical orthogonal functions and statistical weather prediction. *Statistical Forecasting Scientific Rep. 1, Department of Meteorology, Massachusetts Institute of Technology, Cambridge, MA, 57 pp.*

Lorenz, E. N.
1963. Deterministic nonperiodic flow. *Journal of the atmospheric sciences*, 20:130 141.

Lorenz, E. N.
1975. Climatic predictability. *WMO The Phys. Basis of Climate and Climate Modellings*, P. 132 136.

Lyu, K., X. Zhang, J. A. Church, and J. Hu
2015. Quantifying internally generated and externally forced climate signals at regional scales in cmip5 models. *Geophysical Research Letters*, 42(21):9394–9403.

Mahadevan, A., J. Lu, S. P. Meacham, and P. Malanotte-Rizzoli
2001. The predictability of large-scale wind-driven flows. *Nonlinear Processes in Geophysics*, 8(6):449–465.

Marshall, J., A. Adcroft, C. Hill, L. Perelman, and C. Heisey
1997a. A finite-volume, incompressible navier stokes model for studies of the ocean on parallel computers. *Journal of Geophysical Research: Oceans*, 102(C3):5753–5766.

Marshall, J., C. Hill, L. Perelman, and A. Adcroft
1997b. Hydrostatic, quasi-hydrostatic, and nonhydrostatic ocean modeling. *Journal of Geophysical Research: Oceans*, 102(C3):5733–5752.

Marshall, J., H. Johnson, and J. Goodman
2001. A study of the interaction of the north atlantic oscillation with ocean circulation. *Journal of Climate*, 14(7):1399–1421.

Maximenko, N. A., B. Bang, and H. Sasaki
2005. Observational evidence of alternating zonal jets in the world ocean. *Geophysical Research Letters*, 32(12):L12607.

McCalpin, J. D. and D. B. Haidvogel
1996. Phenomenology of the low-frequency variability in a reduced-gravity, quasi-geostrophic double-gyre model. *Journal of Physical Oceanography*, 26(5):739–752.

Meehl, G. a., L. Goddard, G. Boer, R. Burgman, G. Branstator, C. Cassou, S. Corti, G. Danabasoglu, F. Doblas-Reyes, E. Hawkins, A. Karspeck, M. Kimoto, A. Kumar, D. Matei, J. Mignot, R. Msadek, A. Navarra, H. Pohlmann, M. Rienecker,

T. Rosati, E. Schneider, D. Smith, R. Sutton, H. Teng, G. J. van Oldenborgh, G. Vecchi, and S. Yeager
2014. Decadal Climate Prediction: An Update from the Trenches. *Bulletin of the American Meteorological Society*, 95(2):243–267.

Meehl, G. A., L. Goddard, J. Murphy, R. J. Stouffer, G. Boer, G. Danabasoglu, K. Dixon, M. A. Giorgetta, A. M. Greene, E. Hawkins, G. Hegerl, D. Karoly, N. Keenlyside, M. Kimoto, B. Kirtman, A. Navarra, R. Pulwarty, D. Smith, D. Stammer, and T. Stockdale
2009. Decadal prediction. *Bulletin of the American Meteorological Society*, 90(10):1467–1486.

Megann, A., D. Storkey, Y. Aksenov, S. Alderson, D. Calvert, T. Graham, P. Hyder, J. Siddorn, and B. Sinha
2014. Go5. 0: The joint nerc-met office nemo global ocean model for use in coupled and forced applications. *Geoscientific Model Development*, 7(3):1069–1092.

Meyssignac, B., C. G. Piecuch, C. J. Merchant, M.-F. Racault, H. Palanisamy, C. MacIntosh, S. Sathyendranath, and R. Brewin
2017. Causes of the regional variability in observed sea level, sea surface temperature and ocean colour over the period 1993–2011. *Surveys in Geophysics*, 38(1):187–215.

Miles, E. R., C. M. Spillman, J. A. Church, and P. C. McIntosh
2014. Seasonal prediction of global sea level anomalies using an ocean–atmosphere dynamical model. *Climate Dynamics*, 43(7-8):2131–2145.

Mitrovica, J. X., N. Gomez, and P. U. Clark
2009. The sea-level fingerprint of West Antarctic collapse. *Science*, 323:753.

Moore, A. M., C. L. Perez, and J. Zavala-Garay
2002. A non-normal view of the wind-driven ocean circulation. *Journal of Physical Oceanography*, 32(9):2681–2705.

Mu, M., W. S. Duan, and B. Wang
2003. Conditional nonlinear optimal perturbation and its applications. *Nonlinear Processes in Geophysics*, 10(6):493–501.

Munk, W. H.
1950. On the wind-driven ocean circulation. *Journal of Meteorology*, 7(2):80–93.

Newman, M.
2007. Interannual to decadal predictability of tropical and north pacific sea surface temperatures. *Journal of Climate*, 20(11):2333–2356.

Newman, M.
2013. An empirical benchmark for decadal forecasts of global surface temperature anomalies. *Journal of Climate*, 26.14:5260–5269.

Nicholls, R. J.
2004. Coastal flooding and wetland loss in the 21st century: changes under the SRES climate and socio economic scenarios. *Global Environmental Change Human and Policy Dimensions*, 14:69 86.

Nonaka, M., Y. Sasai, H. Sasaki, B. Taguchi, and H. Nakamura
2016. How potentially predictable are midlatitude ocean currents? *Scientific Reports*, 6(10):20153.

North, G. R., T. L. Bell, R. F. Cahalan, and F. J. Moeng
1982. Sampling errors in the estimation of empirical orthogonal functions. *Monthly Weather Review*, 110(7):699–706.

Obukhov, A. M.
1947. Statistically homogeneous fields on a sphere. *Uspethi Mathematicheskikh Nauk*, XXII:196 198.

O'Reilly, C. H., A. Czaja, and J. H. LaCasce
2012. The emergence of zonal ocean jets under large-scale stochastic wind forcing. *Geophysical Research Letters*, 39(11):L11606.

O'Reilly, C. H., S. Minobe, A. Kuwano-Yoshida, and T. Woollings
2017. The gulf stream influence on wintertime north atlantic jet variability. *Quarterly Journal of the Royal Meteorological Society*, 143(702):173–183.

Osychny, V. and P. Cornillon
2004. Properties of rossby waves in the north atlantic estimated from satellite data. *Journal of Physical Oceanography*, 34(1):61–76.

O'Rourke, A. K., B. K. Arbic, and S. M. Griffies
2018. Frequency-domain analysis of atmospherically forced versus intrinsic ocean surface kinetic energy variability in gfdl's cm2-o model hierarchy. *Journal of Climate*, 31(5):1789–1810.

Palmer, T. and R. Hagedorn, eds.
2006. *Predictability of Weather and Climate*. Cambridge University Press. Cambridge Books Online.

Penduff, T., M. Juza, B. Barnier, J. Zika, W. K. Dewar, A.-M. Treguier, J.-M. Molines, and N. Audiffren
2011. Sea level expression of intrinsic and forced ocean variabilities at interannual time scales. *Journal of Climate*, 24(21):5652–5670.

Penland, C.
1989. Random forcing and forecasting using principal oscillation pattern analysis. *Monthly Weather Review*, 117.10:2165–2185.

Penland, C. and P. D. Sardeshmukh
1995. The Optimal Growth of Tropical Sea Surface Temperature Anomalies. *J. Climate*, 8:1999–2024.

Piecuch, C. and R. Pontre
2011. Mechanisms of interannual steric sea level variability. *Geophysical Research Letters*, 38.15:L15605.

Pierini, S.
2014. Kuroshio extension bimodality and the north pacific oscillation: A case of intrinsic variability paced by external forcing. *Journal of Climate*, 27(1):448–454.

Pierini, S., H. a. Dijkstra, and M. Mu
2014. Intrinsic low-frequency variability and predictability of the Kuroshio Current and of its extension. *Advances in Oceanography and Limnology*, 5(2):79–122.

Polkova, Iuliia, A. K. and D. Stammer
2015. Predictive skill for regional interannual steric sea level and mechanisms for predictability. *Journal of Climate*, P. 7407–7419.

Primeau, F.
2002. Long rossby wave basin-crossing time and the resonance of low-frequency basin modes. *Journal of Physical Oceanography*, 32(9):2652–2665.

Qiu, B.
2000. Interannual Variability of the Kuroshio Extension System and Its Impact on the Wintertime SST Field. *Of, Journal Oceanography, Physical*, 30(6):1486–1502.

Qiu, B.

2002. Large-scale variability in the midlatitude subtropical and subpolar north pacific ocean: Observations and causes. *Journal of Physical Oceanography*, 32(1):353–375.

Qiu, B. and S. Chen

2005. Variability of the Kuroshio Extension Jet, Recirculation Gyre, and Mesoscale Eddies on Decadal Time Scales. *Journal of Physical Oceanography*, 35(11):2090–2103.

Qiu, B. and S. Chen

2006. Decadal variability in the large-scale sea surface height field of the south pacific ocean: Observations and causes. *Journal of Physical Oceanography*, 36(9):1751–1762.

Qiu, B. and S. Chen

2010. Eddy-mean flow interaction in the decadally modulating Kuroshio Extension system. *Deep Sea Research Part II: Topical Studies in Oceanography*, 57(13-14):1098–1110.

Qiu, B., S. Chen, N. Schneider, and B. Taguchi

2014. A Coupled Decadal Prediction of the Dynamic State of the Kuroshio Extension System. *Journal of Climate*, 27(4):1751–1764.

Quattrocchi, G., S. Pierini, and H. a. Dijkstra

2012. Intrinsic low-frequency variability of the Gulf Stream. *Nonlinear Processes in Geophysics*, 19(2):155–164.

Rhines, P. B.

1977. *The dynamics of insteady currents. The Sea,*. Wiley and Sons.

Richards, K., N. Maximenko, F. Bryan, and H. Sasaki

2006. Zonal jets in the pacific ocean. *Geophysical research letters*, 33(3):L03605.

Roberts, C. D., D. Calvert, N. Dunstone, L. Hermanson, M. D. Palmer, and D. Smith

2016. On the drivers and predictability of seasonal-to-interannual variations in regional sea level. *Journal of Climate*, 29(21):7565–7585.

Roden, G. I.

2000. Flow and water property structures between the bering sea and fiji in the summer of 1993. *Journal of Geophysical Research: Oceans*, 105(C12):28595–28612.

Sallenger, A. H., K. S. Doran, and P. A. Howd
2012. Hotspot of accelerated sea-level rise on the atlantic coast of north america. *Nature Climate Change*, 2(12):884–888.

Sapsis, T. P. and H. a. Dijkstra
2013. Interaction of Additive Noise and Nonlinear Dynamics in the Double-Gyre Wind-Driven Ocean Circulation. *Journal of Physical Oceanography*, 43(2):366–381.

Sarachik, E. S. and M. A. Cane
2010. *The El Niño-Southern Oscillation Phenomenon.* Cambridge University Press.

Sasaki, Y. N. and N. Schneider
2011. Interannual to decadal gulf stream variability in an eddy resolving ocean model. *Ocean Modelling*, 39.3:209–219.

Scaife, A. A., D. Copsey, C. Gordon, C. Harris, T. Hinton, S. Keeley, A. O'Neill, M. Roberts, and K. Williams
2011. Improved atlantic winter blocking in a climate model. *Geophysical Research Letters*, 38(23).

Schneider, T. and S. M. Griffies
1999. A Conceptual Framework for Predictability Studies. *Journal of Climate*, 12:3133–3155.

Sérazin, G., T. Penduff, B. Barnier, J.-M. Molines, B. K. Arbic, M. Ḿuller, and L. Terray
2018. Inverse cascades of kinetic energy as a source of intrinsic variability: A global ogcm study. *Journal of Physical Oceanography*, 48(6):1385–1408.

Sérazin, G., T. Penduff, S. Grégorio, B. Barnier, J.-M. Molines, and L. Terray
2015. Intrinsic Variability of Sea Level from Global Ocean Simulations: Spatiotemporal Scales. *Journal of Climate*, 28(10):4279–4292.

Shimokawa, S. and T. Matsuura
2010. Chaotic behaviors in the response of a quasigeostrophic oceanic double gyre to seasonal external forcing. *Journal of Physical Oceanography*, 40(7):1458–1472.

Simonnet, E. and H. a. Dijkstra
2002. Spontaneous Generation of Low-Frequency Modes of Variability in the Wind-Driven Ocean Circulation. *Journal of Physical Oceanography*, 32(6):1747–1762.

Simonnet, E., M. Ghil, and H. Dijkstra
2005. Homoclinic bifurcations in the quasi-geostrophic double-gyre circulation. *Journal of Marine Research*, 63(5):931–956.

Slangen, A. B. A., M. Carson, C. A. Katsman, R. S. W. van de Wal, A. Köhl, L. L. A. Vermeersen, and D. Stammer
2014. Projecting twenty-first century regional sea-level changes. *Climatic Change*, 124(1-2):317–332.

Smagorinsky, J.
1963. General circulation experiments with the primitive equations. *Monthly Weather Review*, 91(3):99–164.

Sonnewald, M., C. Wunsch, and P. Heimbach
2018. Linear predictability: A sea surface height case study. *Journal of Climate*, 31(7):2599–2611.

Spall, M.
1996. Dynamics of the Gulf Stream/deep western boundary current crossover. Part II: Low-frequency internal oscillations. *Journal of Physical Oceanography*, P. 2169–2182.

Stammer, D.
2008. Response of the global ocean to Greenland and Antarctic ice melting. *Journal of Geophysical Reseach*, 113:C06022.

Stammer, D., A. Cazenave, R. M. Ponte, and M. E. Tamisiea
2013. Causes for contemporary regional sea level changes. *Annual Review of Marine Science*, 5(1):21–46.

Sterlini, P., H. de Vries, and C. Katsman
2016. Sea surface height variability in the north east atlantic from satellite altimetry. *Climate Dynamics*, 47(3):1285–1302.

Stommel, H.
1948. The western intensification of wind driven ocean currents. *Trans. Am. Geophys. Union*, 29:202–206.

Stommel, H.
1979. Determination of water mass properties of water pumped down from the

ekman layer to the geostrophic flow below. *Proceedings of the National Academy of Sciences*, 76(7):3051–3055.

Sura, P. and C. Penland
2002. Sensitivity of a double-gyre ocean model to details of stochastic forcing. *Ocean Modelling*, 4(3):327 – 345.

Sutton, R. T. and M. Allen
1997. Decadal predictability of north atlantic sea surface temperature and climate. *Nature*, 388:6642.

Sverdrup, H. U.
1947. Wind-driven currents in a baroclinic ocean; with application to the equatorial currents of the eastern pacific. *Proceedings of the National Academy of Sciences of the United States of America*, 33(11):318.

Sérazin, G., B. Meyssignac, T. Penduff, L. Terray, B. Barnier, and J. Molines
2016. Quantifying uncertainties on regional sea level change induced by multidecadal intrinsic oceanic variability. *Geophysical Research Letters*, 43(15):8151–8159.

Taguchi, B., B. Qiu, M. Nonaka, H. Sasaki, S.-P. Xie, and N. Schneider
2010. Decadal variability of the kuroshio extension: Mesoscale eddies and recirculations. *Ocean Dynamics*, 60:673–691.

Taguchi, B., S.-P. Xie, N. Schneider, M. Nonaka, H. Sasaki, and Y. Sasai
2007. Decadal variability of the kuroshio extension: Observations and an eddy-resolving model hindcast. *Journal of Climate*, 20(11):2357–2377.

Talley, L. D., G. L. Pickard, W. J. Emery, and J. H. Swift
2011. *Descriptive Physical Oceanography An Introduction.* Elsevier.

Talley, L. D. and M. E. Raymer
1982. Eighteen degree water variability. *Journal of Marine Research*, 40:757–775. n/a.

Thompson, A. F. and K. J. Richards
2011. Low frequency variability of southern ocean jets. *Journal of Geophysical Research: Oceans*, 116(C9).

Toole, J., R. Curry, T. Joyce, M. McCartney, and B. Peña-Molino
2011. Transport of the north atlantic deep western boundary current about 39 n, 70 w: 2004–2008. *Deep Sea Research Part II: Topical Studies in Oceanography*, 58(17):1768 – 1780. Climate and the Atlantic Meridional Overturning Circulation.

Vallis, G. K.
2006. *Atmospheric and Oceanic Fluid Dynamics.* Cambridge, U.K.: Cambridge University Press.

Wang, B.
2015. *Encyclopedia of Atmospheric Sciences (Second Edition).* Academic Press.

Wang, Q., M. Mu, and H. a. Dijkstra
2013. The similarity between optimal precursor and optimally growing initial error in prediction of Kuroshio large meander and its application to targeted observation. *Journal of Geophysical Research: Oceans*, 118(2):869–884.

Wang, Q., Y. Tang, S. Pierini, and M. Mu
2017. Effects of singular-vector-type initial errors on the short-range prediction of kuroshio extension transition processes. *Journal of Climate*, 30(15):5961–5983.

Wang, Z., Y. Lu, F. Dupont, J. W. Loder, C. Hannah, and D. G. Wright
2015. Variability of sea surface height and circulation in the north atlantic: Forcing mechanisms and linkages. *Progress in Oceanography*, 132:273 – 286. Oceanography of the Arctic and North Atlantic Basins.

Waterman, S. and B. J. Hoskins
2013. Eddy shape, orientation, propagation, and mean flow feedback in western boundary current jets. *Journal of Physical Oceanography*, 43(8):1666–1690.

Waterman, S. and S. R. Jayne
2011. Eddy-Mean Flow Interactions in the Along-Stream Development of a Western Boundary Current Jet: An Idealized Model Study. *Journal of Physical Oceanography*, 41(4):682–707.

Waterman, S. N.
2009. *Eddy-mean flow interactions in western boundary current jets.* PhD thesis, MIT, Woods Hole, MA.

Williams, K. D., C. M. Harris, A. Bodas-Salcedo, J. Camp, R. E. Comer, D. Copsey, D. Fereday, T. Graham, R. Hill, T. Hinton, P. Hyder, S. Ineson, G. Masato, S. F. Milton, M. J. Roberts, D. P. Rowell, C. Sanchez, A. Shelly, B. Sinha, D. N. Walters, A. West, T. Woollings, and P. K. Xavier
2015. The met office global coupled model 2.0 (gc2) configuration. *Geoscientific Model Development*, 8(5):1509–1524.

Williams, P. D., N. J. Howe, J. M. Gregory, R. S. Smith, and M. M. Joshi
2016. Improved climate simulations through a stochastic parameterization of ocean eddies. *Journal of Climate*, 29(24):8763–8781.

Wilson, C. and R. G. Williams
2004. Why are eddy fluxes of potential vorticity difficult to parameterize? *Journal of Physical Oceanography*, 34(1):142–155.

Wunsch, C.
1999. The interpretation of short climate records, with comments on the north atlantic and southern oscillations. *Bulletin of the American Meteorological Society*, 80(2):245–255.

Wunsch, C.
2013. Covariances and linear predictability of the Atlantic Ocean. *Deep Sea Research Part II: Topical Studies in Oceanography*, 85:228–243.

Wunsch, C. and P. Heimbach
2013. Two Decades of the Atlantic Meridional Overturning Circulation: Anatomy, Variations, Extremes, Prediction and Overcoming Its Limitations. *Journal of Climate*, 26.

Xue, Y. and A. Leetmaa
2000. Forecasts of tropical pacific sst and sea level using a markov model. *Geophysical research letters*, 27(17):2701–2704.

Yin, J., M. Schlesinger, and R. Stouffer
2009. Model projections of rapid sea level rise on the northeast coast of the United States. *Nature Geoscience*, 2:262.

Zanna, L.
2012. Forecast Skill and Predictability of Observed Atlantic Sea Surface Temperatures. *Journal of Climate*, 25(14):5047–5056.

Zanna, L. and E. Tziperman
2005. Nonnormal amplification of the thermohaline circulation. *Journal of Physical Oceanography*, 35(9):1593–1605.

Zanna, L. and E. Tziperman
2008. Optimal Surface Excitation of the Thermohaline Circulation. *Journal of Physical Oceanography*, 38(8):1820–1830.

Zhai, X., H. L. Johnson, and D. P. Marshall
2010. Significant sink of ocean-eddy energy near western boundaries. *Nature Geoscience*, 3(9):608–612.

Zhang, X., M. Mu, Q. Wang, and S. Pierini
2017. Optimal precursors triggering the kuroshio extension state transition obtained by the conditional nonlinear optimal perturbation approach. *Advances in Atmospheric Sciences*, 34(6):685–699.